UNIVERSITÀ
DEGLI STUDI
DI PADOVA

Sede Amministrativa: Università degli Studi di Padova
Dipartimento di Fisica e Astronomia "Galileo Galilei"

CORSO DI DOTTORATO DI RICERCA IN FISICA
CICLO XXXI

Glimpsing at the primordial perturbation field

Tesi redatta con il contributo finanziario di INFN

Vice coordinatore: Ch.ma Prof. Cinzia Sada

Supervisore: Ch.mo Prof. Nicola Bartolo

Co-Supervisore: Ch.mo Dott. Michele Liguori

Dottorando: Andrea Ravenni

Abstract

In this thesis I will focus on "non-minimal" properties of the primordial perturbation field; both analysing data, and assessing the constraining power of novel probes. In particular, I will address the problem of finding deviations from a power-law primordial power spectrum, the possibility of better constraining compensated isocurvature perturbations, and detect primordial non-Gaussianity in an ample range of scales.

I present a minimally parametric, model independent reconstruction of the shape of the primordial power spectrum. We use a comprehensive set of the state-of the art cosmological data: *Planck* observations of the temperature and polarisation anisotropies of the cosmic microwave background (CMB), WiggleZ and Sloan Digital Sky Survey Data Release 7 galaxy power spectra, and the Canada-France-Hawaii Lensing Survey correlation function. This reconstruction strongly supports the evidence for a power law primordial power spectrum with a red tilt and disfavours deviations from a power law power spectrum including small-scale power suppression such as that induced by significantly massive neutrinos. This offers a powerful confirmation of the inflationary paradigm, justifying the adoption of the inflationary prior in cosmological analyses.

We develop a linear perturbation theory for the spectral y-distortions of the CMB. The y-distortions generated during the recombination epoch are usually negligible because the energy transfer due to the Compton scattering is strongly suppressed at that time, but they can be significant if there is are compensated isocurvature perturbations with large amplitude. Since y-distortions explicitly depend on the baryon density fluctuations, they can be used to detect and constrain compensated isocurvature perturbations (CIPs) models. We compute the cross correlation functions of the y-distortions with the CMB temperature and the

E-mode polarization anisotropies (T, E respectively). We investigate how well measurements of y-anisotropies provided by a PIXIE-like and a PRISM-like survey, LiteBIRD, and a cosmic variance limited (CVL) survey, will constrain $f' = \Delta^2_{\zeta\mathrm{CIP}}/\Delta^2_{\zeta\zeta}$, and find that the degradation in constraining power due to the presence of Sunyaev Zel'dovich effect from galaxy clusters will prevent detections unless the amplitude of CIP is unnaturally high, with forecasted upper limits of, *e.g.*, $f' < 2\times10^5$ (68% C.L.) with LiteBIRD, and $f' < 2\times10^4$ (68% C.L.) with CVL observations.

Cross-correlations between CMB temperature and y-distortions anisotropies have been previously proposed as a way to measure the local bispectrum parameter $f^{\mathrm{loc}}_{\mathrm{NL}}$ in a range of scales much smaller than those accessible to CMB primary anisotropies. Unfortunately, the primordial y-T signal is strongly contaminated by the late-time correlation between the Integrated Sachs Wolfe and Sunyaev-Zeldovich (SZ) effects. Moreover, SZ itself generates a large noise contribution in the y-parameter map. We consider two original ways to address these issues: To remove the bias due to the SZ-CMB temperature coupling, while also adding new signal, we include in the analysis the y-E cross-correlation. In order to reduce the noise, we propose to clean the y-map by subtracting a SZ template, reconstructed via cross-correlation with external tracers. We combine this SZ template subtraction with the previously adopted solution of directly masking detected clusters. Our forecasts show that, using y-distortions, a PRISM-like survey can achieve $f^{\mathrm{loc}}_{\mathrm{NL}} < 300$ (68% C.L.), while an ideal experiment will achieve $f^{\mathrm{loc}}_{\mathrm{NL}} < 130$, with improvements of a factor ~ 3 from adding the y-E signal, and a further $20\sim30\%$ from template cleaning. These forecasts are much worse than current $f^{\mathrm{loc}}_{\mathrm{NL}}$ boundaries from Planck, but we stress again that they refer to completely different scales.

Acknowledgements

The story of this thesis starts much before any of the following have been typed for the first time. It even starts much before the beginning of my PhD studies. Actually it does not even start with a when, but rather with a where. I had the privilege to live in Padova and to study and work at the *Dipartimento di Fisica* for most of my adult life. It is thanks to all the wonderful people that I have met there that I am now in the position to write these words. And I have to be grateful to two in particular, that have been first my teachers, then my supervisors, and now my mentors. Nicola, Michele, thank you for helping me fulfil my childhood dream.

A similar thanks goes to Jens, as you decided it was fine for me to bug you for months, got me in as if I was part of the crew, and patiently guided me on a path that was completely knew.

A thank to the many companions that shared this path with me: Abir, Aditya, Boris, Dionysis, Giampà, Giorgio, Maria Chiara, Mathieu, Luke, Pippo, Purnendu. Working with you I learnt all the things you cannot find on arXiv, and often those are the more important.

Clara, Ele, Giulia, Jacy, Maddy, Pie e Rebe non potete immaginare quanto voglia dire sentirvi vicini, e sapere che ci siete sempre. Grazie per essere la mia costante.

Grazie alla mia *miglior compagna di ufficio* Valentina, a Davide e a Pobbe, avete portato il sole nelle giornate di nebbia.

Un ringraziamento speciale va a Ave, Carlo e Marco, che in troppe occasioni, con la scusa di fare uno *scozzino*, siete stati la voce della ragione. Per non parlare dell'aiuto nello stimare ogni singolo valore numerico.

Thanks Slađa. It was by luck that you entered my life when everything seemed to be working against me. But it was your merit that I never hit rock bottom.

Concludo con le due persone più importanti su questa lista, Mamma e Babbo. Come ho scritto, questa tesi è il punto fermo al termine di qualcosa molto più lungo del solo dottorato. Dunque vi ringrazio per tutto quello che mi donate ed avete donato da sempre, per essere stati al mio fianco ed avermi sempre dato fiducia (con l'unica — *l'unica!* — eccezione di quando dovevo dare Analisi 1). Grazie di tutto l'amore del mondo.

Contents

"I love deadlines.
I love the whooshing noise they make as they go by."
— Douglas Adams, The Salmon of Doubt

Introduction

All recent cosmological observations are in excellent agreement with the standard ΛCDM model: a spatially flat cosmology model, with matter-energy density dominated by a cosmological constant and cold dark matter, where neutrinos are effectively massless and where the primordial perturbation field was adiabatic and Gaussian, with a power spectrum that is a (almost scale invariant) power law. State-of-the art cosmological observations such as those of the *Planck* satellite [1], measuring cosmic microwave background (CMB) temperature and polarization anisotropies (respectively T and E), provided us with very precise measurements of the parameters of this standard cosmological model [2]. The same kind of observations strongly suggest that the primordial density perturbations were adiabatic; this implies that the number densities of photons, baryons, cold dark matter, and neutrinos fluctuate in the same way [2]. Moreover, the tightest constraints on all parametrizations and models of primordial non-Gaussianity (NG), which also come from *Planck* measurements, in this case of the bispectrum of the CMB anisotropies, are all compatible with 0 [3].

However, does this allow us to be satisfied with our current understanding of the Universe, or should this spur us to search for deviations from the established model, and develop new test that might shed light on new physics? Moved by this second approach, in this thesis I will focus on "non-minimal" properties of the primordial perturbation field; both analysing data, and assessing the constraining power of novel probes. In particular, I will address the problem of finding deviations from a power-law primordial power spectrum, the possibility of further constraining compensated isocurvature perturbations, and detecting primordial non-Gaussianity on an ample range of scales.

Most cosmological analyses assume a power-law primordial power spectrum with a fixed spectral index, and deviations from this assumption are often in the form of a "running" of the spectral index. A nearly scale invariant power spectrum is a generic prediction of the simplest models of inflation, but there are models with (small) deviations from this prediction (e.g., [4–7]). Indeed, small deviations from scale invariance constitute

a critical and generic prediction of inflation. For this reason a model-independent reconstruction of the primordial power spectrum (PPS) shape can be a powerful test of inflationary models. In Section 3.1, which is based on the paper

> **A. Ravenni**, L. Verde and A. J. Cuesta. *"Red, straight, no bends: primordial power spectrum reconstruction from CMB and large-scale structure"*. JCAP 2016, no. 08 028. arXiv:1605.06637,

I will show the results of a minimally parametric reconstruction of the PPS using smoothing spline interpolation in combination with cross validation.

Departure from adiabatic perturbations, such as isocurvature perturbations change the CMB temperature angular power spectrum drastically, and they are therefore constrained very tightly. However in a specific model is it possible to have the baryon isocurvature perturbations cancel exactly with the cold dark matter ones — hence the name of compensated isocurvature perturbations (CIPs) — at linear level in the CMB spectra [8]. The CIPs are less constrained compared to the observed adiabatic perturbations and the other isocurvature perturbations, so it is in principle interesting to propose novel ways to constrain them. In section Section 3.2 I will review the possibility of observing the CIPs using CMB spectral distortion anisotropies as proposed in

> T. Haga, K. Inomata, A. Ota, and **A. Ravenni**. *"Exploring compensated isocurvature perturbations with CMB spectral distortion anisotropies"*. JCAP 2018, no. 08 036. arXiv: 1805.08773.

Current CMB data tightly constrain primordial non-Gaussianity, but leave completely unanswered the question if there might have been one of more field driving cosmological inflation. Multi-field Inflation in fact predicts a potentially detectable bispectrum of the local type, peaking in the so-called squeezed-limit (i.e., on wavenumber triangles with one side much smaller than the other two, indicating a correlation between large and small wavelengths). In a futuristic scenario, the authors of [9] have considered the cross-correlation between CMB temperature and μ-spectral distortion *anisotropies* as a potentially very powerful probe of squeezed-type bispectra. While fascinating, this scenario is out of reach not only with current experimental noise levels, but also taking into account proposed ambitious next generation surveys, such as PRISM [10]. Nonetheless, measurements of $f_{\rm NL}$ via correlations between CMB temperature (polarization) and CMB distortion anisotropies are interesting even before achieving such exquisite levels of sensitivity, as they allow to test possible deviations of $f_{\rm NL}$ from scale independence.

In this respect, not only μ, but also y-distortions can provide useful and interesting information, as pointed out in [10]. In Section 4.1, based on

> **A. Ravenni**, M. Liguori, N. Bartolo, and M. Shiraishi. *"Primordial non-Gaussianity with μ-type and y-type spectral distortions: exploiting Cosmic Microwave Background polarization and dealing with secondary sources"*. JCAP 2017, no. 09 042. arXiv:1707.04759,

I will extend previous analyses by considering not only y-T, but also including the cross-correlation with polarization, y-E, and by exploiting cross-correlations between SZ and external tracers (CMB and galaxy lensing) in order to minimize foregrounds.

Chapter 1.

The standard cosmological model

The need to develop a cosmological concordance model able to explain, and fit together, a plethora of different observations [11] — we will discuss some of them in the following, [12–18] is a non-exhaustive list — resulted in the conception of the ΛCDM model.

This model relies on few principles:

- There is no preferred spatial position in the Universe.
- The Universe is statistically isotropic.
- General Relativity is the correct description of gravity.
- The Universe is filled with photons, baryonic matter, neutrinos, cold dark matter, and a cosmological constant, in proportions that are experimentally determined.

While the last three points can be tested, and have been indeed tested to high degrees of accuracy, the first one is different in that it is a philosophy standpoint called *Copernican principle*.

The Copernican principle, together with Universe isotropy, would guarantee spatial homogeneity. Instead, everyday experience teaches us that the Universe is far from isotropic and homogeneous, however, these conditions are restored on scales larger than $\approx 100\,\mathrm{Mpc}$ [19–21]

If we also assume the validity of GR, the metric that describes the universe is the Friedmann-Lemaître-Robertson-Walker (FLRW) metric that I will discuss in Section 1.1.

Using the fourth ansatz we can write the Friedmann equations that describe the evolution of the Universe expansion and of its content. Those will be discussed in Section 1.2.

While not being technically included in the ΛCDM model, all the anisotropies and inhomogeneities we observe today can be evolved within the ΛCDM framework from a certain primordial perturbations field with 0 mean and power-law power spectrum. Such a field can for example be generated by an inflationary model that we will discuss in Section 1.4.

Apart from this caveats, the true power of the ΛCDM stands in the fact that is able to be highly predictive, in the sense that it can fit (almost) all the physics of the universe (at least on large scales) using only 6 free parameters

$$\omega_{\rm b},\ \omega_{\rm cdm},\ h,\ \tau_{\rm reio},\ A_{\rm s},\ n_{\rm s}\,, \tag{1.1}$$

related respectively with: the abundance of baryonic matter, and cold dark matter, the local expansion rate, the optical depth to reionization, the amplitude, and tilt of the primordial perturbations power spectrum. We will properly define all of those parameters in the rest of this chapter.

1.1. The metric, the distances

In General Relativity, space-time is described by a manifold. The presence of a matter-energy distribution gravitationally generates curvature in it and, reciprocally, space-time curvature influences the trajectory of the matter-energy distribution, which is bounded to follow the geodesics [22]. Therefore, gravitational interaction is described by the metric tensor g, which, given a coordinate system $\{x^\alpha\}$, has components $g_{\mu\nu}$.[1]

If $T^{\mu\nu}$ is the energy-momentum tensor of the matter-energy distribution, the metric $g_{\mu\nu}$ and its evolution are described by *Einstein equations*

$$R_{\mu\nu} - \frac{1}{2} g_{\mu\nu} R = 8\pi G T_{\mu\nu}\ . \tag{1.2}$$

[1] Throughout the thesis we will use Greek letters to indicate 4-dimensional objects ($\mu = 0, 1, 2, 3$), and Latin letters to indicate the 3-dimensional spacial components ($i = 1, 2, 3$).

The LHS is often referred to as the *Einstein tensor*. Here G is the Newton's gravitational constant, and $R_{\mu\nu}$ and R are respectively the *Ricci tensor* and *scalar*, that are defined contracting repeatedly the *Riemann tensor*, defined below, as $R_{\mu\nu} \equiv R^{\alpha}{}_{\mu\alpha\nu}$, $R \equiv R^{\alpha}{}_{\alpha}$. Using the *Christoffel symbols*

$$\Gamma^{\rho}{}_{\mu\nu} \equiv \frac{1}{2} g^{\rho\alpha} \left(\partial_\nu g_{\alpha\mu} + \partial_\mu g_{\alpha\nu} - \partial_\alpha g_{\mu\nu} \right) , \tag{1.3}$$

the Riemann tensor can be written as

$$R^{\rho}{}_{\sigma\mu\nu} \equiv \partial_\mu \Gamma^{\rho}{}_{\nu\sigma} - \partial_\nu \Gamma^{\rho}{}_{\mu\sigma} + \Gamma^{\rho}{}_{\mu\alpha} \Gamma^{\alpha}{}_{\nu\sigma} - \Gamma^{\rho}{}_{\nu\alpha} \Gamma^{\alpha}{}_{\mu\sigma} \, . \tag{1.4}$$

In principle we should be able to derive the expression for the metric sourced by a given energy momentum tensor solving the Einstein eq. (1.2), but this task is usually too cumbersome. Often, a useful operational approach consists in building a suitable metric based on the symmetries of the system. Since the cosmological principle ensures that the background 3-dimensional space at fixed time is maximally symmetric, it can been shown that, on large enough scales, space-time can be described by the Friedmann-Lemaître-Robertson-Walker (FLRW) metric, which is characterized by the invariant line element

$$ds^2 = -(cdt)^2 + a^2(t) \left[\frac{dr^2}{1 - kr^2} + r^2 \left(d\theta^2 + \sin^2\theta \, d\phi^2 \right) \right] . \tag{1.5}$$

Experimentally we observe that the FLRW metric applies at present time on scales $\geq 100\,\mathrm{Mpc}$. The time dependence of the metric — which is in this case solely related to the expansion of the universe — is enclosed in the *scale factor* a, quantity that we are free to normalise to be unity today $a(t_0) = 1$. Finally, the parameter k is the curvature of the 3-dimensional spatial submanifold: for $k > 0$ the universe is closed, for $k = 0$ it is flat, and for $k < 0$ it is hyperbolic. Current observations measure k compatible with 0 [14].

The scale factor relates the *physical distance* d between two point at a given time with the comoving distance

$$d(t) = a(t) r \, . \tag{1.6}$$

Since physical distances increase with time as the Universe expand, photons directed towards an observer get redshifted along their path. The wavelength $\lambda_{\rm em}$ of a photon emitted by a source at time t scales as a, hence its wavelength at present time will be

$$\lambda_0 = \frac{\lambda_{\rm em}}{a(t)}. \tag{1.7}$$

If we define the redshift as

$$z = \frac{\lambda_0 - \lambda_{\rm em}}{\lambda_0}\,, \tag{1.8}$$

we get

$$1 + z(t) = \frac{1}{a(t)}\,. \tag{1.9}$$

Therefore, the redshift of a comoving object is only a function of the ratio of scale factors of the times when the photons were emitted and detected.

In the special case of FLRW metric the information stored in the Einstein equation can be usefully expressed in terms of the Friedmann equations that we will discuss in the next section.

1.2. The background evolution

Isotropy and homogeneity ensure that in FLRW the Einstein tensor is invariant under under diffeomorphism in the isometry group. Consequently the energy-momentum tensor sourcing the FLRW metric has to be invariant under the same isometry group, hence it can be shown that T^{00} is a scalar and $T^{ij} \propto g^{ij}$.[2] This means that the cosmological fluid can be described by a relativistic perfect fluid, as we can identify T^{00} with the energy density $\rho(t)$, and the proportionality constant in $T^{ij} = p(t)g^{ij}$ with the isotropic pressure. The fluid peculiar velocity and anisotropic stresses are instead forced to be identically 0. This argument, implicitly built upon choosing the frame comoving with the fluid, can be generalized imposing that $T^{\mu\nu}$ has to transform as a tensor, to find the definition of the

[2] This descend from the fact that T^{00}, T^{0i} , and T^{ij} are maximally symmetric tensors on the fixed time 3-dimensional spatial submanifold.

cosmological fluid energy-momentum tensor valid in a generic frame

$$T^{\mu\nu} = (\rho + p)u^\mu u^\nu - pg^{\mu\nu} \,, \tag{1.10}$$

where u^μ is the fluid 4-velocity.

Inserting the explicit expression of the FLRW metric and the perfect fluid energy-momentum tensor in the Einstein eq. (1.2) one can easily derive the three Friedmann equations [23, 24].

The time-time component is equivalent to

$$H^2 \equiv \frac{\dot{a}}{a} = \frac{8\pi G}{3}\rho - \frac{k}{a^2} \,, \tag{1.11}$$

while the trace is equivalent to

$$\frac{\ddot{a}}{a} = -\frac{4\pi G}{3}\left(\rho + 3p\right), \tag{1.12}$$

and using the conservation of the energy-momentum tensor, $T^{\mu}{}_{\nu;\mu} = 0$

$$\dot{\rho} + 3H(\rho + p) = 0 \,. \tag{1.13}$$

Here we have defined the *Hubble parameter* $H \equiv \dot{a}/a$. Usually it is parametrized as

$$H \equiv \frac{\dot{a}}{a} = h\,\frac{100\,\mathrm{km\,s^{-1}}}{\mathrm{Mpc}}, \tag{1.14}$$

where h is the dimensionless *reduced Hubble constant*.

Only two of the three Friedmann equations are independent. This is a consequence of the fact that the Bianchi identity

$$R_{\alpha\beta[\mu\nu;\rho]} = 0 \tag{1.15}$$

guarantees that the LHS of Einstein's equation is covariant conserved, so the energy-momentum tensor is too.

Since only two of the Friedmann equations are linearly independent, it is necessary to specify a third constraint in order to determine the time evolution of the universe energy density, the pressure and the growth factor. To do so we specify the relation between the energy density and the pressure, that is called the *equation of state* of the fluid. It can

be parametrized as

$$\rho = w\ P\ . \tag{1.16}$$

If we assume that the fluid is *barotropic*, w is a function of the sole energy density. Loosely speaking $-1 \leq w \leq 1$ [25], and in general the value of w evolves broadly in time for the cosmological fluid. However, each of its constituent that is of interest in the cosmological context assume in practice only one discrete value:

$$w = \begin{cases} \frac{1}{3} & \text{for radiation} \\ 0 & \text{for a pressure-less fluid} \\ -1 & \text{for the cosmological constant.} \end{cases} \tag{1.17}$$

Both cold dark matter and baryons behave as a pressure-less fluid, with $w = 0$.

In the epochs we are interested in, the comoving number density of particles is practically conserved, and the inter-species energy exchange is negligible. Therefore the continuity equation eq. (1.13) can be applied separately to each species. Since, as we have seen, for each species w is constant, we can integrate the equation analytically finding

$$\rho = \rho_* \left(\frac{a}{a_*}\right)^{-3(1+w)} , \tag{1.18}$$

where ρ_* and a_* are respectively the species energy density and scale factor at an arbitrary time t_*. It immediately follows that the energy density scales like $\rho_\gamma \propto a^{-4}$ for radiation, $\rho_m \propto a^{-3}$ for matter, and $\rho_\Lambda \equiv$ constant for the cosmological constant, and that the total energy density follows

$$\rho = \frac{\rho_{\gamma,0}}{a^4} + \frac{\rho_{\mathrm{m},0}}{a^3} + \rho_{\Lambda,0}\ . \tag{1.19}$$

Here, and throughout the whole thesis, the subscript 0 indicates that the quantity is evaluated today, e.g. $\rho_{\gamma,0} \equiv \rho_\gamma(t_0)$.

It is useful to define the *critical density* ρ_c which is the total energy density in a flat universe cfr. eq. (1.11)

$$\rho_\mathrm{c} \equiv \frac{3H^2}{8\pi G}\ . \tag{1.20}$$

The critical density is used to express the energy density of each species α in terms of the *relative density* and *physical density parameters*, respectively

$$\Omega_\alpha \equiv \frac{\rho_\alpha}{\rho_\mathrm{c}} \,, \qquad \omega_\alpha \equiv \Omega_\alpha \, h^2 \,. \tag{1.21}$$

Using this definition in the first Friedmann eq. (1.11) we can rewrite it as

$$H = H_0 \sqrt{\frac{\Omega_{\gamma,0}}{a^4} + \frac{\Omega_{\mathrm{m},0}}{a^3} + \frac{\Omega_{k,0}}{a^2} + \Omega_{\Lambda,0}} \,. \tag{1.22}$$

and defining $E(z) = H(z)/H_0$ we can write the critical density at a given redshift as $\rho_\mathrm{c} = E^2(z)\rho_{\mathrm{c},0}$.

Using the third Friedmann equation we found how the energy density evolves as a function of the scale factor. Now we will use the second Friedmann eq. (1.12) to calculate the time evolution of the scale factor, and consequently of the energy density.

As before, for a single species with constant equation of state the solution is analytic

$$a = \begin{cases} a_* \left(\frac{t}{t_*}\right)^{2/[3(1+w)]} & \text{for } w \neq -1 \\ a_* e^{Ht} & \text{for } w = -1 \,. \end{cases} \tag{1.23}$$

It is worth noticing that for $w = -1$ the Universe undergoes an exponential expansion called *de Sitter stage*.

1.3. Cosmological thermalization

Regardless of the specific model and the exact composition of the Universe, the direct consequence of the Friedmann equations is that going backward in times, as the Universe was smaller and smaller, it also had bigger and bigger energy density as we see from eq. (1.18). This is the main underlying idea of the *Hot Big Bang model* (HBB) (see, *e.g.*, [26], [27]).

The whole thermal history of the Universe is basically characterized by the comparison between the *expansion timescale* $t_H = H^{-1}$ and the *interaction timescale* $t_\Gamma = \Gamma^{-1}$, where Γ is the rate of interaction, for different physical phenomena: if the interaction

timescale exceed the expansion timescale

$$t_\Gamma \gg t_H \tag{1.24}$$

it means that the interaction has become ineffective, as the mean time between two scatterings is of the order of the age of the universe. Generally speaking, in a hotter and denser universe interaction were more likely, coupling the evolutions of different species. As the universe became colder and colder with time, one interaction after the other started freezing-out preventing certain particles from, for example, decay, or thermalize with others.

To prove our point we use this very general argument. Consider a particle with number density n, that has a self interaction with cross section σ. If the interaction is mediated by a massless particle we can see, from dimensional analysis, that $\langle \sigma_L \, v \rangle \approx \frac{\alpha^2}{T^2}$, where v is the relative velocity of the interacting particles, α is the coupling constant, and the brackets indicates the average over the velocity distribution. On the other hand, if the mediator is massive, $\langle \sigma_H \, v \rangle \approx \frac{\alpha^2 T^2}{m_M^4}$, where m_M is the mass of the mediator. Since the particles numerical density scales like $n \propto T^3$, the interaction rate scales like

$$\Gamma = \langle \sigma \, v \rangle n \propto \begin{cases} \alpha^2 \, T & \text{for light mediators} \\ \frac{\alpha^2 \, T^5}{m_M^4} & \text{for heavy mediators} \, . \end{cases} \tag{1.25}$$

The interaction rate has to be compared with the Hubble parameter, which scales like $H \approx \frac{T^2}{M_{\rm Pl}^2}$ during radiation domination, when $\rho \propto T^4$, . Therefore, it results that

$$\begin{aligned} t_H \approx & \frac{\alpha^2 \, M_{\rm Pl}^2}{T} t_{\Gamma_L} \approx \frac{10 \times 10^{16} \, \text{GeV}}{T} t_{\Gamma_L} \, , \\ t_H \approx & \frac{\alpha^2 \, M_{\rm Pl}^2 \, T^5}{m_M^4} t_{\Gamma_H} \, . \end{aligned} \tag{1.26}$$

This means that below the Planck scale (in the second equality of the first line we assumed $\alpha \approx 0.01$) interactions mediated by light particles are effective. In the case of interaction mediated by massive particles, when the temperature is below the mass of the mediator, the interaction strength diminishes, fact that guarantees the decoupling at late enough times.[3]

[3] Obviously, at energies much greater than the mass of the mediator its mass can basically be neglected, and the interaction rate scales as in the case of massless mediator.

redshift	Event
10^{15}	Electro-Weak phase transition
10^{12}	QCD phase transition
?	(Possible) Thermal dark matter freeze-out
6×10^9	Neutrino decoupling
2×10^9	Electron-positron annihilation
4×10^8	Big Bang nucleosynthesis
2×10^6	Double Compton freezes out; beginning of μ-distortions epoch
5×10^5	Compton freezes out; beginning of y-distortions epoch
5500	HeII recombination
3400	matter-radiation equality
1900	HeI recombination
1100	Hydrogen recombination
1000-1100	Photon decoupling
800	electron thermal decoupling
11-30	Reionization
0.4	Dark energy-matter equality

Table 1.1.: Main events in the thermal history of the universe. Based on [26], with additions from [28] and [29].

Most phenomena happening in the early universe can be described in term of interactions between different particles becoming or stopping to be effective, like the possible decoupling of thermal dark matter, that might have set the abundance of dark matter we observe today, or the decoupling of neutrinos. Here however we are mostly interested in the phenomena directly effecting the photon field. In Table 1.1 we report a list of the most important events in the Universe thermal history. We refer to [26] for a more extensive description of every phenomena.

Since we are now convinced that in the primordial universe all species were thermalized, we know that all particles distribution functions would follow a Bose-Einstein or Fermi-Dirac distribution, and in particular the photons would have a Planck distribution. This prediction has been experimentally proven in the early nineties by the measurements of COBE/FIRAS: the CMB spectrum is completely compatible with a Planck spectrum within experimental sensitivity, resulting to be the most perfect black-body known in nature.

As we already anticipated, the fact that CMB photons follow a black-body descends from them being in thermal equilibrium in the early universe. However, this is not a feature that we can take for granted, as it heavily relies on the effectiveness of scattering processes able to create or destroy photons, and change their energy frequency. In fact, after a generic interaction, the photon field will not follow a Planck distribution, even if it was before. For example, let us consider an interaction in which some energy is injected in the photon field, conserving the number of photons. Since in a black-body the photon number density is completely determined by the energy density, an appropriate number of photons needs to be added to the system to restore a Planckian. Moreover, this is not in general enough: even if the photons have the right number density, they still need to have their energies arranged suitably.

Photon thermalization in the early universe is therefore achieved thanks to three different processes: *Compton scattering* (CS), *double Compton scattering* (DC) and *bremsstrahlung* (BR) [30]. The last two processes do not conserve the photon number, and are therefore essential to create or destroy photons after any energy injection or subtraction, respectively. Interestingly enough, on average the extra photons are generated at low frequencies, making even more obvious the need for a different process able to rearrange the photon energy. Through multiple interactions with thermal electrons, the Compton scattering can effectively change the photons occupation number, conserving the total energy and number.

Around $z = z_\mu \equiv 2 \times 10^6$, both double Compton and bremsstrahlung had freezed-out, making energetically expensive to create new photons. As we will soon discuss properly, the fact that photon gained an "effective" chemical potential μ, introduced a departure from the black-body distribution, called μ-distortion. Loosely speaking, for any energy injection happening before z_μ the photon have time to properly thermalize and relax to a black-body; afterwards any injection results in a distortion that we might in principle detect today.

The μ-era ends around $z = z_y \equiv 5 \times 10^5$, when also the Compton scattering becomes ineffective. Afterwards, the scatterings with, say, more energetic electrons leave an imprint in the occupation number, since the up-scattered photons cannot thermalize. This results in a so-called y-distortion, that can be seen in the CMB spectrum.

To describe the evolution of the photon distribution function f [28], and properly define μ- and y-distortions, we have to introduce the Boltzmann equation

$$\frac{\mathrm{d}f}{\mathrm{d}t} = C[f]\,. \tag{1.27}$$

The term at LHS is called *Liouville operator*, and, loosely speaking, it is responsible for the effect of gravity on the evolution of the distribution functions. This is clear in the case of non interacting particles, for which the Boltzmann equation reads $\frac{\mathrm{d}f}{\mathrm{d}t} = 0$. On the other hand, the collision term $C[f]$ takes into account both the self-interactions and the interactions between different species. Since in all the cases relevant in cosmology the interactions happen on very short scales and in very brief times, the collision term is calculated in Minkowski space.

The explicit expression of the Liouville operator is

$$\frac{\mathrm{d}f}{\mathrm{d}t} = \frac{\partial f}{\partial t} + \frac{\mathrm{d}\boldsymbol{x}}{\mathrm{d}t}\cdot\frac{\partial f}{\partial \boldsymbol{x}} + \frac{\mathrm{d}p}{\mathrm{d}t}\frac{\partial f}{\partial p} + \frac{\mathrm{d}\hat{\boldsymbol{n}}}{\mathrm{d}t}\cdot\frac{\partial f}{\partial \hat{\boldsymbol{n}}}\,. \tag{1.28}$$

Since we are interested in the homogeneous part of the distribution, the derivatives with respect to the position and the propagation direction are identically zero. Moreover, the derivative of the momentum is not affected by any density and gravitational potential fluctuation, therefore we only have to account for the redshift due to cosmological expansion [23], so we get

$$\frac{\mathrm{d}f}{\mathrm{d}t} = \frac{\partial f}{\partial t} + H\,p\frac{\partial f}{\partial p}\,. \tag{1.29}$$

The collision term takes into account all the interactions that affect the photon bath, and therefore reads

$$C[f] = C[f]|_{\mathrm{CS}} + C[f]|_{\mathrm{DC}} + C[f]|_{\mathrm{BR}}\ , \tag{1.30}$$

but as we already discussed, when the DC and BR terms are effective, the photon bath eventually relax to a Planck distribution [28]. Therefore, the interesting limit is the one in which only the CS term is present.

Consider a Compton scattering process

$$\mathrm{e}^-(p) + \gamma(k) \longrightarrow \mathrm{e}^-(p') + \gamma(k')\,. \tag{1.31}$$

The relative Compton collision term is [30, 31]

$$C[f]|_{\rm CS} = c \int {\rm d}^3\boldsymbol{p}\, {\rm d}^2\hat{\boldsymbol{k}} \frac{{\rm d}\sigma}{{\rm d}\Omega} \left\{ f_{\rm e}(p') f(k') [1 + f(k)] - f_{\rm e}(p) f(k) [1 + f(k')] \right\}, \tag{1.32}$$

where $f_{\rm e}$ is the electron distribution function — a Maxwell-Boltzmann in the scope of this thesis — and

$$\frac{{\rm d}\sigma}{{\rm d}\Omega} = \frac{3\sigma_{\rm T}}{16\pi} \left[1 + (\hat{\boldsymbol{k}} \cdot \hat{\boldsymbol{k}}')^2 \right] \tag{1.33}$$

is the differential cross section. In the limit of small energy exchange the expression further simplify, and it can be shown to be

$$C[f]|_{\rm CS} = c\, \sigma_{\rm T}\, N_e \frac{\theta_{\rm e}}{x^2} \frac{\partial}{\partial x_{\rm e}} x_{\rm e}^2 \left[\frac{\partial}{\partial x_{\rm e}} f + f(1 + f) \right], \tag{1.34}$$

where we introduced the two adimensional energy parameters $\theta_{\rm e} = k_{\rm B} T_{\rm e} / m_{\rm e} c^2$ and $x_{\rm e} = h\nu / m_{\rm e} c^2$.

We can finally plug eq. (1.29) and eq. (1.34) into eq. (1.27), parametrize the time in term of the optical depth ${\rm d}\tau = c\, \sigma_{\rm T}\, N_e\, {\rm d}t$, and express the momenta dependences in term of the variable $x = h\nu / k T_\gamma$ where $T_\gamma = T_0 (1 + z)$ to absorb the term $-Hp \frac{\partial f}{\partial p}$ and get

$$\frac{\partial f}{\partial \tau} = \frac{\theta_{\rm e}}{x^2} \frac{\partial}{\partial x} x^2 \left[\frac{\partial}{\partial x} f + \frac{T_\gamma}{T_{\rm e}} f(1 + f) \right], \tag{1.35}$$

which is the *Kompaneets equation* [32]. Notice that the first term in the square brakets is related to the Doppler effect, whereas the second accounts for the recoil effects.

μ-distortions. When the Compton scattering is efficient, in the period of time we called μ-epoch, the photon distribution reaches a quasi-stationary solution $\frac{{\rm d}f}{{\rm d}\tau} \approx 0$, hence, from eq. (1.35), we get

$$\frac{\partial}{\partial x} f + \frac{T_\gamma}{T_{\rm e}} f(1 + f) \approx 0\,. \tag{1.36}$$

Notice that if $T_{\rm e} = T_\gamma$ the solution is a Planck distribution, as we would expect for photons in thermal equilibrium. In general we can integrate it to get

$$f = \frac{1}{e^{x_e + \mu_0} - 1}\,, \tag{1.37}$$

where μ_0 is an integration constant, that we can interpret as an effective chemical potential.[4] This do not conflict with the fact that massless particles should have 0 chemical potential because we are considering a system which is out of the equilibrium.

We now need to understand how the presence of a μ-distortion modifies the photon distribution, i.e., we want to define the distortion frequency spectrum. Expanding the distorted spectrum in eq. (1.37) for small values of μ_0 we get

$$f = \frac{1}{e^{x_e} - 1} - \frac{\mathcal{G}(x_e)}{x_e}\mu_0 + \mathcal{O}(\mu_0^2)\,, \qquad \mathcal{G} \equiv \frac{x\, e^x}{(e^x - 1)^2}\,, \tag{1.38}$$

where is important to notice that $\mathcal{G}$ is the spectrum of a temperature shift

$$f_{\rm Pl}(T + \Delta T) = f_{\rm Pl}(T) + \mathcal{G}\frac{\Delta T}{T} + \mathcal{O}\left(\frac{\Delta T^2}{T^2}\right). \tag{1.39}$$

One might naively define the μ-distortion spectra as $\mathcal{G}/x$, but that definition would not satisfy the constrain on the fact that Compton scattering conserves the number of photons: $-\int x^2\, \mathcal{G}/x\ \mathrm{d}x \neq 0$. As it turns out a more sensible definition is [28]

$$\mathcal{M}(x) = 1.401\left(\frac{\pi^2}{18\zeta(3)} - \frac{1}{x}\right)\mathcal{G}(x)\,, \tag{1.40}$$

which also has the nice property that the relative change of photon energy density is normalized to 1. The two terms in the parenthesis have important physical interpretations: the $1/x$ term corresponds to the naive definition of the μ-distortion spectra we discussed before, while the other, being proportional to $\mathcal{G}$ is a shift in the black-body temperature. In practice, if energy is injected in the photon bath during the μ-epoch, part of it is spent to create a new black-body with slightly higher temperature, and part is spent to create a distortion as described in eq. (1.38). The photons that would be needed to create the higher-temperature black-body exactly balance with those removed by the distortion in its naive definition.

It will be useful for future reference to provide an approximate estimate of the amount of μ-distortions generated in the primordial universe. We assume that the beginning and end of the μ-epoch are abrupt transitions — thing that, in reality, is far from true, see [28]. In this regime, if some energy $\Delta\rho_\gamma$ is injected in the photon field, it will completely

[4] Usually the proper chemical potential is defined with the opposite sign.

converted in a μ-distortion such as

$$\mu \approx 1.401 \left.\frac{\Delta\rho_\gamma}{\rho_\gamma}\right|_\mu . \tag{1.41}$$

***y*-distortions.** When the Compton scattering becomes inefficient, we can write the response of a Planck distribution $f_{\rm Pl}$ to a scattering using again eq. (1.35)

$$\begin{aligned} \Delta f \approx & \frac{\theta_{\rm e}}{x^2}\frac{\partial}{\partial x}x^2\left[\frac{\partial}{\partial x}f_{\rm Pl} + \frac{T_\gamma}{T_{\rm e}}f_{\rm Pl}(1+f_{\rm Pl})\right]\Delta\tau \\ \approx & \mathcal{Y}(x)y\,, \end{aligned} \tag{1.42}$$

where we have defined the y-distortion spectrum

$$\mathcal{Y}(x) \equiv \mathcal{G}(x)\left(x\frac{e^x+1}{e^x-1} - 4\right), \tag{1.43}$$

and the Compton-y parameter

$$y \equiv \int_0^\tau (\theta_{\rm e} - \theta_\gamma)\,{\rm d}\tau' = \int_0^t \frac{k_{\rm B}(T_{\rm e}-T_\gamma)}{m_{\rm e}c^2}\sigma_{\rm T}N_{\rm e}c\,{\rm d}t'\,. \tag{1.44}$$

For example, an important source of y distortions is the Sunyaev-Zeldovich effect [33, 34]. When photons travel through clusters of galaxies they can interact with hot electrons that can up-scatter them into higher frequencies through the mechanism we just described.

Assuming again abrupt transitions between the μ and y era, we can write the approximate relation

$$y \approx \left.\frac{1}{4}\frac{\Delta\rho_\gamma}{\rho_\gamma}\right|_y . \tag{1.45}$$

1.4. Inflation and the primordial perturbation field

Inflation is a period of accelerated expansion, that may have taken place *before* what is usually considered the initial time in the HBB model. It was firstly invoked in the early eighties of the last century to solve the main shortcomings of the standard HBB model [35], namely the horizon problem, the flatness problem, and the absence of relics (see for example [23]), but today the feature that is widely considered its biggest success

is providing a mechanism that can set the primordial perturbation field which we will define in the following [36, 37].

The inflationary paradigm as a whole has some telltale signs, namely a certain amount of primordial tensor modes being generated on the largest physical scales and of non-Gaussianity in the primordial perturbation field.

Whereas the most vanilla model does not predict any other additional features, there are huge classes of non-minimal models that can create a richer phenomenology [38]. Moreover, these non-minimal model are often the most natural to build from a particle physics or string theory point of view. It is therefore important both to test the validity of the inflationary paradigm as a whole, and to investigate which kind of model might be the best description of the first instants of the Universe, shedding light over possible fundamental physics implications.

1.4.1. The inflaton classical evolution

From the first Friedmann eq. (1.11) we know that to achieve a period of accelerated expansion, the cosmic fluid have to satisfy $p \leq -\rho/3$. For example, this relation is satisfied if the energy density is dominated by the potential energy of a scalar field, condition that is easily achieved in the presence of a *slow rolling* scalar field, as we will discuss now discuss.

There are countless models that use a wide range of different mechanism to achieve an inflationary phase. Here we will briefly review the simplest one: highlighting all the simplifying assumption that might be broken in more general models.

The action of a single scalar field ϕ minimally coupled to the metric is

$$S = \int \mathrm{d}^4x\sqrt{g}\left[\frac{M_{\mathrm{Pl}}^2}{2}R + D_\mu\phi D^\mu\phi + V(\phi)\right] . \tag{1.46}$$

In general there might be multiple fields that are active during inflation and that drive the accelerated expansion, and they might also be coupled with other spectator fields that do not contribute to the inflation dynamics themselves, but might be crucial for brief or later phases (see, *e.g.*, [39–44] and references therein). Whereas scalar degrees of freedom arise naturally from considerations related to the evident isotropy of our universe, there are models that predict vector or tensor fields active during inflation (see,

e.g., [45–50]). Finally, the inflaton can have a non-minimal coupling with the metric (see, *e.g.*, [51]), including some of the very first inflation models to be proposed [52, 53].

Going back to our minimal model, eq. (1.46) leads to the Klein-Gordon equation

$$\ddot{\phi} + 3H\dot{\phi} - \frac{\nabla^2\phi}{a^2} = -V_\phi. \tag{1.47}$$

To understand the inflation mechanics, it is convenient to separate the *classical background* of the inflaton, i.e., its vacuum expectation value $\phi_0(t) \equiv \langle\phi(\boldsymbol{x}, t)\rangle$, and its quantum fluctuations $\delta\phi(\boldsymbol{x}, t) \equiv \phi(\boldsymbol{x}, t) - \phi_0(t)$. The classical component is responsible for the energy density of the universe, and controls the universe background evolution,i.e., its expansion history. The quantum fluctuation modulate spatially the time evolution of the background (as we will explicitly see later), and are responsible of creating all the inhomogeneities that are present in all the later stages of the Universe evolution.

For this homogeneous field the Klein-Gordon eq. (1.47) reduces to

$$\ddot{\phi}_0 + 3H\dot{\phi}_0 = -V_\phi\,. \tag{1.48}$$

Since we assumed that the inflaton is minimally coupled to the metric, calculating its energy-momentum tensor is trivial

$$\begin{aligned} T_{\mu\nu} \equiv & \frac{-2}{\sqrt{g}}\frac{\delta S}{\delta g^{\mu\nu}} \\ = & \partial_\mu\phi\ \partial_\nu\phi + \mathcal{L}_\phi g_{\mu\nu}. \end{aligned} \tag{1.49}$$

where $g \equiv -\det g_{\mu\nu}$. Therefore the inflaton energy density and its pressure are respectively

$$\rho_{\phi_0} = \frac{1}{2}\dot{\phi_0}^2 + V(\phi_0), \tag{1.50}$$

$$p_{\phi_0} = \frac{1}{2}\dot{\phi_0}^2 - V(\phi_0), \tag{1.51}$$

showing that if the energy density is dominated by the potential energy, i.e. if the inflaton satisfy the *slow-roll condition*

$$V(\phi_0) \gg \dot{\phi_0}^2\,, \tag{1.52}$$

the inflaton behave like a cosmological constant, with equation of state parameter $w \approx -1$. One might question how likely it is for a generic scalar field to respect the last condition. The crucial point is that flat enough potentials (in a way that we will soon quantify) actually constitute attractor solutions. In fact if the field is on the plateau it means that the scalar energy density due to the potential is approximately constant as the Universe expands. On the other hand using eq. (1.13) on the scalar field kinetic energy alone, i.e. by neglecting the potential in eq. (1.51) and eq. (1.50), we see that the kinetic term scales like a^{-6}, ensuring the validity of the slow-roll condition.

During slow-roll, at sufficiently-late times, the evolution of the classical inflaton field is driven by the friction term,

$$\ddot{\phi}_0 \ll 3H\dot{\phi}_0 \,, \tag{1.53}$$

so eq. (1.48) reduces to

$$3H\dot{\phi}_0 + V_\phi = 0 \,, \tag{1.54}$$

whereas using eq. (1.52) in eq. (1.11), we get

$$H^2 \approx \frac{8\pi G}{3} V \,. \tag{1.55}$$

We can employ these results to write the inflaton potential Taylor expansion in an handy way: eq. (1.52) and eq. (1.53) are respectively equivalent to

$$\epsilon \equiv \frac{M_{\rm Pl}^2}{2}\left(\frac{V_\phi}{V}\right)^2 \ll 1 \,, \tag{1.56}$$

and

$$\eta \equiv M_{\rm Pl}^2 \frac{V_{\phi\phi}}{V} \ll 1 \,, \tag{1.57}$$

where we defined the *slow-roll parameters* ϵ and η [54–56]. During the inflaton slow-roll phase the two parameters are small and constant at first order; direct calculation shows that $\dot{\epsilon}, \dot{\eta} = \mathcal{O}(\epsilon^2, \eta^2)$. In particular, it is important to note that $\epsilon \geq 1$ implies the end of the inflationary phase. This does not prevent however from building viable models that briefly exit the inflationary phase before re-entering a "second" inflation, before the inflaton reaches its true minimum. The theoretical constraints on η are even more

relaxed, and it can, under certain conditions, exceed unity without stopping inflation (see, *e.g.*, [53, 57–61]).

Moreover some models display potentials with features that cannot easily be captured by an expansion in slow-roll parameters, such as, for example, oscillations [62–64].

1.4.2. The inflaton quantum fluctuations and curvature perturbations

We now want to quantize the inflaton field around its VEV $\phi_0(t)$, and study the evolution of its linear perturbations $\delta\phi$.

It is mathematically convenient to renormalize the amplitude of the inflaton field by the scale factor. The renormalized field

$$\widehat{\delta\phi} = a\delta\phi \tag{1.58}$$

can be expressed in terms of its Fourier transform

$$\widehat{\delta\phi}(\mathbf{x},\tau) = \int \frac{d^3k}{(2\pi)^3}\left[u_{\mathbf{k}}(\tau)a_{\mathbf{k}}e^{i\mathbf{x}\cdot\mathbf{k}} + u^*_{\mathbf{k}}(\tau)a^\dagger_{\mathbf{k}}e^{-i\mathbf{x}\cdot\mathbf{k}}\right]. \tag{1.59}$$

We apply second quantization promoting the fields to operators that satisfy the commutation relations

$$[a_{\mathbf{k}}, a_{\mathbf{k}'}] = 0, \qquad \left[a_{\mathbf{k}}, a^\dagger_{\mathbf{k}'}\right] = \delta^{(3)}(\mathbf{k}-\mathbf{k}'), \tag{1.60}$$

and the normalization condition

$$u^*_{\mathbf{k}}u'_{\mathbf{k}} - u_{\mathbf{k}}(u^*_{\mathbf{k}})' = -i. \tag{1.61}$$

We use the Bunch-Davies vacuum choice, i.e. the quantum fluctuations must reduce to quantum field theory in flat space-time on very small physical scales

$$u_{\mathbf{k}}(\tau) \xrightarrow[k\gg aH]{} \frac{e^{i\tau k}}{\sqrt{2\omega_k}}. \tag{1.62}$$

However, even this choice is optional, as it can be argued, for example, that the initial condition should rather be set at a finite time in the past, on finite dimension scales [65,66].

Metric perturbations. To consistently write the equation of motion of the inflaton linear perturbations we also need to perturb the metric at linear order.

As we will discuss, it is convenient to organize the perturbations according to how they transform upon spatial diffeomorphisms. Considering only linear perturbations we can write the RW metric as [67, 68]

$$\mathrm{d}s^2 = a^2(t)\left\{-(1+2\Psi)\,\mathrm{d}\tau^2 + w_i\,\mathrm{d}\tau\,\mathrm{d}x^i + \left[(1-2\Phi)g_{ij} + h_{ij}\right]\mathrm{d}x^i\,\mathrm{d}x^j\right\}. \tag{1.63}$$

By construction, since $\mathrm{d}\tau^2, \mathrm{d}\tau\,\mathrm{d}x^i, \mathrm{d}x^i\,\mathrm{d}x^j$ are respectively a scalar, a vector and a tensor under spacial transformation, Ψ and Φ are scalars, w_i is a vector and h_{ij} is a traceless symmetric tensor.

We can further decompose these quantities in objects with well-defined transformation properties under spatial rotations exploiting Helmholtz theorem. w_i can be written as

$$w_i = \partial_i w^{\parallel} + w_i\,, \tag{1.64}$$

where the *longitudinal component* $w^{\parallel}$ is a scalar, and the *transverse component* w_i is a solenoidal vector (i.e., $\partial^i w_i = 0$). Similarly

$$h_{ij} = D_{ij}h^{\parallel} + \partial_{(i}h^{\perp}_{j)} + {h^{\mathrm{TT}}}_{ij}\,, \tag{1.65}$$

where we introduced the differential operator $D_{ij} \equiv \partial_i\partial_j - \delta_{ij}\partial_k\partial^k/3$ to decompose h_{ij} in the longitudinal component $h^{\parallel}$, the solenoidal *vector component* $h^{\perp}_i$, and the *transverse-traceless tensor* ${h^{\mathrm{TT}}}_{ij}$.

It can be shown that at linear level the evolution equations of scalar, vector, and tensor perturbations are decoupled. Since in this thesis we will mainly be interested in scalar quantities we will not consider the vector and tensor perturbations in the metric. Moreover, we can always employ the *Newtonian* or *Longitudinal gauge* [69], in which $w^{\parallel} = h^{\parallel} = 0$. Then we can rewrite the perturbed metric eq. (1.63) as

$$\mathrm{d}s^2 = a^2(t)\left[-(1+2\Psi)\,\mathrm{d}\tau^2 + (1-2\Phi)g_{ij}\,\mathrm{d}x^i\,\mathrm{d}x^j\right]. \tag{1.66}$$

Perturbed evolution equations. We are now ready to write the perturbed Klein-Gordon equation (1.47)

$$\delta\phi'' + 2\mathcal{H}\delta\phi' - \nabla^2\delta\phi + a^2 V_{\phi\phi}\,\delta\phi + 2\Psi V_\phi - \phi_0'\left(\Psi' + 3\Phi' + \nabla^2\omega^{\parallel}\right) = 0\,. \tag{1.67}$$

In order to easily solve eq. (1.67), it is helpful to introduce the Mukhanov variable [70]

$$Q \equiv\ \delta\phi + \frac{\phi_0'}{\mathcal{H}}\mathcal{R}\,, \tag{1.68}$$

where $\mathcal{R} \equiv \Phi + h^{\parallel}/3$ is the perturbation in the intrinsic spatial curvature, and reduces to $\mathcal{R} \equiv \Phi$ in the Newtonian gauge we are working in. Contrary to $\mathcal{R}$ or $\delta\phi$, Q is a gauge-invariant quantity. To get some insight on its physical interpretation, we can notice that it is equivalent to the scalar field perturbations in the spatially flat gauge ($Q = \delta\phi$ for $\mathcal{R} = 0$), or to the spatial curvature perturbation in the comoving gauge ($Q = \frac{\phi_0'}{\mathcal{H}}\mathcal{R}$ for $\delta\phi = 0$).

Using the fixed time 3-dimensional Fourier transform of aQ in a flat space, $\chi_{\boldsymbol{k}}$, the different modes decouple and eq. (1.67) becomes

$$\chi_{\boldsymbol{k}}'' + \left(k^2 - \frac{a''}{a} + \mathcal{M}_\phi^2\, a^2\right)\chi_{\boldsymbol{k}} = 0\,, \tag{1.69}$$

where we defined the *effective mass* term $\mathcal{M}_\phi^2 = V_{\phi\phi} - 8\pi G\phi_0^2/H$.

During slow-roll we can approximate the terms in the parenthesis in terms of ϵ and η

$$\frac{a''}{a} = \frac{2}{\eta}(1 + \frac{3}{2}\epsilon + O(\epsilon^2, \eta^2))\,, \qquad \frac{\mathcal{M}_\phi^2}{H^2} = 3\eta - 6\epsilon\,, \tag{1.70}$$

that plugged into eq. (1.69) give

$$\chi_{\boldsymbol{k}}''(\tau) + \left(k^2 - \frac{\nu^2 - 1/4}{\tau^2}\right)\chi_{\boldsymbol{k}}(\tau) = 0\,, \qquad \nu = \frac{3}{2} + 3\epsilon - \eta\,. \tag{1.71}$$

In the limit of constant ν, which is the case during slow roll, this equation is called Bessel equation, and it has known solutions

$$\chi_{\boldsymbol{k}}(\tau) = \frac{\sqrt{\pi}}{2}e^{i\left(\nu+\frac{1}{2}\right)\frac{\pi}{2}}\sqrt{-\tau}H_\nu^{(1)}(-k\tau)\,, \tag{1.72}$$

where $H_\nu^{(1)}$ is the Hankel function of the first kind, and we already imposed the Bunch-Davies vacuum choice eq. (1.62). We specify for future reference that the for small value of its parameter — which, in this case, correspond to the super-horizon regime — the Hankel function has the following asymptotic limit

$$H_\nu^{(1)}(x \ll 1) \sim \sqrt{\frac{2}{\pi}} e^{-i\frac{\pi}{2}} 2^{\nu-\frac{3}{2}} \frac{\Gamma(\nu)}{\Gamma(3/2)} x^{-\nu} \tag{1.73}$$

Curvature perturbations The inflaton fluctuations described here are the primordial seeds of all inhomogeneities we observe in the Universe today. However they are quantistic in nature, and generated on very small scales. During inflation a given perturbation mode with wavelength λ is stretched outside of the horizon by the accelerated expansion. When inflation ends a *reheating phase* takes place: when the inflaton field reaches the minimum of its potential inflation stops and it start decaying, repopulating the universe with matter and radiation. The fundamental point is that modes outside the horizon, being not causally connected with the modes inside the horizon, are effectively freezed and do not follow the same evolution. It can be shown that this difference in the evolution causes a decorrelation that makes the quantum fluctuation classical upon horizon re-entry.

Translating the inflaton fluctuations in the energy density fluctuation we observe today in various forms is not trivial either, as both are gauge-dependent quantities.

We can define another gauge-invariant variable, closely related to the Mukhanov variable [67, 71]

$$\zeta \equiv \mathcal{R} - \mathcal{H}\frac{\delta\rho}{\rho'}\,, \tag{1.74}$$

which, in particular, during the slow-roll phase reduces to

$$\zeta = -\frac{\mathcal{H}}{\phi'} Q\,. \tag{1.75}$$

ζ has the useful property of being conserved on super-horizon scales, if the evolution is adiabatic [67, 72]. Hence, the perturbation field that re-enters the horizon during the radiation and matter dominated epoch is characterized by the amplitude of the ζ perturbations evaluated upon horizon-exit.

In the super-horizon limit $|k\tau| \ll 1$ we can expand eq. (1.72) at first order in the slow-roll parameter, remembering that the Fourier transform of the Mukhanov variable

is $Q_{\boldsymbol{k}} = \chi_{\boldsymbol{k}}/a$. Hence we get

$$|\zeta_{\boldsymbol{k}}| = \frac{H^2}{\sqrt{2k^3\dot{\phi}}}\left(\frac{k}{aH}\right)^{\eta-3\epsilon}, \tag{1.76}$$

expression that, as we will see in the next section, is fundamental to understand the generation of observable perturbations.

1.4.3. The primordial power spectrum

By construction, the curvature perturbations VEV is 0, but in general the n-points correlation might have non-vanishing expectation value

$$\langle \zeta(\boldsymbol{x_1}, t) \cdots \zeta(\boldsymbol{x_n}, t)\rangle \neq 0\,. \tag{1.77}$$

It is convenient to work in terms of the Fourier transforms of the n-points correlators, defining the *power spectrum* as the transform of the 2-points correlation function, the *bispectrum* for the 3-point and so forth.

Explicitly writing the curvature perturbations in term of their Fourier transform in the 2-points correlation function we get

$$\langle \zeta(\boldsymbol{x_1}, t)\zeta(\boldsymbol{x_2}, t)\rangle = \int \frac{\mathrm{d}^3\boldsymbol{k_1}}{(2\pi)^3} e^{i\boldsymbol{k_1}\boldsymbol{x_1}} \int \frac{\mathrm{d}^3\boldsymbol{k_2}}{(2\pi)^3} e^{i\boldsymbol{k_2}\boldsymbol{x_2}} \langle \zeta_{\boldsymbol{k_1}}\zeta_{\boldsymbol{k_2}}\rangle\,. \tag{1.78}$$

$\langle \zeta_{\boldsymbol{k_1}}\zeta_{\boldsymbol{k_2}}\rangle$ is in full generality a function of both $\boldsymbol{k_1}$ and $\boldsymbol{k_2}$. However, since we assume the universe to be homogeneous and isotropic, we can require the LHS to be a function of the sole correlation length,i.e., $\langle \zeta(\boldsymbol{x_1}, t)\zeta(\boldsymbol{x_2}, t)\rangle = f(|\boldsymbol{x_1} - \boldsymbol{x_2}|)$. If this is the case, is easy to see that $\langle \zeta_{\boldsymbol{k_1}}\zeta_{\boldsymbol{k_2}}\rangle$ must have the form $\delta^{(3)}(\boldsymbol{k_1} + \boldsymbol{k_2})\, g(k_1)$. Therefore we define the primordial power spectrum $P(k)$ through

$$\langle \zeta_{\boldsymbol{k_1}}\zeta^*_{\boldsymbol{k_2}}\rangle \equiv (2\pi)^3\, \delta^{(3)}(\boldsymbol{k_1} - \boldsymbol{k_2}) P(k)\,. \tag{1.79}$$

It is often convenient to express this quantity in terms of the dimensionless power spectrum $\Delta^2(k)$ defined as

$$\Delta^2(k) \equiv \frac{k^3}{2\pi^2} P(k)\,. \tag{1.80}$$

Simple considerations about the symmetries of the Universe allowed us to understand what is the functional form of $\langle \zeta_{\boldsymbol{k_1}} \zeta^*_{\boldsymbol{k_2}} \rangle$ and define the power-spectrum. Now we can evaluate $\langle \zeta_{\boldsymbol{k_1}} \zeta^*_{\boldsymbol{k_2}} \rangle$ to compute the theoretical prediction of the power-spectrum from (standard single-field models of) inflation. Working in the spatially flat gauge $\zeta = -\frac{H}{\phi_0'} Q$, hence we can directly employ the expressions we introduced quantizing the inflaton field.

$$\langle \zeta_{\boldsymbol{k_1}} \zeta^*_{\boldsymbol{k_2}} \rangle = \left(\frac{H}{\phi_0'} \right)^2 \langle a_{\boldsymbol{k_1}} a^\dagger_{\boldsymbol{k_2}} \rangle = (2\pi)^3 \, \delta^{(3)}(\boldsymbol{k_1} - \boldsymbol{k_2}) |\zeta_{\boldsymbol{k1}}|^2 \,, \tag{1.81}$$

where we used eq. (1.60) in the first equality. Therefore, $P(k) = |\zeta_{\boldsymbol{k1}}|^2$, i.e.,

$$\Delta^2(k) = \left(\frac{H^2}{2\pi \dot{\phi}} \right)^2 \left(\frac{k}{aH} \right)^{2\eta - 6\epsilon} \,. \tag{1.82}$$

If the slow roll parameters ϵ and η were constant throughout the whole inflationary phase, then the primordial power-spectrum is a power-law. Small deviations can still be parametrized choosing a pivot k and performing a Taylor expansion

$$\Delta^2(k) = A_\mathrm{s} \left(\frac{k}{k_\mathrm{p}} \right)^{n_\mathrm{s} - 1 + \frac{1}{2} \frac{\mathrm{d}n_\mathrm{s}}{\mathrm{d}\ln k} \ln(k/k_\mathrm{p}) + \cdots} \,, \tag{1.83}$$

where, for single-field slow-roll inflation, $A_\mathrm{s} = \left(\frac{H^2}{2\pi\dot{\phi}} \right)^2 \Big|_{k_\mathrm{p}}$, and $n_\mathrm{s} - 1 = 2\eta - 6\epsilon$. The most common approach used when fitting data is however the opposite [14, 73] the "phenomenological" parameters A_s and n_s are fit to data, and *a posteriori* the various theoretical model parameters are mapped in A_s and n_s.

1.4.4. The primordial bispectrum

As we have discussed in the previous section, the primordial power spectrum is closely related to the value of the potential and its derivatives along the inflaton trajectory, and as such it is a powerful probe of the inflationary physics. We can however argue that it is basically insensitive to the interactions that affected the inflaton, and to the physics that shaped the inflaton potential in the form it has. Therefore, completely different inflationary models can lead to very similar primordial power spectra.

Non-Gaussianity of the primordial perturbation field instead naturally arises from interactions of the field(s) driving inflation and therefore contains crucial information

about the physics that was operative at the time. Therefore, detecting primordial non-Gaussianity would arguably be the most powerful probe of fundamental physics during inflation [74–78].

In the single field slow-roll inflation with canonic kinetic term and Bunch-Davies vacuum, that we have described before, the perturbations are very close to Gaussian [79–81]. However, most of the various deviations from this minimal model that we enumerated generate some amount of non-Gaussianity that can be detected measuring higher order correlators [75–77]. In particular, here we will discuss about the primordial bispectrum, *i.e.*, the Fourier transform of the 3-point correlation functions. It is defined in a similar fashion to the primordial power spectrum eq. (1.79)

$$\langle \zeta_{\boldsymbol{k_1}} \zeta_{\boldsymbol{k_2}} \zeta_{\boldsymbol{k_3}} \rangle \equiv (2\pi)^3 \, \delta^{(3)}(\boldsymbol{k_1} + \boldsymbol{k_2} + \boldsymbol{k_3}) B(k_1, k_2, k_3) \,, \tag{1.84}$$

and likewise the Dirac delta reflects the translation invariance, and B depending only by the norms of the wave-vector reflects the statistical isotropy of the universe.

It is important to notice that different classes of models generate signals that peak in different bispectrum configurations, *i.e.*, for different shapes of the triangle formed by k_1, k_2, k_3. Multi-field inflation generates large values of the bispectrum in the squeezed configuration ($k_1 \approx k_2 \gg k_3$) [82–90]. Non-canonical kinetic terms (*i.e.*, kinetic terms with higher-than-second-order derivatives) produce equilateral bispectrum configurations $k_1 \approx k_2 \approx k_3$ [65, 91]. Folded shape bispectrum ($k_1 \approx k_2 \approx 2k_3$) is generated, *e.g.*, by vacuum choices different from Bunch-Davies [92, 93].

Local non-Gaussianity. Among the models that predict sizeable non-Gaussianity, the simplest and probably the most studied is the *local model* [94–97], which is built by expanding the perturbation field in real space as a Taylor series in terms of its Gaussian part

$$\zeta(\boldsymbol{x}) = \zeta_G(\boldsymbol{x}) - \frac{3}{5} f_{\rm NL}^{\rm loc} \left[\zeta_G^2(\boldsymbol{x}) - \langle \zeta_G^2(\boldsymbol{x}) \rangle \right] + \dots \,, \tag{1.85}$$

where $f_{\rm NL}^{\rm loc}$ is a dimensionless constant that quantifies the deviation from Gaussianity at the second order in the perturbations.

The interest in this model lies in the fact that it acts as a proxy for models that generate the local bispectrum shape, that can be derived from eq. (1.85) with easy

calculations

$$B^{\rm loc}(k_1,k_2,k_3) = -\frac{6}{5} f_{\rm NL}^{\rm loc} \left[P(k_1)P(k_2) + P(k_2)P(k_3) + P(k_3)P(k_1)\right], \tag{1.86}$$

which strongly peaks on squeezed configurations. The importance of this shape comes also from the fact that, for *any* single field inflation model, a *consistency relation* holds in the squeezed limit [80, 98].[5]

$$B(k_1,k_2,k_3 \to 0) \to (1-n_{\rm s})P(k_1)P(k_2)\,. \tag{1.87}$$

which is of the local type (in the squeezed limit). Therefore, a detection of a local signal higher than this bound would automatically rule out all single field models in one go.

Up to now, the tightest constraints on this crucial parameter, $f_{\rm NL}^{\rm loc}$ has been set by the *Planck* satellite studying the CMB anisotropies bispectrum (see Section 2.3.2) [3]: $f_{\rm NL}^{\rm loc} = 0.8 \pm 5$ (68% C.L.). While impressive, this constraints is far from reaching the bound set by the consistency relation, and far from giving definitive answers in the search for non-Gaussianity.

Noticeably, *Planck* has set tight constraints also on the amplitude of many other bispectrum shapes, among which the equilateral and the orthogonal shape that we mentioned earlier. Respectively, the best fits are $f_{\rm NL}^{\rm eq} = -4 \pm 43$ and $f_{\rm NL}^{\rm ortho} = -26 \pm 21$ (68% C.L.).

1.5. The perturbed Universe

1.5.1. CMB anisotropies

The CMB displays anisotropies that are closely related with the primordial perturbation field. A crucial feature of the CMB, object of a large number of observations, is the presence of small fluctuations in its average intensity, when we look in different directions in the sky. We often refer to them as the *temperature anisotropies* $T(\hat{\boldsymbol{n}})$, with the understanding that we are assuming that in each direction the CMB follows a Planck distribution with temperature $T(\hat{\boldsymbol{n}})$. Talking in these terms, it is useful to consider the

[5] see also [99, 100] and refs therein for further discussions on this consistency relation and its link to observations.

temperature fluctuations with respect to the average temperature

$$\Theta(\eta, \mathbf{x}, \mathbf{n}) = \frac{T(\eta, \mathbf{x}, \mathbf{n}) - \bar{T}(z)}{\bar{T}(z)} \,. \tag{1.88}$$

As we anticipated in Section 1.3, the CMB anisotropies are generated by small inhomogeneities of the metric and energy density that are present during the whole history of the universe, before, during, and after recombination.

Once the initial conditions are set, the evolution of the photon field is determined by its direct interaction with the baryons and the metric, which is in turn coupled with all the other species: dark energy, dark matter, baryons and radiation. Therefore, in order to describe the photon anisotropies, we need a set of evolution equations for every element in the universe. This is provided by a set of coupled Boltzmann equations

$$\frac{\mathrm{d}\boldsymbol{f}}{\mathrm{d}t} = C[\boldsymbol{f}] \,, \tag{1.89}$$

where $f_i(t, \boldsymbol{x}, p\,\hat{\boldsymbol{n}})$ is the distribution function of the species i. The difference with respect with Section 1.3, is that in this case we are interested to the spatially varying part rather then the homogeneous component alone.

To make its solution manageable, eq. (1.89) is usually expanded in perturbations up to a suitable order. In this thesis we will mainly deal with first order quantities, but we will also consider phenomena happening at second order. The theory of second order perturbations is well established [101–107] but its full analytical treatment is long and complex and beyond the scope of this work. In some of our applications, we will make use of second order analytical results, for specific numerical implementations. In such cases, we will refer the reader to the relevant literature, for the full analytical derivation. The aim of this section is mostly that of clarifying some useful general concepts at the basis of the full detailed treatment of CMB anisotropies. Therefore, for such illustrative purposes, it will suffice to keep the analytical treatment at first order.

For analogous reasons we will not derive all the equations for all the species, as they are well known from the literature (see [23] for a clear derivation). We will just focus on the Boltzmann equation for the photons, both because it provides a good explanatory example, and because in Section 3.2 we will generalize the standard treatment outlined here in order to take into account the generation of spectral distortions.

The Liouville operator. Like we did when treating the inflaton perturbation, we need to specify a perturbed metric and choose a gauge. We will work again in the Newtonian gauge eq. (1.66).

If we consider again the explicit expression of the Liouville operator eq. (1.28), and restrict ourselves to consider first order perturbations, we can drop the last term at RHS, as it is the product of two intrinsically first order quantities.

The logarithmic derivative of the momentum reads [69]

$$\frac{1}{p}\frac{\mathrm{d}p}{\mathrm{d}t} = -H - \frac{\partial \Phi}{\partial t} - \hat{\boldsymbol{n}} \cdot \nabla \psi. \tag{1.90}$$

It is important to notice for future reference that this quantity is p-independent for massless particles. Therefore, the Liouville operator for massless particles, valid at first order in the perturbations reads

$$\frac{\mathrm{d}f}{\mathrm{d}t} = \frac{\partial f}{\partial t} + \frac{\hat{\boldsymbol{n}}}{a} \cdot \nabla f - p \frac{\partial f}{\partial p}\left(H + \frac{\partial \Phi}{\partial t} + \hat{\boldsymbol{n}} \cdot \nabla \Psi\right). \tag{1.91}$$

Since the deviations from a black-body spectrum and the anisotropies are small, we can perturb the distribution function around its zero-order Planck value

$$f(t, \boldsymbol{x}, p\hat{\boldsymbol{n}}) = \frac{1}{\exp\left\{\frac{p}{T(t)[1+\Theta(t,\boldsymbol{x},\hat{\boldsymbol{n}})]}\right\} - 1} + \Delta f(t, \boldsymbol{x}, p\hat{\boldsymbol{n}}), \tag{1.92}$$

where Δf is a generic deviation from the direction-dependent Planck spectrum. Neglecting it, we can expand f in powers of Θ

$$f(t, \boldsymbol{x}, p\hat{\boldsymbol{n}}) \approx f^{(0)}(t, p) - p \frac{\partial f^{(0)}(t, p)}{\partial p}\Theta + \cdots, \tag{1.93}$$

where the zeroth order distribution is an homogeneous Planck distribution with temperature $T(t)$,

$$f^{(0)}(t, p) \equiv \frac{1}{\exp\left[p/T(t)\right] - 1}, \tag{1.94}$$

and we used the property $T\partial f^{(0)}/\partial T = -p\partial f^{(0)}/\partial p$.

Plugging eq. (1.93) in eq. (1.91), and noticing that

$$p\frac{\partial}{\partial t}p\frac{\partial f^{(0)}}{\partial p}\Theta = +p\frac{\partial f^{(0)}}{\partial p}\frac{\partial \Theta}{\partial t} - p\Theta\frac{\mathrm{d}T}{T\,\mathrm{d}t}\frac{\partial}{\partial p}p\frac{\partial f^{(0)}}{\partial p} \tag{1.95}$$

we can rewrite the Liouville operator as

$$\begin{aligned}\frac{\mathrm{d}f}{\mathrm{d}t} =& -p\frac{\partial f^{(0)}}{\partial p}\left(\frac{\mathrm{d}T}{T\,\mathrm{d}T} + \frac{\partial \Theta}{\partial t} + \frac{\hat{\boldsymbol{n}}}{a}\cdot\nabla\Theta + H + \frac{\partial \Phi}{\partial t} + \hat{\boldsymbol{n}}\cdot\nabla\Psi\right)\\ &- p\Theta\frac{\partial}{\partial p}p\frac{\partial f^{(0)}}{\partial p}\left(\frac{\mathrm{d}T}{T\,\mathrm{d}t} + H\right).\end{aligned} \tag{1.96}$$

In a moment we will show that the second line is zero, therefore all the frequency dependence is factorized in the common factor $p\frac{\partial f^{(0)}}{\partial p}$ and we can fully describe the evolution of anisotropies with the frequency-independent variables Θ, Ψ, Φ. This is not the case if we consider second order perturbations of the primordial field [101], or if we consider non-negligible energy exchange in the interaction between photons and matter, as we will discuss in Section 3.2.

The collision operator. As we showed in Section 1.3, the collision operator contains all the possible interaction terms. However, Thomson scattering, i.e, the Compton scattering in the limit of zero energy exchange, is in practice the only one which is relevant for the generation of CMB anisotropies. In this limit the collision term reads [23]

$$C_{\mathrm{T}}[f] = n_{\mathrm{e}}\,\sigma_{\mathrm{T}}\left[f_0 - f + \hat{\boldsymbol{n}}\cdot\boldsymbol{v}_{\mathrm{b}}\left(-p\frac{\partial f^{(0)}}{\partial p}\right) - \frac{1}{2}P_2 f_2\right], \tag{1.97}$$

and, similarly to the Liouville terms, using eq. (1.93), it can be massaged into

$$C_{\mathrm{T}}[f] = n_{\mathrm{e}}\,\sigma_{\mathrm{T}}\left(\Theta_0 - \Theta + \hat{\boldsymbol{n}}\cdot\boldsymbol{v}_{\mathrm{b}} - \frac{1}{2}P_2\Theta_2\right)\left(-p\frac{\partial f^{(0)}}{\partial p}\right). \tag{1.98}$$

Here we introduced the baryonic velocity $\boldsymbol{v}_{\mathrm{b}}$, and we also defined the ℓ-th multipole moment of a field X as

$$X_\ell = \frac{1}{(-i)^\ell}\int\frac{\mathrm{d}\mu}{2}P_\ell(\mu)X(\theta). \tag{1.99}$$

where we defined $\mu = \hat{\boldsymbol{n}} \cdot \hat{\boldsymbol{v}}_{\rm b}$.[6]

Zeroth and first order Boltzmann equation for the photons We now have all the quantities we need to write the explicit expression of eq. (1.89), that we can divide by perturbation order. Since the collision term accounts for interactions, it is intrinsically a first order contribution, as we can directly see in eq. (1.98). Therefore, the zeroth order equation is

$$\frac{\mathrm{d}T}{T\,\mathrm{d}T} + \frac{\mathrm{d}a}{a\,\mathrm{d}t} = 0 \tag{1.100}$$

Hence $T(t) = T_0/a(t)$, as we anticipated in Section 1.3. This result guarantees that the second line of eq. (1.96) is identically zero, and we can completely drop the frequency dependence from the first order Boltzmann equation. Doing that it reads

$$\frac{\partial \Theta}{\partial t} + \frac{\hat{\boldsymbol{n}}}{a} \cdot \nabla \Theta + \frac{\partial \Phi}{\partial t} + \hat{\boldsymbol{n}} \cdot \nabla \Psi = n_{\rm e}\, \sigma_{\rm T} \left(\Theta_0 - \Theta + \hat{\boldsymbol{n}} \cdot \boldsymbol{v}_{\rm b} - \frac{1}{2} P_2 \Theta_2 \right). \tag{1.101}$$

Solving the Boltzmann equation The same approach we have outlined here can be applied to all the other species to derive all the Boltzmann equations. Then they can be solved alongside the linearised Einstein equation.

The first step is to write the Boltzmann equations in Fourier space. The Fourier transform of the real space linear Θ can be defined as

$$\Theta(t, \boldsymbol{k}, \hat{\boldsymbol{n}}) \equiv \int \mathrm{d}^3 \boldsymbol{x} e^{-i\boldsymbol{k}\cdot\boldsymbol{x}} \Theta(t, \boldsymbol{x}, \boldsymbol{n}) \,, \tag{1.102}$$

and, switching from proper time to conformal time, we get

$$\Theta' + ik\mu\,\Theta + \Phi' + ik\mu\,\Psi = -\tau' \left(\Theta_0 - \Theta + \mu v_{\rm b} - \frac{1}{2} P_2 \Theta_2 \right), \tag{1.103}$$

where we defined the optical depth[7]

$$\tau(\eta) \equiv \int_{\eta}^{\eta_0} \mathrm{d}\eta' n_{\rm e} \sigma_{\rm T} a \,. \tag{1.104}$$

[6] Strictly speaking, this is not always true, but it holds if the baryon velocity is irrotational, thing that we assume here for simplicity.

[7] To avoid awkward notation here we use η instead of τ to indicate the conformal time.

A possible approach would be to decompose it in a hierarchy of coupled differential equations for each multipole moment. Since with current experiment resolution we can easily probe angular scale up to $\ell \gg 1000$ this might still prove to be infeasible to the required accuracy in a time short enough to be used in a MCMC for parameter estimation (see Section 2.2).

A smarter approach is to use the formal integral solution of eq. (1.103) and solve a very limited number of hierarchy equations to obtain its source function [108]. The line-of-sight solution of eq. (1.103), conveniently evaluated at $\eta = \eta_0$ is

$$\begin{aligned}\Theta(\eta_0) =& \Theta(\eta_{\rm in}) e^{ik\mu(\eta_{\rm in}-\eta_0)} e^{-\tau(\eta_{\rm in})} \\ &+ \int_{\eta_{\rm in}}^{\eta_0} {\rm d}\eta \left[-\dot\Phi - ik\mu\Psi - \dot\tau\left(\Theta_0 + \mu v_{\rm b} - \frac{1}{2}P_2\Theta_2\right)\right] e^{ik\mu(\eta-\eta_0)} e^{-\tau(\eta)} \,.\end{aligned} \tag{1.105}$$

Provided that the initial condition are set early enough, the first line in the RHS is vanishingly small, since it exponentially suppressed by the extremely large optical depth. For the same reason the second term can be arbitrarily extended from $\eta_{\rm in}$ to the origin of time, hence

$$\Theta(\eta_0, \boldsymbol{k}, \hat{\boldsymbol{n}}) = \int_0^{\eta_0} {\rm d}\eta \left[-\dot\Phi - ik\mu\Psi - \dot\tau\left(\Theta_0 + \mu v_{\rm b} - \frac{1}{2}P_2\Theta_2\right)\right] e^{ik\mu(\eta-\eta_0)} e^{-\tau(\eta)} \,. \tag{1.106}$$

We are almost ready to decompose this expression in multipoles, but for one detail: the terms in the square brakets have some dependence on μ. However, thanks to the exponential, we can replace every power of μ with a derivative with respect to η and integrate by parts, getting

$$\Theta(\eta_0, \boldsymbol{k}, \hat{\boldsymbol{n}}) = \int_0^{\eta_0} {\rm d}\eta \, e^{ik\mu(\eta-\eta_0)} S(k,\eta) \,, \tag{1.107}$$

$$S(k,\eta) = -\dot\Phi e^{-\tau(\eta)} + g(\eta)\,\Theta_0 + g(\eta)\,\frac{1}{4}\Theta_2 - \frac{\rm d}{{\rm d}\eta}\left(\Psi\, e^{-\tau(\eta)} - \frac{g(\eta)\,\mu v_{\rm b}}{i\,k}\right) - \frac{{\rm d}^2}{{\rm d}\eta^2}\frac{3\,g(\eta)\,\Theta_2}{4\,k^2} \,, \tag{1.108}$$

where $g(\eta) \equiv -\dot\tau e^{-\tau}$ is the *visibility function*.

Since, as we already discussed, perturbation are sourced by the primordial perturbation field $\zeta_{\boldsymbol{k}}$ we can define a *source function* $\Delta(k,\eta)$ "renormalized" to the amplitude of the primordial perturbations

$$S(k,\eta) = \Delta(k,\eta)\zeta_{\boldsymbol{k}} \,. \tag{1.109}$$

Now we can decompose the line of sight solution in multipoles using the definition eq. (1.99), and since it holds

$$\int \frac{\mathrm{d}\mu}{2} P_\ell(\mu) e^{ik\mu(\eta-\eta_0)} = (-i)^\ell \, j_\ell[k(\eta_0-\eta)] \,, \tag{1.110}$$

we get

$$\Theta_\ell(\boldsymbol{k}, \eta_0) = \mathcal{T}_\ell(k) \, \zeta_{\boldsymbol{k}} \,. \tag{1.111}$$

where we defined the transfer functions

$$\mathcal{T}_\ell(k) = \int_0^{\eta_0} \mathrm{d}\eta \, \Delta(k,\eta) \, j_\ell[k(\eta_0-\eta)] \,. \tag{1.112}$$

It is somewhat useful to point out that we can rewrite eq. (1.108) as

$$\Theta(\eta_0, \boldsymbol{k}, \hat{\boldsymbol{n}}) = \sum_\ell (-i)^\ell \, (2\ell+1) \, P_\ell \, \mathcal{T}_\ell(k) \, \zeta_{\boldsymbol{k}} \,. \tag{1.113}$$

In general, eq. (1.111) can be evaluated numerically using Boltzmann codes such as `CLASS` [109]. However an approximated analytical discussion can give us some insights on its properties.

Since the visibility function is strongly peaked around recombination, we can evaluate all functions multiplied by it at $\eta = \eta_{\mathrm{rec}}$. Moreover we can use $v_{\mathrm{b}} \approx -3i\Theta_1$ at recombination, and integrate that term by part. With some massaging, we get

$$\begin{aligned} \Theta_\ell(\boldsymbol{k}, \eta_0) \approx {} & [\Theta_0(k, \eta_{\mathrm{rec}}) + \Psi(k, \eta_{\mathrm{rec}})] \, j_\ell[k(\eta_0 - \eta_{\mathrm{rec}})] \\ & + 3\Theta_1(k, \eta_{\mathrm{rec}}) \left\{ j_{\ell-1}[k(\eta_0-\eta_{\mathrm{rec}})] - \frac{(\ell+1)\, j_\ell[k(\eta_0-\eta_{\mathrm{rec}})]}{k(\eta_0-\eta_{\mathrm{rec}})} \right\} \\ & + \int_0^{\eta_0} e^{-\tau} \, \left[\dot{\Psi}(k,\eta) - \dot{\Phi}(k,\eta) \right] j_\ell[k(\eta_0-\eta)] \,. \end{aligned} \tag{1.114}$$

The first line of the RHS is the value of the "effective" monopole at recombination on a scale k. The physical monopole is side by side with the potential Ψ because photons that were in a potential well at recombination had to climb out of it before propagating to us. Each mode k is then projected by the spherical Bessel function on the sphere taking into account the distance that separate us from the last scattering surface $\eta_0 - \eta_{\mathrm{rec}}$. As a zeroth order approximation a perturbation of wavelength k is projected onto an

angular scale with $\ell \approx k(\eta_0 - \eta_{\rm rec}) - 1/2$, with smaller contribution to larger angular scales too [110]. It can be shown that the monopole is constant on large scales, that were outside of the horizon at recombination, and equal to the Newtonian potential $\Theta_0(k, \eta_{\rm rec}) + \Psi(k, \eta_{\rm rec}) \approx -\Phi(k, \eta_{\rm rec})/3$. This behaviour gets the name of *Sachs-Wolfe effect* (SW). On smaller scales the monopole displays an oscillatory behaviour, that is due to the plasma *acoustic oscillations* in the gravitational wells before and during recombination.

The second line describes the contribution due to the local dipole at recombination, which account for the bulk motion of the plasma. Like the monopole on small scales, it follows an oscillatory pattern, which is out of phase with the monopole oscillations. This means that its main effect is to increase the power in the troughs of the monopole oscillation.

The third line accounts for the integrated effect of the evolution of the potential on the photon propagation along the line of sight, the *integrated Sachs-Wolfe effect* (ISW). If a photon traverse a potential well that evolves in time, it gets redshifted of blueshifted by the well becoming deeper or shallower while the photon is in it.

Temperature anisotropies harmonic decomposition It is useful, mainly for observational purposes, to express the anisotropies of the 2-dimensional projection of a field, as seen from our position in space and time, in harmonic coefficients. They are defined as

$$\begin{aligned} a_{\ell m} \equiv a_{\ell m}(\boldsymbol{x}_{\mathbf{o}}, \eta_0) &= \int \mathrm{d}^2\hat{\boldsymbol{n}}\, Y^*_{\ell m}(-\hat{\boldsymbol{n}})\, \Theta(\eta_0, \boldsymbol{x}_{\mathbf{o}}, \hat{\boldsymbol{n}}) = \\ &= \int \frac{\mathrm{d}^3\boldsymbol{k}}{(2\pi)^3} e^{i\boldsymbol{k}\cdot\boldsymbol{x}} \int \mathrm{d}^2\hat{\boldsymbol{n}}\, Y_{\ell m}(-\hat{\boldsymbol{n}})\, \Theta(\eta_0, \boldsymbol{k}, \hat{\boldsymbol{n}}) \end{aligned} \tag{1.115}$$

where the minus sign in the spherical harmonics is due to the fact that looking in the direction $-\hat{\boldsymbol{n}}$ we can detect photons travelling along $\hat{\boldsymbol{n}}$. Using the eq. (1.113) and the identity (A.9) we get

$$a_{\ell m} = 4\pi\, i^\ell \int \frac{\mathrm{d}^3\boldsymbol{k}}{(2\pi)^3}\, \zeta_{\boldsymbol{k}}\, \mathcal{T}_\ell(k)\, Y_{\ell m}(\hat{\boldsymbol{k}})\,. \tag{1.116}$$

By construction the harmonic coefficients have ensemble average equal to 0. Instead, their variance, far from being negligible, is one of the most important observables we

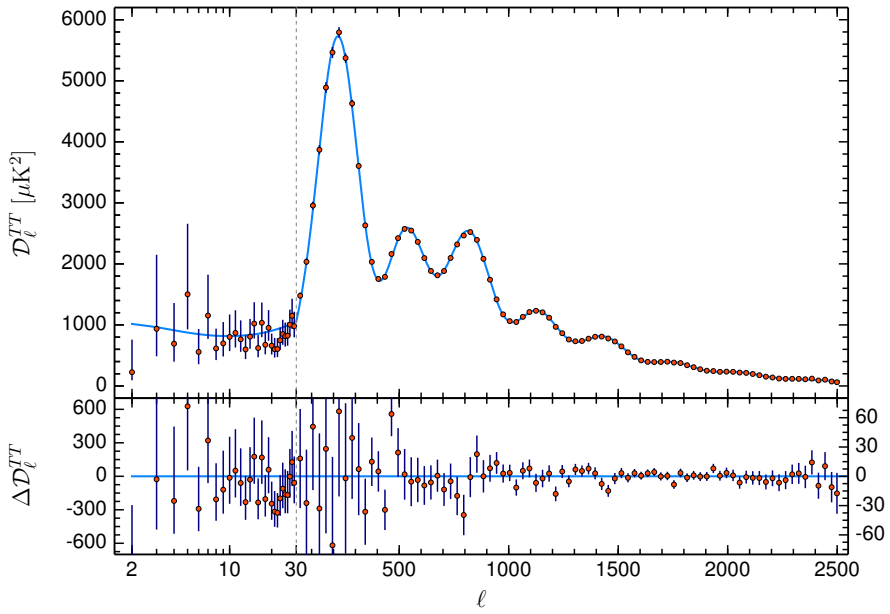

Figure 1.1.: CMB Temperature power spectrum as measured by *Planck*. Taken from [14].

have at our disposal in cosmology. As we will discuss in more length in Section 2.3 it is

$$\langle a_{\ell m}\, a_{\ell' m'}\rangle = \delta_{\ell\ell'}\delta_{mm'}C_\ell\,, \tag{1.117}$$

where C_ℓ is the *Temperature power spectrum*. As we can see in Figure 1.1, it displays all the features we discussed before: a plateau on larger angular scales given by the SW and ISW, and acoustic peaks with non-vanishing troughs given by the combined contribution of monopole and dipole oscillations.

1.5.2. Large scale structures

The second family of phenomena that, alongside the CMB anisotropies, can give us information about the primordial perturbation field is the 3-dimensional distribution of matter. It can be probed through a huge variety of tracers, such as gravitational lensing, Sunyaev-Zeldovich, and direct detection of galaxy clusters and their peculiar velocities. Here however we are not interested in discussing the properties of the specific tracers, but rather to sketch how the primordial perturbations evolve into the density perturbations we observe today. As usual we will make a number of simplifying assumptions that allow

solving the problem analytically. The same Boltzmann codes used to calculate the CMB anisotropies offer a solid tool to numerically solve the complete problem.

On larger scales the evolution of the perturbations is linear and therefore quite well understood. We will start by describing them during the matter domination epoch.

On smaller scales, non linearities become more and more important, and they need to be accounted for with more sophisticated methods. A viable approach is to expand perturbations at some higher perturbation order. Otherwise one can resort to different approximate non-perturbative methods, such as the halo model, that we will here apply to galaxy clusters to calculate the angular power spectrum of the Sunyaev-Zeldovich effect.

Evolution of the linear perturbation in matter domination

A convenient way to parametrize density fluctuations is to define the *fractional overdensity* with respect to the background

$$\delta(\tau, \boldsymbol{x}) \equiv \frac{\rho(\tau, \boldsymbol{x}) - \bar{\rho}(\tau)}{\bar{\rho}(\tau)} \,. \tag{1.118}$$

Is implicit in the definition, as we are treating ρ as a classical field, that the local density is smoothed over some typical scale $1/k$. In this section we are interested only to scales large enough to guarantee that $\delta \ll 1$ and in particular small enough to be effectively described using linear perturbations [68–70]. $k \leq k_{\rm lin} \equiv 0.1\,{\rm Mpc}^{-1}$ is a safe assumption.

The set of equations describing the evolution of the perturbations can be derived perturbing the Einstein equations, in a similar fashion as it can be done with background quantities. In Section 1.4.2, we already described the linear metric perturbation in the conformal gauge. With long, but straightforward calculations, one can use the eq. (1.63) to calculate the perturbed Einstein tensor (see e.g. [101] for the explicit calculation and expression).

The energy-momentum tensor can be perturbed in the same way. Its component, in the longitudinal gauge are [69]

$$\delta T^0{}_0 = -\bar{\rho}\,\delta\,, \tag{1.119}$$

$$\delta T^0{}_i = -\delta T^i{}_0 = (\bar{\rho}+\bar{p})v_i\,, \tag{1.120}$$

$$\delta T^i{}_j = -c_s^2\bar{\rho}\,\delta\,\delta^i_j + \Sigma^i_j\,. \tag{1.121}$$

Where v_i is the fluid velocity field, $\Sigma^{i\parallel}_j$ is the anisotropic shear perturbation, a traceless symmetric tensor. As discussed before, v_i and Σ_{ij} can be decomposed according with how they transform under spatial rotations thanks to the Helmholtz theorem. Considering scalar perturbations we can neglect the vector and tensor components and just consider the longitudinal components.

The various components of the linearised Einstein equation, conveniently expressed in Fourier space, read

$$k^2\,\Phi + 3\mathcal{H}(\Phi' + \mathcal{H}\,\Psi) = -\,4\pi\,G\,a^2\,\bar{\rho}\,\delta\,, \tag{1.122}$$

$$k^2(\Phi' + \mathcal{H}\,\Psi) = 4\pi\,G\,a^2(\bar{\rho}+\bar{p})\theta\,, \tag{1.123}$$

$$\Phi'' + \mathcal{H}(\Psi' + 2\Phi') + \left(2\frac{a''}{a} - \mathcal{H}^2\right)\Psi + \frac{k^2}{3}(\Phi - \Psi) = \frac{4\pi}{3}G\,a^2\,c_s^2\,\bar{\rho}\,\delta\,, \tag{1.124}$$

$$k^2(\Phi - \Psi) = 12\pi\,G\,a^2(\bar{\rho}+\bar{p})\sigma\,. \tag{1.125}$$

Here we defined the *velocity divergence*

$$\theta \equiv i\boldsymbol{k}\cdot\boldsymbol{v}\,, \tag{1.126}$$

and the *shear stress*

$$(\bar{\rho}+\bar{p})\sigma \equiv -\left(k^i k_j - \frac{1}{3}\delta_{ij}k^2\right)\Sigma^i{}_j\,. \tag{1.127}$$

From the conservation of the energy-momentum tensor — which we stress again is not independent from the Einstein equations — we get instead

$$\delta' = -\,(1+w)(\theta - 3\Phi') - 3\mathcal{H}(c_s^2 - w)\delta\,, \tag{1.128}$$

$$\theta' = -\,\mathcal{H}(1-3w)\theta - \frac{w'}{1+w}\theta + k^2\,\Psi - k^2\,\sigma + \frac{w}{1+w}k^2\,\delta\,. \tag{1.129}$$

These two relations are exact so they can be evaluated at any time. Here we are interested in describing the evolution of the matter fluctuations, both baryonic and cold dark matter, that on large scales contribute in the same way to the formation of structures. They are well described by a collision-less fluid with $w = c_2^2 = 0$, therefore, eq. (1.128) combined with eq. (1.129) gives

$$\delta_{\rm m}'' + \mathcal{H}\delta_{\rm cdm}' = -k^2\Psi + 3(\Phi'' + \mathcal{H}\Phi')\,. \tag{1.130}$$

Deep inside the Hubble radius the comoving gradient $-k^2\Psi$ dominates the source term. In the absence of shear it can be approximate by $-k^2\Phi$ thanks to eq. (1.125), and finally using the Poisson eq. (1.122) we get

$$\delta_{\rm cdm}'' + \mathcal{H}\delta_{\rm cdm}' \approx 4\pi\, G\, a^2\, \delta\rho\,. \tag{1.131}$$

It is important to notice for later reference (see Section 3.1.2) that $\delta\rho$ is the total energy density perturbation, i.e.,

$$\begin{aligned}\delta\rho &= \delta\rho_{\rm rad} + \delta\rho_{\rm cdm} + \delta\rho_{\rm b} + \delta\rho_\nu + \delta\rho_\Lambda + \cdots = \\ &= \rho_{\rm rad}\,\delta_{\rm rad} + \rho_{\rm cdm}\,\delta_{\rm cdm} + \rho_{\rm b}\,\delta_{\rm b} + \rho_\nu\,\delta_\nu + \rho_\Lambda\,\delta_\Lambda + \cdots\,.\end{aligned} \tag{1.132}$$

For simplicity we will focus on the matter dominated epoch, and we will not consider any exotic species. Neutrinos instead display an interesting behaviour: on scales larger that their free-streaming scale $k_{\rm fs}$ [111], they behave like normal matter. On smaller scales instead their perturbations are completely smoothed out by the free-streaming itself, hence $\delta_\nu \ll \delta_{\rm cdm}$. Therefore

$$\delta\rho = \begin{cases}(\rho_{\rm cdm} + \rho_{\rm b} + \rho_\nu)\delta_{\rm cdm} & \text{for } k < k_{\rm fs} \\ (\rho_{\rm cdm} + \rho_{\rm b})\delta_{\rm cdm} & \text{for } k_{\rm fs} < k < k_{\rm lin}\,.\end{cases} \tag{1.133}$$

Even though there could be both massive and massless neutrino, it is safe to assume that ρ_ν is dominated by the massive ones, so it scales just like matter energy density a^{-3} [111]. Then we know that the quantity

$$f_\nu = \frac{\rho_\nu}{\rho_{\rm cdm} + \rho_{\rm b} + \rho_\nu} \tag{1.134}$$

is approximately a constant.

Solving eq. (1.12) for $\rho \propto a^{-3}$ we get $a(\tau) \propto \tau^2$. Then eq. (1.131) is (cf. Ref. [111])

$$\delta''_{\rm cdm} + \frac{2}{\tau}\delta'_{\rm cdm} - \frac{6}{\tau^2}(1-f_\nu)\delta_{\rm cdm} = 0\,, \tag{1.135}$$

that can be easily solved imposing the ansatz $\delta_{cdm} \propto \tau^{2p}$: the two roots for p are

$$p = \frac{-1 \pm \sqrt{1+24(1-f_\nu)}}{4}\,. \tag{1.136}$$

so expanding at first order in f_ν, we get the result

$$\delta_{\rm cdm} = D_+(\tau)\,\delta_{\rm i} + D_-(\tau)\,\delta_{\rm i} \approx D^+(\tau)\,\delta_{\rm i}\,, \tag{1.137}$$

where we defined the linear growth functions

$$D_+(\tau) = a^{1-\frac{3}{5}f_\nu}\,, \qquad D_-(\tau) = a^{-\frac{3}{2}+\frac{3}{5}f_\nu}\,. \tag{1.138}$$

During the matter domination, for scales bigger than the one typical of neutrino relativistic to non-relativistic transition, the growth of cold dark matter perturbation is damped by the presence of massive neutrino, as described in eq. (1.137).

Exactly as in the case of CMB temperature anisotropies, the matter fractional over-density averages to 0 by construction. Therefore we can refer to its 2-points correlation function to gain some insight on its physical properties, or to its Fourier transform, the matter power spectrum, which is defined in a similar fashion to the primordial one (cf. eq. (1.79))

$$\langle \delta_{\boldsymbol{k_1},z}\delta^*_{\boldsymbol{k_2},z}\rangle \equiv (2\pi)^3\,\delta^{(3)}(\boldsymbol{k_1}-\boldsymbol{k_2})P_{\rm m}(k,z)\,. \tag{1.139}$$

It can be shown that the matter power spectrum can be related to the primordial one through [23]

$$P_{\rm m}(k,z) = \frac{3}{5}\frac{k^4}{\Omega_m^2 H_0^4}P_\zeta(k)\mathcal{T}_m^2(k)\,D_+^2(z)\,. \tag{1.140}$$

We will not discuss the details here, as they will not be relevant for the scope of this thesis; we refer to [23] for an accurate explanation. Here we just want to point out that varying the neutrino masses modify their total energy density, which in turn suppresses the linear matter power spectrum on small scales, as we can infer from eq. (1.140) even

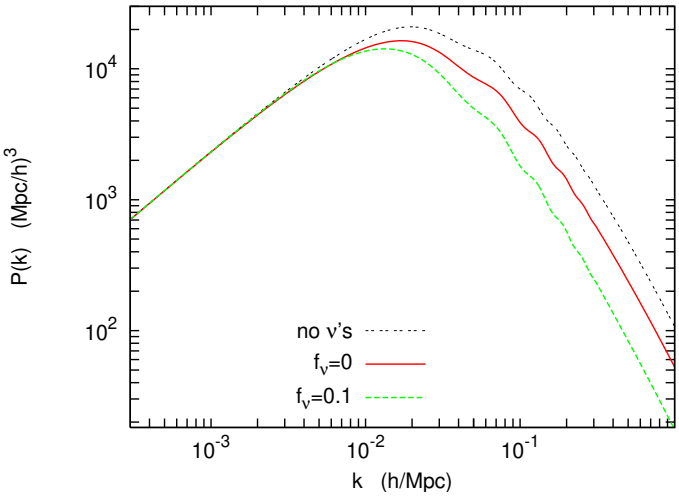

Figure 1.2.: Matter power spectrum for different neutrino models. Taken from [111].

just through our very simplified analytic discussion, or as we can see in Figure 1.2 where the exact equations have been solved numerically.

Halo distribution and Sunyaev-Zeldovich effect

Often, we are interested in describing processes that happen on scales similar to or smaller than $k_{\rm lin}$, the scale where the linear perturbation theory breaks down. One way to describe this processes is using the *halo model*, an approximate non-perturbative formalism that relies on the assumption that all matter in the universe resides in collapsed halos, that can in principle span the whole spectrum of possible masses. The description of physical processes is then divided in two. Since we will be interested in modelling the Sunyaev-Zeldovich power spectrum we will talk of the electron pressure distribution in the universe, that sources it. Instead of providing a full description in the whole universe, we can use a model of how electrons behave inside the single halo, and then combine it with the statistical distribution of halos with a given mass at a given time.

Halo mass function. When the over-density, which as we saw is a random field, exceeds a certain threshold δ_c in a region, the gravitational forces prevail over the universe expansion, and the region start collapsing. Therefore the gravitational collapse can be described as a stochastic process, and the halo number density per mass interval, called *halo mass function* (HMF) can be calculated in that framework.

In [112], Press and Schechter (PS) derived analytically the functional forms of the HMF that is (with some small adjustments) still in use. In a given point $\boldsymbol{x}$ we can consider the density field smoothed over a radius R

$$\delta(\boldsymbol{x}, R) = \int \frac{\mathrm{d}^3\boldsymbol{k}}{(2\pi)^3}\delta(\boldsymbol{k})\, W(k, R)\, e^{-i\boldsymbol{k}\cdot\boldsymbol{x}}\,, \tag{1.141}$$

where W is a window function. We can then define the variance of the over-density field

$$\sigma(R)^2 \equiv \langle\delta^2(\boldsymbol{x}, R)\rangle = \int \mathrm{d}k \frac{k^2}{2\pi^2} P_m(k)\, |W(k, R)|^2\,. \tag{1.142}$$

Notice that for $R \to \infty$, $\delta(\boldsymbol{x}, R) \to 0$ and also $\sigma(R) \to 0$, and as R decreases, σ increases monotonically. Therefore we can formally invert the relation and express R as a function of σ.

Assuming Gaussian perturbations, for a given σ, the probability of $\delta(\boldsymbol{x}, \sigma) > \delta_c$, i.e., the probability of starting the collapse on the scale σ, is

$$P_{\delta>\delta_c}(\sigma) = \int_{\delta_c}^{\infty} \mathrm{d}\delta \frac{1}{\sqrt{2\pi}\sigma} e^{-\frac{\delta^2}{2\sigma^2}}\,, \tag{1.143}$$

resulting in the HMF

$$\frac{\mathrm{d}n}{\mathrm{d}M} = \frac{1}{\sqrt{2\pi}} \frac{\bar{\rho}}{3M^2} \frac{\delta_c}{\sigma} e^{-\frac{\delta^2}{2\sigma^2}} \left(-\frac{R}{\sigma}\frac{\mathrm{d}\sigma}{\mathrm{d}R}\right). \tag{1.144}$$

The PS treatment has been corrected [113–115] and extended in various theoretical works [116–118].

This huge theoretical effort over the course of 40 years has provided significant insight on the physical mechanism of structure formation. However, theoretical calculation do not provide sufficiently accurate fits to precise N-body simulations. Therefore, theoretically motivated functional forms are directly fit to N-body simulations. Namely, using the parametrization

$$\frac{\mathrm{d}n}{\mathrm{d}M} = \frac{\bar{\rho}}{M} f(\sigma) \frac{\mathrm{d}\ln\sigma^{-1}}{\mathrm{d}M}\,, \tag{1.145}$$

the Press and Schechter HMF would correspond to

$$f(\sigma) = 2\frac{\delta_c}{\sqrt{2\pi}\sigma} e^{-\frac{\delta_c}{2\sigma^2}} , \tag{1.146}$$

whereas the HMF fitted to N-body provided in [119], that we will use throughout the thesis is

$$f(\sigma) = A\left[\left(\frac{b}{\sigma}\right)^a + 1\right] e^{-\frac{c}{\sigma^2}} , \tag{1.147}$$

where A, a, b, and c are redshift dependent free parameters.

Electron pressure profile. The SZ effect is sourced by hot electron that up-scatter the CMB photons we observe. Most of these hot electrons reside inside the *intra-cluster medium* (ICM) of each galaxy cluster that, according to the halo model, resides in halos. We are therefore interested in describing the electron distribution inside the halos, and to be precise, their pressure distribution that appears in the y-distortion definition eq. (1.44).

The fully analytic approaches to the problem [120] usually rely on some modified NFW profile for the matter density, and impose hydrodynamical equilibrium of the electrons to compute the pressure profile. However, direct measurements [121] proved how this simplistic models are disproved by data. Consequently different authors used different techniques to numerically or semi-analytically add baryonic effect to the model [122, 123]. A different approach is fitting the ICM to a sample of clusters [124], that however being quite close and very massive might not be representative of the whole ensemble.

Sunyaev-Zeldovich angular power spectrum. To calculate the SZ power spectrum we use a halo model approach, following [120, 125, 126]. We parametrize the density of dark matter halos in terms of the matter overdensity distribution δ, using a halo bias parameter $b_H(z, M)$, which depends on redshift and mass of the halo. The mass distribution of halos is given in terms of the halo mass function $\frac{\mathrm{d}n}{\mathrm{d}M}(z, M)$. Since the SZ is sensitive to the electron distribution rather than to the matter distribution, this has to be convolved with the halo Compton y-parameter image

$$y_{3D}(z, M, x) = \frac{\sigma_\mathrm{T}}{m_\mathrm{e}c^2} P_\mathrm{e}(z, M, x) , \tag{1.148}$$

where x is the distance from the center of the halo.

The SZ powerspectrum is given by the sum of the one- and two-halo terms [125, 126], which, in the Limber approximation, respectively read

$$C_\ell^{1h} = \int \mathrm{d}z \frac{\mathrm{d}^2V}{\mathrm{d}z\,\mathrm{d}\Omega} \int \mathrm{d}M \frac{\mathrm{d}n}{\mathrm{d}M}(z,M)|\tilde{y}_\ell(z,M)|^2, \tag{1.149}$$

$$C_\ell^{2h} = \int \mathrm{d}z \frac{\mathrm{d}^2V}{\mathrm{d}z\,\mathrm{d}\Omega} D_+^2(z) P_m(k) \left[\int \mathrm{d}M \frac{\mathrm{d}n}{\mathrm{d}M}(z,M) b_H(z,M) \tilde{y}_\ell(z,M)\right]^2 \Bigg|_{k=\left(\frac{\ell+1/2}{\chi(z)}\right)}. \tag{1.150}$$

Here $P_m(k)$ is the linear matter power spectrum, $D_+(z)$ is the growth factor, $\mathrm{d}^2V/\,\mathrm{d}z\,\mathrm{d}\Omega = c\chi^2(z)/H(z)$ is the comoving volume element per steradians and $\tilde{y}_\ell(z,M)$ is the 2D Fourier transform of the projected y-parameter image of the halo

$$\tilde{y}_\ell(z,M) = \frac{4\pi r_{s,y}}{\ell_{s,y}^2} \int \mathrm{d}x x^2 j_0\left(\frac{kx}{\ell_s}\right) y_{3D}(z,M,x), \tag{1.151}$$

$r_{s,y}$ is the typical scale radius of the y-image of the halo and $\ell_{s,y} = a(z)\chi(z)/r_{s,y}$. We refer to the appendix of [126] for a clear derivation of these two formulae.

Chapter 2.

Selected arguments of statistics and data analysis

In this chapter we provide a short summary of selected topics in statistics, which will be useful in the following. As it is customary in Cosmology we will take a Bayesian approach. According to the Bayesian interpretation, the probability expresses the degree of belief in a proposition.

From a more philosophical standpoint, this is the natural approach as cosmologists, because this interpretation is useful as it circumvents some shortcoming of the Frequentist approach, which is based on measuring the outcomes of repeated trials: in fact, it allows to make quantitative assessments about non-repeatable events. However its true power lies in the possibility to naturally address inverse probabilities using the Bayes theorem. Generally speaking, as physicists we are not interested in assessing how probable data are, given the true model of Nature, but rather in understanding how likely our model is, given the data we collected. Bayes theorem allow us to easily do that — even though, unfortunately, this interpretation is not exempt of possible critics.

From a practical standpoint, on the other hand, the Bayesian approach is linked to useful applications, such as Markov Chain Monte Carlo, that allow an easy treatment of nuisance parameters (via marginalization), and provides a consistent framework for model comparison and selection.

Bayes theorem and parameter estimation Let us start by considering two random events, A and B, with associated probability $P(A)$ and $P(B)$ — all the following also holds for a probability density function (PDF) $p(\theta)$ of a continuous random variable θ.

The joint probability of two events A and B is given by

$$P(A;B) \equiv P(A|B)\,P(B)\,, \tag{2.1}$$

where we defined the conditional probability of A given B, $P(A|B)$. Since $P(A;B) = P(B;A)$ we can infer that the conditional probability of A to be true, given that B was already realized is

$$P(A|B) = \frac{P(B|A)\;P(A)}{P(B)}\;. \tag{2.2}$$

This is the *Bayes theorem*, which the cornerstone of the Bayesian statistical approach.

In Physics, we often describe our model in terms of a set of parameters $\boldsymbol{\theta}$. We then try to infer their value collecting some data $\boldsymbol{x}$ (see, *e.g.*, [127] and references therein). In the frequentist approach, this is done building an *estimator* $\hat{\boldsymbol{\theta}}$ of the parameters, and then quantifying how likely is that it lies a given range around the true value of $\boldsymbol{\theta}$. In the Bayesian interpretation instead one uses the Bayes theorem to quantify how probable a set of parameters $\boldsymbol{\theta}$ is, given the data:

$$P(\boldsymbol{\theta}|\boldsymbol{x}) = \frac{P(\boldsymbol{x}|\boldsymbol{\theta})\;P(\boldsymbol{\theta})}{P(\boldsymbol{x})}\;. \tag{2.3}$$

Let us discuss every term in this expression separately.

$P(\boldsymbol{\theta}|\boldsymbol{x})$ is called the *posterior probability*, which usually is the relevant quantity we are interested in, as discussed.

$P(\boldsymbol{\theta})$ is the *prior probability* of the model. It parametrizes all previous knowledge we had about the model before performing the experiment. For example, it may carry information about previous measures of a parameter, or restrict the allowed domain of a parameter value (e.g., by requiring mass or intensities to be ≥ 0, or velocities to be $\leq c$). In general, the choice of prior can bias the evaluation of the posterior, especially if the prior is not chosen with care. As such, it is arguably the most criticized point of Bayesian probability. Dwelling in a discussion about prior legitimacy and sensible prior choices is outside the scope of this chapter, and we refer to [128] for a review of the possible criticalities.

$P(\boldsymbol{x})$ is the *evidence*. In the scope of this thesis it can be treated a normalizing constant that is irrelevant for all the discussed results. It is instead important e.g. to deal with model selection [129].

Finally, $P(\boldsymbol{x}|\boldsymbol{\theta})$ is the probability of collecting the measured data given the model. Conversely to the posterior, this quantity can be in principle — often simplifying assumptions need to be made — modelled and calculated knowing how the data have been collected and given a good knowledge of the instrument used. Interpreted as function of the sole model parameters, with the data evaluated on the one experimentally measured, this quantity is called *likelihood*.

$$\mathcal{L}(\boldsymbol{\theta}) \equiv p(\boldsymbol{x} = \boldsymbol{x}_{\rm exp}|\boldsymbol{\theta})\,. \tag{2.4}$$

Regardless of the prior, two different datasets can be combined and used together, applying eq. (2.1) to the likelihood. Given two sets of data $\boldsymbol{x}$ and $\boldsymbol{y}$, the likelihood of the joint analysis is

$$\mathcal{L}(\boldsymbol{x};\boldsymbol{y}|\boldsymbol{\theta}) = \mathcal{L}(\boldsymbol{x}|\boldsymbol{y};\boldsymbol{\theta})\,\mathcal{L}(\boldsymbol{y}|\boldsymbol{\theta}) = \mathcal{L}(\boldsymbol{x}|\boldsymbol{\theta})\,\mathcal{L}(\boldsymbol{y}|\boldsymbol{\theta})\,. \tag{2.5}$$

The second equality holds only if the two datasets are independent (otherwise the appropriate covariance have to be accounted for). In that case the likelihoods of the two experiments can just be multiplied together. However, this operation cannot be performed mindlessly: the likelihood is insensitive to the possibility that the data are inconsistent with each other. If this is the case, the produced results are mathematically well defined, but might be physically nonsensical. We will see an instance of this case in Section 3.1.

One of the main goals in data analysis is that of finding a set of "best-fit" model parameters, given our observed data.[1] This is called the problem of "parameter estimation". As mentioned, the approach to parameter estimation changes in a frequentist vs Bayesian framework. Even though the focus here is on Bayesian statistical inference, we will briefly discuss also the frequentist approach, as it allows us to introduce some important concepts about likelihoods.

[1] the other being hypothesis testing, in a frequentist setting, or model selection, in a Bayesian scenario. We do not discussed this here, as we never perform such tasks in the remainder of this thesis, and we focus instead on parameter estimation and forecasting.

Frequentist parameter estimation The general idea in the frequentist approach is to use the data we possess $\boldsymbol{x}$ to build an estimate $\hat{\boldsymbol{\theta}}$ of the parameters $\boldsymbol{\theta}$, whose true value is $\boldsymbol{\theta}_{\mathbf{o}}$. The best estimate would be the one that is unbiased

$$\langle \hat{\boldsymbol{\theta}} \rangle = \boldsymbol{\theta}_{\mathbf{o}} \,, \tag{2.6}$$

and minimizes the parameters variance

$$\mathrm{Var}(\theta_i) = \langle \hat{\theta}_i^2 \rangle - \langle \hat{\theta}_i \rangle^2 \,. \tag{2.7}$$

An estimator attaining this properties is said to be *optimal*.

In this optics, the maximum likelihood estimator (MLE) $\boldsymbol{\theta}_{\mathrm{ML}}$ such that

$$\mathcal{L}(\boldsymbol{\theta}_{\mathrm{ML}}) = \max_{\boldsymbol{\theta}} \mathcal{L}(\boldsymbol{\theta}) \tag{2.8}$$

is the best choice, whenever its explicit computation is possible. With best we mean that MLE has the following two crucial properties [127]

1. The MLE is asymptotically the unbiased estimator with minimum variance.
2. If an unbiased estimator with minimum variance (i.e., the *Cramér-Rao bound* that we will introduce in the next section) exist, it is equivalent to the MLE.

The first properties ensures that the MLE is the best estimate when dealing with a large enough amount of data, whereas the second guarantees that if an optimal estimator exist, than it can be found maximising the likelihood.

Bayesian parameter estimation In a Bayesian context one uses the posterior to assess the probability, therefore one of the most sensible estimates is the posterior mean, that coincides with the expectation value in the limit in which the posterior recover the right parameter PDF

$$\langle \boldsymbol{\theta} \rangle = \int \boldsymbol{\theta}\, p(\boldsymbol{\theta}|\boldsymbol{x})\, \mathrm{d}\boldsymbol{\theta} \,, \tag{2.9}$$

Calculating the MLE or the posterior mean might appear as an harmless process by the definition, but often, when the likelihood is a particularly complicated, or if the problem has a large dimensionality, one has to resort to sophisticated numerical approaches to get it (see Section 2.2).

Estimates are meaningless without quantifying their errors. In a frequentist setting, these are computed by sampling the likelihood distribution, and building suitable *confidence intervals*. We do not discuss this here (see e.g. [127] for a comprehensive treatment) and focus just on the Bayesian approach instead. In Bayesian statistics, *confidence regions* (CR) (also called *credible regions*, to distinguish from the frequentist limits) are defined in parameter spaces such that

$$\int_{\mathrm{CR}} p(\boldsymbol{\theta}|\boldsymbol{x})\,\mathrm{d}\boldsymbol{\theta} = \mathrm{CL}\,, \tag{2.10}$$

where the confidence level CL is usually set to 68.3% or 95.4% (values chosen because they respectively correspond to 1σ and 2σ fora a Gaussian distribution). There is some arbitrariness in choosing the region that would satisfy eq. (2.10) [130]. Common choices are selecting a region that is symmetric around the maximum likelihood, or selecting it in such a way that $P(\boldsymbol{\theta}|\boldsymbol{x}) > P(\boldsymbol{\theta}'|\boldsymbol{x})\ \forall\ \boldsymbol{\theta} \in \mathrm{CR} \wedge \boldsymbol{\theta}' \notin \mathrm{CR}$, but other criteria are often used. Note that by construction the confidence region depend on the prior. In cases when it is desirable to quote prior-independent results, the *Likelihood ratio* might get employed instead. A set of parameters $\boldsymbol{\theta}$ is compared with the maximum of the likelihood via

$$Z = -2\ln\left[\frac{\mathcal{L}(\boldsymbol{\theta})}{\mathcal{L}_{max}}\right]. \tag{2.11}$$

The interpretation of Z is clear in the case of Gaussian likelihood as parameters deviating $z\,\sigma$ from the MLE have $Z = z$.[2]

More often than not, in multi-parameter analysis we are interested in providing estimates and confidence regions for a single parameter, regardless of the value of the others. For example we may want to remove some nuisance parameters needed to represent foregrounds, or detector properties. Or we may want to study the bounds on a single parameter out of the many required by our physical model of interest. In both cases, in order to get the posterior of the parameters we are interested in (say $\theta_1, \cdots, \theta_m$) we need to *marginalize* over "uninteresting" parameters (say $\theta_{m+1}, \cdots, \theta_n$) integrating the posterior over their whole parameter space.

$$p(\theta_1, \cdots, \theta_m|\boldsymbol{x}) = \int p(\theta_1, \cdots, \theta_n|\boldsymbol{x})\ \mathrm{d}\theta_{m+1} \cdots \mathrm{d}\theta_n \tag{2.12}$$

[2] In cosmology often the covariance depends on the model, therefore the normalization of the Gaussian distribution depends on the model too. For this reason data may be Gaussian distributed and still the χ^2 and likelihood ratio analysis may give different results [131].

As in the case of the CR selection, the marginalization is prior dependent. In general, the location of the posterior mean before and after marginalization over some parameters might not coincide. Which one of the two estimates is the most relevant one depends on the specific circumstances of the problem, and shall be evaluated on a case-by-case basis.

In the case in which a flat prior (*i.e.*, a box prior probability between some minimum and maximum allowed parameter values) is used, the posterior probability is proportional to the Likelihood. This means that the maximum of the posterior coincide with the maximum of the Likelihood, and shares its properties. This is exactly the case in the analysis we present in Section 3.1.

2.1. Fisher information matrix

If the likelihood is unimodal and smooth, its logarithm can be Taylor-expanded around its maximum.

$$\ln \mathcal{L} = \ln \mathcal{L}(\boldsymbol{\theta}_{\rm ML}) + \frac{1}{2} \sum_{ij} (\theta_i - \theta_{{\rm ML},i}) \left. \frac{\partial^2 \ln \mathcal{L}}{\partial \theta_i \partial \theta_j} \right|_{\boldsymbol{\theta}_{\rm ML}} (\theta_j - \theta_{{\rm ML},j}) + ... \tag{2.13}$$

If we can neglect the cubic and higher-order terms, the information about the parameters (Co)variance is embedded in the Hessian of the likelihood. The Fisher information matrix is defined as its expectation value

$$F_{ij} = - \left\langle \frac{\partial^2 \ln \mathcal{L}}{\partial \theta_i \partial \theta_j} \right\rangle \tag{2.14}$$

therefore it is related to the covariance of the parameters through

$$\mathbf{Cov}(\theta_i, \theta_j) \equiv \langle \theta_i \, \theta_j \rangle - \langle \theta_i \rangle \langle \theta_j \rangle = [F^{-1}]_{ij} \, . \tag{2.15}$$

In this context the expectation value has to be intended as the ensemble average over the observational data we would gather if the Universe were described by the considered fiducial model.

The usefullness of the Fisher matrix comes from the Cramér-Rao inequality [129]. It states that for any unbiased estimator holds the relation

$$\sigma(\theta_i) \equiv \sqrt{{\rm Var}(\theta_i)} \geq \sqrt{[F^{-1}]_{ii}} \, . \tag{2.16}$$

The quantity defined at RHS is commonly referred to as *marginal error*, as it is the value one would obtain marginalizing over all the other parameters $\theta_j,\ j \neq i$, if the likelihood were Gaussian. It is worth noticing that it is greater or equal than the *conditional error* $1/\sqrt{F_{ii}}$, that is the error over θ_i assuming perfect knowledge of all the other parameters true value. The two errors coincide if and only if the estimator $\hat{\theta}_i$ is uncorrelated with the other parameters estimators, i.e., if F is block-diagonal.

It descends trivially from the property of the likelihood eq. (2.5) that the joint Fisher matrix of two independent experiment is the sum of the Fisher matrices.

Besides allowing a rigorous definition of the information content of the data and of estimator optimality, the Fisher matrix is also a crucial quantity for forecasting how well an experiment might perform even before collecting data. It must be noted that, due to the Cramér-Rao inequality, a Fisher matrix forecast is only an upper limit on what a given survey might achieve in term of constraining power. However, the ability of quickly assess at least the order of magnitude, is a valuable information when comparing many different possible experimental design.

2.1.1. Fisher matrix for Gaussian likelihood

If we are willing to approximate the data distribution with a Gaussian, the definition of the Fisher information matrix in eq. (2.14) can be massaged into a much more handy expression [129], that we will use in the following chapters.

Let $\boldsymbol{\mu}$ be the mean and $\mathbf{D}$ the data matrix

$$\mathbf{D} = (\boldsymbol{x} - \boldsymbol{\mu})(\boldsymbol{x} - \boldsymbol{\mu})^T \,. \tag{2.17}$$

If the model is evaluated at the true value of the parameters $\boldsymbol{\theta}$, the mean coincides with the data expectation value, and the expectation value of the data matrix is the covariance, i.e.,

$$\boldsymbol{\mu} = \langle \boldsymbol{x} \rangle \,, \qquad \langle \mathbf{D} \rangle = \mathbf{Cov} \,. \tag{2.18}$$

Extracting the logarithm from the definition of a multivariate Gaussian

$$\mathcal{L} = \frac{1}{(2\pi)^{n/2}\sqrt{\det \mathbf{Cov}}} \exp\left[-\frac{1}{2}(\boldsymbol{x} - \boldsymbol{\mu})\mathbf{Cov}^{-1}(\boldsymbol{x} - \boldsymbol{\mu})^T\right], \tag{2.19}$$

we get

$$\begin{aligned} 2\ln\mathcal{L} &= \ln\det\mathbf{Cov} + (\boldsymbol{x}-\boldsymbol{\mu})\mathbf{Cov}^{-1}(\boldsymbol{x}-\boldsymbol{\mu})^T + n\ln(2\pi) \\ &= \mathrm{Tr}\left[\ln\mathbf{Cov} + \mathbf{Cov}^{-1}\mathbf{D}\right]. \end{aligned} \tag{2.20}$$

Where, in the second line, we used the matrix identity $\ln\det\mathbf{Cov} = \mathrm{Tr}[\ln\mathbf{Cov}]$ and we dropped the irrelevant addend $n\ln(2\pi)$. Notice that in full generality both the mean and the covariance matrix are functions of the model parameters $\boldsymbol{\theta}$.

It is straightforward to calculate the first and second derivatives of the likelihood with respect to the model parameters θ_i and θ_j. They respectively read

$$2\ln\mathcal{L}_{,i} = \mathrm{Tr}[\mathbf{Cov}^{-1}\mathbf{Cov}_{,i} - \mathbf{Cov}^{-1}\mathbf{Cov}_{,i}\mathbf{Cov}^{-1}\mathbf{D} + \mathbf{Cov}^{-1}\mathbf{D}_{,i}]\,, \tag{2.21}$$

and

$$\begin{aligned} 2\ln\mathcal{L}_{,ij} = \mathrm{Tr}[&- \mathbf{Cov}^{-1}\mathbf{Cov}_{,i}\mathbf{Cov}^{-1}\mathbf{Cov}_{,j} + \mathbf{Cov}^{-1}\mathbf{Cov}_{,ij} \\ &+ \mathbf{Cov}^{-1}(\mathbf{Cov}_{,i}\mathbf{Cov}^{-1}\mathbf{Cov}_{,j} + \mathbf{Cov}_{,j}\,\mathbf{Cov}^{-1}\mathbf{Cov}_{,i})\mathbf{Cov}^{-1}\mathbf{D} \\ &- \mathbf{Cov}^{-1}(\mathbf{Cov}_{,i}\mathbf{Cov}^{-1}\mathbf{D}_{,j} + \mathbf{Cov}_{,j}\,\mathbf{Cov}^{-1}\mathbf{D}_{,i}) \\ &- \mathbf{Cov}^{-1}\mathbf{Cov}_{,ij}\mathbf{Cov}^{-1}\mathbf{D} + \mathbf{Cov}^{-1}\mathbf{D}_{,ij}]\,. \end{aligned} \tag{2.22}$$

Taking the expectation value of eq. (2.21), and using the relations

$$\langle\mathbf{D}_{,i}\rangle = 0\,, \qquad \langle\mathbf{D}_{,ij}\rangle = \boldsymbol{\mu}_{,i}\boldsymbol{\mu}_{,j}^T + \boldsymbol{\mu}_{,j}\boldsymbol{\mu}_{,i}^T\,. \tag{2.23}$$

we obtain

$$\langle\mathcal{L}_{,i}\rangle = 0\,. \tag{2.24}$$

On the ensemble average, the likelihood has an extreme on the true value of the parameters. Since by definition the extreme point is the maximum likelihood, this shows the unbiasedness of MLE.

We can now use eq. (2.22), (2.18), and (2.23) in the definition of the Fisher matrix eq. (2.14). With some algebra we get

$$F_{ij} = \langle\mathcal{L}_{,ij}\rangle = \frac{1}{2}\,\mathrm{Tr}[\mathbf{Cov}^{-1}\mathbf{Cov}_{,i}\mathbf{Cov}^{-1}\mathbf{Cov}_{,j} + \mathbf{Cov}^{-1}(\boldsymbol{\mu}_{,j}\boldsymbol{\mu}_{,i}^T)]\,, \tag{2.25}$$

This equation shows that the Fisher matrix depends on the physical model, and on the characteristics of the hypothetical experiment that would collect the data, but do not depends on data themselves. As mentioned earlier, this allows using a Fisher matrix approach to quickly forecast the maximum expected performance of an experiment before it is even operational.

2.2. Inference and Monte Carlo Markov Chains

The general goal, working in the Bayesain inference framework, is accurately sampling the posterior distribution. Unless we are in very simple cases, the posterior can be very complicated and in general not treatable analytically. Therefore it is necessary to resort to numerical approaches to sample it.

Markov chain monte carlo (MCMC) [132, 133] are useful to map probabilities in high dimensional parameter space in an efficient and accurate way. The evaluation time for a grid of fixed spacing scales exponentially with the number of dimension and the grid doesn't adjust to get more precision where is needed. On the other hand MCMC scales approximately linearly with the number of parameters and by construction has a larger point density in places where the likelihood is bigger, thus giving more accuracy around the maxima, which eventually are what we are interested in.

The goal is to generate a collection of points in parameters space, called *steps*, distributed according to a desired PDF, in this case the posterior. The MCMC is a method that uses the properties of *Markov processes* to do that. In particular, the MCMC is purposely build to be a Markov process that asymptotically reaches a unique stationary distribution $\pi_{\boldsymbol{x}}(\boldsymbol{\theta})$, proportional to the posterior $p(\boldsymbol{\theta}|\boldsymbol{x})$.

A generic *discrete-time stochastic process* is a system in which a "time"-dependent random variable $\boldsymbol{\Theta}(t)$ exist [134].[3] Given a set of times $t_0 \leq t_1 \leq \cdots \leq t_n$, the stochastic process is described by the joint probability of measuring the value $\boldsymbol{\theta}^{(i)}$ of $\boldsymbol{\Theta}(t)$ at each time t_i

$$p\left(\boldsymbol{\theta}^{(n)}, t_n; \boldsymbol{\theta}^{(n-1)}, t_{n-1}; \boldsymbol{\theta}^{(n-2)}, t_{n-2}; \dots\right). \tag{2.26}$$

[3] For explanatory purpose we refer here to a "time" in loose sense. In an MCMC it is replaced the iteration index.

Therefore, the probability of measuring $\boldsymbol{\theta}^{(n+1)}$ at time t_{n+1} conditional to the previous evolution of the system is

$$p\left(\boldsymbol{\theta}^{(n+1)}, t_{n+1}\middle|\, \boldsymbol{\theta}^{(n)}, t_n; \boldsymbol{\theta}^{(n-1)}, t_{n-1}; \dots\right) = \frac{p\left(\boldsymbol{\theta}^{(n+1)}, t_{n+1}; \boldsymbol{\theta}^{(n)}, t_n; \boldsymbol{\theta}^{(n-1)}, t_{n-1}; \dots\right)}{p\left(\boldsymbol{\theta}^{(n)}, t_n; \boldsymbol{\theta}^{(n-1)}, t_{n-1}; \dots\right)} . \tag{2.27}$$

Markov processes are a subset of stochastic processes that satisfy the condition

$$p\left(\boldsymbol{\theta}^{(n+1)}, t_{n+1}\middle|\, \boldsymbol{\theta}^{(n)}, t_n; \boldsymbol{\theta}^{(n-1)}, t_{n-1}; \dots\right) \equiv p\left(\boldsymbol{\theta}^{(n+1)}, t_{n+1}\middle|\, \boldsymbol{\theta}^{(n)}, t_n\right) . \tag{2.28}$$

The conditional probability at the time t_n is completely determined by the knowledge of the most recent condition alone, and $p\left(\boldsymbol{\theta}^{(n+1)}, t_{n+1}\middle|\, \boldsymbol{\theta}^{(n)}, t_n\right)$ can be interpreted as the *transition probability* from state $\boldsymbol{\theta}^{(n)}$ to $\boldsymbol{\theta}^{(n+1)}$ at the time t_n. One of the fundamental properties of Markov processes that we will exploit is that they might admit a unique *stationary distribution* π such that for any $n > \bar{n}$ for some $\bar{n}$

$$p(\boldsymbol{\theta}^{(n)}, t_n|\boldsymbol{\theta}^{(n-1)}, t_{n-1}) = \pi(\boldsymbol{\theta}) \quad \Rightarrow \quad p(\boldsymbol{\theta}^{(n+1)}, t_{n+1}|\boldsymbol{\theta}^{(n)}, t_n) = \pi(\boldsymbol{\theta}) , \tag{2.29}$$

that also is the *limiting distribution* regardless of the Markov process initial conditions.

MCMC are generally constructed with algorithms that exploit this property. One of the most widely spread, and easy to understand, is Metropolis-Hastings (MH). A sufficient condition for a Markov process to admit a stationary solution $\pi_{\boldsymbol{x}}$ is to satisfy the detailed balance relation

$$\pi_{\boldsymbol{x}}\left(\boldsymbol{\theta}^{(\boldsymbol{n+1})}\right)\ p\left(\boldsymbol{\theta}^{(n+1)}, t_{n+1}\middle|\, \boldsymbol{\theta}^{(n)}, t_n\right) = \pi_{\boldsymbol{x}}\left(\boldsymbol{\theta}^{(\boldsymbol{n})}\right)\ p\left(\boldsymbol{\theta}^{(n)}, t_n\middle|\, \boldsymbol{\theta}^{(n+1)}, t_{n+1}\right) . \tag{2.30}$$

MH builds a Markov process with transition probability that satisfies the detail balance condition with $\pi_{\boldsymbol{x}}(\boldsymbol{\theta}) = p(\boldsymbol{\theta}|\boldsymbol{x})$, as described.

The chain is initialized by selecting a random point in parameter space and adding it to the chain. Then an iterative process takes place.

1. Start from the last step in the chain, a set of parameters $\boldsymbol{\theta}^{(n)}$, and it computes the associated posterior probability $p_n \equiv p(\boldsymbol{\theta}^{(n)}|\boldsymbol{x})$.

2. Select a random point $\boldsymbol{\theta}'$ in parameter space following a *proposal distribution* $g_{\boldsymbol{\theta}^{(n)}}(\boldsymbol{\theta})$. The parameters describing the proposal distribution can in principle depend on the

previous point $\boldsymbol{\theta}^{(n)}$, hence the lower-script. To give an example, in the application we will describe in Section 2.2, it will be a multivariate Gaussian distribution.

3. Compute the new posterior in the proposed point $p' \equiv p(\boldsymbol{\theta}'|\boldsymbol{x})$.

4. Calculate the acceptance threshold

$$\alpha(\boldsymbol{\theta}', \boldsymbol{\theta}^{(n)}) = \min\left(1, \frac{p'}{p_n} \frac{g_{\boldsymbol{\theta}'}(\boldsymbol{\theta}^{(n)})}{g_{\boldsymbol{\theta}^{(n)}}(\boldsymbol{\theta}')}\right) \tag{2.31}$$

5. Draw a uniform random number in $[0, 1]$. If it exceed the acceptance probability the new proposed point is accepted in the chain: $\boldsymbol{\theta}^{(n+1)} \equiv \boldsymbol{\theta}'$. Otherwise the previous point is duplicated: $\boldsymbol{\theta}^{(n+1)} \equiv \boldsymbol{\theta}^{(n)}$.

6. Iterate.

Using this algorithm eq. (2.30) is verified by construction. The transition probability is in fact the product of the proposal distribution times the acceptance probability $p\left(\boldsymbol{\theta}^{(n+1)}, t_{n+1} \middle| \boldsymbol{\theta}^{(n)}, t_n\right) = \alpha(\boldsymbol{\theta}', \boldsymbol{\theta}^{(n)})\ g_{\boldsymbol{\theta}^{(n)}}(\boldsymbol{\theta}^{(n+1)})$, hence

$$\frac{p\left(\boldsymbol{\theta}^{(n+1)}, t_{n+1} \middle| \boldsymbol{\theta}^{(n)}, t_n\right)}{p\left(\boldsymbol{\theta}^{(n)}, t_n \middle| \boldsymbol{\theta}^{(n+1)}, t_{n+1}\right)} = \frac{p^{(n+1)}}{p^{(n)}}\,. \tag{2.32}$$

When running a chain we need to know when it has converged and if it has explored the whole parameter space. Therefore, it is crucial to select *a priori* a convergence criterion to tell when it is appropriate to stop the iteration.

One possible choice is the Gelman-Rubin method [135]. M chains are started in different points in parameter space, and every of them collects 2N steps. The first N points of each chain are discarded as burn in. Now we can refer to the i-th element of the j-th chain as $\boldsymbol{\theta}^{(i,j)}$ with $i = 1, \ldots, N$ and $j = 1, \ldots, M$.

The mean of the j-th chain is

$$\bar{\boldsymbol{\theta}}^{(j)} = \frac{1}{N} \sum_{i=1}^{N} \boldsymbol{\theta}^{(i,j)}\,, \tag{2.33}$$

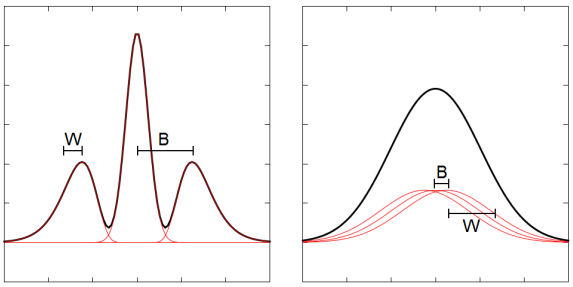

Figure 2.1.: Pictorial representation of the idea underlying the Gelman-Rubin criteria. On the left side 3 chains that haven't explored the parameter space properly. On the right side the same chains when they begin to converge

and the mean of the sample is

$$\bar{\boldsymbol{\theta}} = \frac{1}{N\,M} \sum_{i,j=1}^{N,M} \boldsymbol{\theta}^{(i,j)} \,. \tag{2.34}$$

Then the variance between the chains is

$$B = \frac{1}{M-1} \sum_{j=1}^{M} (\bar{\boldsymbol{\theta}}^{(j)} - \bar{\boldsymbol{\theta}})^2 \,, \tag{2.35}$$

and the mean of the variances within single chains

$$W = \frac{1}{M(N-1)} \sum_{i,j=1}^{M,N} (\bar{\boldsymbol{\theta}}^{(i,j)} - \bar{\boldsymbol{\theta}}^{(j)})^2 \,. \tag{2.36}$$

We can define the ratio between two estimates of the variance of the distribution

$$R = \frac{\frac{N-1}{N} W + (1 + \frac{1}{M}) B}{W} \,. \tag{2.37}$$

The numerator is an unbiased estimator of the variance if the distribution is stationary, but is otherwise an overestimation. On the other hand the denominator underestimates the variance if the individual sequences have not converged yet. In Figure 2.1 we give a qualitative representation of the quantities used to compute R.

Before the sampling is performed, a threshold value of R is selected, and the iterations are not stopped before the value of R is inferior to the threshold. $R < 1.03$ is generally considered a good choice that guarantees proper convergence [136].

Once the chain converge the burn-in are discarded and what is left is merged together. By construction the density of the chains point in parameter space is proportional to the posterior probability of said point. It is therefore trivial to deduce best fit parameters and confidence levels: The posterior mean eq. (2.9) is

$$\langle \boldsymbol{\theta} \rangle \approx \frac{1}{N} \sum_{i=1}^{N} \boldsymbol{\theta}^{(i)} \,, \tag{2.38}$$

and the marginal probability for parameter for parameter θ_j in eq. (2.12) is constructed by removing from each point of the chain the information about all θ_i with $i \neq j$. What is left, is N steps drawn from the θ_j parameter space with density proportional to the marginal probability. All information about variance and confidence intervals are therefore constructed building binning the marginal probability in an histogram.

The same marginalization procedure can be use to produce the 2D marginal probability of a couple of parameters. The resulting data can be showed in a scatter plots to describe the parameters correlations. The *triangle plots* that we will later show (e.g., in Figure 3.13a) are an example.

MH is just one of many possible approaches to MCMC sampling. Other useful and powerful methods are e.g. Gibbs sampling or Hamiltonian sampling, but which method is best depends on the problem at hand. For a detailed discussion see e.g. [128].

2.3. Statistic of a statistically isotropic random field on a sphere

Here we are interested in discussing the general properties of the projection on a sphere of a statistically homogeneous and isotropic scalar random field, regardless of the underlying physical properties. To fix the notation and help the interpretation, we consider here of the concrete physical example of the CMB temperature anisotropy field here. Of course all results can be directly applied or easily geenralized to any scalar field on the sphere (e.g. CMB E and B polarization modes, the galaxy overdensity field in tomographic spherical shells, etc.).

Temperature anisotropies are represented by the coefficients $a_{\ell m}$ of the spherical harmonic expansion of the CMB sky

$$T(\hat{\boldsymbol{n}}) = \sum_{\ell m} a_{\ell m} Y_{\ell m}(\hat{\boldsymbol{n}}) \ . \tag{2.39}$$

where

$$a_{\ell m} \equiv \int \mathrm{d}\hat{\boldsymbol{n}}\, T(\hat{\boldsymbol{n}})\, Y^*_{\ell m}(\hat{\boldsymbol{n}})\,. \tag{2.40}$$

To obtain the projection of a 3D field $T(\boldsymbol{x})$ on the sphere, we ought to integrate the field along the line of sight, in the required direction $\hat{\boldsymbol{n}}$. For temperature the leading order term, as seen in 1.5.1 (cfr. [137]), has the form

$$T(\hat{\boldsymbol{n}}) = \int_0^{\tau_0} \mathrm{d}\tau \int \frac{\mathrm{d}^3\boldsymbol{k}}{(2\pi)^3}\, e^{i\boldsymbol{k}\cdot\hat{\boldsymbol{n}}\chi} \Delta(k,\tau)\, \zeta_{\boldsymbol{k}} \tag{2.41}$$

for some known *source function* Δ, and where $\chi = \tau_0 - \tau$ is the comoving distance. Plugging this equation in eq. (2.40), and using identity (A.7), it is straightforward to find

$$a_{\ell m} = 4\pi\, i^\ell \int \frac{\mathrm{d}^3\boldsymbol{k}}{(2\pi)^3}\, \zeta_{\boldsymbol{k}}\, \mathcal{T}_\ell(k)\, Y_{\ell m}(\hat{\boldsymbol{k}})\,, \tag{2.42}$$

where we defined the *transfer function* $\mathcal{T}_\ell(k)$ as

$$\mathcal{T}_\ell(k) \equiv \int_0^{\tau_0} \mathrm{d}\tau\, \Delta(k,\tau)\, j_\ell(k\chi)\,. \tag{2.43}$$

2.3.1. Angular power spectrum

The variance of the harmonic coefficients is

$$\begin{aligned} \langle a_{\ell m}\, a^*_{\ell' m'} \rangle &= (4\pi)^2\, i^{\ell-\ell'} \int \frac{\mathrm{d}^3\boldsymbol{k}}{(2\pi)^3} \int \frac{\mathrm{d}^3\boldsymbol{k}'}{(2\pi)^3} \mathcal{T}_\ell(k)\, \mathcal{T}_{\ell'}(k')\, Y_{\ell m}(\hat{\boldsymbol{k}})\, Y^*_{\ell' m'}(\hat{\boldsymbol{k}}')\, \langle \zeta_{\boldsymbol{k}} \zeta_{k'} \rangle \\ &= \delta_{\ell\ell'}\, \delta_{mm'}\, \frac{2}{\pi} \int \mathrm{d}k\, k^2\, \mathcal{T}^2_\ell(k) P(k) \\ &\equiv \delta_{\ell\ell'}\, \delta_{mm'}\, C_\ell\,, \end{aligned} \tag{2.44}$$

where, in the second line we used the statistical homogeneity and isotropy properties of the random field $\zeta_{\boldsymbol{k}}$ expressed in eq. (1.79), and in the third we defined the *angular power spectrum* C_ℓ.

If we wish to estimate the power-spectrum from data (real or simulated) we can resort to the MLE. Since in the rest of this thesis we will mainly be interested assessing future detectability of physical effect through Fisher matrix analysis, in this chapter we will consider a very idealized setting, assuming Gaussian likelihoods and without delving into all the practical complications of e.g. correlated noise, systematics, foreground contamination, partial sky coverage, etc. Under these assumptions the MLE is

$$\hat{C}_\ell = \frac{1}{2\ell+1}\sum_m |a_{\ell m}|^2 \,. \tag{2.45}$$

The power spectrum covariance computation is straightforward from the definition

$$\mathbf{Cov}(\hat{C}_\ell, \hat{C}_{\ell'}) = \langle \hat{C}_\ell \, \hat{C}_{\ell'} \rangle - \langle \hat{C}_\ell \rangle \langle \hat{C}_{\ell'} \rangle \,. \tag{2.46}$$

The first term reads

$$\begin{aligned}
\langle \hat{C}_\ell \, \hat{C}_{\ell'} \rangle =& \frac{1}{(2\ell+1)(2\ell'+1)} \sum_{m,m'} \langle a_{\ell m} \, a^*_{\ell m} \, a_{\ell' m'} \, a^*_{\ell' m'} \rangle = \\
& \frac{1}{(2\ell+1)(2\ell'+1)} \sum_{m,m'} \Big(\langle a_{\ell m} \, a^*_{\ell m} \rangle \langle a_{\ell' m'} \, a^*_{\ell' m'} \rangle + \langle a_{\ell m} \, a_{\ell' m'} \rangle \langle a^*_{\ell m} \, a^*_{\ell' m'} \rangle + \\
& + \langle a_{\ell m} \, a^*_{\ell' m'} \rangle \langle a_{\ell' m'} \, a^*_{\ell m} \rangle + \langle a_{\ell m} \, a^*_{\ell m} \, a_{\ell' m'} \, a^*_{\ell' m'} \rangle_c \Big) \\
\approx & C_\ell \, C_{\ell'} + \delta_{\ell \ell'} \, \frac{2 C_\ell \, C_{\ell'}}{2\ell+1} \,,
\end{aligned} \tag{2.47}$$

where in the second equation we used the Wick theorem to expand the 4-points correlations in its connected contributions, and in the third we used the *weakly non-Gaussian approximation* to neglect the 4-points connected function. Hence

$$\mathbf{Cov}(\hat{C}_\ell, \hat{C}_{\ell'}) = \delta_{\ell \ell'} \, \frac{2 C_\ell \, C_{\ell'}}{2\ell+1} \,. \tag{2.48}$$

In the weakly non-Gaussian approximation the Covariance matrix is diagonal, i.e., each C_ℓ is independent from the other coefficients with $\ell \neq \ell'$.

Thanks to this property, it is trivial to generalize this treatment to the joint analysis of multiple observables like CMB temperature and polarization. In full generality, the covariance matrix for $([C_\ell^{TT}]_{\ell=1,\cdots,\ell_{\rm max}}, [C_\ell^{EE}]_{\ell=1,\cdots,\ell_{\rm max}})$ would be a $2\ell_{\rm max} \times 2\ell_{\rm max}$ matrix

of the kind

$$\mathbf{Cov}(\hat{C}_\ell^{\Xi\Xi}, \hat{C}_\ell^{\Xi'\Xi'}) = \left(\begin{array}{c|c} \langle a^T_{\ell m}\, a^{T*}_{\ell m}\, a^T_{\ell' m'}\, a^{T*}_{\ell' m'}\rangle & \langle a^T_{\ell m}\, a^{T*}_{\ell m}\, a^E_{\ell' m'}\, a^{E*}_{\ell' m'}\rangle \\ \hline \langle a^E_{\ell m}\, a^{E*}_{\ell m}\, a^T_{\ell' m'}\, a^{T*}_{\ell' m'}\rangle & \langle a^E_{\ell m}\, a^{E*}_{\ell m}\, a^E_{\ell' m'}\, a^{E*}_{\ell' m'}\rangle \end{array} \right), \tag{2.49}$$

where $\Xi = T, E$. However, due to the decorrelation of different multipoles in the weekly non-Gaussian limit, we can just analyse the power-spectrum ℓ by ℓ.

For instance, the one dimensional Fisher matrix for the angular power spectum amplitude (that is, the detectability of the angular power spectrum itself) is

$$\begin{aligned} F([C_\ell^{TT}]_{\ell=1,\cdots,\ell_{\max}}, [C_\ell^{EE}]_{\ell=1,\cdots,\ell_{\max}}) &= \sum_{\ell=1}^{\ell_{\max}} F_\ell(C_\ell^{TT}, C_\ell^{EE}) \equiv \\ \equiv \sum_{\ell=1}^{\ell_{\max}} \frac{2}{2\ell+1} &\begin{pmatrix} C_\ell^{TT} \\ C_\ell^{EE} \end{pmatrix} \cdot \begin{pmatrix} C_\ell^{TT} C_\ell^{TT} & C_\ell^{TT} C_\ell^{EE} + 2(C_\ell^{TE})^2 \\ C_\ell^{TT} C_\ell^{EE} + 2(C_\ell^{TE})^2 & C_\ell^{EE} C_\ell^{EE} \end{pmatrix}^{-1} \begin{pmatrix} C_\ell^{TT} \\ C_\ell^{EE} \end{pmatrix}. \end{aligned} \tag{2.50}$$

2.3.2. Angular bispectrum

The bispectrum is defined in a similar way, as the harmonic transform of the three point correlation function

$$\begin{aligned} B^{\ell_1\ell_2\ell_3}_{m_1 m_2 m_3} \equiv& \langle a_{\ell_1 m_1} a_{\ell_2 m_2} a_{\ell_3 m_3}\rangle \\ =& (4\pi)^3\, i^{\ell_1+\ell_2+\ell_3} \int \frac{\mathrm{d}^3\boldsymbol{k_1}}{(2\pi)^3} \int \frac{\mathrm{d}^3\boldsymbol{k_2}}{(2\pi)^3} \int \frac{\mathrm{d}^3\boldsymbol{k_3}}{(2\pi)^3}\, \mathcal{T}_{\ell_1}(k_1)\, \mathcal{T}_{\ell_2}(k_2)\, \mathcal{T}_{\ell_3}(k_3) \times \\ & \times Y_{\ell_1 m_1}(\hat{\boldsymbol{k}}_{\boldsymbol{1}})\, Y_{\ell_2 m_2}(\hat{\boldsymbol{k}}_{\boldsymbol{2}})\, Y_{\ell_3 m_3}(\hat{\boldsymbol{k}}_{\boldsymbol{3}})\, \langle \zeta_{\boldsymbol{k_1}} \zeta_{\boldsymbol{k_2}} \zeta_{\boldsymbol{k_3}}\rangle = \\ =& (4\pi)^3\, i^{\ell_1+\ell_2+\ell_3} \int \frac{\mathrm{d}^3\boldsymbol{k_1}}{(2\pi)^3} \int \frac{\mathrm{d}^3\boldsymbol{k_2}}{(2\pi)^3} \int \frac{\mathrm{d}^3\boldsymbol{k_3}}{(2\pi)^3}\, \mathcal{T}_{\ell_1}(k_1)\, \mathcal{T}_{\ell_2}(k_2)\, \mathcal{T}_{\ell_3}(k_3) \times \\ & \times Y_{\ell_1 m_1}(\hat{\boldsymbol{k}}_{\boldsymbol{1}})\, Y_{\ell_2 m_2}(\hat{\boldsymbol{k}}_{\boldsymbol{2}})\, Y_{\ell_3 m_3}(\hat{\boldsymbol{k}}_{\boldsymbol{3}})\, (2\pi)^3\, \delta^{(3)}(\boldsymbol{k_1}+\boldsymbol{k_2}+\boldsymbol{k_3})\, B_\zeta(k_1,k_2,k_3) = \\ =& \left(\frac{2}{\pi}\right)^3 \int \mathrm{d}k_1\, \mathrm{d}k_2\, \mathrm{d}k_3\, k_1^2\, k_2^2\, k_3^2\, \mathcal{T}_{\ell_1}(k_1)\, \mathcal{T}_{\ell_2}(k_2)\, \mathcal{T}_{\ell_3}(k_3)\, B_\zeta(k_1,k_2,k_3) \times \\ & \times \int \mathrm{d}x\, x^2\, j_{\ell_1}(k_1 x)\, j_{\ell_2}(k_2 x)\, j_{\ell_3}(k_3 x) \int \mathrm{d}^2\hat{\boldsymbol{x}}\, Y_{\ell_1 m_1}(\hat{\boldsymbol{x}})\, Y_{\ell_2 m_2}(\hat{\boldsymbol{x}})\, Y_{\ell_3 m_3}(\hat{\boldsymbol{x}})\,. \end{aligned} \tag{2.51}$$

Here in the second equation we used the definition of the primordial bispectrum eq. (1.84), and to get the last equation we used the Rayleigh expansion of the Dirac delta eq. (A.8).

The last integral over $\hat{\boldsymbol{x}}$, known as *Gaunt integral* can be expressed in terms of Wigner-3j symbols as

$$\mathcal{G}^{\ell_1\ell_2\ell_3}_{m_1m_2m_3} \equiv \int \mathrm{d}^2\hat{\boldsymbol{x}} Y_{\ell_1m_1}(\hat{\boldsymbol{x}}) Y_{\ell_2m_2}(\hat{\boldsymbol{x}}) Y_{\ell_3m_3}(\hat{\boldsymbol{x}}) = h_{\ell_1\ell_2\ell_3} \begin{pmatrix} \ell_1 & \ell_2 & \ell_3 \\ m_1 & m_2 & m_3 \end{pmatrix}, \tag{2.52}$$

where in the second equality we used eq. (A.20), defining

$$h_{\ell_1\ell_2\ell_3} \equiv \sqrt{\frac{(2\ell_1+1)(2\ell_2+1)(2\ell_3+1)}{4\pi}} \begin{pmatrix} \ell_1 & \ell_2 & \ell_3 \\ 0 & 0 & 0 \end{pmatrix}. \tag{2.53}$$

The fact that in eq. (2.51) the Gaunt integral carries all the information about the azimuthal-m dependence is a direct consequence of the statistical isotropy of the random field. Therefore, it is convenient to factor out the Gaunt integral from the bispectrum and work with the *reduced bispectum* $b_{\ell_1\ell_2\ell_3}$ defined through

$$B^{\ell_1\ell_2\ell_3}_{m_1m_2m_3} = \mathcal{G}^{\ell_1\ell_2\ell_3}_{m_1m_2m_3} b_{\ell_1\ell_2\ell_3}\,. \tag{2.54}$$

Another quantity that is commonly used is the *angle averaged bispectrum* defined as

$$B_{\ell_1\ell_2\ell_3} = \sum_{m_{1,2,3}} \begin{pmatrix} \ell_1 & \ell_2 & \ell_3 \\ m_1 & m_2 & m_3 \end{pmatrix} B^{\ell_1\ell_2\ell_3}_{m_1m_2m_3}\,, \tag{2.55}$$

and that is related to the reduced bispectrum via

$$B_{\ell_1\ell_2\ell_3} = h_{\ell_1\ell_2\ell_3}\, b_{\ell_1\ell_2\ell_3}\,. \tag{2.56}$$

So, similarly to the case for the power-spectrum, it can be shown that the optimal estimator of the bispectrum [138–140], assuming again statistically isotropic, Gaussian, uncorrelated noise and full sky coverage, is

$$\hat{b}_{\ell_1\ell_2\ell_3} \equiv \frac{1}{N_{\ell_1\ell_2\ell_3}} \sum_{m_1m_2m_3} \mathcal{G}^{m_1m_2m_3}_{\ell_1\ell_2\ell_3} a_{\ell_1m_1}\, a_{\ell_2m_2}\, a_{\ell_3m_3}\,, \tag{2.57}$$

where $N_{\ell_1\ell_2\ell_3}$ is the number of valid triangles that can be built for the triplet (ℓ_1, ℓ_2, ℓ_3). It is defined as

$$N_{\ell_1\ell_2\ell_3} \equiv (h_{\ell_1\ell_2\ell_3})^2 = \sum_{m_1 m_2 m_3} (\mathcal{G}^{m_1 m_2 m_3}_{\ell_1\ell_2\ell_3})^2 \,, \tag{2.58}$$

where in the second equality we exploited eq. (A.18).

From the definition of the bispectrum estimator eq. (2.57) we get

$$\langle \hat{b}_{\ell_1\ell_2\ell_3}\, \hat{b}_{\ell_4\ell_5\ell_6} \rangle \equiv \frac{1}{N_{\ell_1\ell_2\ell_3}\, N_{\ell_4\ell_5\ell_6}} \sum_{m_1 \cdots m_6} \mathcal{G}^{m_1 m_2 m_3}_{\ell_1\ell_2\ell_3} \mathcal{G}^{m_4 m_5 m_6}_{\ell_4\ell_5\ell_6} \langle a_{\ell_1 m_1}\, a_{\ell_2 m_2} \cdots a_{\ell_6 m_6} \rangle \,. \tag{2.59}$$

As before, the expression simplifies noticeably in the weakly non-Gaussian approximation, and the covariance is just

$$\mathbf{Cov}(\hat{b}_{\ell_1\ell_2\ell_3}, \hat{b}_{\ell_4\ell_5\ell_6}) \approx \langle \hat{b}_{\ell_1\ell_2\ell_3}\, \hat{b}_{\ell_4\ell_5\ell_6} \rangle \approx \frac{\Delta_{\ell_1\ell_2\ell_3}}{N_{\ell_1\ell_2\ell_3}} C_{\ell_1}\, C_{\ell_2}\, C_{\ell_3}\, \delta^{\ell_4}_{\ell_1}\, \delta^{\ell_5}_{\ell_2}\, \delta^{\ell_6}_{\ell_3} \,, \tag{2.60}$$

where $\Delta_{\ell_1\ell_2\ell_3}$ is a coefficients that accounts for the multiplicity of the various configurations:

$$\Delta_{\ell_1\ell_2\ell_3} = \begin{cases} 6 & \text{for equilateral configurations } (\ell_1 = \ell_2 = \ell_3) \\ 2 & \text{for the isosceles configurations } (\ell_1 = \ell_2 \neq \ell_3, \text{ or cycl.}) \\ 1 & \text{for the scalene configurations } (\ell_1 \neq \ell_2 \neq \ell_3 \neq \ell_1) \,. \end{cases} \tag{2.61}$$

As stated before, for the scope of this thesis we are less interested in extracting the bispectrum from data, than to forecast detectability of various models. For explanatory purpose, the one dimensional Fisher matrix for the amplitude of the bispectrum, in the weakly non-Gaussian limit reads

$$F_{ij} = \sum_{\ell_1 \leq \ell_2 \leq \ell_3}^{\ell_{\max}} \frac{N_{\ell_1\ell_2\ell_3}\, b^2_{\ell_1\ell_2\ell_3}}{\Delta_{\ell_1\ell_2\ell_3} C_{\ell_1}\, C_{\ell_2}\, C_{\ell_3}} \tag{2.62}$$

Generalize this result to a joint analysis of multiple probes is a more complicated task. In principle, the optimal estimator is found minimizing the log-likelihood, as it is done in [138]. The estimator that is found simply applying this approach cannot be computed easily either analytically or numerically. However it has been proven in [141] that it is equivalent to the more manageable KSW estimator [142]. Therefore, we can

easily calculate F as the expectation value of the KSW estimator

$$F_{ij} = \sum_{\Xi_1\Xi_2\Xi_3} \sum_{\Xi_1'\Xi_2'\Xi_3'} \sum_{\ell_1 \leq \ell_2 \leq \ell_3}^{\ell_{\max}} \frac{N_{\ell_1\ell_2\ell_3}}{\Delta_{\ell_1\ell_2\ell_3}} \frac{\partial b_{\ell_1\ell_2\ell_3}^{\Xi_1\Xi_2\Xi_3}}{\partial\theta_i} (C^{-1})_{\ell_1}^{\Xi_1\Xi_1'} (C^{-1})_{\ell_2}^{\Xi_2\Xi_2'} (C^{-1})_{\ell_3}^{\Xi_3\Xi_3'} \frac{\partial b_{\ell_1\ell_2\ell_3}^{\Xi_1'\Xi_2'\Xi_3'}}{\partial\theta_i} \tag{2.63}$$

where in the relative sums $\Xi_i = T, E$ for $i = 1, 2, 3$.

Chapter 3.

Testing the power spectrum

3.1. Features of the primordial power spectrum and neutrino masses

Here we perform a minimally parametric reconstruction of the PPS using smoothing spline interpolation in combination with cross validation. This approach follows [143–145].

The idea is simple: we choose a functional form that allows a great deal of freedom in the shape of the deviations from a power-law. Because most models predict the PPS to be smooth, among the possible choices we use a smoothing spline. The ensuing challenge is to avoid over-fitting the data; a complex function that fits the data set extremely well is of no interest if we are simply fitting statistical noise. To prevent over-fitting we use cross-validation and a roughness penalty. The roughness penalty is an additional parameter that penalises a high degree of structure in the functional form. By performing cross-validation as a function of this penalty, we can judge the amount of freedom in the smoothing spline that the data require, without fitting the noise.

The *Planck* collaboration has performed an analysis with the same goals in mind, but with different methods [146], built upon [147–149]. They carried out both a parametric search for deviations from a power law, using a set of theoretically motivated shapes for the PPS, and a minimally parametric analysis to reconstruct the PPS. In all cases there is no strong evidence for deviations from a power law.

Our analysis differs from that of the *Planck* collaboration and from others existing in the literature (e.g. [150, 151]) in that we analyse jointly a comprehensive set of

state-of-the-art experiments probing the matter power spectrum and the latest *Planck* measurements.

Because we assume standard late-time evolution of density perturbations and consider both early-time observables (CMB) and late-time ones (i.e., large-scale structure), our reconstruction is also sensitive to late-time effects on structure formation. In particular a non-negligible neutrino mass would suppress the growth of structures below the neutrino free-streaming scale, inducing an "effective" loss of small scale power in our reconstructed PPS. Reconstructing in a model-independent way a possible neutrino signature on the shape of the matter power spectrum is of particular importance as [152–157] claims that relatively large neutrino masses ($\Sigma_\nu \gtrsim 0.4$ eV) could solve the tension between CMB and local measurements, whilst other studies [158–165] rule out this possibility.

The rest of the section is organised as follows: in Section 3.1.1 we briefly summarise the methodology adopted, the data chosen and how they are analysed. In Section 3.1.2 we show how our analysis will be able to give us information not only about the primordial power spectrum, but also about late time effects. Then in Section 3.1.3 we present our findings and we discuss them in Section 3.1.4.

3.1.1. Methodology and data overview

Spline reconstruction

We perform a minimally-parametric reconstruction of the primordial power spectrum based on the cubic smoothing spline technique [166]. This method has been firstly applied to this same problem in [143] and has been further refined in [144, 145].

As we already anticipated, the goal is to recover a smooth function — in this case the PPS — using as few assumptions about its functional form as possible. This approach is complimentary to the usual fit to a theoretically motivated family of functions, that is widely employed in the literature [73]. In the latter case, we make some *a priori* assumptions about the function we are studying, and this allows us to test specific models, eventually enhancing our understanding of the underlying physical mechanisms. Moreover, if the chosen functional form is appropriate, the range of viable free parameters will be tightly constraint, with respect to what we can achieve with a minimally parametric reconstruction. However this does not mean that a minimally parametric approach is un-interesting or un-informative. Firstly, it provides a useful, and blind, double check of

the goodness of our theoretical prior about the commonly used functional form. Second, it allows us to automatically understand if an unexpected deviation from the most minimal model is significantly supported by the data, or if it is a byproduct of the imposed prior. We anticipate here (it will be the topic of the next section) that using this kind of blind approach over-fitting is a possibility, *i.e.*, we might end up using an unnecessarily over-complicated function to fit the data, that improves the likelihood, but at the expense of fitting the noise. This would result in a less predictive model, that would perfectly interpolate existing — noisy — data, but would miserably fail to reproduce the underlying physical behaviour.

Summarizing, we want to let the data tell their story about what was the primordial power spectrum, imposing the least possible amount of prior information, apart from the fact that we require the PPS to be a smooth function, whereas avoiding to incur in over-fitting the data. Our choice is to to use a cubic spline interpolation.

We can define a spline $S(x)$ of degree k on a domain $[a, b]$ as a function such that

1. $S(x)$ is well defined on $x \in [a, b]$.
2. $S(x)$ and its derivatives $S'(x), S''(x), \ldots, S^{(k-1)}(x)$ are continuous for $x \in [a, b]$.
3. For some $n \geq 2$, $\exists\ x_1, \ldots, x_n \in [a, b]$ such that $a = x_1 < \cdots < x_i < \cdots < x_n = b$ and $S(x)$ is a polynomial of degree at most k on $[x_{i-1}, x_i]$ $i = 1, \ldots, n$. The points $(x_i, S(x_i))$ are called *knots*.

It could be shown that, among the $\mathcal{C}^2$ functions defined on a given domain that interpolate a given set of *knots*, the cubic spline is the one minimizing the quantity $I[f] \equiv \int (f''(x))^2 dx$ in said domain [167].[1] This is the reason why, since we are interested in removing any jaggedness not actually required by the data, we choose to use a cubic spline for our reconstruction.

Given $n + 1$ knots, the cubic spline is defined by n polynomials of third degree, hence in total $4n$ parameter have to be determined. $2n$ conditions are fixed by asking that each cubic pass for the knots at the beginning and the end of the interval in which it is defined. Other $2(n - 1)$ conditions come from the request of continuity of first and second derivative. This leaves 2 extra degrees of freedom that have to be fixed with

[1] The integral is a measure of the total curvature of the function, and therefore can be intuitively associate with the notion of how straight, rather than wiggly a curve is. In the following, to lighten the notation we will generically describe a curve f as *straight* if $I[f]$ is small, and as *wiggly* if that quantity is large. When needed we will leave aside qualitative adjectives and report proper numerical values.

some arbitrary choice. Multiple different possibilities are reasonable, depending on the specific application one is considering [167]. Therefore, by specifying a set of knots, and 2 boundaries condition, the interpolating cubic spline is completely determined.

In our application we parametrize the PPS with a cubic spline, and we treat the value of the spline on the knots $S(x_i)$ as the free parameters we wish to determine from the data. Regarding the boundary conditions, we proceed as follows. As we will show later (see Figure 3.3), the data we are considering span a finite set of scales, and that is where the majority of the *knots* are located. However, to avoid computational inefficiencies we will use splines with two extra knots at each of the spline ends. Since those two extra knots are not directly involved in our simulation, and are indeed function of the other knots, we will address to them as *false* knots in the following. Then the natural choice to deal with the last two degrees of freedom a spline has is the *not-a-knot* condition, which requires the jump in the third derivative across the first and last *real* knots to be forced to zero. In this way the cubic polynomial pieces at the left and right of said knots are made to coincide. The spline is constructed using C. de Boor's algorithm defined in [167].

Cross-Validation

As we anticipated, when using blind tecniques to fit data, one should take extra care to avoid the possibility of overfitting. To prevent this behaviour we add a roughness penalty to the log-likelihood. The penalty function is built in such a way that it increases its value as the spline gets more and more wiggly. Our choice is to use the integral of the second derivative squared of the spline over its domain

$$\log(\mathcal{L}) = \log(\mathcal{L}_{\rm exp}) - \alpha_p \int_{\ln k_1}^{\ln k_n} \Big(S''(\ln k)\Big)^2 \, d\ln k \tag{3.1}$$

where S'' denotes the second derivative of the spline with respect to $\ln k$, k_i and k_f are respectively the position of the first and of the last knots, α_p is a weight that controls the penalty, and $\mathcal{L}_{\rm exp}$ is the likelihood given by the experiments.

The roughness penalty effectively reduces the degrees of freedom, disfavouring more and more jagged functions as it increases. As α_p goes to infinity, one effectively implements linear regression; as α_p goes to zero one is interpolating.

Cross-validation comes into play in selecting the appropriate value of α_p [166]. In generic applications of smoothing splines, cross-validation is a rigorous statistical tech-

nique for choosing the optimal roughness penalty [166]. Cross-validation (CV) quantifies the notion that if the PPS has been correctly recovered, we should be able to accurately predict new independent data.

The idea is to divide available data in two groups, fit the first group with a chosen value for α_p and try to see how well the fit results approximates the other data group. If the fit is correct it will predict in an accurate way the second group. Ideally the most rigorous way to use cross-validation would be to remove one point at a time and evaluate the discrepancy between the point and its prediction for each point. Each of those errors are summed in a value called *cross-validation score*. The correct α_p is the one that minimizes the CV score.

In practice removing one point at a time implies repeating the analysis as many times as the number of points, so it is too computationally expensive. To make the problem computationally manageable, we follow [143]. We split the data set in two halves A and B. A Markov chain Monte Carlo (MCMC) parameter estimation analysis (for a given roughness penalty) is carried out on A, finding the best-fit model. We define the best-fit as the point of the parameter space subset sampled by the MCMC that maximise the likelihood in that subset. Then the $-\log$ likelihood of B given the best-fit model for A, $CV_{B|A}$, is computed and stored. This is repeated by switching the roles of the two halves, obtaining $CV_{A|B}$. The sum $CV_{A|B} + CV_{B|A}$, gives the CV score for that penalty weight. With this construction, the smoothing parameter that best describes the entire data set is the one that minimises the CV score.

In this way, using different combinations of experiments in A and B, we can not only check if our reconstruction is right, but also if some experiments lead to a PPS which is inconsistent with the others. Let's say we got two compatible experiments 1, 2 and a third experiment 3 affected by some previously unknown systematics or physical effects. We could arrange the experiments in the two cross-validation sets in various configurations. What we would see is that every set of parameter fitted on 3 would fail in predict the data in 1 and 2. Cross-validation score would be much bigger, giving a warning that there is some newly introduced tension between the data. From there we can draw our conclusion on the fact that the experiment 3 analysis is missing something. Of course, simplistic examples aside, it won't be possible to spot the "right" and the "wrong" data, as it is entirely possible that 1 and 2 are biased instead.

The cross validation data sets are described below (see Table 3.1).

In general, MCMC is not the best tool to find the multi-dimensional maximum likelihood location and using MCMC to estimate the maximum likelihood introduces an error in the procedure. A better technique would be a likelihood maximisation routine which we have found to be very fragile in this application. However, in similar contexts the MCMC approximation to the maximum likelihood has been used before, and in those cases the error introduced was not large enough to invalidate the results. Here we quantify this error (by comparing results from independent MCMCs) to be $\Delta \ln L \lesssim 1$, which propagates into a CV score error $\lesssim 2$. This is not large enough to invalidate our findings.

We choose to use 5 knots equally spaced in $\log k$ between $k = 1 \times 10^5\,\mathrm{Mpc}^{-1}$ and $k = 1\,\mathrm{Mpc}^{-1}$, i.e., $(k_1,\ k_2,\ k_3,\ k_4,\ k_5) = (1 \times 10^{-5}\,\mathrm{Mpc}^{-1},\ 1.78 \times 10^{-4}\,\mathrm{Mpc}^{-1},\ 3.16 \times 10^{-3}\,\mathrm{Mpc}^{-1},\ 5.62 \times 10^{-2}\,\mathrm{Mpc}^{-1},\ 1\,\mathrm{Mpc}^{-1})$ (see Figure 3.3 bottom panel for knots placement visualisation). The number and position of the knots is fixed throughout the analysis. As discussed in reference [144], beyond a minimum number of knots, there is a trade-off between the number of knots and the penalty, and the form of the reconstructed function does not depend significantly on the number of knots beyond this minimum number. As the main goal of this work is to explore, in a minimally parametric way, smooth deviations from a power law, a few (> 3) knots are sufficient.

The basic cosmological parameters, $\omega_b = \Omega_b h^2$, $\omega_c = \Omega_c h^2$, h, and τ_{reio} — physical baryonic matter density parameter, physical cold dark matter parameter, dimensionless Hubble parameter and optical depth to last scattering surface — are varied in the MCMC alongside the values f_i of the reconstruction at the knots. A flat geometry is assumed so that $\Omega_m + \Omega_\Lambda = 1$.

The prediction for cosmological observables, the calculation of the likelihood and the MCMC parameter inference are implemented using the standard Boltzmann code `CLASS` [168] and its MCMC sampler code, Monte Python (MP) [169], suitably modified to use a given spline as primordial power spectrum and to factor the penalty in the likelihood evaluation.[23]

As we will discuss in greater detail in Section 3.1.2, even though we reconstruct the primordial power spectrum, we are sensitive to late-time cosmological effects. Indeed, one of our main focus is on massive neutrinos: the presence of neutrinos with non-negligible

[2] `http://class-code.net`
[3] `http://baudren.github.io/montepython.html`

mass would distort our reconstruction in a way that is predictable due to the linearity of the growth functions [23].

Of course neutrino masses do not actually affect the physical PPS. But assuming standard gravity, standard growth of structure, and massless neutrinos in the analysis, would yield a reconstructed PPS with an artificial distortion, if neutrino masses were not negligible. In fact a detectable signature of massive neutrinos in the real data would appear as a power suppression in the reconstructed PPS. Of course a detection of such a feature cannot be univocally interpreted as signature of neutrino masses; other particles beyond the standard model could easily share the same properties of neutrinos when it comes to damping perturbations or it could be a real feature in the PPS.

Working in logarithmic space

As we already discussed, the signal we try to recover is expected to be a small deviation form a power-law. A power-law as in eq. (1.83) can be linearised by taking the logarithm of both sides

$$\log \Delta^2(k) = \log A_s + (n_s - 1)[\log(k) - \log(k_0)]. \tag{3.2}$$

Small deviations on the power-law translate into small deviation on this linearised expression.

The advantage is that splines approximate way better the linearised expression than the original one. It is really evident checking both Figure 3.1 where a spline is used to approximate a power-law and Figure 3.2 where a little bump is added to a power-law. Moreover, the same procedure has already been applied in literature, e.g. [143].

Datasets

We use a comprehensive set of CMB power spectra measurement by *Planck* and WMAP, and large scale structure power spectra measurement, derived either from weak lensing measurement performed by *Planck* and the Canada-France-Hawaii Lensing Survey, or from galaxy maps, as it is the case for WiggleZ and Sloan Digital Sky Survey. Basically, we consider in our work all current-generation experiments that probe a range of scales big enough to give information on the actual shape of the PPS rather than its normalization

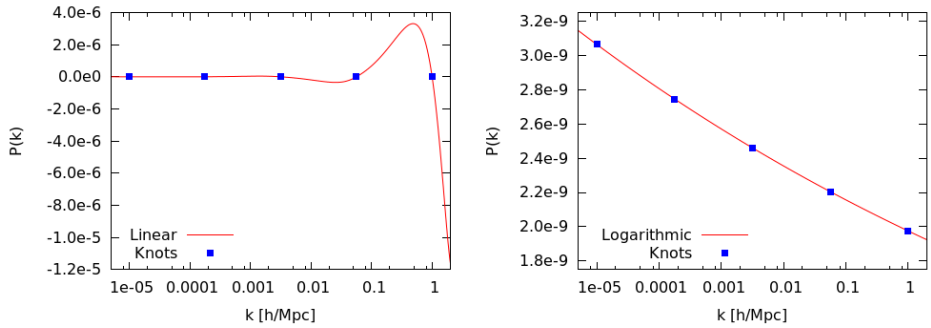

Figure 3.1.: Splines interpolating mock knots placed alongside a power-law signal. On the left the spline is a function of k taken in linear space, on the right in logarithmic space. Notice the difference in the scale.

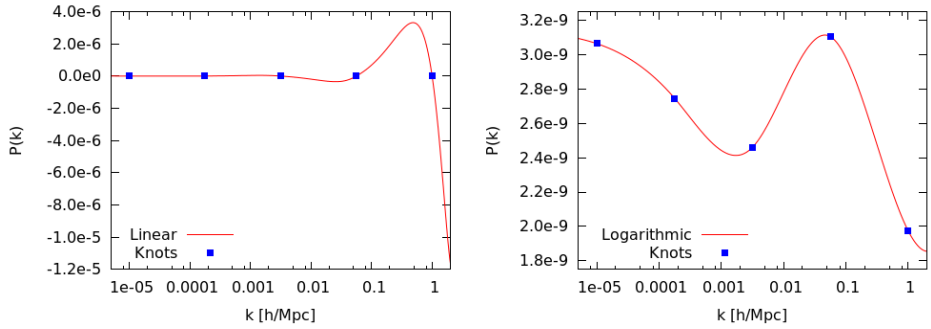

Figure 3.2.: Splines interpolating mock knots placed alongside a power-law signal with a bump in it. On the left the spline is working in linear space, on the right in Logarithm space. Notice the difference in the scale.

on a small range of frequencies. In greater detail the datasets we use and the surveys providing them are:

- *Planck* power spectra of temperature and polarisation of the CMB. The *Planck* collaboration released in 2013 the temperature data from the first half of the mission [170]. We complement the *Planck* 2013 data with the WMAP polarisation. We refer to this as CMB13. In 2015 the results of the full analysis has been released [171]. Temperature and E-mode polarisation power spectra (and their cross-correlation) data and likelihoods come in two sets: a *low* ℓ from $\ell = 2$ to $\ell = 29$, and the *high* ℓ angular power spectrum, that provides data up to $\ell = 2508$ for TT and up to $\ell = 1996$ for TE and EE. We use all these temperature and polarisation data and we refer to them as CMB15.

- Beside the CMB power spectrum, *Planck* reconstructed the CMB lensing potential [172], which contains information on the amplitude of large scale structure integrated from recombination to present time. Such data are inferred from the study of the four point function of temperature anisotropies (in the 2015 data release, both temperature and polarization are included). We will refer to it as *Planck*Lens.

- The Canada-France-Hawaii Lensing Survey (CFHTLenS) [173] combined weak lensing data processing with THELI [174], shear measurement with lensfit [175], and photometric redshift measurement with PSF-matched photometry [176] to provide the two point correlation function of the tomographic weak lensing signal, which we use in our analysis. A full systematic error analysis of the shear measurements in combination with the photometric redshifts is presented in [177], with additional error analyses of the photometric redshift measurements presented in [178].

- The WiggleZ Dark Energy Survey (WiggleZ) has been a large scale galaxy survey carried out at the Anglo-Australian Telescope in Siding Spring Observatory, New South Wales. Measuring the position and redshift of 238,000 galaxies, it mapped a volume of one cubic Gigaparsec over seven regions of the sky up to a redshift $z \lesssim 1$. The data has been used to calculate the galaxy power spectrum in 4 redshift bins equally spaced between $0.1 < z < 0.9$ [18], that we employ in our analysis.

- The Sloan Digital Sky Survey used its 2.5 m telescope based in Apache Point Observatory, New Mexico, to collect 929,555 galaxy spectra. In data release 7, the collaboration used a sample of luminous red galaxies to reconstruct the halo density field and its power spectrum roughly between $k = 0.02h/\mathrm{Mpc}$ and $k = 0.2h/\mathrm{Mpc}$ [17].

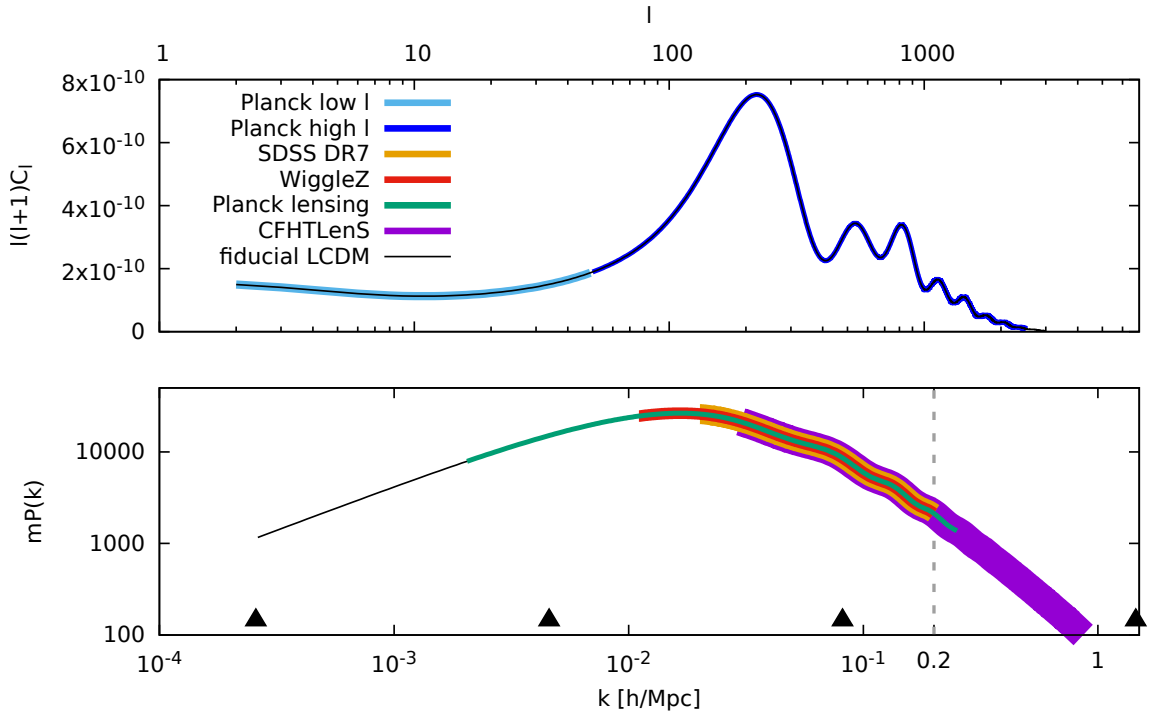

Figure 3.3.: Comoving scales covered by the experiments used in our analysis. The vertical dashed line show the limit of the quasi-linear scales. The triangles show the position of the knots. The leftmost one is not visible in the plot.

In Figure 3.3 we show the scales probed by each experiment along with the location of the knots.

Runs set-up

We now describe the cross validation set up. In order to constrain both the shape of the PPS and the cosmological parameters, we have to consider CMB primary data in all CV runs. Because of time constraints CMB13 is used in the set up CV runs but CMB15 is used in the final run. This choice is conservative, favouring slightly more freedom (lower penalty) to the reconstructed PPS, and its validity will be discussed at the end of this paragraph. Besides these two datasets, we consider 4 other surveys, 2 measuring weak lensing and 2 using galaxy catalogues. We perform 3 CV runs in a pyramidal scheme as summarised in Table 3.1. We start performing in parallel two different cross-validation analysis on two pairs of experiments where each pair is formed by a weak lensing experiment and by a galaxy catalogue. The dependence of the CV score on α_p was mapped by sampling several α_p values. The results of these preliminary runs show no unexpected behaviour or tension, i.e., the reconstructed PPS shows no

Run	A	B
1.1	CMB13, *Planck*Lens	CMB13, SDSS DR7
1.2	CMB13, CFHTLenS	CMB13, WiggleZ
2	CMB13, *Planck*Lens, SDSS DR7	CMB13, CFHTLenS, WiggleZ
Rec.	CMB15, *Planck*Lens, SDSS DR7, CFHTLenS, WiggleZ	

Table 3.1.: Cross-validation datasets A and B for the various runs. The reconstruction (Rec.) involve all the experiments together.

significant deviation from a power-law, and the shape of the CV score is the same for both run 1.1 and run 1.2. Knowing this, we then combine the large scale structure data to have one weak lensing and one galaxy survey in each CV set. The best roughness penalty found from this CV is used in the final run which includes all experiments (this is called "Rec." run in the Table 3.1). The penalty parameter value to use in the reconstruction is determined by the CV score of run 2 alone: its dependence on α_p is illustrated in Figure 3.4. The fact that the shapes of the three CV scores — from run 1.1, 1.2, and 2 — shown in Figure 3.4 are very similar, indicate robustness and that there are no significant tensions between the datasets. To check the consistency of using CMB15 in the final run despite having tuned the cross validation with CMB13, we coarsely re-sampled only the run 2 CV curve using CMB15. The difference induced on the CV scores by this change is consistent with the intrinsic noise of the MCMC sampling discussed in Section 3.1.1.

The CV score has a fairly well defined "wall" for high penalties , but is quite constant under a certain threshold at $\alpha_p \sim 10$. For high α_p the penalty starts being the dominant contribution to the likelihood, so the sharp increase in the limit of high α_p is expected. On the other hand, if small values of the penalty were to lead to overfitting, the CV score should increase as α_p decreases. This is not what we see and can be understood as follows. CMB angular power spectra are always included in the analysis and in this limit, it is the statistical power of these data (not the penalty) that drives the smoothness of the reconstruction and therefore the CV score. In other words, for low values of the penalty below $\alpha_p \sim 10$, all datasets are well consistent with the Planck-inferred PPS reconstruction: the CMB data alone disfavour unnecessarily wiggly shapes, even when there is a low penalty.

Since there is not a well defined minimum for the CV score, we opt for presenting two different cases. One is more conservative, in the sense that it has a stronger penalty

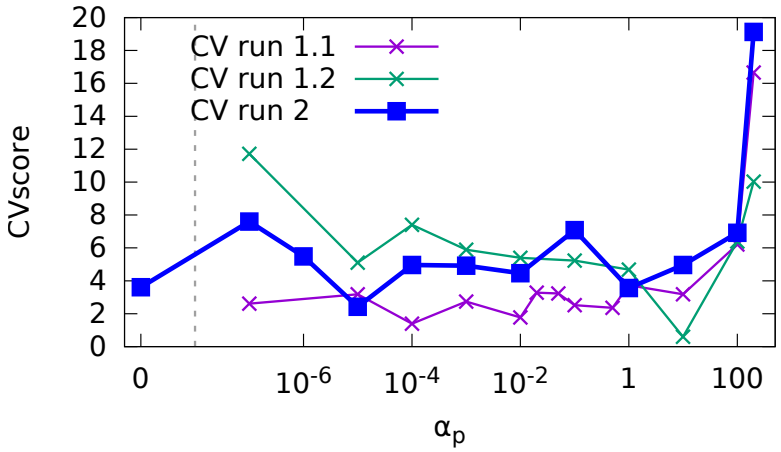

Figure 3.4.: CV score as a function of α_p for the different cross-validation runs. A different arbitrary offset has been subtracted from each CV score. The noise in the CV score curves, approximately ΔCV score ~ 2 for run 2 and ~ 1 for run 1, is due to the fact that MCMC are used to find the best-fit point. The sharp increase in CV score for $\alpha_p > 10$ is much larger than this error and is therefore considered physical.

that allows only small deviations from the concordance power-law model. For this one we choose $\alpha_p = 1$.

The other leaves more freedom to the data, as we choose a more relaxed penalty $\alpha_p = 0.01$. A reconstruction with $\alpha_p \ll 0.01$ is pretty much uninformative. In fact recall that the free parameters in our MCMC runs are the physical baryon density ω_b, the physical cold dark matter density $\omega_{\rm cdm}$, the rescaled Hubble parameter h, the optical depth to reionization $\tau_{\rm reio}$, and the value of the five knots of the spline that we used to parametrize the shape of the PPS. At such low penalty values the reconstruction transfers in part the features of the radiation transfer function and the effect of the optical depth to reionization into the PPS opening up degeneracies in parameter space.

3.1.2. Reconstruction sensitivity to non-primordial effects

Figure 3.5A.1–3.5R.2 visualises the concept — exploited here — that in the reconstructed primordial power spectrum the effect of a non-zero neutrino mass is degenerate with a power suppression. This is a good approximation especially on scales where the evolution is linear or mildly non-linear, i.e., $k < 0.2\,h\,{\rm Mpc}^{-1}$. To study quantitatively this degeneracy we shall consider two toy models. First let us assume a ΛCDM universe

$\sum m_\nu$	maximum damping	maximum error
0.06 eV	3%	0.5%
0.1 eV	5%	0.8%
0.4 eV	20%	4%

Table 3.2.: Damping in the matter power spectrum induced by massive neutrino compared with the maximum error in the reconstruction.

with massive neutrinos, where all the cosmological parameters are known and with a power law PPS at the end of inflation (Figure 3.5A.1). From these initial conditions we evolve the perturbations assuming massive neutrino (different values for the total mass are shown). On small physical scales neutrino free streaming [111] suppresses power (Figure 3.5A.2) yielding a resulting power spectrum shown in Figure 3.5R.1. Now we can think of an alternative scenario that implement the neutrino power suppression (Figure 3.5B.1) directly on the initial PPS as a deviation from a power law as shown in Figure 3.5B.2. This initial power spectrum is then evolved assuming massless neutrinos. The linearity of the perturbation evolution equations guarantees that the generated matter and CMB power spectra would be the same as in the first case (Figure 3.5R.1). In Figure 3.5R.2 we can appreciate the fact that discrepancies in the prediction made in the two cases come from non-linearities.

To be sure that our reconstruction is accurate enough to be sensitive to the damp we have tried to recover a known signal. We multiplied the damping ratio generated with CLASS to a power-law signal as in Figure 3.5B.2. Then we tried to use a spline to reconstruct it and we checked the difference. As it came out we have errors much smaller than the effect of the damping. Figure Figure 3.6 shows the ratio of the spline reconstruction to the signal for various neutrino masses. By comparing it with figure Figure 3.5A.2 we can obtain the data shown in Table 3.2. As shown the error of the reconstruction is always less than one fifth of the signal. After this preliminary test, we are thus confident that we are able to retrieve a neutrino damping signal, if present in the data and if the value of the mass is high enough. In fact here we have quantified only the error due to the use of the spline, and not the errors due to the fit procedure. Those will be know once the likelihood distribution is known. A discussion about errors is carried when the results are shown in the Figure 3.1.3.

Another source of error that might contribute is given by the use of spline with a limited number of knots. If the number of knots, or their position, is not suitably chosen,

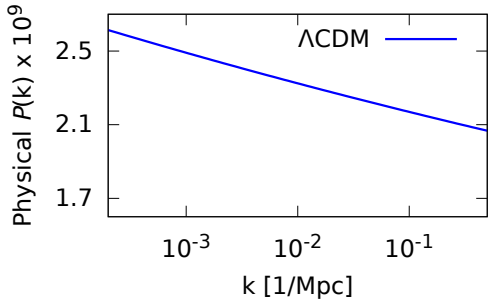

(A.1) In the first case the initial condition is a power-law PPS.

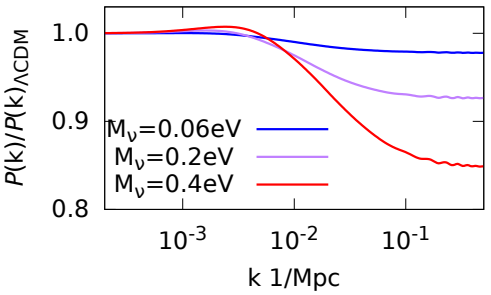

(A.2) Then the evolution takes into account the presence of massive neutrino.

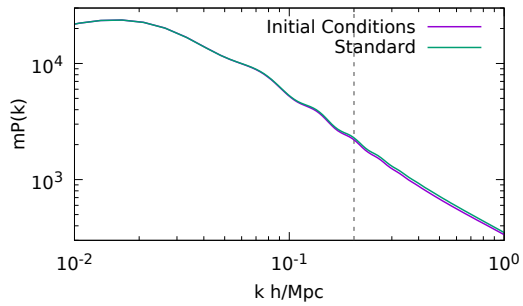

(R.1) The two methods generate the same observables in the scales of interest. Here we show the non-linear matter power spectrum.

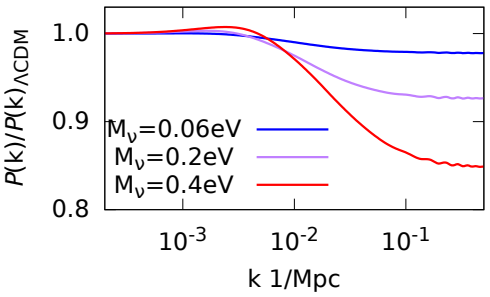

(B.1) In the second case the neutrino damping is considered in the initial conditions.

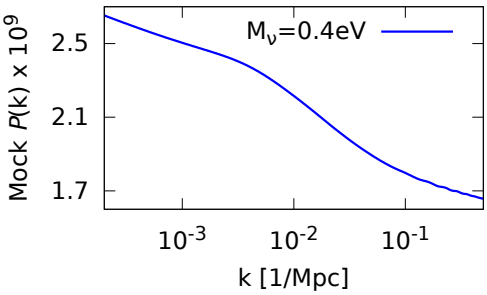

(B.2) The initial condition is a power-law multiplied by the neutrino power suppression. Then the evolution equation with massless neutrino is used.

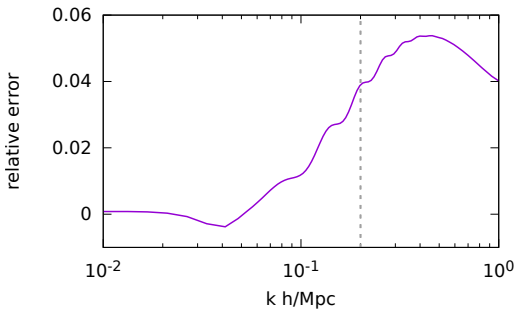

(R.2) The error do not exceed 1% at scales larger than $k = 0.1\ h/\mathrm{Mpc}$ and is due to non-linearities.

Figure 3.5.: How a non-zero neutrino mass would induce a power suppression in the reconstructed power spectrum. Both method A.1–A.2 and B.1–B.2 give the same result R.1–R.2 at linear level.

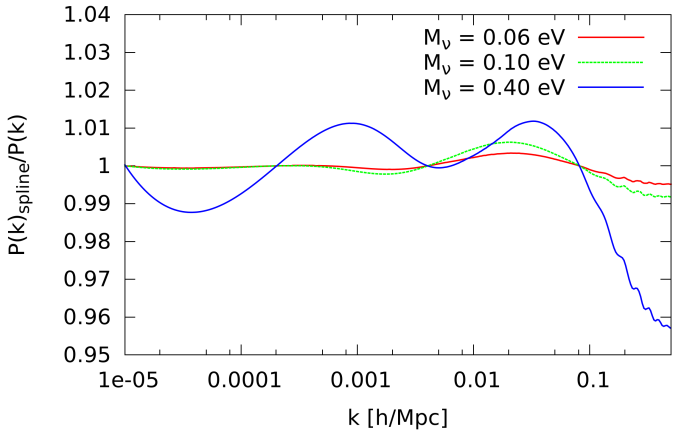

Figure 3.6.: Ratio of the spline reconstruction to the signal for various neutrino masses.

one could be unable to reconstruct a given signal. This is not our case, with our choice of knots we have verified that we can reconstruct any neutrino power suppression with a 10^{-3} accuracy.

Interest in massive neutrinos The vanilla ΛCDM model assumes zero mass neutrinos. As we already pointed out it is fairly in good agreement with current data, but since considering massive neutrinos is one of the more straightforward possible extension of the ΛCDM model, cosmologists have always been interested in it. With oscillation experiments results confirming that at least two neutrino states are massive, extending the ΛCDM model was no more a speculation and became necessary. Even though flavour oscillation experiments are really helpful in providing a lower bound on the mass sum, they are clueless about determining the absolute mass scale, and the stringent upper limit come from beta decay experiments. Quantitatively, relying on particle physics experiments alone, one gets the constraints [111]

$$0.056\,\text{eV} \leq \sum m_\nu \leq 6\,\text{eV}\ (95\%\ \text{C.L.}). \tag{3.3}$$

Luckily, cosmological observations allows to put a stricter upper bound, improving the beta decay one by at least one order of magnitude. Such a constraint do not come without caveats: there is an ongoing debate in the cosmological community on how to interpret some tensions between measurements coming from different datasets. The topic is of particular importance because it has been linked to a more general tension between CMB and local measurements of H_0 and σ_8. The Hubble parameter has been measured extrapolating up to today the best fit of the *Planck* CMB power spectra [2, 158] and with

Hubble telescope redshift measurements [16]. The two estimates differs by 2.5σ. On the other hand, if inferring it from CMB data give the value $\sigma_8 = 0.8233 \pm 0.0097$ [158], local measurement fluctuate around the value $\sigma_8 = 0.77 \pm 0.02$ [179].

Many recent studies claimed that some expansions in the neutrino sector of the ΛCDM model could help solve the problem. Changes in the number of families, addiction of sterile neutrinos, different sums of the masses and numbers of relativistic species have been all considered as possible solutions of the tension on H_0 [152] and σ_8 [153–157]. Other works rejects those conclusions, favouring model with no sterile neutrinos and lower masses [158–165].

What we are going to do then is to set CLASS so that in the Monte Carlo Markov Chains neutrino masses are set to 0. If there were detectable massive neutrinos in the real data, we would recover the damp feature in the primordial power spectrum, just as we explained before.

3.1.3. Minimally parametric reconstruction

Here we present the results with the *Planck* 2015 likelihood and all the large scale structure power spectrum data (*Planck* Lensing 2015, WiggleZ, CFHTLenS, and SDSS DR7), with the two different roughness penalties ($\alpha_p = 1$ and $\alpha_p = 0.01$) justified above.

As discussed in refs. [158, 180–183] there is a tension between the inferred matter power spectrum amplitude from CMB and from CFHTLenS, which may arise from possible systematic errors in the photometric redshifts of CFHTLenS. For this reason we present results first without and then with CFHTLenS.

Reconstruction omitting CFHTLenS

In Figure 3.7a and Figure 3.7b we show the reconstructed PPS for $\alpha_p = 1$ and $\alpha_p = 0.01$ respectively. The colour-bars on the upper side show the scales probed by each experiment as in Figure 3.3, green for *Planck*Lens, red for WiggleZ, gold for SDSS DR7. CMB15 covers the whole plot. The best-fit reconstruction is shown in white and errors are shown by plotting in dark blue (light blue) a random sample of 400 reconstructions chosen among the 68.27% most likely points (points in the range 68.27% - 95.45%) in the MCMC. The 95.5% confidence regions appear to almost coincide with the 68.3%: this is because

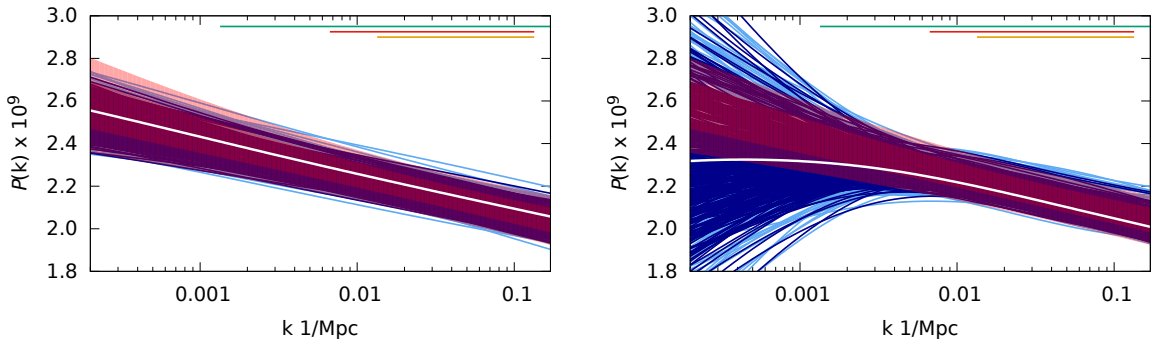

(a) $\alpha_p = 1$. **(b)** $\alpha_p = 0.01$.

Figure 3.7.: Reconstructed PPS. The best-fit reconstruction is shown in white. Errors are shown by plotting in dark blue (light blue) 400 spline picked at random among the 68.27% most likely points (points in the range 68.27% - 95.45%) in the MCMC. The red (pale red) region shows the 68% (95%) confidence intervals for *Planck* 2015 TT, TE, EE + Low P. The colour-bars on the upper side show the scales probed by each experiment as in Figure 3.3, green for *Planck*Lens, red for WiggleZ, gold for SDSS DR7. CMB15 covers the whole plot.

the reconstructed spectra are simply more wiggly, while a larger deviation of the overall amplitude is disfavoured.

In the figure the red and pale red regions show the 68 and 95% confidence intervals for the standard power law ΛCDM *Planck* 2015 TT, TE, EE + Low P analysis [2].

Note that for the more conservative choice of the penalty, errors of the reconstructed PPS are comparable with errors from *Planck* parametric fit at all scales. For the less conservative penalty this is also true on scales corresponding to $\ell > 30$. This did not happen with the previous generation of cosmological data (see [145]) where the PPS reconstructed with the same approach was significantly less constrained than with a power law fit.

The main difference between the "stiff" reconstruction, with $\alpha_p = 1$, and the more flexible reconstruction, with $\alpha_p = 0.01$, is at low k (low ℓ) where the cosmic variance error is large. Even if there was a feature at low ℓ, it is not significative enough to clearly ask for a low α_p. Even with a low penalty the reconstructed power spectrum does not show features or deviations from a power law at high k, which is where we would expect to see something if this analysis were to confirm some of the claims in the literature [152–157]. Instead the additional freedom in the PPS allowed by the lower penalty $\alpha_p = 0.01$ is used on scales corresponding to low CMB multipoles $\ell < 30$. As discussed, these scales

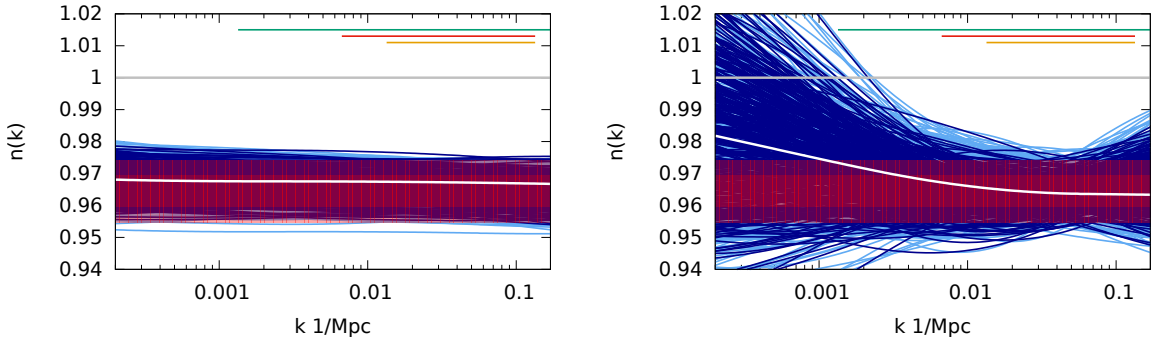

(a) $\alpha_p = 1$. **(b)** $\alpha_p = 0.01$.

Figure 3.8.: Reconstructed PPSs spectral index. The white line corresponds to the best-fit reconstruction. Errors are shown by plotting in dark blue (light blue) 400 reconstructions randomly selected from the 68.27% most likely points (points in the range 68.27% - 95.45%) in the MCMC. The red (pale red) region shows 68% (95%) confidence intervals for the power law *Planck* 2015 TT, TE, EE + Low P fit. The colour-bars on the upper side show the scales probed by each experiment as in Figure 3.3, green for *Planck*Lens red for WiggleZ, gold for SDSS DR7. CMB15 covers the whole plot. In the right figure, the grey line is $n(k) \equiv 1$, i.e., scale invariance.

are dominated by cosmic variance and are known to be lower than the standard ΛCDM prediction e.g., [170, 182–185] and refs therein.

In Figure 3.8a and Figure 3.8b we also show the reconstructed $n(k) \equiv d\ln P(k)/d\ln k$ ($\alpha_p = 1$ and $\alpha_p = 0.01$) for ease of comparison with the standard power law results.[4] We find no evidence that any scale dependence of the power spectrum spectral slope is necessary, which is in agreement with previous analyses. However with this new data set we find that $n = 1$ is highly disfavoured by the data, in particular for $\alpha_p = 1$ the significance of the departure from scale invariance is comparable with that obtained when adopting the "inflation–motivated" power-law prior. Even for the more flexible reconstruction, not even one point of the more than 4×10^5 MCMC points falls near scale invariance.

The results shown in Figure 3.7 and Figure 3.8 offer a powerful confirmation of the inflationary paradigm, justify the adoption of the inflationary prior in cosmological analyses.

Finally in Figure 3.9a and Figure 3.9b we show the ratio of the reconstructed PPS to the best-fit *Planck* 2015 (temperature, polarisation, and lensing) power law model.

[4]Recall that the quantity that was actually reconstructed using cross-validation to find the optimal penalty is in reality the power spectrum.

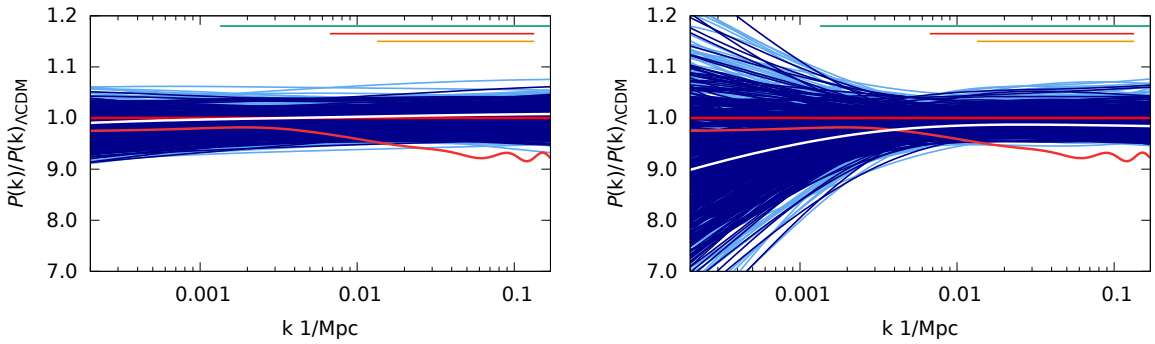

(a) $\alpha_p = 1$. **(b)** $\alpha_p = 0.01$.

Figure 3.9.: Reconstructed PPS divided by the *Planck* 2015 TT, TE, EE + LowP + Lensing power-law PPS best-fit using the same conventions as Figure 3.7 for the legend and the reconstructed $P(k)$. The red lines show the small-scales power suppression effect due to massive neutrinos. The upper line is the $\Sigma m_\nu = 0\,\mathrm{eV}$ theoretical prediction based on the conditional best-fit to *Planck* 2015 TT, TE, EE + Low P + Lensing + BAO + JLA + H_0 data, the lower line is the same with $\Sigma m_\nu = 0.2\,\mathrm{eV}$.

The reconstruction is fully compatible with the parametric fit. The figure also shows the expected effect of small scale power suppression due to massive neutrino free-streaming for two representative values of neutrino masses $\Sigma m_\nu = 0\,\mathrm{eV}$ and $0.2\,\mathrm{eV}$. The two models are the conditional (i.e., keeping Σm_ν fixed at the required value) best-fit to the data (*Planck* 2015 TT, TE, EE + Low P + Lensing + BAO + JLA + H_0 data). Clearly models with $\Sigma m_\nu > 0.2$ eV are highly disfavoured by the data even with this minimally parametric reconstruction: not a single step of a 4×10^5 size MCMC goes near the $\Sigma m_\nu = 0.2$ eV line. This of course does not exclude the — admittedly contrived — case with a arbitrarily large neutrino mass inducing a small scale power suppression which is cancelled by a compensating boost of the PPS on the same scales. Occam's razor disfavours this scenario.

Reconstruction with CFHTLenS

The reconstructed $P(k)$, $n(k)$ and $P(k)$ relative to the power law best-fit are shown in Figure 3.10, 3.11, and 3.12 using the same conventions as in Figure 3.7, 3.8, and 3.9.

Comparison with the results of Section 3.1.3 (in Figure 3.7, 3.8, 3.9) shows that qualitatively the reconstructions are very similar, there is no strong evidence for deviations from the power law behaviour and scale invariance is still excluded. However quantitatively

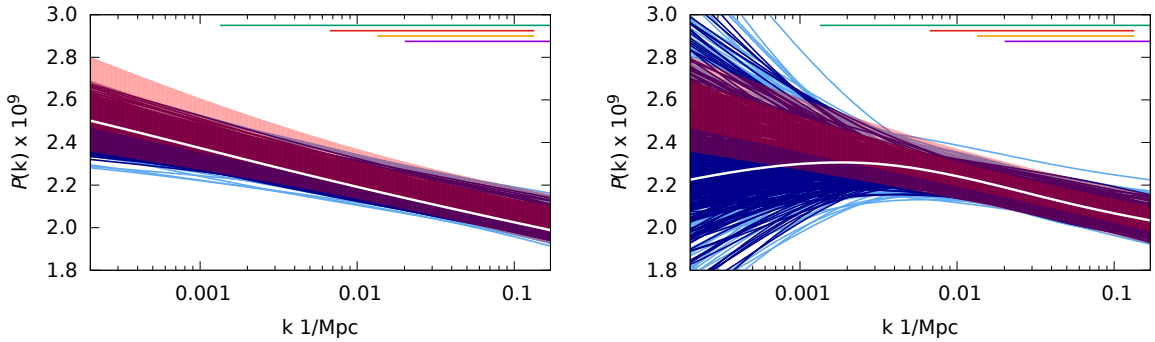

(a) $\alpha_p = 1$. **(b)** $\alpha_p = 0.01$.

Figure 3.10.: Reconstructed PPS. Refer to Figure 3.7 for explanation and colour code. In addition, the purple line shows the scales covered by CFHTLenS.

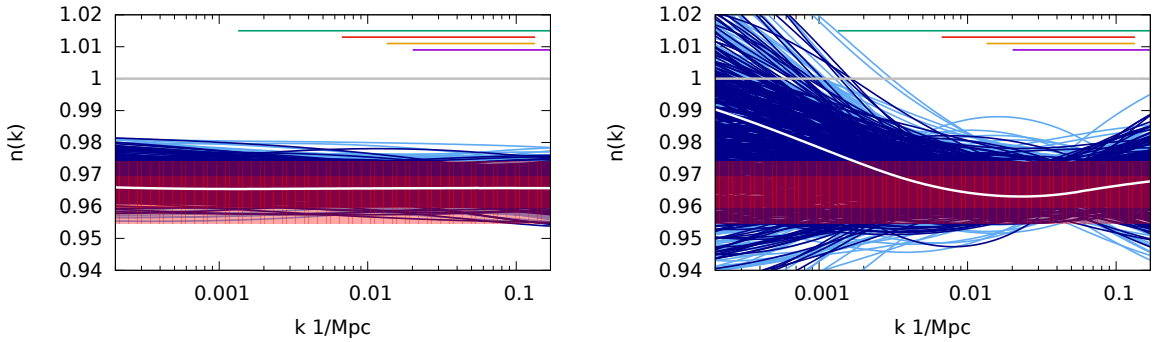

(a) $\alpha_p = 1$. **(b)** $\alpha_p = 0.01$.

Figure 3.11.: Reconstructed PPSs spectral index. Refer to Figure 3.8 for explanation and colour code. In addition, the purple line shows the scales covered by CFHTLenS.

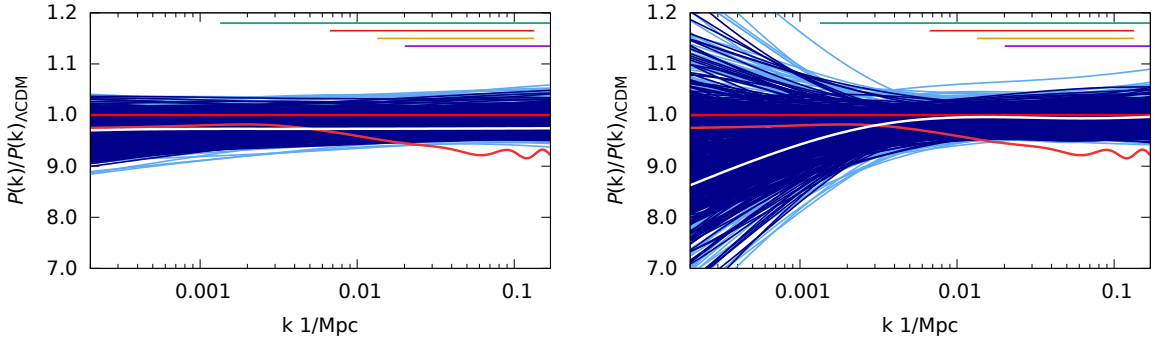

(a) $\alpha_p = 1$. **(b)** $\alpha_p = 0.01$.

Figure 3.12.: Reconstructed PPS relative to *Planck* 2015 TT, TE, EE + LowP + Lensing power-law PPS best-fit. Refer to Figure 3.9 for explanation and colour code. In addition, the purple line shows the scales covered by CFHTLenS.

Omitting CFHTLenS $-\ln\mathcal{L}_{\min} = 6727.02$				
Param	best-fit	mean $\pm\,\sigma$	95% lower	95% upper
$100\ \omega_b$	2.226	$2.229^{+0.015}_{-0.015}$	2.199	2.258
$\omega_{\rm cdm}$	0.1194	$0.1191^{+0.0011}_{-0.0011}$	0.1168	0.1214
h	0.6795	$0.6815^{+0.0052}_{-0.0053}$	0.6712	0.6919
τ	0.0542	$0.05982^{+0.0092}_{-0.013}$	0.04001	0.07955
$10^{+9}K_1$	2.788	$2.736^{+0.11}_{-0.12}$	2.507	2.965
$10^{+9}K_2$	2.546	$2.534^{+0.07}_{-0.07}$	2.395	2.673
$10^{+9}K_3$	2.307	$2.32^{+0.043}_{-0.049}$	2.231	2.412
$10^{+9}K_4$	2.072	$2.108^{+0.036}_{-0.053}$	2.028	2.194
$10^{+9}K_5$	1.872	$1.9^{+0.047}_{-0.059}$	1.802	2.006
With CFHTLenS $-\ln\mathcal{L}_{\min} = 6777.64$				
Param	best-fit	mean $\pm\,\sigma$	95% lower	95% upper
$100\ \omega_b$	2.244	$2.236^{+0.015}_{-0.014}$	2.207	2.264
$\omega_{\rm cdm}$	0.1182	$0.1182^{+0.0011}_{-0.001}$	0.1161	0.1204
h	0.6867	$0.6854^{+0.0048}_{-0.0051}$	0.6757	0.6953
τ	0.05239	$0.05852^{+0.0087}_{-0.013}$	0.04001	0.07795
$10^{+9}K_1$	2.721	$2.697^{+0.12}_{-0.12}$	2.463	2.931
$10^{+9}K_2$	2.512	$2.504^{+0.069}_{-0.071}$	2.363	2.645
$10^{+9}K_3$	2.281	$2.3^{+0.041}_{-0.048}$	2.213	2.389
$10^{+9}K_4$	2.065	$2.098^{+0.035}_{-0.051}$	2.021	2.182
$10^{+9}K_5$	1.869	$1.9^{+0.045}_{-0.058}$	1.802	2.003

Table 3.3.: Best-fit, mean and confidence intervals for the MCMC parameters in the reconstruction with $\alpha_p = 1$

some differences may be appreciated. Adding the CFHTLenS datasets has the effect of lowering the overall PPS normalisation (clearly visible by comparison with Figure 3.7).

The ratio with Planck power law best-fit in Figure 3.12 highlights how, independently from our choice of datasets, high neutrino masses are disfavoured. Quantitatively the $\Sigma m_\nu > 0.2\,\text{eV}$ bound is excluded at more than 95% confidence if we assume a power law PPS, as discussed in Section 3.1.3.

For completeness we also report the recovered values and errors for all the model parameters in Table 3.3 and Table 3.4 for the two penalties $\alpha_p = 1$ and $\alpha_p = 0.01$ respectively.

Omitting CFHTLenS $-\ln\mathcal{L}_{\min} = 6726.32$				
Param	best-fit	mean $\pm\,\sigma$	95% lower	95% upper
$100\ \omega_b$	2.239	$2.226^{+0.016}_{-0.016}$	2.194	2.259
$\omega_{\rm cdm}$	0.1173	$0.1193^{+0.0013}_{-0.0012}$	0.1168	0.1218
h	0.6898	$0.6806^{+0.0055}_{-0.006}$	0.6694	0.6922
τ	0.07136	$0.05974^{+0.0088}_{-0.014}$	0.04	0.08061
$10^{+9}K_1$	1.968	$2.351^{+0.67}_{-0.69}$	1.014	3.711
$10^{+9}K_2$	2.159	$2.351^{+0.29}_{-0.3}$	1.769	2.934
$10^{+9}K_3$	2.272	$2.31^{+0.059}_{-0.062}$	2.191	2.431
$10^{+9}K_4$	2.148	$2.106^{+0.036}_{-0.056}$	2.024	2.198
$10^{+9}K_5$	1.933	$1.923^{+0.073}_{-0.078}$	1.773	2.074
With CFHTLenS $-\ln\mathcal{L}_{\min} = 6776.95$				
Param	best-fit	mean $\pm\,\sigma$	95% lower	95% upper
$100\ \omega_b$	2.235	$2.234^{+0.015}_{-0.016}$	2.203	2.266
$\omega_{\rm cdm}$	0.1179	$0.1182^{+0.0012}_{-0.0011}$	0.116	0.1205
h	0.686	$0.6853^{+0.0052}_{-0.0054}$	0.6749	0.6958
τ	0.06203	$0.05911^{+0.0085}_{-0.014}$	0.04	0.07976
$10^{+9}K_1$	2.241	$2.42^{+0.67}_{-0.69}$	1.09	3.784
$10^{+9}K_2$	2.294	$2.373^{+0.28}_{-0.31}$	1.787	2.962
$10^{+9}K_3$	2.28	$2.292^{+0.056}_{-0.063}$	2.176	2.414
$10^{+9}K_4$	2.106	$2.1^{+0.035}_{-0.055}$	2.019	2.189
$10^{+9}K_5$	1.899	$1.919^{+0.071}_{-0.08}$	1.772	2.071

Table 3.4.: Best-fit, mean and confidence intervals for the MCMC parameters in the reconstruction with $\alpha_p = 0.01$

The degeneracies among the parameters for the PPS value at the knots can be appreciated in the triangle plots of Figure 3.13a for $\alpha_p = 1$ and Figure 3.13b for $\alpha_p = 0.01$. Correlations with and among the cosmological parameters not shown are negligible. As expected, higher penalty induce correlations among the knots which are stronger between neighbouring ones.

Interestingly the only cosmological parameter that correlates with the knots is $\tau_{\rm reio}$, which show degeneracy with the knots at higher k (Figure 3.13c and 3.13d). This behaviour is however not unexpected. The $\tau_{\rm reio}$ parameter only affects the CMB and in particular its main effect is to suppress the temperature power spectrum at multipoles $\ell \gtrsim 80$. With our choice for the location of the knots, the most affected knots are

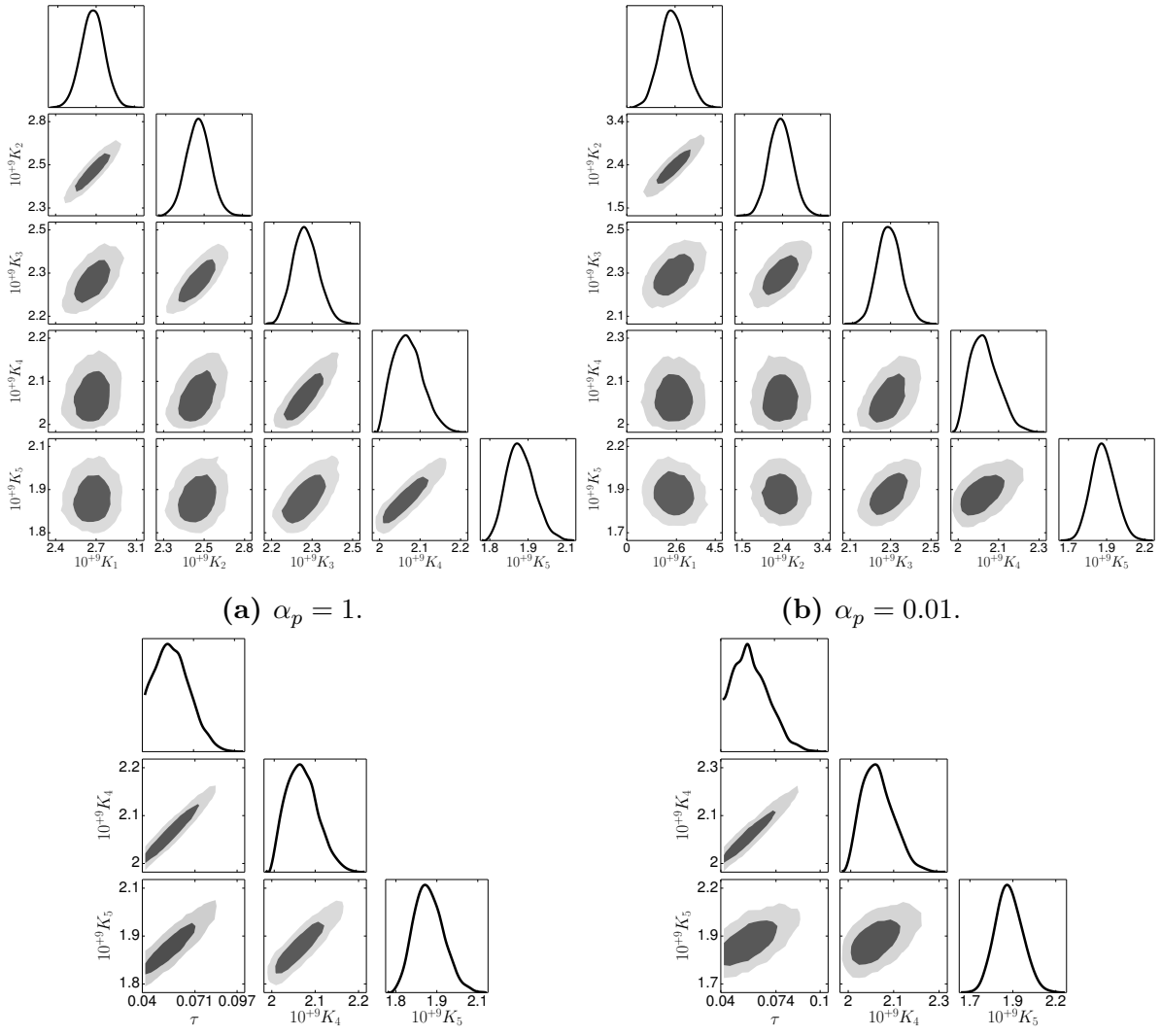

(a) $\alpha_p = 1$. **(b)** $\alpha_p = 0.01$.

(c) $\alpha_p = 1$. **(d)** $\alpha_p = 0.01$.

Figure 3.13.: Triangular plots for the run with all the datasets combined. We refer to the value of the spline function evaluated at the i-th knot as K_i.

therefore K_4 and K_5. Improved polarisation data at low ℓ should reduce this degeneracy. The figure excluding the CFHTLenS dataset is qualitatively very similar and thus is not shown here.

3.1.4. Implication for cosmological models

The analysis of the latest cosmological data [2] indicates a highly significant deviation from scale invariance of the primordial power spectrum (PPS) when parameterized by a power law or by a spectral index and a "running". This offers a powerful tool to discriminate among theories for the origin of perturbations and among inflationary models. In fact, the deviation from scale invariance of the PPS is a critical prediction of inflation and is the only signature that is generic to all inflationary models. It is therefore a vital test of the inflationary paradigm.

One may wonder if a strong theoretical prior on the form of the power spectrum, such as the power law prescription, can lead to artificially tight constraints or even a spurious detection of a deviation from scale invariance, if the adopted model were not a good fit to the data.

Here we have built on the work of [143, 144] to reconstruct the PPS with a minimally parametric approach, using the cross-validation technique as the smoothness criterion. We consider a comprehensive set of state-of-the art cosmological data including probes of the Cosmic Microwave Background, and of large scale structure via gravitational lensing and galaxy redshift surveys. While the spline reconstruction used here is best suited for smooth features in the PPS, it is also sensitive to sharp features if they have high enough signal-to-noise.

We find that there is no evidence for deviations from a power law PPS, and that errors of the reconstructed PPS are comparable with errors obtained with a power law fit. These results should be compared with those presented in [145], to appreciate the increase in statistical power brought about by the latest generation of experiments. In fact with current data a scale-invariant power spectrum is highly disfavoured even with this minimally parametric reconstruction. In particular for our conservative choice of smoothness penalty parameter values the significance of the departure from scale invariance is comparable with that obtained when adopting the "inflation-motivated" power-law prior. Constraints no longer relax significantly when generic forms of the PPS are allowed.

Because of its flexibility, our reconstruction would be able to detect the tell-tale signature of small scale power suppression induced by free streaming of neutrino if they are sufficiently massive. Of course in reality the suppression happens in the late-time power spectrum, not in the primordial one. But as we do not include the effect of neutrino masses in the matter transfer function, the reconstruction would recover an "effective" small scale damping. Our reconstruction detects no such signature, ruling out a model with a power law PPS and sum of neutrino masses of 0.2 eV or larger.

Our results, which recover in a model independent way a power law power spectrum with a small but highly significant red tilt, offer a powerful confirmation of the inflationary paradigm, justifying adoption of the inflationary prior in cosmological analyses.

3.2. Compensated isocurvature perturbations

The observation of the cosmic microwave background (CMB) strongly suggests that the primordial density perturbations were adiabatic [2]. Departure from adiabatic perturbations, such as additional isocurvature perturbations on top of the adiabatic ones, change the CMB temperature angular power spectrum drastically, therefore they are tightly constrained. However, the isocurvature perturbations of the single species can be combined in such a way that they leave no imprint on the linear CMB power spectrum. In this case they are called compensated isocurvature perturbations (CIPs) [8]. This kind of configuration could possibly be related to the curvaton model [186] or to spontaneous baryogenesis [187]. At the level of linear CMB anisotropies there is an exact degeneracy between baryon isocurvature perturbations and CDM ones [8]. The linearised continuity equations for the baryons and the photons differ only because the baryon sector has additional terms proportional to the sound velocity squared c_s^2. During the recombination period, we approximately have $c_s^2 \approx \bar{\rho}_\gamma/\bar{\rho}_b \approx (T_\gamma/m_\mathrm{p}) \approx 10^{-9}$ with T_γ and m_p being the temperature of photon at recombination and the proton mass, respectively [188]. Therefore, the fluctuations of each sector follow the exact same equations before the sound horizon entry, and hence we cannot make a clear distinction between these two isocurvature modes. For the temperature angular power spectrum, the relative Jeans scale corresponds to the multipole $\ell \sim 10^6$, where the anisotropies are exponentially suppressed due to Silk damping, preventing a clear detection. Thus studying linear anisotropies, we can only constrain the neutrino and the total matter isocurvature perturbations, but not baryonic and CDM perturbations separately.

The current upper bounds on CIPs are given by looking at the secondary modulation of the baryon (electron) distribution in the presence of CIPs at recombination [186, 188–191]. The amplitude of the dimensionless CIP power spectrum Δ^2_rms has been constrained with the *Planck* data using different methodologies, such as looking for modifications of the CMB angular power spectrum due to second order contributions, or through the analysis of the CMB trispectrum. The most recent upper limit have been given, for example, in [189], $\Delta^2_\mathrm{rms} < 5.0 \times 10^{-3}$ (68% C.L.); in [191] $\Delta^2_\mathrm{rms} < 1.2 \times 10^{-2}$ (95% C.L.); and [192] $\Delta^2_\mathrm{rms} < 1.1 \times 10^{-2}$ (95% C.L.). As pointed out in Refs. [186, 190], further understanding is expected from the data analysis of a cosmic variance limited (CVL) CMB-polarization survey, such as CMB-S4 [193]. There are also studies about the effects of CIPs on the baryon acoustic oscillation [194, 195]. Another possibility is to see directly the spatial electron distribution by observing the redshift of 21 cm line of the neutral hydrogen

hyperfine structure [196]. While most studies so far only provided upper limit to the existence of CIPs, the author in Ref. [191] has instead recently reported a 2σ detection of the CIPs as the result of a full parameter estimation of Planck data, providing a hint that a sizable amount of CIPs might exist. Therefore, it is interesting to pursue this trail using future cosmological data, and to find novel probes of CIPs signatures.

In this section, we explore the possibility of observing the CIPs using CMB spectral distortion anisotropies. The spectrum of the CMB has been measured with great precision by COBE/FIRAS, and within experimental accuracy it perfectly follows a (direction dependent) Planck distribution. However, it is actually non trivial that the deviation from the isotropic blackbody spectrum can be described solely by the local temperature parameter since the early universe is out of thermal equilibrium at redshifts $z \sim \mathcal{O}(10^3)$ as discussed in Section 1.3. Since there was some energy transfer between photons and electrons during this period, the CMB spectrum was no more at equilibrium. Such an energy transfer can be characterized by $T_{\rm e}/m_{\rm e}$ with $T_{\rm e}$ and $m_{\rm e}$ being the electron temperature and electron mass. This correction is so tiny that it is usually ignored in the standard cosmological perturbation theory, but it would be non negligible if a considerable amount of CIP is present. Distribution functions for non equilibrium systems are highly non trivial, but it is known that in the regime of inefficient Compton scattering the photon distribution has a characteristic shape described by the y-distortion we defined in eq. (1.44).

We consider the linear modulation of the y-distortions due to the electron density fluctuations in the presence of CIPs. The vital point is that linear anisotropies of the y-distortions can resolve the degeneracy between CDM and baryon isocurvature perturbation, even though the signal is tiny because the energy transfer is suppressed as we mentioned above. Here, we investigate the spectral distortion anisotropies by employing a systematic formulation proposed in Refs. [197–199]. The idea of using spectral distortions has been originally proposed in Ref. [200], but it was shown that the quadratic spectral distortions from Silk damping are insensitive to the CIPs. Instead in this article we consider the linear modulation of the Background spectral distortions.

The discussion is organized as follows. In Section 3.2.1 we derive the linear y-distortion collision terms for the Compton scattering by using a set of frequency basis, obtain the Boltzmann equation, and estimate the linear y anisotropies by using the Boltzmann code `CLASS` [201]. Then, in Section 3.2.2 we show the y-distortions anisotropies cross correlations with T and E, and we discuss the dependence with the CIPs parametrization we employ. A Fisher matrix analysis about the possibility of constraining the CIPs

with future surveys is given in Section 3.2.3, and finally we draw our conclusions in Section 3.2.4.

3.2.1. Linear order spectral distortions anisotropies

In Section 1.5.1 we showed how at leading order it is possible to factor out the frequency dependence from the photon Boltzmann equation, and transform it into eq. (1.101). The same cannot trivially be done if we consider energy exchange between electrons and photons. Therefore we develop a momenta expansion for the CMB energy spectrum.

Beyond the Thompson scattering limit

Let us go beyond the Thomson scattering limit, that is, we consider the collision processes of the Compton scattering, which, contrary to the Thompson scattering limit, allow energy transfer between photons and electrons. Though the Thomson collision effect does not have the homogeneous part at the zeroth order, this is not the case if we include the Compton scattering correction as explicitly shown below [202]:

$$
\begin{aligned}
&(n_{\rm e}\sigma_{\rm T}a)^{-1}C^{(0)}_{\rm CS}[f] = \\
&\frac{T_{\rm e}}{m_{\rm e}}\left(p^2\frac{\partial^2 f^{(0)}}{\partial p^2}+4p\frac{\partial f^{(0)}}{\partial p}\right)+\frac{p(1+z)}{m_{\rm e}}\left(2f^{(0)}p\frac{\partial f^{(0)}}{\partial p}+p\frac{\partial f^{(0)}}{\partial p}+4f^{(0)2}+4f^{(0)}\right).
\end{aligned}
\tag{3.4}
$$

As it evident, the frequency dependence cannot be factorized as we did in the Thompson limit.

The linear order collision term for the Compton scattering is more complicated since we need to expand the collision terms up to the cubic order in the electron velocity. The statistical average of the electron momentum cube can be divided into a thermal part that goes like $T_{\rm e}/m_{\rm e}\times v$ and a bulk velocity part such as v^3, which we drop for simplicity. We can drop the second order terms such as v^2 due to the Gaussian initial condition we assume. This point will be discussed later. The expression was first derived in Ref. [31] and rederived in Ref. [199], and has the form

$$
\begin{aligned}
&(n_{\rm e}\sigma_{\rm T}a)^{-1}\mathcal{C}^{(1)}_{\rm CS}[f] \\
&=\frac{p(1+z)}{m_{\rm e}}\left[2p\frac{\partial f^{(0)}}{\partial p}f^{(1)}(\mathbf{p})+4f^{(0)}f^{(1)}(\mathbf{p})+2f^{(1)}(\mathbf{p})\right.
\end{aligned}
$$

$$
\begin{aligned}
&+4f^{(0)}f_0^{(1)} + p\frac{\partial f_0^{(1)}}{\partial p} + 2f_0^{(1)} + 2f^{(0)}p\frac{\partial f_0^{(1)}}{\partial p} \\
&+(\hat{\mathbf{v}}\cdot\mathbf{n})\left(\frac{24}{5}if^{(0)}f_1^{(1)} + \frac{12}{5}if_1^{(1)} + \frac{12i}{5}f^{(0)}p\frac{\partial f_1^{(1)}}{\partial p} + \frac{6i}{5}p\frac{\partial f_1^{(1)}}{\partial p}\right) \\
&+(\mathbf{v}\cdot\mathbf{n})\left(-8f^{(0)2} - 8f^{(0)} - \frac{7}{5}p^2\frac{\partial^2 f^{(0)}}{\partial p^2} - \frac{14}{5}f^{(0)}p^2\frac{\partial^2 f^{(0)}}{\partial p^2} - \frac{31}{5}p\frac{\partial f^{(0)}}{\partial p} - \frac{62}{5}f^{(0)}p\frac{\partial f^{(0)}}{\partial p}\right) \\
&+P_2\left(-2f^{(0)}f_2^{(1)} - f_2^{(1)} - f^{(0)}p\frac{\partial f_2^{(1)}}{\partial p} - \frac{1}{2}p\frac{\partial f_2^{(1)}}{\partial p}\right) \\
&+P_3\left(-\frac{3i}{5}f_3^{(1)} - \frac{6i}{5}f^{(0)}f_3^{(1)} - \frac{3i}{5}f^{(0)}p\frac{\partial f_3^{(1)}}{\partial p} - \frac{3i}{10}p\frac{\partial f_3^{(1)}}{\partial p}\right)\Bigg] \\
&+\frac{T_\mathrm{e}}{m_\mathrm{e}}\Bigg[(\mathbf{v}\cdot\mathbf{n})\left(-\frac{7}{5}p^3\frac{\partial^3 f^{(0)}}{\partial p^3} - \frac{47}{5}p^2\frac{\partial^2 f^{(0)}}{\partial p^2} - \frac{15}{2}p\frac{\partial f^{(0)}}{\partial p}\right) + \\
&(\hat{\mathbf{v}}\cdot\mathbf{n})\left(\frac{6i}{5}p^2\frac{\partial^2 f_1^{(1)}}{\partial p^2} + \frac{24i}{5}p\frac{\partial f_1^{(1)}}{\partial p} + \frac{6i}{5}f_1^{(1)}\right) + P_2\left(-\frac{1}{2}p^2\frac{\partial^2 f_2^{(1)}}{\partial p^2} - 2p\frac{\partial f_2^{(1)}}{\partial p} + 3f_2^{(1)}\right) \\
&+P_3\left(-\frac{3i}{10}p^2\frac{\partial^2 f_3^{(1)}}{\partial p^2} - \frac{6i}{5}p\frac{\partial f_3^{(1)}}{\partial p} + \frac{6i}{5}f_3^{(1)}\right) + p^2\frac{\partial^2 f_0^{(1)}}{\partial p^2} + 4p\frac{\partial f_0^{(1)}}{\partial p}\Bigg], \qquad (3.5)
\end{aligned}
$$

where $f^{(1)}$ implies the linear fluctuations of the photon distribution function, which cannot be expressed solely in terms of temperature perturbation as we will see below. Obviously, frequency dependence for the linear Compton collision term cannot be treated in a simple manner. This clearly shows that our local equilibrium ansatz eq. (1.93) is no more applicable, and we only have the effective temperature perturbation

$$\Theta(\eta, \mathbf{x}, \mathbf{n}) \to \Theta(\eta, \mathbf{x}, p\mathbf{n})\,. \qquad (3.6)$$

In principle we have to solve an infinite number of equations for each $(\eta, \mathbf{x}, \mathbf{n})$. This would be time consuming and requires tough numerical simulations. In the next section, we solve this problem by employing a moment expansion, which was introduced in Refs. [197–199].

CMB energy spectrum momenta expansion

Ref. [199] found out that the following three basis functions would be minimum to handle the frequency dependence of the $T_\mathrm{e}/m_\mathrm{e} \to 0$ limit Boltzmann equation up to cubic order

in the primordial fluctuations:

$$\mathcal{G} \equiv \left(-p\frac{\partial}{\partial p}\right) f^{(0)}, \tag{3.7}$$

$$\mathcal{Y} \equiv \left(-p\frac{\partial}{\partial p}\right)^2 f^{(0)} - 3\mathcal{G}, \tag{3.8}$$

$$\mathcal{K} \equiv \left(-p\frac{\partial}{\partial p}\right)^3 f^{(0)} - 3\mathcal{Y} - 9\mathcal{G}. \tag{3.9}$$

The following relations for the basis functions will be useful throughout this section:

$$\begin{aligned} p^2\frac{\partial^2}{\partial p^2} f^{(0)} &= \mathcal{Y} + 4\mathcal{G}, \\ p^3\frac{\partial^3}{\partial p^3} f^{(0)} &= -\mathcal{K} - 6\mathcal{Y} - 20\mathcal{G}. \end{aligned} \tag{3.10}$$

On the other hand, $T_\mathrm{e}/m_\mathrm{e}$ corrections make the problem more complicated in principle, but we newly found that adding the following frequency function is a minimal revision for the present linear case:

$$\mathcal{U} \equiv \frac{p^2}{T_\mathrm{ref}^2}\left(-p\frac{\partial}{\partial p}\right) f^{(0)}. \tag{3.11}$$

Using the above frequency basis, let us consider the following ansatz:

$$f = f^{(0)} + \Theta\mathcal{G} + y\mathcal{Y} + \kappa\mathcal{K} + u\mathcal{U}. \tag{3.12}$$

We will justify this ansatz in the later calculations. As we already stated, the temperature perturbation is comparable to the order of the primordial fluctuation that is denoted by δ: $\Theta = \mathcal{O}(\delta)$. On the other hand, the other coefficients would be the first order in both the energy transfer $\varepsilon = \mathcal{O}(T_\mathrm{e}/m_\mathrm{e})$ and δ: $\{y, \kappa, u\} = \mathcal{O}(\delta\varepsilon)$.

The homogeneous component

Before going to the main discussion, we comment on the homogeneous part of the Compton scattering. It is well known that eq. (3.4) can be recast into a simple form:

$$(n_\mathrm{e}\sigma_\mathrm{T}a)^{-1}\mathcal{C}_\mathrm{CS}^{(0)}[f] = \frac{T_\mathrm{e} - T_\gamma}{m_\mathrm{e}}\mathcal{Y}, \tag{3.13}$$

where we have defined the physical temperature of photons as $T_\gamma \equiv T_{\rm ref}(1+z)$. Note that we used eq. (3.10) with the following relations:

$$\begin{aligned} f^{(0)}(1+f^{(0)}) &= \frac{T_{\rm ref}}{p}\mathcal{G}, \\ \left(-p\frac{\partial}{\partial p}\right) f^{(0)}(1+f^{(0)}) &= \frac{T_{\rm ref}}{p}(\mathcal{Y}+4\mathcal{G}), \\ \left(-p\frac{\partial}{\partial p}\right)^2 f^{(0)}(1+f^{(0)}) &= \frac{T_{\rm ref}}{p}(\mathcal{K}+5\mathcal{Y}+16\mathcal{G}). \end{aligned} \tag{3.14}$$

eq. (3.13) implies that y has $O(\varepsilon)$ contribution

$$y = \int d\eta n_{\rm e}\sigma_{\rm T} a \frac{T_{\rm e}-T_\gamma}{m_{\rm e}} + \cdots . \tag{3.15}$$

However, this term is not what we want. We consider the CIPs, which produce the linear anisotropies of the spectral distortions, and hence we ignore this contribution.

The linear component

In addition to eq. (3.5), we include the electron number density fluctuation on the top of homogeneous y-distortion in the previous subsection. This is done by replacing the electron temperature and the number density as

$$T_{\rm e} \to T_{\rm e}(1+\Theta_{\rm e}),\ n_{\rm e} \to n_{\rm e}(1+\delta_{n_{\rm e}}), \tag{3.16}$$

where $\delta_{n_{\rm e}}$ is the ionized electron number density perturbation and $\Theta_{\rm e}$ is the electron temperature perturbation. We also solve the perturbed recombination for the evolution of $\delta_{n_{\rm e}}$ and $\Theta_{\rm e}$ following the equations in Ref. [203].[5] Note that the equations for $\delta_{n_{\rm e}}$ and $\Theta_{\rm e}$ in Ref. [203] are valid only up to reionization and the precise calculation of $\delta_{n_{\rm e}}$ and $\Theta_{\rm e}$ during reionization is beyond the scope of this calculation.[6]

Here, we comment on the initial conditions for the perturbed recombination. We set $\delta_{n_{\rm e}} = \delta_b$ (δ_b: baryon density perturbation) and $\Theta_{\rm e} = \Theta_0$ since we consider the photon baryon plasma to be in equilibrium state in the very early universe. Note that $\Theta_{\rm e} = \delta_b/3$ is not necessarily established in the very early universe if we do not start with adiabatic perturbations. For example, in the case of baryon isocurvature perturbations, δ_b depends

[5] The perturbed recombination is discussed also in Refs. [204–207].

[6] We have confirmed that the reionization effect on y-distortions is subdominant at least in our setup.

on not only $\Theta_{\rm e}$ but also the chemical potential, and the spatial fluctuation of the chemical potential corresponds to the baryon isocurvature perturbations. Therefore $\Theta_{\rm e} = \delta_b/3$ is not established in the case of the baryon isocurvature perturbations.

From eq. (3.5) and the modification eq. (3.16), we obtain the following collision terms for the Compton scattering:

$$
\begin{aligned}
&(n_{\rm e}\sigma_{\rm T}a)^{-1}\mathcal{C}^{(1)}_{\rm CS}[f] = \\
&\frac{T_{\rm e}(\Theta_{\rm e}+\delta_{n_{\rm e}})}{m_{\rm e}}\left(p^2\frac{\partial^2 f^{(0)}}{\partial p^2}+4p\frac{\partial f^{(0)}}{\partial p}\right)\\
&+\frac{p(1+z)\delta_{n_{\rm e}}}{m_{\rm e}}\left(2f^{(0)}p\frac{\partial f^{(0)}}{\partial p}+p\frac{\partial f^{(0)}}{\partial p}+4f^{(0)2}+4f^{(0)}\right)\\
&+\frac{p(1+z)}{m_{\rm e}}\left[2p\frac{\partial f^{(0)}}{\partial p}f^{(1)}(\mathbf{p})+4f^{(0)}f^{(1)}(\mathbf{p})+2f^{(1)}(\mathbf{p})\right.\\
&+4f^{(0)}f^{(1)}_0+p\frac{\partial f^{(1)}_0}{\partial p}+2f^{(1)}_0+2f^{(0)}p\frac{\partial f^{(1)}_0}{\partial p}\\
&+(\hat{\mathbf{v}}\cdot\mathbf{n})\left(\frac{24}{5}if^{(0)}f^{(1)}_1+\frac{12}{5}if^{(1)}_1+\frac{12i}{5}f^{(0)}p\frac{\partial f^{(1)}_1}{\partial p}+\frac{6i}{5}p\frac{\partial f^{(1)}_1}{\partial p}\right)\\
&+(\mathbf{v}\cdot\mathbf{n})\left(-8f^{(0)2}-8f^{(0)}-\frac{7}{5}p^2\frac{\partial^2 f^{(0)}}{\partial p^2}-\frac{14}{5}f^{(0)}p^2\frac{\partial^2 f^{(0)}}{\partial p^2}-\frac{31}{5}p\frac{\partial f^{(0)}}{\partial p}-\frac{62}{5}f^{(0)}p\frac{\partial f^{(0)}}{\partial p}\right)\\
&+P_2\left(-2f^{(0)}f^{(1)}_2-f^{(1)}_2-f^{(0)}p\frac{\partial f^{(1)}_2}{\partial p}-\frac{1}{2}p\frac{\partial f^{(1)}_2}{\partial p}\right)\\
&\left.+P_3\left(-\frac{3i}{5}f^{(1)}_3-\frac{6i}{5}f^{(0)}f^{(1)}_3-\frac{3i}{5}f^{(0)}p\frac{\partial f^{(1)}_3}{\partial p}-\frac{3i}{10}p\frac{\partial f^{(1)}_3}{\partial p}\right)\right]\\
&+\frac{T_{\rm e}}{m_{\rm e}}\left[(\mathbf{v}\cdot\mathbf{n})\left(-\frac{7}{5}p^3\frac{\partial^3 f^{(0)}}{\partial p^3}-\frac{47}{5}p^2\frac{\partial^2 f^{(0)}}{\partial p^2}-\frac{15}{2}p\frac{\partial f^{(0)}}{\partial p}\right)+\right.\\
&(\hat{\mathbf{v}}\cdot\mathbf{n})\left(\frac{6i}{5}p^2\frac{\partial^2 f^{(1)}_1}{\partial p^2}+\frac{24i}{5}p\frac{\partial f^{(1)}_1}{\partial p}+\frac{6i}{5}f^{(1)}_1\right)+P_2\left(-\frac{1}{2}p^2\frac{\partial^2 f^{(1)}_2}{\partial p^2}-2p\frac{\partial f^{(1)}_2}{\partial p}+3f^{(1)}_2\right)\\
&\left.+P_3\left(-\frac{3i}{10}p^2\frac{\partial^2 f^{(1)}_3}{\partial p^2}-\frac{6i}{5}p\frac{\partial f^{(1)}_3}{\partial p}+\frac{6i}{5}f^{(1)}_3\right)+p^2\frac{\partial^2 f^{(1)}_0}{\partial p^2}+4p\frac{\partial f^{(1)}_0}{\partial p}\right]. \qquad (3.17)
\end{aligned}
$$

The above expression is tedious but can be expanded in the four frequency basis functions eq. (3.7) to (3.11). Since eq. (3.17) is already ordered in terms of the Legendre polynomials, we easily obtain the multipole components of the Compton scattering for the Boltzmann hierarchy equation:

$$(n_{\rm e}\sigma_{\rm T}a)^{-1}\mathcal{C}^{(1)}_{{\rm CS}\,0}[f] = \left[\frac{T_{\rm e}}{m_{\rm e}}(\delta_{n_{\rm e}}+\Theta_{\rm e}) - \frac{T_\gamma}{m_{\rm e}}(\delta_{n_{\rm e}}+\Theta_0)\right]\mathcal{Y} + \frac{T_{\rm e}-T_\gamma}{m_{\rm e}}\Theta_0\mathcal{K}\,, \tag{3.18}$$

$$\begin{aligned}(n_{\rm e}\sigma_{\rm T}a)^{-1}\mathcal{C}^{(1)}_{{\rm CS}\,1}[f] = &\left[\frac{T_\gamma}{m_{\rm e}}\left(-\frac{1}{15}\Theta_1 - \frac{14}{45}iv\right) + \frac{T_{\rm e}}{m_{\rm e}}\left(-\frac{2}{5}\Theta_1 + \frac{7}{15}iv\right)\right]\mathcal{K}\\ &+\left[\frac{T_\gamma}{m_{\rm e}}\left(\frac{2}{5}\Theta_1 + \frac{1}{5}iv\right) + \frac{T_{\rm e}}{m_{\rm e}}\left(-\frac{1}{3}iv\right)\right]\mathcal{Y}\\ &+\left[\frac{T_\gamma}{m_{\rm e}}\left(\frac{28}{15}\Theta_1 - \frac{28}{45}iv\right) + \frac{T_{\rm e}}{m_{\rm e}}\left(-\frac{2}{5}\Theta_1 - \frac{7}{10}iv\right)\right]\mathcal{G}\\ &+\left[\frac{T_\gamma}{m_{\rm e}}\left(\frac{7}{15}\Theta_1 - \frac{7}{45}iv\right)\right]\mathcal{U}\,,\end{aligned} \tag{3.19}$$

$$\begin{aligned}(n_{\rm e}\sigma_{\rm T}a)^{-1}\mathcal{C}^{(1)}_{{\rm CS}\,2}[f] = &\left(-\frac{2}{5}\frac{T_\gamma}{m_{\rm e}} + \frac{1}{10}\frac{T_{\rm e}}{m_{\rm e}}\right)\Theta_2\,\mathcal{K} + \left(-\frac{1}{10}\frac{T_\gamma}{m_{\rm e}}\right)\Theta_2\,\mathcal{Y}\\ &+\left(\frac{6}{5}\frac{T_\gamma}{m_{\rm e}} - \frac{3}{5}\frac{T_{\rm e}}{m_{\rm e}}\right)\Theta_2\,\mathcal{G} + \left(\frac{3}{10}\frac{T_\gamma}{m_{\rm e}}\right)\Theta_2\,\mathcal{U}\,,\end{aligned} \tag{3.20}$$

$$\begin{aligned}(n_{\rm e}\sigma_{\rm T}a)^{-1}\mathcal{C}^{(1)}_{{\rm CS}\,3}[f] = &\left(-\frac{32}{105}\frac{T_\gamma}{m_{\rm e}} - \frac{3}{70}\frac{T_{\rm e}}{m_{\rm e}}\right)\Theta_3\,\mathcal{K} + \left(\frac{3}{70}\frac{T_\gamma}{m_{\rm e}}\right)\Theta_3\,\mathcal{Y}\\ &+\left(\frac{146}{105}\frac{T_\gamma}{m_{\rm e}} + \frac{6}{35}\frac{T_{\rm e}}{m_{\rm e}}\right)\Theta_3\,\mathcal{G} + \left(\frac{73}{210}\frac{T_\gamma}{m_{\rm e}}\right)\Theta_3\,\mathcal{U}\,,\end{aligned} \tag{3.21}$$

where $\mathcal{C}^{(1)}_{{\rm CS}\,\ell}[f]$ is zero for $\ell > 3$ and we used eq. (3.10) and eq. (3.14) with the following relations:

$$\left(-p\frac{\partial f^{(0)}}{\partial p}\right)^2 = \frac{T_{\rm ref}}{6p}(\mathcal{K}+6\mathcal{Y}+20\mathcal{G}-\mathcal{U})\,, \tag{3.22}$$

$$p^2\frac{\partial^2}{\partial p^2}\left(-p\frac{\partial}{\partial p}\right)f^{(0)} = \mathcal{K}+4\mathcal{Y}+12\mathcal{G}, \tag{3.23}$$

$$p^2\frac{\partial^2}{\partial p^2}f^{(0)}(1+f^{(0)}) = \frac{T_{\rm ref}}{p}(\mathcal{K}+6\mathcal{Y}+20\mathcal{G}). \tag{3.24}$$

On the other hand, the LHS of the Boltzmann equation is simpler. If one starts with the new ansatz eq. (3.12), eq. (1.96) is modified to

$$\frac{df}{d\eta} = \left(\frac{d\Theta}{d\eta} - \frac{d\ln p}{d\eta}\right)\mathcal{G} + \frac{dy}{d\eta}\mathcal{Y} + \frac{d\kappa}{d\eta}\mathcal{K} + \frac{du}{d\eta}\mathcal{U} + \cdots\,, \tag{3.25}$$

where dots imply the next-to-leading order corrections. Note that $d\ln p/d\eta = \mathcal{O}(\delta)$ so that the time derivatives of the frequency basis become at least linear order in the

primordial perturbations. As long as we consider Gaussian initial conditions, $\mathcal{O}(\delta^2)$ can be dropped since these terms do not contribute to the cross correlations with the linear perturbations in the following discussions. Though $\mathcal{O}(\delta^3)$ has potential to be comparable to $\mathcal{O}(\delta\epsilon)$, we neglect these contributions for simplicity. Combining eq. (3.25) with eq. (3.18) to (3.21), we find the 4 coefficient equations for each $(\eta, \mathbf{x})$.

Boltzmann equation for the *y*-distortions

We write the Boltzmann hierarchy equations in Fourier space to solve the linear y evolution. The Fourier integral of the real space linear y-distortions can be defined as

$$y(\eta, \mathbf{k}, \mathbf{n}) \equiv \int d^3x e^{-i\mathbf{k}\cdot\mathbf{x}} y(\eta, \mathbf{x}, \mathbf{n}). \tag{3.26}$$

The Fourier space perturbations are linearly coming from the primordial perturbations. The transfer functions $y_\ell^{(I)}(\eta, k)$ can be then given as

$$y(\eta, \mathbf{k}, \mathbf{n}) = \sum_\ell (-i)^\ell (2\ell+1) P_\ell(\hat{k}\cdot\mathbf{n}) \sum_I y_\ell^{(I)}(\eta, k)\xi_{\mathbf{k}}^{(I)}, \tag{3.27}$$

where $\xi^{(I)}$ is the scalar random variables, i.e., $\xi^{(I)} = (\zeta, S_{c\gamma}, S_{b\gamma}, \cdots)$: ζ is the adiabatic perturbation, and the isocurvature perturbations are defined as

$$S_{\alpha\gamma} \equiv \frac{1}{1+\omega_\alpha}\frac{\delta\rho_\alpha}{\rho_\alpha} - \frac{3}{4}\frac{\delta\rho_\gamma}{\rho_\gamma}. \tag{3.28}$$

Note that $\omega_\gamma = \omega_\nu = 1/3$ and $\omega_c = \omega_b = 0$. We ignore the vector and the tensor perturbations for simplicity, and the following relation is satisfied for CIPs:

$$S_{c\gamma} = -\frac{\Omega_b}{\Omega_c} S_{b\gamma}. \tag{3.29}$$

The Liouville terms for the linear y-distortion can be given in the same form with the temperature perturbations without metric perturbations. Then eq. (3.18) to eq. (3.21)

yield

$$\dot{y}_0 + k y_1 = n_{\rm e}\sigma_{\rm T} a \left[\frac{T_{\rm e}}{m_{\rm e}} (\delta_{n_{\rm e}} + \Theta_{\rm e}) - \frac{T_\gamma}{m_{\rm e}} (\delta_{n_{\rm e}} + \Theta_0) \right], \tag{3.30}$$

$$\dot{y}_1 + \frac{2k}{3} y_2 - \frac{k}{3} y_0 = -n_{\rm e}\sigma_{\rm T} a y_1 + n_{\rm e}\sigma_{\rm T} a \left[\frac{T_\gamma}{m_{\rm e}} \left(\frac{2}{5}\Theta_1 + \frac{1}{5} iv \right) + \frac{T_{\rm e}}{m_{\rm e}} \left(-\frac{1}{3} iv \right) \right], \tag{3.31}$$

$$\dot{y}_2 + \frac{3k}{5} y_3 - \frac{2k}{5} y_1 = -\frac{9}{10} n_{\rm e}\sigma_{\rm T} a y_2 + n_{\rm e}\sigma_{\rm T} a \left(-\frac{1}{10} \frac{T_\gamma}{m_{\rm e}} \right) \Theta_2, \tag{3.32}$$

$$\dot{y}_3 + \frac{4k}{7} y_4 - \frac{3k}{7} y_2 = -n_{\rm e}\sigma_{\rm T} a y_3 + n_{\rm e}\sigma_{\rm T} a \left(\frac{3}{70} \frac{T_\gamma}{m_{\rm e}} \right) \Theta_3. \tag{3.33}$$

$\ell > 3$ equations do not have collision effect and we simply obtain [23]

$$\dot{y}_\ell + \frac{\ell + 1}{2\ell + 1} k y_{\ell+1} - \frac{\ell}{2\ell + 1} k y_{\ell-1} = -n_{\rm e}\sigma_{\rm T} a y_\ell \quad (\ell > 3). \tag{3.34}$$

In the following we use the synchronous gauge when we perform numerical calculations. Figure 3.14 shows the evolutions of $|y_0|$ and $|y_1|$, which are calculated numerically using `CLASS`. The rapid increases of values before $z = 10^4$ is due to the specification of an initial time for integration. We have checked that the final results are not sensitive to the choice of initial time as long as we start well before recombination. From the figures, we can see that $|y_0|$ and $|y_1|$ grow only in the late epoch before recombination when the discrepancy between $T_{\rm e}$ and T_γ becomes manifest. This implies that the chemical potential μ distortions are not generated in this way. After recombination, the sub-horizon modes oscillate because the RHS of eq. (3.30) and eq. (3.31) is zero and so we have

$$\ddot{y}_0 - \frac{k^2}{3} y_0 \approx 0. \tag{3.35}$$

Note that super-horizon evolution of the linear y-distortions does not violate causality. The super-horizon y-distortions only appear along the super-horizon primordial fluctuations that already exist.

Line-of-sight formalism for the spectral distortion anisotropies

The remaining procedures to get the angular power spectra are exactly the same as for the usual linear anisotropies. The angular power spectrum up to $\ell = 1000$ requires us to solve 1000 Boltzmann hierarchy equations, which is time consuming. Instead, we usually use the integral solution and solve a very limited number of hierarchy equations to obtain

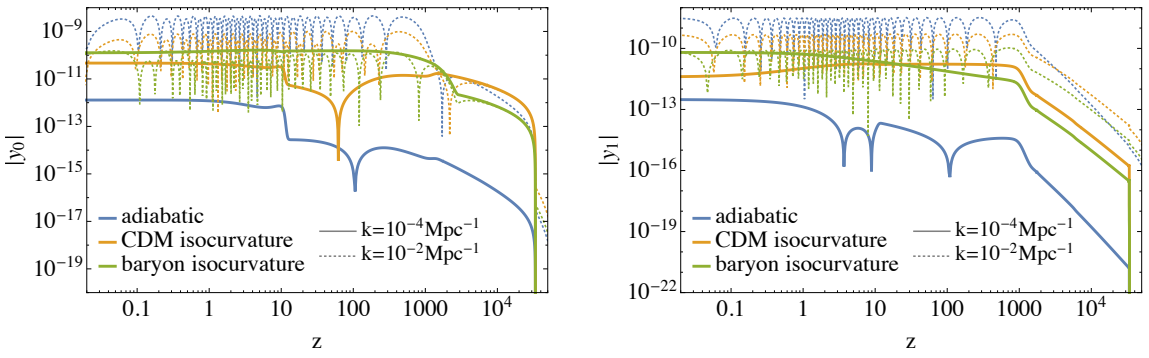

Figure 3.14.: The redshift dependences of $|y_0|$ (left) and $|y_1|$ (right). Blue, green, yellow lines show the case of adiabatic perturbations, CDM isocurvature perturbations, and baryon isocurvature perturbations, respectively. In the solid (dotted) lines, we take the wave number as $k = 10^{-4}\,\mathrm{Mpc}^{-1}$ ($k = 10^{-2}\,\mathrm{Mpc}^{-1}$). For example, blue solid line shows the case of the adiabatic perturbation with $k = 10^{-4}\,\mathrm{Mpc}^{-1}$.

the source function for the integral solution [108]. The line-of-sight solution for the linear y-distortion is

$$y(\eta_0, k, \lambda) = \int_0^{\eta_0} d\eta\, g \left(y_0 - \frac{1}{2} P_2 y_2 + \mathcal{S}_y \right) e^{ik\lambda(\eta - \eta_0)}, \tag{3.36}$$

where the multipole coefficients for the source function are

$$\mathcal{S}_{y0} = \frac{T_\mathrm{e}}{m_\mathrm{e}}(\delta_{n_\mathrm{e}} + \Theta_\mathrm{e}) - \frac{T_\gamma}{m_\mathrm{e}}(\delta_{n_\mathrm{e}} + \Theta_0)\,, \tag{3.37}$$

$$\mathcal{S}_{y1} = \frac{T_\gamma}{m_\mathrm{e}}\left(\frac{2}{5}\Theta_1 + \frac{1}{5} iv\right) + \frac{T_\mathrm{e}}{m_\mathrm{e}}\left(-\frac{1}{3} iv\right), \tag{3.38}$$

$$\mathcal{S}_{y2} = -\frac{1}{10}\frac{T_\gamma}{m_\mathrm{e}}\Theta_2\,, \tag{3.39}$$

$$\mathcal{S}_{y3} = \frac{3}{70}\frac{T_\gamma}{m_\mathrm{e}}\Theta_3\,. \tag{3.40}$$

Note that the baryon isocurvature perturbation dependences of δ_{n_e} and Θ_e are different from the CDM ones. This is essential to distinguish the baryon isocurvature perturbations from the CDM ones, and therefore to observe the CIPs. This is specific to y-distortions; Θ, κ and u do not have such a source and therefore we only focus on the y-distortion linear anisotropies in this section. Note that the following form is more practical to use

in CLASS:

$$y_\ell(\eta_0,k,\lambda) = \int_0^{\eta_0} d\eta\, g \left[y_0 + \mathcal{S}_{y0} + 3\mathcal{S}_{y1}\left(\frac{\partial}{\partial(k\eta_0)}\right) + \left(5\mathcal{S}_{y2} + \frac{1}{2}y_2\right)\frac{1}{2}\left(3\left(\frac{\partial}{\partial(k\eta_0)}\right)^2 + 1\right) + 7\mathcal{S}_{y3}\frac{1}{2}\left(5\left(\frac{\partial}{\partial(k\eta_0)}\right)^3 + 3\left(\frac{\partial}{\partial(k\eta_0)}\right)\right)\right] j_\ell[k(\eta_0-\eta)]\,. \tag{3.41}$$

The anisotropies of X on the celestial sphere can be expanded in spherical harmonics as follows:

$$X(\eta_0, \mathbf{x}=0, \mathbf{n}) = \sum_{\ell=0}^{\infty}\sum_{m=-\ell}^{\ell} a_{X,\ell m} Y_{\ell m}(\mathbf{n}), \tag{3.42}$$

where $Y_{\ell m}$ are the spherical harmonics and $X = \Theta,\ y$ and polarization E mode. The harmonic coefficients are related to the primordial random fields as

$$a_{X,\ell m} = 4\pi(-i)^\ell \int \frac{d^3k}{(2\pi)^3} Y^*_{\ell m}(\hat{k}) \sum_I X_\ell^{(I)}(\eta_0,k)\xi^{(I)}_{\mathbf{k}}. \tag{3.43}$$

The angular power spectrum is also defined as in the usual linear anisotropies case:

$$\langle a_{X,\ell m} a^*_{Z,\ell' m'}\rangle = C_\ell^{XZ}\delta_{\ell\ell}\delta_{mm'}. \tag{3.44}$$

Then, we find

$$C_\ell^{XZ} = \sum_{II'} 4\pi \int \frac{dk}{k}\mathcal{P}_{II'}(k) X_\ell^{(I)}(\eta_0,k) Z_\ell^{(I')}(\eta_0,k), \tag{3.45}$$

where we defined the power spectra of the random variables as:

$$\langle \zeta_{\mathbf{k}}\zeta_{\mathbf{k}'}\rangle = (2\pi)^3\delta^{(3)}(\mathbf{k}+\mathbf{k}')\frac{2\pi^2}{k^3}\mathcal{P}_{\zeta\zeta}(k), \tag{3.46}$$

$$\langle \zeta_{\mathbf{k}} S_{\alpha\gamma,\mathbf{k}'}\rangle = (2\pi)^3\delta^{(3)}(\mathbf{k}+\mathbf{k}')\frac{2\pi^2}{k^3}\mathcal{P}_{\zeta\alpha}(k), \tag{3.47}$$

$$\langle S_{\alpha\gamma,\mathbf{k}} S_{\beta\gamma,\mathbf{k}'}\rangle = (2\pi)^3\delta^{(3)}(\mathbf{k}+\mathbf{k}')\frac{2\pi^2}{k^3}\mathcal{P}_{\alpha\beta}(k). \tag{3.48}$$

Note that the baryon isocurvature power spectrum and the CDM isocurvature one are not independent in the CIPs model: the relations

$$\mathcal{P}_{cc} = \left(\frac{\Omega_b}{\Omega_c}\right)^2 \mathcal{P}_{bb},\ \mathcal{P}_{c\zeta} = -\frac{\Omega_b}{\Omega_c}\mathcal{P}_{b\zeta} \tag{3.49}$$

are always satisfied.

In this section, for simplicity, we assume that CIPs scales as the adiabatic perturbations. Then CIPs can be parameterized by only two parameters, $f_{\rm bi}$ and $\cos\theta$, which are defined as

$$f_{\rm bi} \equiv \sqrt{\frac{\mathcal{P}_{bb}(k_0)}{\mathcal{P}_{\zeta\zeta}(k_0)}}\,, \tag{3.50}$$

$$\cos\theta \equiv \frac{\mathcal{P}_{b\zeta}(k_0)}{\sqrt{\mathcal{P}_{bb}(k_0)\mathcal{P}_{\zeta\zeta}(k_0)}}\,, \tag{3.51}$$

where $k_0 (= 0.05\,\mathrm{Mpc}^{-1})$ is the pivot scale. While $f_{\rm bi}$ measure the amplitude of CIPs relative to the adiabatic perturbations, $\cos\theta$ parametrize the degree of correlation between the two kinds. As we will discuss at length, our analysis is sensitive not only to $f_{\rm bi}$, like other methods developed in the literature, but also to $\cos\theta$. This would allow, in principle, the possibility of discerning correlated and uncorrelated CIPs. Figure 3.15 shows C_ℓ^{yT}, C_ℓ^{yE}, and C_ℓ^{yy} in both cases of adiabatic perturbations and CIPs. From this figure, we can see that CIPs affect C_ℓ^{yT}, C_ℓ^{yE}, and C_ℓ^{yy} and there is a possibility to detect CIPs with the y-distortion anisotropies.

3.2.2. Detecting CIP using y-distortions anisotropies

In this section we will investigate how well future CMB survey will constrain CIP models, exploiting the y-distortions anisotropies. To assess this we will produce Fisher forecasts for a PIXIE-like experiment [208], a PRISM-like experiment [209], for LiteBIRD [210] and for a Cosmic Variance Limited (CVL), very futuristic, experiment.

Before discussing the Fisher matrix analysis, we explain the $f_{\rm bi}$ dependence of the angular power spectra. For the CIPs, $\Theta_\ell^{(c)} S_{c\gamma} + \Theta_\ell^{(b)} S_{b\gamma} \approx 0$ is satisfied so that angular

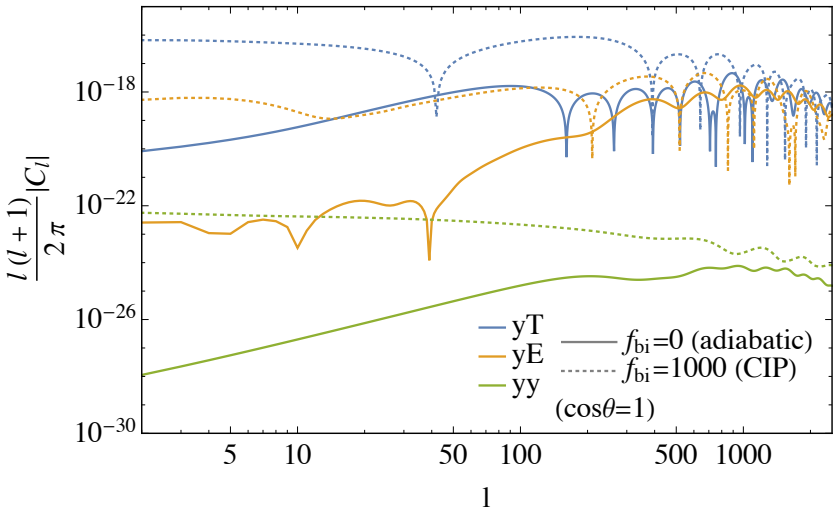

Figure 3.15.: $|C_\ell^{yT}|$, $|C_\ell^{yE}|$, and $|C_\ell^{yy}|$ in the case of adiabatic perturbations and CIP with $\cos\theta = 1$. Blue, orange, and green lines show $|C_\ell^{yT}|$, $|C_\ell^{yE}|$, and $|C_\ell^{yy}|$ and solid and dotted lines show the case of $f_{\rm bi} = 0$ (corresponding to adiabatic) and $f_{\rm bi} = 1000$ (corresponding to CIP), respectively. For example, the blue solid line shows $|C_\ell^{yT}|$ in the case of $f_{\rm bi} = 0$.

power-spactra do not have auto correlation of the CIPs in eq. (3.45) as follows:

$$C_\ell^{yT} \approx 4\pi \int \frac{dk}{k} \Big(\mathcal{P}_{\zeta\zeta}(k) y_\ell^{(\zeta)}(\eta_0, k) \Theta_\ell^{(\zeta)}(\eta_0, k) + \mathcal{P}_{c\zeta}(k) y_\ell^{(S_c)}(\eta_0, k) \Theta_\ell^{(\zeta)}(\eta_0, k) + \mathcal{P}_{b\zeta}(k) y_\ell^{(S_b)}(\eta_0, k) \Theta_\ell^{(\zeta)}(\eta_0, k) \Big), \tag{3.52}$$

$$C_\ell^{yE} \approx 4\pi \int \frac{dk}{k} \Big(\mathcal{P}_{\zeta\zeta}(k) y_\ell^{(\zeta)}(\eta_0, k) E_\ell^{(\zeta)}(\eta_0, k) + \mathcal{P}_{c\zeta}(k) y_\ell^{(S_c)}(\eta_0, k) E_\ell^{(\zeta)}(\eta_0, k) + \mathcal{P}_{b\zeta}(k) y_\ell^{(S_b)}(\eta_0, k) E_\ell^{(\zeta)}(\eta_0, k) \Big). \tag{3.53}$$

Using the angular power spectra for the adiabatic perturbations $C_{\ell,\rm ad}$ and those for the CIPs $C_{\ell,\rm CIP}$ at $f_{\rm bi}\cos\theta = 1$, the above expressions are simply written as

$$C_\ell^{yT} \approx C_{\ell,\rm ad}^{yT} + f_{\rm bi}\cos\theta\, C_{\ell,\rm CIP}^{yT}, \tag{3.54}$$

$$C_\ell^{yE} \approx C_{\ell,\rm ad}^{yE} + f_{\rm bi}\cos\theta\, C_{\ell,\rm CIP}^{yE}. \tag{3.55}$$

Thus, the angular power spectra linearly depend on the correlated CIPs. Figure 3.16 shows the $f_{\rm bi}\cos\theta$ dependence of $C_\ell - C_{\ell,\rm ad}$ in $\ell = 2$, $\ell = 300$, and $\ell = 700$. From this figure, we can see that $C_\ell - C_{\ell,\rm ad}$ is indeed proportional to $f_{\rm bi}\cos\theta$. Since the amplitudes of the $C_{\ell,\rm CIP}^{yT}$ and $C_{\ell,\rm CIP}^{yE}$ are proportional to the product of $f_{\rm bi}$ and $\cos\theta$, our analysis will not be independently sensitive to each of these parameters, but we can

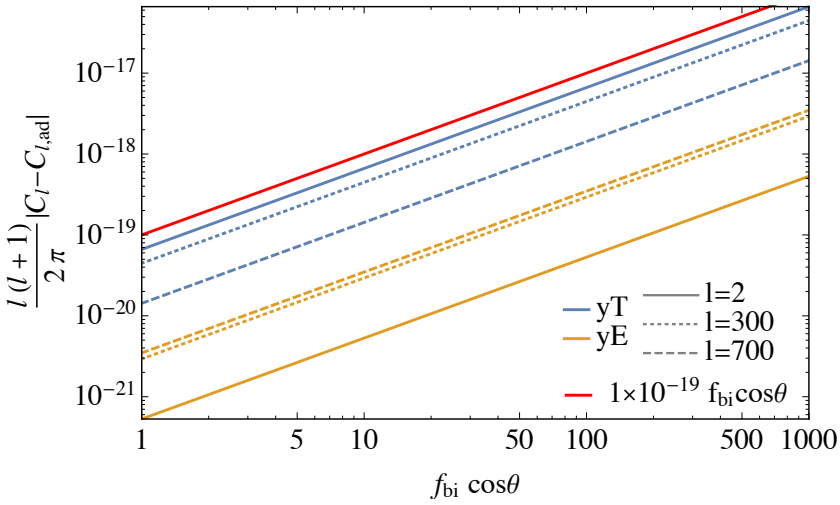

Figure 3.16.: f_{bi} dependences of $|C_\ell^{yT} - C_{\ell,\mathrm{ad}}^{yT}|$ and $|C_\ell^{yE} - C_{\ell,\mathrm{ad}}^{yE}|$. Blue and orange lines show $|C_\ell^{yT} - C_{\ell,\mathrm{ad}}^{yT}|$ and $|C_\ell^{yE} - C_{\ell,\mathrm{ad}}^{yE}|$ and solid, dotted and dashed lines show the case of $\ell = 2$, $\ell = 300$ and $\ell = 700$, respectively. For example, the blue solid line shows $|C_\ell^{yT} - C_{\ell,\mathrm{ad}}^{yT}|$ in the case of $\ell = 2$. For comparison, we also plot $1 \times 10^{-19} f_{\mathrm{bi}} \cos\theta$ with a red line.

test $f' \equiv f_{\mathrm{bi}} \cos\theta$. On the other hand, $C_{\ell,\mathrm{CIP}}^{yy}$ is quadratic in f_{bi} but is dominated by astrophysical contamination discussed below.

Fisher forecast

In the scope of our work, the Sunyaev-Zeldovich effect constitutes a foreground. Its power spectrum adds an important contribution to the variance of the CIPs-generated y-T and y-E cross correlation. We will show how masking resolved clusters [211, 212] can greatly improve the constraining capabilities of all future surveys. Moreover, the coupling of SZ effect with low redshifts sources of temperature (ISW) and polarization anisotropies could in principle bias the measurements of y-T_{CIP} y-E_{CIP}, and therefore needs to be properly accounted for [212]. Luckily, the spectral shapes of the signals and of the spurious secondary sources are not much correlated. Therefore marginalizing over them will not degrade the constraining power by much. As long as we consider the Gaussian universe, other sources of y-distortions — such as reionization, Silk damping — contribute negligibly to the total y-T and y-E cross correlations [212] therefore we will not consider them here. In the case of primordial non-Gaussianity, it has been shown that foregrounds can degrade the constraints obtained with naive Fisher forecast by a

factor $5 \sim 10$ [213]. Given the similarity of our analysis with the search for primordial non-Gaussianity, we might expect a similar effect. However, account properly for the galactic foregrounds would be beyond the (path-finding) scope of this thesis. Therefore we will neglect them completely in our analysis. For this reason our results will be one order of magnitude too optimistic.

In this case, to calculate the Fisher information matrix defined in eq. (2.14), we can use the eq. (2.25) that we report here for convenience

$$F_{ij} = f_{\rm sky} \sum_{\ell} (\mathbf{Cov}_\ell^{-1})_{\alpha\beta} \frac{\partial (\mathbf{Cov}_\ell)_{\beta\gamma}}{\partial p_i} (\mathbf{Cov}_\ell^{-1})_{\gamma\delta} \frac{\partial (\mathbf{Cov}_\ell)_{\delta\alpha}}{\partial p_j} \,, \tag{3.56}$$

where $f_{\rm sky}$ is the fraction of the sky covered by the survey, $\mathbf{Cov}_\ell$ is the covariance matrix of the observables and repeated matrix indices $(\alpha, \ldots, \delta)$ are summed. We will first discuss the results achieved considering only the cross correlation of y-distortions with temperature anisotropies (the same applies also to polarization). The same approach will be then extended to the joint analysis of the cross correlation with both temperature and polarization anisotropies. The covariance matrix of $(a^T_{\ell m}, a^y_{\ell m})$ reads

$$\mathbf{Cov}_\ell = \frac{1}{2\ell+1} \begin{pmatrix} C_\ell^{TT} & C_\ell^{yT} + C_\ell^{\rm SZT} \\ C_\ell^{yT} + C_\ell^{\rm SZT} & C_\ell^{yy} + C_\ell^{\rm SZSZ} + C_\ell^{yy,N} \end{pmatrix} , \tag{3.57}$$

where we have explicitly separated the primordial component of the y-distortions from the signal coming from the SZ effect. We have also considered its instrumental noise contribution $C_\ell^{yy,N}$.

In principle all the six standard cosmological parameters and f' need to be considered free parameters in the Fisher forecast. However the uncertainties on the cosmological parameters are so small compared with the one of f' that we consider them fixed to their true value when we calculate the temperature (and polarization) anisotropies. This is a safe choice since f' is completely orthogonal to the changes in TT, TE and EE [8]. Uncertainties on H_0, σ_8, and Ω_m have a much bigger impact on the SZ power spectrum. Moreover, the halo mass bias b, which is the parameter that links the spectroscopic mass of the halo with its true mass (lensing mass), introduces another source of uncertainty in the SZ auto and cross-correlations. As discussed in [121, 214–216], the effects of varying these parameters are degenerate, and, on low ℓ ($\lesssim 1000$), can be parametrized as a shift in the overall amplitude of the SZ power spectrum. Following [211], we will take into account the combined effect of these parameters by simply introducing an unknown

amplitude parameter α, in front of the SZ-spectra, and marginalizing over it. We will calculate the SZ auto- and cross-correlation used here in the following section. Using the covariance matrix eq. (3.57) in eq. (3.56) with eq. (3.54) , we can obtain the Fisher matrix for the parameters (f', α)

$$F_{ij} = f_{\rm sky} \sum_{\ell=2}^{\ell_{\rm max}} (2\ell+1) \begin{pmatrix} \frac{(C_{\ell,\rm CIP}^{yT})^2}{C_\ell^{TT}(C_\ell^{\rm SZSZ}+C_\ell^{yyN})} & \frac{C_\ell^{\rm SZT} C_{\ell,\rm CIP}^{yT}}{C_\ell^{TT}(C_\ell^{\rm SZSZ}+C_\ell^{yyN})} \\ \frac{C_\ell^{\rm SZT} C_{\ell,\rm CIP}^{yT}}{C_\ell^{TT}(C_\ell^{\rm SZSZ}+C_\ell^{yyN})} & \frac{(C_\ell^{\rm SZT})^2}{C_\ell^{TT}(C_\ell^{\rm SZSZ}+C_\ell^{yyN})} \end{pmatrix}. \tag{3.58}$$

To get this result we assumed that $(C_\ell^{\rm SZT})^2 \ll C_\ell^{\rm SZSZ} C_\ell^{TT}$, and $C_\ell^{yy} \ll C_\ell^{\rm SZSZ}$. This treatment can be trivially generalized to produce joint analysis of C_ℓ^{yT} and C_ℓ^{yE}, using the appropriate covariance matrix for $(a_{\ell m}^T, a_{\ell m}^E, a_{\ell m}^y)$:

$$\mathbf{Cov}_\ell = \frac{1}{(2\ell+1)} \begin{pmatrix} C_\ell^{TT} & C_\ell^{TE} & C_\ell^{yT} + C_\ell^{\rm SZT} \\ C_\ell^{TE} & C_\ell^{EE} & C_\ell^{yE} + C_\ell^{\rm SZE} \\ C_\ell^{yT} + C_\ell^{\rm SZT} & C_\ell^{yE} + C_\ell^{\rm SZE} & C_\ell^{yy} + C_\ell^{\rm SZSZ} + C_\ell^{yy,N} \end{pmatrix}. \tag{3.59}$$

The temperature and polarization auto- and cross-correlation can be easily computed with `CLASS` [109], whereas the SZ powerspectrum and cross correlation with temperature and polarization anisotropies can be calculated using the halo model we reviewed in Section 1.5.2, as we are going to do in the next section.

Sunyaev-Zeldovich

While CMB photons propagates towards us, their wavelength gets continuously blueshifted and redshifted by the fact that they fall and climb up the gravitational potential wells. In the Dark-Energy-dominated era gravitational potential inhomogeneities tends to decay, so a photon exiting a potential well doesn't get redshifted as much as it got blue shifted when it entered it. Similarly, a photon that has to firstly climb and then fall from a hill loses a net amount of energy in the process. It is then clear that this effect, called integrated Sachs-Wolfe (ISW) strongly correlates with any tracer of the gravitational potential inhomogeneity distribution, and in particular with tracers of the galaxy clusters, that tend to form inside gravitational wells. The tracer we are interested in is the (thermal) SZ effect. Photons can be up-scattered by hot electrons, that populate mostly the intergalactic medium of galaxy clusters as we anticipated in Section 1.3. The

correlation of those two observables has been studied in detail [125, 211, 217], and it is a cumbersome foreground for the signal generated by linear y-distortions.

To calculate the SZ we use a halo model approach as discussed in greater detail in Section 1.5.2. We use the halo bias given in table 2 of [218], the halo mass function of [119] with the updated parameters given in [218], and the halo Compton y-parameter measured in [124]. We also follow the prescription given in [214], using a single definition of mass ($M_{500,c}$) and interpolate the bias and halo mass function to the correct value. We remind the reader that the one- and two-halo terms, introduced in eq. (1.149) and eq. (1.150) respectively read

$$C_\ell^{1h} = \int \mathrm{d}z \frac{\mathrm{d}^2V}{\mathrm{d}z\,\mathrm{d}\Omega} \int \mathrm{d}M \frac{\mathrm{d}n}{\mathrm{d}M}(z,M)|\tilde{y}_\ell(z,M)|^2\,, \tag{3.60}$$

$$C_\ell^{2h} = \int \mathrm{d}z \frac{\mathrm{d}^2V}{\mathrm{d}z\,\mathrm{d}\Omega} D_+^2(z) P_m(k) \left[\int \mathrm{d}M \frac{\mathrm{d}n}{\mathrm{d}M}(z,M) b(z,M) \tilde{y}_\ell(z,M)\right]^2 \Bigg|_{k=\left(\frac{\ell+1/2}{\chi(z)}\right)}. \tag{3.61}$$

The SZ effect cross correlate with T through the late ISW effect, given by

$$\frac{\Delta T^{\mathrm{ISW}}}{T}(\hat{\boldsymbol{n}}) = -\frac{2}{c^2}\int \mathrm{d}z \frac{\mathrm{d}\phi}{\mathrm{d}z}(\chi(z)\hat{\boldsymbol{n}}, z). \tag{3.62}$$

In our numerical evaluation, we will use the full transfer functions, extracted from `CLASS` [109], which of course encode the ISW contribution. It is useful to define real space transfer functions [219, 220]

$$\mathcal{T}_\ell^T(\chi) = \frac{2}{\pi}\int \mathrm{d}k\, k^2 \mathcal{T}_\ell^T(k) j_\ell(\chi k)\,, \tag{3.63}$$

where $\mathcal{T}_\ell^T(k)$ is the full temperature transfer function. The multipolar coefficients can then be expressed as

$$a_{\ell m}^T = \int \mathrm{d}\chi\, \chi^2 \mathcal{T}_\ell^T(\chi) \zeta_{\ell m}(\chi)\,, \tag{3.64}$$

where $\zeta_{\ell m}(\chi) = \frac{(-i)^\ell}{2\pi^2}\int \mathrm{d}^3\boldsymbol{k}\, \zeta(\boldsymbol{k}) j_\ell(\chi k) Y_\ell^m(\hat{\boldsymbol{k}})$.

Using the Poisson equation, $\delta(\boldsymbol{k}, z) = \frac{3}{5}(\Omega_M H_0^2)^{-1}\frac{D(z)}{a(z)}\mathcal{T}_m(k)k^2\phi(\boldsymbol{k}, z=0)$, to express the overdensity contrast as a function of the gravitational potential we can write the

temperature-SZ cross correlation:

$$C_\ell^{\text{SZ-}T} = \int \frac{c\,\mathrm{d}z}{H(z)} \frac{3}{5} \frac{c^2 k^2 \chi^2(z) \mathcal{T}_m(k)}{\Omega_m H_0^2} D_+(z) \int \mathrm{d}M \frac{\mathrm{d}n}{\mathrm{d}M}(z,M) \tilde{y}_\ell\Big(z,M) b_H(z,M) \times \\ \times \mathcal{T}_\ell^T(\chi(z)) P_\zeta(k)\Big|_{k=\left(\frac{\ell+1/2}{\chi(z)}\right)}. \tag{3.65}$$

Notice that one can write the same quantity for polarization just replacing $T \to E$ in the last two equations, *i.e.*, using the appropriate transfer functions. In much smaller terms, the SZ effect also correlates with E. The reason is that after reionization the universe remains ionized and therefore free electrons generate polarization anisotropies even at very low redshift. SZ is generated in the same epoch on similar scales, so this gives rise to a non-vanishing y-E. This is expected to be a very small effect at low redshifts, but we consider it as it might still constitute a sizeable bias if the primordial signal is small too.

Even though, practically, all the SZ signal comes from $z < 4$ [126], since E is sourced at reionization we extend all the redshift integrations to z well above the time of reionization. As expected, the contributions from $z > 4$ are negligible.

3.2.3. Bias, variance, and Fisher results

We now have all the ingredients to calculate numerically the Fisher matrix for T and E (separately), eq. (3.58), and for the joint analysis of T and E, eq. (3.59).

All the results that we will present are obtained marginalizing over α, that is the amplitude of the SZ-T and SZ-E cross correlations. However it is worth noticing that marginalizing over α do not degrade the constraints on f' by much. To quantify this statement we calculate the correlation between the two parameters. Those are

$$\frac{\left[\sum_\ell \frac{\partial C_\ell^{yT}}{\partial f'} \frac{\partial C_\ell^{\text{SZ}T}}{\partial \alpha}\right]}{\sqrt{\left[\sum_\ell \left(\frac{\partial C_\ell^{yT}}{\partial f'}\right)^2\right]\left[\sum_\ell \left(\frac{\partial C_\ell^{\text{SZ}T}}{\partial \alpha}\right)^2\right]}} = 0.28, \quad \frac{\left[\sum_\ell \frac{\partial C_\ell^{yE}}{\partial f'} \frac{\partial C_\ell^{\text{SZ}E}}{\partial \alpha}\right]}{\sqrt{\left[\sum_\ell \left(\frac{\partial C_\ell^{yE}}{\partial f'}\right)^2\right]\left[\sum_\ell \left(\frac{\partial C_\ell^{\text{SZ}E}}{\partial \alpha}\right)^2\right]}} = 0.53. \tag{3.66}$$

In the limit of 0 correlation, omitting $f_{\rm sky}$ and considering only the temperature anisotropies, the signal-to-noise ratio (SNR) for the parameter f' would have been

$$\mathrm{SNR}(f') \approx \sqrt{\sum_\ell \frac{(C_\ell^{yT})^2}{C_\ell^{TT}(C_\ell^{\rm SZSZ} + C_\ell^{yyN})}}\,. \tag{3.67}$$

We are not using this approximate formula in the analysis, but it is useful to clarify the methodology. Since we do not have any control over the signal, the only way to increase the SNR is to try to minimize the noise. The temperature anisotropies measurements are already dominated by cosmic variance up to very high multipoles. The variance of the y-distortions is instead composed by two contributions: the cosmic variance term and the instrumental noise. We consider different experimental setup to understand what is the sensitivity needed by future experiments to reach the lower limit imposed by cosmic variance. The noise term is $C_\ell^{yy,N} = 4\pi \times N \times e^{\ell^2/\ell^2_{\rm beam}}$; where $(N, \ell_{\rm beam})$ is $(0, -)$ for the CVL survey, $(4\times10^{-18}, 84)$ for PIXIE, $(4\times10^{-20}, 100)$ for the PRISM spectrometer (PRISM spec) and $(4\times10^{-20}, 4000)$ for the PRISM imager, which could be easily calibrated using the on-board spectrometer but is not bounded by low angular resolution [10, 212, 221]. Since we are interested in differential measurements of y distortions, the LiteBIRD satellite can also be employed [210]. Differential measurements of small signals still rely on very precise inter-channel calibration of the instrument that will probably be challenging if not unfeasible without a calibrator on board [221]. This point is even more crucial if we consider that component separation will be required to discern the foregrounds. As shown in [213], the calibration relative errors must be of order 0.01% in order to recover the correct μ-T cross correlation. However, assessing correctly the effect of inter-channel calibration error is beyond the scope of this thesis. Instead, we use two different noise levels for LiteBIRD: an optimistic estimate (Opt) assuming perfect inter-channel calibration $(2\times10^{-20}, 200)$ and a more conservative (Cons) estimate discussed below. From [213], we can assess that the ratio of the PIXIE and LiteBIRD noise contribution (neglecting all foregrounds) to $C_\ell^{\mu\mu}$ is $C_\ell^{\mu\mu,\ \rm Noise,\ LiteBIRD}/C_\ell^{\mu\mu,\ \rm Noise,\ PIXIE} = 0.06$. Here we assume that the noise contribution to C_ℓ^{yy} follows the same scaling for the two experiments. Therefore, the parameters we use for LiteBIRD - Cons are $(0.24\times10^{-18}, 200)$, though we acknowledge that this is a very coarse, order-of-magnitude, estimate. However, any finer estimate would be beyond the intrinsic uncertainties of a Fisher matrix analysis. Moreover, our result will not be very sensitive to this parameter because it does not affect the other major contribution to the noise: the SZ effect.

Survey	Clusters masked
Unmasked	None
eROSITA	$M > 2 \times 10^{14} M_\odot/h$ for $z < 0.15$
PRISM	$M > 10^{13} M_\odot h^{-1}$

Table 3.5.: We assume to use each survey to mask all clusters with the given characteristics.

Since the dominant contribution to the SZ power spectrum is given by big galaxy clusters at low redshift [121], masking resolved clusters is a viable way to reduce the overall noise [126, 211, 212]. Following the procedure we outlined in Ref. [212], we consider the use of two different sky masks based on two different full sky surveys that will produce maps of galaxy clusters. We will present the forecasts based on the PIXIE-like and LiteBIRD satellite both for the unmasked case and with a mask based on eROSITA [222] expected performance. We will assume to mask all the clusters with mass greater than $2 \times 10^{14} M_\odot/h$ at $z < 0.15$. The forecast for PRISM and the CVL instrument will similarly involve the unmasked case, and a mask based on the expected PRISM cluster catalogue. We will assume to mask all the clusters with mass greater than $10^{13} M_\odot h^{-1}$. We chose those regions of the mass-redshift plane because the eROSITA and PRISM catalogues are expected to be complete in those respective areas. We summarize the mask boundaries in Table 3.5.

In our analysis we account for the effect of masking the galactic plane and resolved cluster according with eq. (3.56). For PIXIE, LiteBIRD, and PRISM, we assume to use an $f_{\rm sky}$ similar to the one used by *Planck* to calculate the SZ power spectrum [121], namely $f_{\rm sky} = 50\%$ to remove the galactic plane. To account for the reduced sky area after applying the eROSITA and PRISM mask, we reduce $f_{\rm sky}$ to 35%. According with [212], this is a conservative estimate for both cluster masks. In the case of the CVL survey we show the results assuming $f_{\rm sky} = 100\%$, since they have to be intended as upper limits that might in principle be reached with other techniques that we are not investigating here.

In Figure 3.17 we show the 1σ forecasted error bars on f' as a function of the max ℓ considered. The same results are summarized in Table 3.6. There we assume the use of all the multipoles available in each experimental configuration, i.e., to relate these results with Figure 3.17 one has to take $\ell_{\rm max} \gg \ell_{\rm beam}$. We notice that for the linearity of $C_\ell^{yT(E)}$ with respect to f', the forecasted error bars are independent from the chosen f' fiducial value. As it is clear from Figure 3.17, none of the experimental setups is

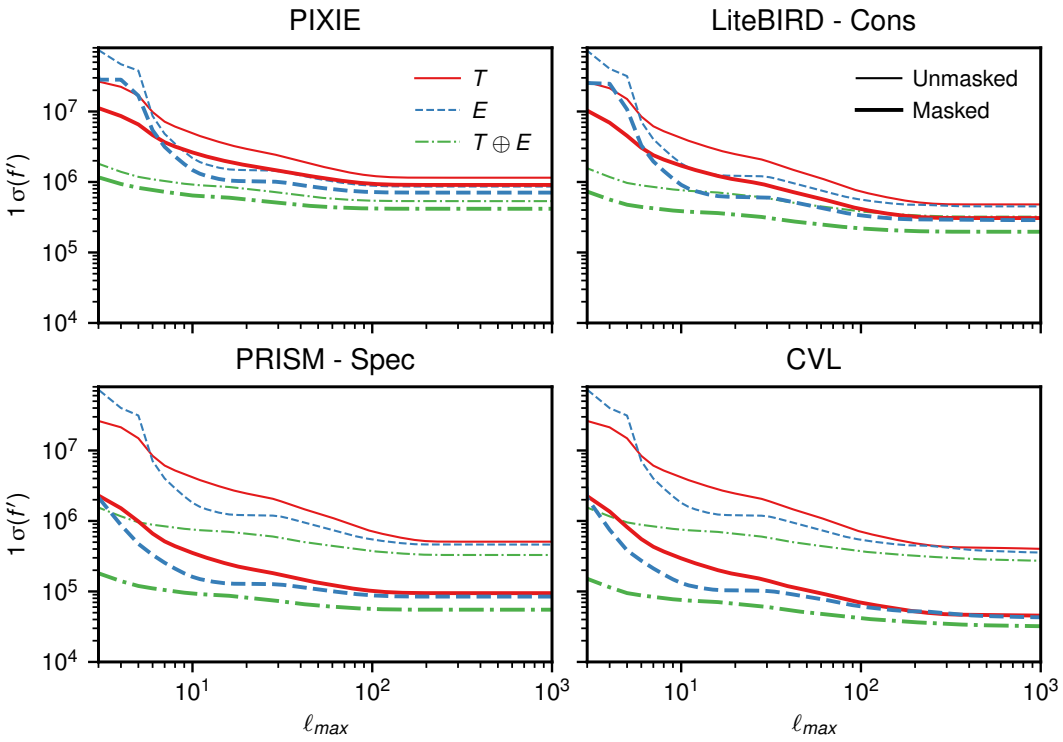

Figure 3.17.: Forecasted 1 σ error on f'. We compare the different experimental setup, and evaluate their performance both masking and not-masking the most massive clusters in the y-distortions map. We consider the cross correlation with temperature and polarization anisotropies, taken one at a time and analyzed jointly. We consider the mask based on eROSITA for PIXIE and LiteBIRD, and the one based on PRISM for PRISM itself and the CVL experiment.

bounded by raw detector sensitivity. The two main limiting factors are the SZ power spectrum — more and more aggressive masks give better results — and the survey beam. Since the primordial signal increases as ℓ increases, it is convenient to exploit the higher multipoles to extract some degree of information. Trying to exploit relatively high multipoles ($\ell \approx$ few hundreds) is beneficial also for an instrument with higher detector sensitivity than PIXIE. The PRISM imager has much higher angular resolution than the on-board spectrometer. It is therefore possible to envision its use to make differential measurements of the spectral distortion anisotropies up to small angular scales. In this case uncertainties in the inter-channel calibration would not be a problem, since the spectrometer can provide a reference spectrum. If we consider the use of the imager to achieve higher angular resolution, PRISM will basically reach the limit set by cosmic variance.

	Unmasked			eROSITA mask		
	T	E	$T \oplus E$	T	E	$T \oplus E$
PIXIE	11×10^5	8.6×10^5	5.3×10^5	9.1×10^5	7.1×10^5	4.2×10^5
LiteBIRD - Opt	4.3×10^5	4.0×10^5	2.9×10^5	2.5×10^5	2.4×10^5	1.7×10^5
LiteBIRD - Cons	4.8×10^5	4.5×10^5	3.2×10^5	3.1×10^5	2.9×10^5	2.0×10^5
	Unmasked			PRISM mask		
PRISM - spec	5.1×10^5	4.6×10^5	3.3×10^5	9.5×10^4	8.5×10^4	5.5×10^4
PRISM - imager	4.1×10^5	3.6×10^5	2.8×10^5	7.0×10^4	6.7×10^4	4.7×10^4
CVL	2.8×10^5	2.5×10^5	1.9×10^5	3.0×10^4	2.9×10^4	2.2×10^4

Table 3.6.: 1σ forecasted error bars on f'. T, E, and $T \oplus E$ indicate respectively the forecast using temperature, polarization, and both. In all the forecasts we marginalize over the amplitude of $C_\ell^{\mathrm{SZ}T}$ and $C_\ell^{\mathrm{SZ}E}$.

3.2.4. Discussion

In this section, we provided a new framework to calculate the linear fluctuation of the spectral y-distortions. It was shown that a solution to the Boltzmann equation for the Compton scattering can be constructed from 4 parameters including the temperature perturbation and the spectral y-distortion. Then we derived the evolution equation for the y-distortion, which is sensitive to the baryon isocurvature perturbations. This implies that it can resolve the degeneracy between baryon isocurvature perturbations and the CDM ones in contrast to the standard linear perturbations such as the temperature perturbations and the polarizations. We numerically estimated the transfer function of the y-distortions based on `CLASS` and computed the auto and the cross correlations with the temperature perturbations and the polarization E modes. The resulting C_ℓ's completely resolve the degeneracy between baryon isocurvature perturbations and the CDM isocurvature perturbations as we expected, and we found that only the correlated CIPs contribute to them. The auto correlation of the spectral y-distortions is strongly contaminated by SZ power spectrum and therefore we could not get any information on the f_{bi} parameter alone from it. Note that linear y anisotropies are not contaminated by lensing effect in contrast to the previous methods based on the nonlinear modulation of the CMB anisotropy. Then we produced a forecast for the upper bounds on correlated CIPs for different future observational projects. While we carefully consider the contamination induced by SZ effect in our analysis, we are neglecting other foregrounds, because properly accounting for would go beyond the path-finding scope of this thesis; and because their impact would highly depend on the various methods of component separation chose to

analyze data. Even in the absence of foregrounds, none of the surveys we consider will be able to set stringent constraints on CIPs. For instance, $f' < 2 \times 10^5$ at 68% C.L. is obtained for LiteBIRD, while $f' < 5 \times 10^4$ for PRISM, and $f' < 2 \times 10^4$ for a cosmic variance limited survey. As we have shown, the fundamental limit is set by the noise contribution due to the SZ power spectrum. However it is important to remember that our method can resolve the degeneracy between the correlated and uncorrelated CIPs. This implies that we can in principle distinguish the correlated and uncorrelated CIPs by combining our analysis with the other methods discussed before. Our method would be more useful if more powerful techniques were developed to remove the SZ-induced noise term in the future.

We do not focus on the specific models that produce the CIPs in this section. As discussed in Ref. [186], models based on the curvaton only produce CIPs as big as $f_{\rm bi} < 16$, while the spontaneous baryogenesis in Ref. [187] does not generate the correlated CIPs. Therefore, the known scenarios do not expect huge f', which we may observe in our method; nevertheless, it would be interesting as the author in Ref. [191] reported the possibility of sizeable CIPs. In other words, highly non trivial early universe physics would be suggested if significant CIP were detected.

In our calculations we dropped $\mathcal{O}(\delta^3)$ terms for simplicity, but these may have comparable contributions to the spectral distortions for the Gaussian adiabatic perturbations. Therefore, cumbersome cubic order analysis would be required if the sizeable linear y-distortions are really detected in the future. We did not discuss the κ distortion and the u distortion, which is introduced for the first time in this section, because they do not explicitly depend on the baryon isocurvature perturbations. Still it would be interesting to consider the anisotropy of these new spectral distortions in different contexts. This would be investigated in our future works.

Chapter 4.

Testing the bispectrum

4.1. Primordial non-Gaussianity and spectral distortions anisotropies

At present, the tightest constraints on all parametrizations and models of primordial non-Gaussianity (NG) come from measurements of the bispectrum (Fourier transform of the 3-point function in configuration space) of Cosmic Microwave Background temperature and polarization anisotropies (respectively T and E), made by the *Planck* satellite [3].

As we have already stated in Section 1.4.4, among many aspects and applications of these constraints, a very important one is the possibility to set stringent bounds on inflationary scenarios characterized by more than one field. Multi-field Inflation in fact predicts a potentially detectable bispectrum of the local type, peaking in the squeezed-limit. We recall that such bispectrum explicitly reads (cfr. eq. (1.86))

$$B(k_1, k_2, k_3) = -\frac{6}{5} f_{\rm NL}^{\rm loc} \left[P(k_1)P(k_2) + 2 \text{ perm.} \right], \tag{4.1}$$

where $f_{\rm NL}^{\rm loc}$ is the dimensionless local NG amplitude parameter, which is measured by fitting the local shape to the data (since we will consider only local NG in the following, we will omit the superscript "loc" from now on). Currently, *Planck* constrains $f_{\rm NL} = 0.8 \pm 5.0$ (68% C.L.) [3]. A crucial threshold to fully distinguish single from multi-field scenarios would be however $f_{\rm NL} \sim 1$. This value is in fact a lower bound for a large class of multi-field models (e.g. curvaton [83]). Unfortunately there are not enough modes in the CMB temperature and polarization angular bispectra to achieve enough sensitivity for a clear detection of $f_{\rm NL} \sim 1$, even assuming a perfectly noiseless, ideal survey (see, e.g. [223]).

Several new observational strategies will therefore have to be implemented in the future. One of the most promising approaches in the near future involves measuring NG signatures in the galaxy bias, using forthcoming Large Scale Structure surveys [224, 225].

In a more futuristic scenario, the authors of [9] have considered the cross-correlation between CMB temperature and μ-spectral distortion *anisotropies* as a potentially very powerful probe of squeezed-type bispectra. An experiment producing cosmic-variance limited T and μ maps could in principle be able to detect $f_{\rm NL} \sim 10^{-2}$, 10^{-3} (this argument has been extended in different ways [10, 211, 221, 226–233], to take into account different primordial bispectrum models and higher-order correlation functions). While fascinating, this scenario is out of reach not only with current experimental noise levels, but also taking into account proposed, ambitious next generation surveys, such as PRISM [10].

Nonetheless, measurements of $f_{\rm NL}$ via correlations between CMB temperature (polarization) and CMB distortion anisotropies are interesting even before achieving such exquisite levels of sensitivity, as they allow to test possible deviations of $f_{\rm NL}$ from scale independence. In this respect, not only μ, but also y-distortions can provide useful and interesting information, as pointed out in [10]. Indeed, while *Planck* measured $f_{\rm NL}$ on the scales typical of CMB T, E anisotropies ($k \lesssim 0.15$ Mpc^{-1}), and μ-distortion anisotropies can in principle probe it on much smaller scales (46 Mpc$^{-1} \lesssim k \lesssim 10^4$ Mpc^{-1}), y-distortions allow probing the transition between those two regimes (0.15 Mpc$^{-1} \lesssim k \lesssim 46$ Mpc^{-1}). The issue with using y-distortions is, however, that the total signal is affected by contributions from secondary sources, which completely dominate over the primordial component. The most important source of contamination is the y-T signal generated by the correlation between the Integrated Sachs Wolfe (ISW) and Sunyaev-Zeld'ovich (SZ) effects. This problem has been initially addressed for the y-T cross-correlation in [211], where a cosmic-variance limited experiment was considered, and the SZ contamination was reduced by masking detected clusters at low redshift.

In this section, we will extend previous analyses by considering not only y-T, but also including the cross-correlation with polarization, y-E, and by exploiting cross-correlations between SZ and external tracers (CMB and galaxy lensing). Aside from adding a new signal, using polarization presents the clear advantage of giving a much less biased signal, since the E-mode correlate less than T with the SZ effect. Nevertheless, in this case we will have to worry about potential spurious contamination from reionization. An explicit numerical evaluation, using second-order transfer functions from the Boltzmann

integrator `SONG` [234–236] will show that this is negligible.[1] The correlation between SZ and lensing can instead be used to estimate a template of the y-parameter map generated by SZ, which can then be subtracted from the data, in order to partially remove spurious SZ contributions from unresolved clusters and reduce the noise. We will consider a PIXIE-like [208], PRISM-like [209] and an ideal, cosmic-variance limited experiment, and show how including these new ingredients can lead to interesting improvements in the final forecasts, by an overall factor between 2.5 and 4.4 depending on the experiment and on the mask applied.

While we will focus mostly on y-distortions, we will also extend previous μ-distortions/ E-polarization cross-correlation analyses. Specifically, we will re-analyse in detail the μ-E cross-spectrum initially discussed in [233], where only large scales and reionization contributions to the CMB polarization transfer functions were included. In that case, it was found that μ-E does not provide any further constraining power with respect to μ-T. By considering all scales and using full transfer functions we will show that μ-E performs slightly better than μ-T and combining the two leads to $\sim 30\%$ improvement in the final constraints.

Even though we are interested in a $f_{\rm NL} = f_{\rm NL}(k_1, k_2, k_3)$, which depends on scale, we will follow [10, 211] to assume that the scale-dependence is such that $f_{\rm NL}$ stays approximately constant (separately) on both the y-scales ($0.15\ {\rm Mpc}^{-1} \lesssim k \lesssim 46\ {\rm Mpc}^{-1}$) and the μ-scales ($46\ {\rm Mpc}^{-1} \lesssim k \lesssim 10^4\ {\rm Mpc}^{-1}$). As discussed in [10] the constraints on $f_{\rm NL}$ from y-distortions (μ-distortions) can then be interpreted as a constraint on $f_{\rm NL}(k)$ evaluated at the logarithmic mid-point value over the y (μ) scales: $f^y_{\rm NL} \equiv f_{\rm NL}(7\ {\rm Mpc}^{-1})$ and $f^\mu_{\rm NL} \equiv f_{\rm NL}(740\ {\rm Mpc}^{-1})$ respectively for y- and μ-distortions.

The section is organized as it follows: In subsection 4.1.1 we will calculate the primordial contributions to the cross correlation of T and E with μ- and y-spectral distortions. in subsection 4.1.2 we will calculate the secondary sources for the T and E cross correlations with y — we recall that μ does not have cosmological secondary sources. In subsection 4.1.3 and 4.1.4 we will forecast $f^\mu_{\rm NL}$ and $f^y_{\rm NL}$ constraints, achievable by a PIXIE-like, a PRISM-like, and by a cosmic-variance limited survey, considering all sources of noise and contamination, different masks for resolved clusters (based on future X-ray and CMB surveys) and different external tracers for unresolved contributions. In subsection 4.1.5 we will summarize our conclusions.

[1] `https://github.com/coccoinomane/song`.

4.1.1. Primordial contributions

In this subsection we review the calculation to obtain the cross-correlation of CMB temperature and polarization anisotropies with μ- or y_p-CMB-spectral-distortions anisotropies, when primordial NG is present. Since secondary sources generate y-distortion in the late universe we indicate with y_p the primordial contribution to the total y.

As shown in eq. (1.116), that we repeat here for convenience, the primordial primordial curvature perturbation $\zeta(\boldsymbol{k})$ and CMB fluctuations are linked via

$$a^X_{\ell m} = 4\pi i^\ell \int \frac{\mathrm{d}^3\boldsymbol{k}}{(2\pi)^3} \mathcal{T}^X_\ell(k) Y^{m*}_\ell(\hat{\boldsymbol{k}})\zeta(\boldsymbol{k}), \tag{4.2}$$

where $X = T, E$ indicate the temperature T or the E-mode polarization, and $\mathcal{T}^X_\ell$ is the radiation transfer function. We will use the full transfer function generated by `CLASS` [109]. For $\Xi = \mu$-, y_p-type spectral distortions the analogous relation reads instead [221, 232]

$$\begin{aligned} a^\Xi_{\ell m} = 4\pi(-i)^\ell \int \frac{\mathrm{d}^3\boldsymbol{k_1}}{(2\pi)^3}\frac{\mathrm{d}^3\boldsymbol{k_2}}{(2\pi)^3}\,\mathrm{d}^3\boldsymbol{k_3}\delta^{(3)}(\boldsymbol{k_1}+\boldsymbol{k_2}+\boldsymbol{k_3}) \\ Y^{m*}_\ell(\hat{\boldsymbol{k}}_{\boldsymbol{3}}) j_\ell(k_3 r_{\rm ls}) f^\Xi(k_1,k_2,k_3)\zeta(\boldsymbol{k_1})\zeta(\boldsymbol{k_2}), \\ f^\mu(k_1,k_2,k_3) = 2.3\; W\left(\frac{k_3}{k_D(z_{\mu y})}\right)\left[e^{-(k_1^2+k_2^2)/k_D^2(z)}\right]^{z_\mu}_{z_{\mu y}} \\ f^y(k_1,k_2,k_3) = 0.4\; W\left(\frac{k_3}{k_D(z_y)}\right)\left[e^{-(k_1^2+k_2^2)/k_D^2(z)}\right]^{z_{\mu y}}_{z_y}. \end{aligned} \tag{4.3}$$

Here $r_{\rm ls}$ is the comoving distance to last scattering surface, $W(x) = 3j_1(x)/x$, and k_D is the diffusion damping scale evaluated at the beginning of the μ-era $k_D(z_\mu) \approx 12000$ Mpc^{-1}, at the μ-y transition $k_D(z_{\mu y}) \approx 46$ Mpc^{-1}, and at the end of the y-era $k_D(z_y) \approx 0.15$ Mpc^{-1} [10]. As said, we consider $f_{\rm NL}$ constant on μ- and y-scales: $f_{\rm NL}(k) \equiv f^y_{\rm NL}$ for 0.15 Mpc$^{-1} \lesssim k \lesssim 46$ Mpc^{-1} and $f_{\rm NL}(k) \equiv f^\mu_{\rm NL}$ for 46 Mpc$^{-1} \lesssim k \lesssim 12000$ Mpc^{-1}.

More accurate expressions for the transfer function have been discussed in [237]. We will use the simpler approximations in eq. (4.3), but with two adjustments. We will re-normalize the amplitude of the expected monopoles of μ- and y-distortion to the values computed in [238], $\langle\mu\rangle = 2.3\times10^{-8}$ and $\langle y\rangle = 4.2\times10^{-9}$. Moreover we will add to the cross correlation the factor $\exp[-15k^2/(8k_D^2(z_{\rm rec}))]$, where $k_D^2(z_{\rm rec})$ is the damping scale at recombination, which account the damping of power by photon diffusion, and which was introduced in [237]. This "zero-order" approximation is accurate enough for a Fisher forecast and allow a simple, direct comparison with other results in the literature.

The cross-correlation can be found as:

$$\left\langle a^X_{\ell m} a^{\Xi *}_{\ell' m'} \right\rangle = 8\ \delta^{\ell'}_{\ell}\, \delta^{m'}_{m} \int \frac{k^2\,\mathrm{d}k}{2\pi^2} \mathcal{T}^X_\ell(k) j_{\ell'}(kr_{\rm ls}) e^{-\frac{15k^2}{8k^2_D(z_{\rm rec})}} \int \frac{q_1^2 q_2^2\,\mathrm{d}q_1\,\mathrm{d}q_2}{2\pi^2} f^{\Xi}(q_1,q_2,k) B(k,q_1,q_2) \int x^2\,\mathrm{d}x j_0(q_1 x) j_0(q_2 x) j_0(kx). \tag{4.4}$$

In [231] it has been discussed how the generation mechanism for μ via acoustic dissipation, encoded in the $f^\mu(q_1,q_2,k)$ function, strongly selects squeezed configuration $k_1 \approx k_2 \gg k$ in the T-μ correlation. The same argument holds for the E-μ cross-correlation. Since the diffusion damping scale of y_p is much smaller than the μ one, the same approximation is less accurate in the X-y_p cross-correlations. However it should be noted that the more accurate transfer function provided in [237] explicitly suppress configuration with too different q_1 and q_2. This means that also when using y-distortions we are allowed to take the squeezed limit $k_1 \approx k_2 \gg k$.

In the squeezed limit, eq. (4.4) reduces to

$$C_\ell^{X\Xi} \approx -4\pi \frac{12}{5} \int \frac{k^2\,\mathrm{d}k}{2\pi^2} \mathcal{T}^X_\ell(k) j_{\ell'}(kr_{\rm ls}) P(k) e^{-\frac{15k^2}{8k^2_D(z_{\rm rec})}} \int \frac{q_1^2\,\mathrm{d}q_1}{2\pi^2} f^{\Xi}(q_1,q_1,k) P(q_1). \tag{4.5}$$

Notice that the last integral in this equation is exactly the definition of the monopole of the Ξ-type spectral distortion. Thus, renormalizing the $\langle\mu\rangle$ and $\langle y\rangle$ to the right vale as discussed above translate linearly into a renormalization of the C_ℓ [10].

In figure 4.1 we show the cross-correlations between μ- or y_p-distortion, and T or E anisotropies. The prediction for μ-T is in good agreement with [231].[2] Only the primordial contribution to the cross-correlations is shown in the plot, even though other effects contribute to the same signals. We are going to consider them in the next subsection, since those secondary sources will constitute foregrounds to these primordial signal.

[2]The tiny differences come from the fact that in the present section we are using a different and independent numerical implementation of the calculation. As a sanity check we verified that the C_ℓ^{TT} and C_ℓ^{EE} calculated with the our code match the same `CLASS` results up to its accuracy.

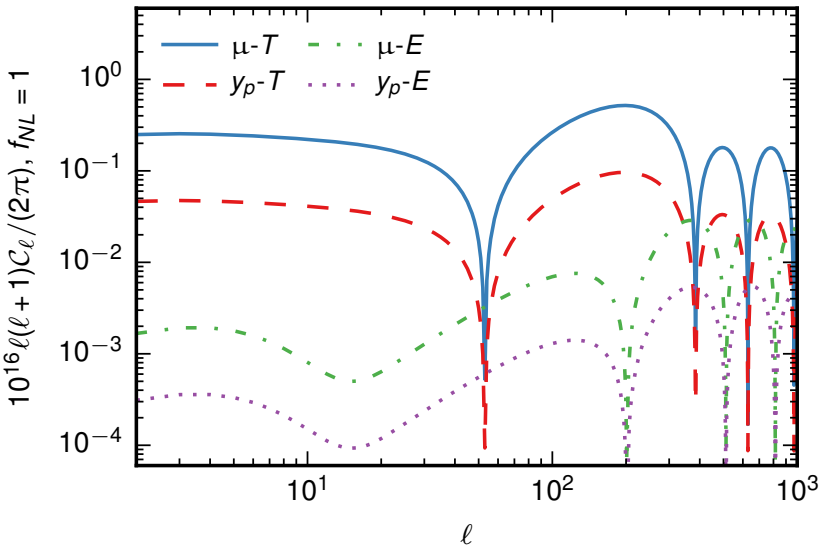

Figure 4.1.: Absolute value of the cross-correlations. The prediction for μ-T is in good agreement with [231].

4.1.2. Secondary sources

In this subsection we will consider the main non-primordial contributions to the y-T and y-E spectra, namely the cross-correlation between Sunyaev-Zeldovich and the integrated-Sachs-Wolfe effect, for y-T, and the cross correlation between CMB polarization and the quadratic Doppler effect, for y-E.

Sunyaev-Zeldovich

The cross-correlation of temperature and y-distortions is far from negligible even in the Gaussian case. As discussed in Section 3.2.2, the SZ-ISW cross correlation constitute an important foreground for this type of analysis that is always present. We use the formalism described there to calculate the SZ power spectrum and cross correlation with T and E. In this application we consider the bias given in table 2 of [218], the halo mass function of [119] with the updated parameters given in [218], and the halo Compton y-parameter computed in [122]. As a lower integration limit we choose $z > 0.02$; this ensure that the redshift integrals do not get contributions from unphysical $z = 0$ objects. We also integrate over the masses $10^{10} M_\odot h^{-1} < M < 10^{16} M_\odot h^{-1}$. We checked our spectra against those shown in [126], changing our integration boundaries to match their choices, and we are in very good agreement.

As previously mentioned, one of the main goals of this section is to study the $f_{\rm NL}$ dependence in the y-E cross-correlation spectrum, which was not accounted for in previous works [125, 211, 217] on the subject. One of the main advantages of using y-E in place of, or in combination with, y-T, is that contamination from SZ is expected to be strongly suppressed for y-E, therefore the main source of bias that afflicts y-T-based measurements of $f_{\rm NL}$ [211] would be eliminated. While much smaller than the y-T contribution, a non-primordial y-E correlation is still present: after reionization the quadrupole of free electrons still acts as a source of E. SZ is generated in the same epoch on similar scales, so this gives rise to a non-vanishing y-E. This is expected to be a very small effect at low redshifts. However, also the primordial y_p-E signal we are after is very small, therefore, it is important to explicitly compare the two effects.

y-distortion from reionization

Another source of contamination comes from the cross-correlation of E with the quadratic Doppler effect (see [239, 240] and references therein). Being proportional to the velocity of the baryons squared, this observable tracks the primordial density squared $y_{\rm reio} \sim \zeta(k)^2$. It is then clear that its cross-correlation with first order CMB polarization anisotropies is proportional to the primordial bispectrum $C_\ell^{y_{\rm reio}\text{-}E} \propto \left\langle \zeta(\boldsymbol{k_1})\zeta(\boldsymbol{k_2})\zeta(\boldsymbol{k_3}) \right\rangle$. However, we neglect this potential contribution to the signal here, leaving its study for future work, and focus instead on spurious, non-primordial contamination, which need to be removed from the primordial y-E contribution at recombination.

To simplify the notation we will omit "C_ℓ" in defining cross-correlations (i.e., $y_{\rm reio}\text{-}E \equiv C_\ell^{y_{\rm reio}\text{-}E}$) and we will indicate the n-th order term of a quantity with an apex "(n)", i.e., $E^{(n)}$.

Assuming perfectly Gaussian primordial perturbations, the leading term of the quadratic Doppler effect-Polarization cross-correlation is of fourth order in the primordial density perturbation: $y_{\rm reio}\text{-}E = y^{(2)}_{\rm reio}\text{-}E^{(2)} + y^{(3)}_{\rm reio}\text{-}E^{(1)} + \mathcal{O}(\zeta^6)$. We expect the second addendum to be of the same order of the first. Calculating it would require developing new formalism to describe higher-order-contributions to spectral distortions. Since, as we anticipate, we found after a complete calculation that the first term is negligible, we neglect the calculation of the second.

The authors of [239] provide an analytic expression for $y^{(2)}_{\rm reio}$. The second order transfer function for CMB polarization anisotropies can instead be obtained numerically, using the publicly available code `SONG` [234–236].

Let's consider a perturbation field X that can be written as an expansion over the primordial density perturbation field ζ. Up to second order, in term of its linear $\mathcal{T}^{(1)}_{X\,\ell m}$ and second order $\mathcal{T}^{(2)}_{X\,\ell m}$ transfer functions the field projection on the sphere can be written as [236]

$$a^X_{\ell m}(\boldsymbol{k}) = \mathcal{T}^{(1)}_{X\,\ell m}(\boldsymbol{k})\zeta(\boldsymbol{k}) + \int \frac{\mathrm{d}^3\boldsymbol{q_1}\,\mathrm{d}^3\boldsymbol{q_2}}{(2\pi)^3}\delta^{(3)}(\boldsymbol{k}-\boldsymbol{q_1}-\boldsymbol{q_2})\mathcal{T}^{(2)}_{X\,\ell m}(\boldsymbol{q_1},\boldsymbol{q_2},\boldsymbol{k})\zeta(\boldsymbol{q_1})\zeta(\boldsymbol{q_2}) + ... \tag{4.6}$$

In full generality, the cross-correlation of the second order contributions of two field X and Y will be

$$\begin{aligned}\left\langle a^{X(2)}_{\ell m} a^{Y(2)}_{\ell' m'}\right\rangle = \int \frac{\mathrm{d}^3\boldsymbol{k_1}}{(2\pi)^3}\int\frac{\mathrm{d}^3\boldsymbol{q_1}\,\mathrm{d}^3\boldsymbol{q_2}}{(2\pi)^3}\mathcal{T}^{(2)}_{X\,\ell m}(\boldsymbol{q_1},\boldsymbol{q_2},\boldsymbol{k_1})\delta^{(3)}(\boldsymbol{k_1}-\boldsymbol{q_1}-\boldsymbol{q_2})\\ \int \frac{\mathrm{d}^3\boldsymbol{k_2}}{(2\pi)^3}\int\frac{\mathrm{d}^3\boldsymbol{p_1}\,\mathrm{d}^3\boldsymbol{p_2}}{(2\pi)^3}\mathcal{T}^{(2)}_{Y\,\ell' m'}(\boldsymbol{p_1},\boldsymbol{p_2},\boldsymbol{k_2})\delta^{(3)}(\boldsymbol{k_2}-\boldsymbol{p_1}-\boldsymbol{p_2})\\ \langle\zeta(\boldsymbol{q_1})\zeta(\boldsymbol{q_2})\zeta(\boldsymbol{p_1})\zeta(\boldsymbol{p_2})\rangle\,.\end{aligned} \tag{4.7}$$

Using Wick theorem, under the assumption that the primordial perturbation field is Gaussian, and using the fact that this expression in symmetric in $\boldsymbol{q_1}\leftrightarrow\boldsymbol{q_2}$ one gets

$$\langle\zeta(\boldsymbol{q_1})\zeta(\boldsymbol{q_2})\zeta(\boldsymbol{p_1})\zeta(\boldsymbol{p_2})\rangle = 2(2\pi)^6\delta^{(3)}(\boldsymbol{q_1}+\boldsymbol{p_1})\delta^{(3)}(\boldsymbol{q_2}+\boldsymbol{p_2})P(q_1)P(q_2). \tag{4.8}$$

$$\begin{aligned}\left\langle a^{X}_{\ell m} a^{Y}_{\ell' m'}\right\rangle = 2\int \frac{\mathrm{d}^3\boldsymbol{k_1}}{(2\pi)^3}\int\frac{\mathrm{d}^3\boldsymbol{q_1}\,\mathrm{d}^3\boldsymbol{q_2}}{(2\pi)^3}\mathcal{T}^{(2)}_{X\,\ell m}(\boldsymbol{q_1},\boldsymbol{q_2},\boldsymbol{k_1})\mathcal{T}^{(2)}_{Y\,\ell' m'}(-\boldsymbol{q_1},-\boldsymbol{q_2},-\boldsymbol{k_1})\\ \delta^{(3)}(\boldsymbol{k_1}-\boldsymbol{q_1}-\boldsymbol{q_2})P(q_1)P(q_2).\end{aligned} \tag{4.9}$$

If we assume rotational invariance we can rotate our reference system to match $\hat{\boldsymbol{z}}$ with the direction of $\boldsymbol{k}$. For the rest of the section we will write $\int_x \equiv \int \mathrm{d}x\; x^2$ to shorten

the notation.

$$\begin{aligned}\left\langle a^X_{\ell m} a^Y_{\ell' m'}\right\rangle =& 2\int \frac{\mathrm{d}^3\boldsymbol{q_1}\,\mathrm{d}^3\boldsymbol{q_2}}{(2\pi)^3}\int_{k_1}\frac{1}{(2\pi)^3}\sqrt{\frac{4\pi}{(2\ell+1)}}\sqrt{\frac{4\pi}{(2\ell'+1)}}\\ &\sum_{m_1 m_2}\mathcal{T}^{(2)}_{X\ \ell m_1}(\boldsymbol{q_1},\boldsymbol{q_2},k_1)\mathcal{T}^{(2)}_{Y\ \ell' m_2}(-\boldsymbol{q_1},-\boldsymbol{q_2},k_1)\\ &\delta^{(3)}(-\boldsymbol{q_1}-\boldsymbol{q_2}+k_1\hat{\boldsymbol{z}})P(q_1)P(q_2)\int \mathrm{d}^2\Omega(\hat{\boldsymbol{k}}_{\boldsymbol{1}})(-1)^{\ell'}\ {}_{-m_1}Y^m_\ell(\hat{\boldsymbol{k}}_{\boldsymbol{1}})\ {}_{m_2}Y^{m'}_{\ell'}(\hat{\boldsymbol{k}}_{\boldsymbol{1}}) =\\ =&\frac{8\pi}{2\ell+1}\int\frac{\mathrm{d}^3\boldsymbol{q_1}\,\mathrm{d}^3\boldsymbol{q_2}}{(2\pi)^6}\int_{k_1}\delta^{(3)}(-\boldsymbol{q_1}-\boldsymbol{q_2}+k_1\hat{\boldsymbol{z}})P(q_1)P(q_2)\\ &\sum_{m_1}\mathcal{T}^{(2)}_{X\ \ell m_1}(\boldsymbol{q_1},\boldsymbol{q_2},k_1)\mathcal{T}^{(2)}_{Y\ \ell' m_1}(-\boldsymbol{q_1},-\boldsymbol{q_2},k_1)(-1)^{l'+m_1-m}\delta^{\ell'}_{\ell}\,\delta^{m_2}_{m_1}\delta^{-m'}_{m}.\end{aligned} \tag{4.10}$$

In the first line we used the fact that the transfer functions transform under rotations as spherical harmonics; and in the second $\int \mathrm{d}^2\Omega(\hat{\boldsymbol{k}}_{\boldsymbol{1}})\ {}_{-m_1}Y^m_\ell(\hat{\boldsymbol{k}}_{\boldsymbol{1}})\ {}_{-m_2}Y^{m'}_{\ell'}(\hat{\boldsymbol{k}}_{\boldsymbol{1}}) = (-1)^{m1+m}\delta^{\ell'}_{\ell}\,\delta^{-m_2}_{m_1}\delta^{-m'}_{m}$.

Now we specialize in the case we are interested in: X being the CMB polarization and Y being the quadratic Doppler effect effect. To uniform our notation with [236] and factor out the quantities that `SONG` actually calculates $\overline{\mathcal{T}}$, we perform the substitution

$$\mathcal{T}^{(2)}_{X\ \ell m_1}(\boldsymbol{q_1},\boldsymbol{q_2},k_1) = (-1)^{m_1}\sqrt{\frac{4\pi}{2|m_1|+1}}\overline{\mathcal{T}}^{(2)}_{X\ \ell m_1}(q_1,q_2,k_1)Y^{m_1}_{|m_1|}(\hat{\boldsymbol{q}}_{\boldsymbol{1}}) \tag{4.11}$$

$$\begin{aligned}\left\langle a^X_{\ell m} a^Y_{\ell' m'}\right\rangle =&\delta^{\ell'}_{\ell}\delta^{-m'}_{m}\frac{8\pi}{2\ell+1}\int\frac{\mathrm{d}^3\boldsymbol{q_1}\,\mathrm{d}^3\boldsymbol{q_2}}{(2\pi)^6}P(q_1)P(q_2)\sum_{m_1}\sqrt{\frac{4\pi}{2|m_1|+1}}(-1)^{\ell'+2m_1-m}\\ &\int_{k_1}\delta^{(3)}(\boldsymbol{k_1}-\boldsymbol{q_1}-\boldsymbol{q_2})\overline{\mathcal{T}}^{(2)}_{X\ \ell m_1}(q_1,q_2,k_1)Y^{m_1}_{|m_1|}(\hat{\boldsymbol{q}}_{\boldsymbol{1}})\mathcal{T}^{(2)}_{Y\ \ell' m_1}(-\boldsymbol{q_1},-\boldsymbol{q_2},k_1).\end{aligned} \tag{4.12}$$

For spectral distortion from reionization [239]

$$\begin{aligned}\mathcal{T}^{(2)}_{Y\ \ell' m_1}(\boldsymbol{q_1},\boldsymbol{q_2},k_1) =&(2\ell'+1)\left[\frac{-\delta^0_{m_1}}{3}I^{(1)}_{\ell'}(q_1,q_2,k_1)\ \hat{\boldsymbol{q}}_{\boldsymbol{1}}\cdot\hat{\boldsymbol{q}}_{\boldsymbol{2}}+\right.\\ &\left.+\frac{11\pi}{45}I^{(2)}_{\ell',m_1}(q_1,q_2,k_1)\sum_{n=-1}^{1}\alpha_{n,m_1}\Big(Y_1^{-m_1-n}(\hat{\boldsymbol{q}}_{\boldsymbol{1}})Y_1^n(\hat{\boldsymbol{q}}_{\boldsymbol{2}})\Big)^*\right]\end{aligned} \tag{4.13}$$

with

$$\begin{aligned} I^{(1)}_{\ell'}(q_1,q_2,k_1) &= \int_{\eta_{reio}}^{\eta_0} \mathrm{d}\eta\ g(\eta) j_\ell(k_1 r(\eta)) F(q_1,\eta) F(q_2,\eta) \\ I^{(2)}_{\ell',m_1}(q_1,q_2,k_1) &= \int_{\eta_{reio}}^{\eta_0} \mathrm{d}\eta\ g(\eta) j^{(2,m_1)}_\ell(k_1 r(\eta)) F(q_1,\eta) F(q_2,\eta). \end{aligned} \tag{4.14}$$

and

$$\alpha_{0,m} \equiv \sqrt{4-m^2} \quad \alpha_{\pm 1,m} \equiv \sqrt{(2\pm m)(2\pm m-1)/2}. \tag{4.15}$$

Here $F(k,\eta)$ is the baryon velocity transfer function, defined as

$$\boldsymbol{v}_b(k,\eta) = -i\frac{\boldsymbol{k}}{k} F(k,\eta)\zeta(\boldsymbol{k})\ , \tag{4.16}$$

and $g(\eta)$ is the visibility function.

Plugging everything back in, we can use the identity eq. (A.6) and the Rayleigh expansion of the Dirac delta (A.8) to get

$$\begin{aligned} \left\langle a^X_{\ell m} a^Y_{\ell' m'} \right\rangle =& \delta^{\ell'}_{\ell}\,\delta^{-m'}_{m} \frac{64\pi}{2\ell+1} \int \frac{\mathrm{d}^3\boldsymbol{q_1}\,\mathrm{d}^3\boldsymbol{q_2}}{(2\pi)^6} \int_{k_1}\int_x \sum_L \sum_{L_1 M_1} \sum_{L_2 M_2} j_L(xk_1) j_{L_1}(xq_1) j_{L_2}(xq_2) \\ & \sqrt{\frac{2L+1}{4\pi}} (-1)^{L_1+L_2} Y^{M_1 *}_{L_1}(\hat{\boldsymbol{q}}_{\boldsymbol{1}}) Y^{M_2 *}_{L_2}(\hat{\boldsymbol{q}}_{\boldsymbol{2}}) i^{L+L_1+L_2} h_{L_1 L_2 L} \begin{pmatrix} L_1 & L_2 & L \\ M_1 & M_2 & 0 \end{pmatrix} \\ & \sum_{m_1} \sqrt{\frac{4\pi}{2|m_1|+1}} (-1)^{\ell'+2m_1-m} \overline{\mathcal{T}}^{(2)}_{X\,\ell m_1}(q_1,q_2,k_1) Y^{m_1}_{|m_1|}(\hat{\boldsymbol{q}}_{\boldsymbol{1}}) \\ & (2\ell'+1)\Bigg[\frac{-\delta^0_{m_1}}{3} I^{(1)}_{\ell'}(q_1,q_2,k_1)\ \frac{4\pi}{3} \sum_{m_2=-1}^{1} Y^{m_2 *}_1(\hat{\boldsymbol{q}}_{\boldsymbol{1}}) Y^{m_2}_1(\hat{\boldsymbol{q}}_{\boldsymbol{2}}) + \\ & + \frac{11\pi}{45} I^{(2)}_{\ell',m_1}(q_1,q_2,k_1) \sum_{n=-1}^{1} \alpha_{n,m_1} \left(Y^{m_1-n}_1(\hat{\boldsymbol{q}}_{\boldsymbol{1}}) Y^{n}_1(\hat{\boldsymbol{q}}_{\boldsymbol{2}}) \right)^* \Bigg] P(q_1) P(q_2) \end{aligned}$$

$$
\begin{aligned}
\left\langle a^X_{\ell m} a^Y_{\ell' m'} \right\rangle =& \delta^{\ell'}_{\ell}\, \delta^{-m'}_{m}\, 64\pi \frac{2\ell'+1}{2\ell+1} \\
& \sum_L \sum_{L_1 M_1} \sum_{M_2} \sqrt{\frac{2L+1}{4\pi}} (-1)^{L_1+1} i^{L+L_1+1} h_{L_1\ 1\ L} \begin{pmatrix} L_1 & 1 & L \\ M_1 & M_2 & 0 \end{pmatrix} \\
& \sum_{m_1} \sqrt{\frac{4\pi}{2|m_1|+1}} (-1)^{\ell'+2m_1-m} \\
& \int_{q_1} \int_{q_2} \int_{k_1} \frac{1}{(2\pi)^6} P(q_1) P(q_2) \overline{\mathcal{T}}^{(2)}_{X\ \ell m_1}(q_1, q_2, k_1) \\
& \left[\frac{-\delta^0_{m_1}}{3} I^{(1)}_{\ell'}(q_1, q_2, k_1)\ \frac{4\pi}{3} \sum_{m_2=-1}^{1} (-1)^{m_2} \delta^{m_2}_{M_2} \frac{3}{\sqrt{4\pi}} \delta^1_{L_1} \delta^{-m_2}_{M_1} + \right. \\
& \frac{11\pi}{45} I^{(2)}_{\ell', m_1}(q_1, q_2, k_1) \sum_{n=-1}^{1} \alpha_{n, m_1} h_{L_1 |m_1| 1} \begin{pmatrix} L_1 & |m_1| & 1 \\ -M1 & m_1 & -m_1+n \end{pmatrix} \\
& \left. (-1)^{M_1+m_1-n} \delta^{-n}_{M_2} \right] \int_x j_L(xk_1) j_{L_1}(xq_1) j_1(xq_2)
\end{aligned}
\tag{4.17}
$$

where we defined

$$
h_{L_1 L_2 L_3} \equiv \sqrt{\frac{(2L+1)(2L_1+1)(2L_2+1)}{4\pi}} \begin{pmatrix} L & L_1 & L_2 \\ 0 & 0 & 0 \end{pmatrix}. \tag{4.18}
$$

The first term is further reduced to

$$
\begin{aligned}
1st =& (-1)^{\ell'-m}\, \delta^{\ell'}_{\ell}\, \delta^{-m'}_{m}\, 64\pi \int \frac{q_1^2\, \mathrm{d}q_1 q_2^2\, \mathrm{d}q_2}{(2\pi)^6} \int k_1^2\, \mathrm{d}k_1 \int x^2\, \mathrm{d}x j_0(xk_1) j_1(xq_1) j_1(xq_2) \\
& \overline{\mathcal{T}}^{(2)}_{X\ \ell,0}(q_1, q_2, k_1) \frac{1}{3} I^{(1)}_{\ell'}(q_1, q_2, k_1) P(q_1) P(q_2)
\end{aligned}
\tag{4.19}
$$

where we used the identity (A.21); whereas the second is

$$
\begin{aligned}
2nd =&(-1)^{\ell'-m}\delta_\ell^{\ell'}\delta_m^{-m'}64\pi\int\frac{q_1^2\,\mathrm{d}q_1 q_2^2\,\mathrm{d}q_2}{(2\pi)^6}\int k_1^2\,\mathrm{d}k_1\sum_L\sum_{L_1}\sum_{n=-1}^{1}\int x^2\,\mathrm{d}x j_L(xk_1)j_{L_1}(xq_1)j_1(xq_2)\\
&\sum_{m_1}\overline{\mathcal{T}}^{(2)}_{X\;\ell m_1}(q_1,q_2,k_1)\frac{11\pi}{45}I^{(2)}_{\ell',m_1}(q_1,q_2,k_1)P(q_1)P(q_2)\\
&(-1)^{L_1+1}i^{L+L_1+1}(-1)^{3m_1}\frac{3(2L+1)(2L_1+1)}{4\pi}\alpha_{n,m_1}\begin{pmatrix}L_1&1&L\\0&0&0\end{pmatrix}\begin{pmatrix}L_1&1&L\\n&-n&0\end{pmatrix}\\
&\begin{pmatrix}L_1&|m_1|&1\\0&0&0\end{pmatrix}\begin{pmatrix}L_1&|m_1|&1\\-n&m_1&-m_1+n\end{pmatrix}\,.
\end{aligned}
\tag{4.20}
$$

The structure of the 4 three-j symbol that appear in the second term guarantees that the sum over L, L_1 is not infinite. In fact we found that their product is non zero only for $L<4, L_1<3$.

As the integral over x, for both terms, has to be computed for small values of the multipolar indices, therefore it is convenient to evaluate it analytically using the identity (A.23) [241].

Wrapping up we get

$$
\begin{aligned}
y^{(2)}_{\mathrm{reio}}\text{-}E^{(2)} =&(-1)^{\ell'-m}64\pi\int\frac{q_1^2\,\mathrm{d}q_1 q_2^2\,\mathrm{d}q_2}{(2\pi)^3}\int\frac{k_1^2\,\mathrm{d}k_1}{(2\pi)^3}P(q_1)P(q_2)\delta_\ell^{\ell'}\delta_m^{-m'}\\
&\Bigg[\overline{\mathcal{T}}^{(2)}_{X\;\ell,0}(q_1,q_2,k_1)\frac{1}{3}I^{(1)}_{\ell'}(q_1,q_2,k_1)I(0,1,1,k_1,q_1,q_2)+\\
&+\sum_L^4\sum_{L_1}^3\sum_{m_1}\sum_{n=-1}^{1}(-1)^{L_1+1}i^{L+L_1+1}(-1)^{3m_1}\frac{3(2L+1)(2L_1+1)}{4\pi}\alpha_{n,m_1}\\
&\begin{pmatrix}L_1&1&L\\0&0&0\end{pmatrix}\begin{pmatrix}L_1&1&L\\n&-n&0\end{pmatrix}\begin{pmatrix}L_1&|m_1|&1\\0&0&0\end{pmatrix}\begin{pmatrix}L_1&|m_1|&1\\-n&m_1&-m_1+n\end{pmatrix}\\
&\frac{11\pi}{45}I^{(2)}_{\ell',m_1}(q_1,q_2,k_1)\overline{\mathcal{T}}^{(2)}_{X\;\ell m_1}(q_1,q_2,k_1)I(L,L_1,1,k_1,q_1,q_2)\Bigg].
\end{aligned}
\tag{4.21}
$$

While the angular — moments independent — part can be computed analytically, the integrals over q_1, q_2, and k_1 have to be evaluated numerically. Luckily enough the structure of these integrals is the same one finds when calculating the intrinsic bispectrum of the CMB. Therefore [235] provides a good insight of what are the properties of the

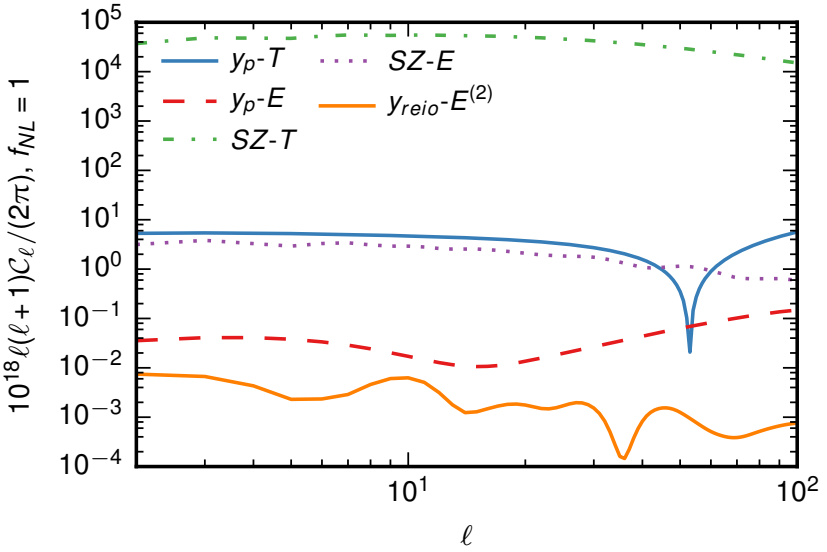

Figure 4.2.: The main components (primordial and secondary) of the y-T and y-E cross-correlations. SZ-T is the only non-negligible contaminant to y_p-T, but is four orders of magnitude bigger, and correlates more with it. y_p-E suffers the presence of both SZ-E and $y_{\rm reio}$-E, but both secondary signals are proportionally smaller and less correlated than SZ-T.

integrand. In fact we found that it oscillates both along k_1, and along q_1 and q_2, however the frequency of oscillation along k_1 is one order of magnitude higher than the other. For this reason we computed the k_1 integral over a coarse grid of q_1 and q_2, and only then we performed the integral of the now smoother function. Moreover the symmetry $\boldsymbol{q_1} \leftrightarrow \boldsymbol{q_2}$ allows us to pick only the configurations with $q_2 < q_1$ and double the result of the integral in the end.

To calculate this signal we use the transfer function extracted from `SONG` with 10% accuracy. Since the convergence of the tensor modes has not been tested by the authors for more than 10% accuracy [236], using higher precision run would require extensive testing of the code. Moreover, as the final $y^{(2)}$-$E^{(2)}$ contribution will turn out to be negligible, our results will not depend on this quantity, making accuracy improvements not important for our purposes.

In figure 4.2 we compare the y_p-E signal with the secondary sources of E-y. The SZ-E cross-correlation is approximately 100 times bigger than the signal, while the $y_{\rm reio}$-$E^{(2)}$ cross-correlation is 10-100 times smaller than the signal in the first 100 multipoles, and their ratio decreases as ℓ increases. The slightly different slopes allow disentangling of the signal from the secondary sources, as we will show in subsection 4.1.4. For comparison, the

SZ-T cross-correlation in 10^4 bigger than the primordial signal. The same marginalization over the foregrounds can be performed also in this case, but with worse results since the shape of the primordial signal is more degenerate with the shape of the secondary sources. This can be quantified calculating the correlation of the primordial signal with the secondary signal:

$$\frac{\left[\sum_\ell C_\ell^{y_pT} C_\ell^{\mathrm{SZ}T}\right]}{\sqrt{\left[\sum_\ell \left(C_\ell^{y_pT}\right)^2\right]\left[\sum_\ell \left(C_\ell^{\mathrm{SZ}T}\right)^2\right]}} = 0.92, \quad \frac{\left[\sum_\ell C_\ell^{y_pE} C_\ell^{\mathrm{SZ}E}\right]}{\sqrt{\left[\sum_\ell \left(C_\ell^{y_pE}\right)^2\right]\left[\sum_\ell \left(C_\ell^{\mathrm{SZ}E}\right)^2\right]}} = 0.64. \quad (4.22)$$

4.1.3. f_{NL}^{μ} forecast

As first considered in [233], we can try enhancing the f_{NL} signal-to-noise ratio, extracted using T-μ, by adding polarization to the analysis. In [233], simplified "Sachs-Wolfe"-limit transfer functions were used both for temperature and polarization anisotropies, finding no f_{NL}-sensitivity improvements with the inclusion of polarization. However, we found via explicit computation that the inclusion of full transfer functions does change this picture at $\ell > 10$, outside the limits of validity of the Sachs-Wolfe approximation.

As in Section 3.2.3 the Fisher matrix is

$$F_{ij} = \sum_\ell (\mathbf{Cov}_\ell^{-1})_{\alpha\beta} \frac{\partial (\mathbf{Cov}_\ell)_{\beta\gamma}}{\partial p_i} (\mathbf{Cov}_\ell^{-1})_{\gamma\delta} \frac{\partial (\mathbf{Cov}_\ell)_{\delta\alpha}}{\partial p_j} \quad (4.23)$$

where $\mathbf{Cov}_\ell$ is the covariance matrix and repeated matrix indices $(\alpha, \ldots, \delta)$ are summed.

The f_{NL}^{μ} Fisher matrix, when considering only T or only E, reads [9]

$$\left(\frac{S}{N}\right)^2 = F = \sum_{\ell=2}^{\ell_{\max}} \frac{C_\ell^{\mu X} C_\ell^{\mu X}}{\left(\sigma_\ell^{\mu X}\right)^2}, \quad (4.24)$$

where we recall that $X = T, E$. For a PIXIE- or PRISM-like experiment it is expected that $C_\ell^{X\mu} C_\ell^{X\mu} \ll (C_\ell^{XX})_{\mathrm{obs}} (C_\ell^{\mu\mu})_{\mathrm{obs}}$, and $(C_\ell^{\mu\mu})_{\mathrm{obs}} \approx (C_\ell^{\mu\mu})_N \gg C_\ell^{\mu\mu}$ where "obs" stands for observed and "N" for noise. Again, for PIXIE (PRISM) the expected noise is $C_\ell^{\mu\mu,N} = 4\pi \times (1.4 \times 10^{-8})^2 \times e^{\ell^2/84^2}$ ($C_\ell^{\mu\mu,N} = 4\pi \times 10^{-18} \times e^{\ell^2/100^2}$) [10, 221]. Here we do not account for galactic foregrounds. In [242] it has been shown that the error on the measurement of the spectral distortion monopole can degrade as much as one order of magnitude with respect to earlier, more optimistic estimates. The spatially varying part

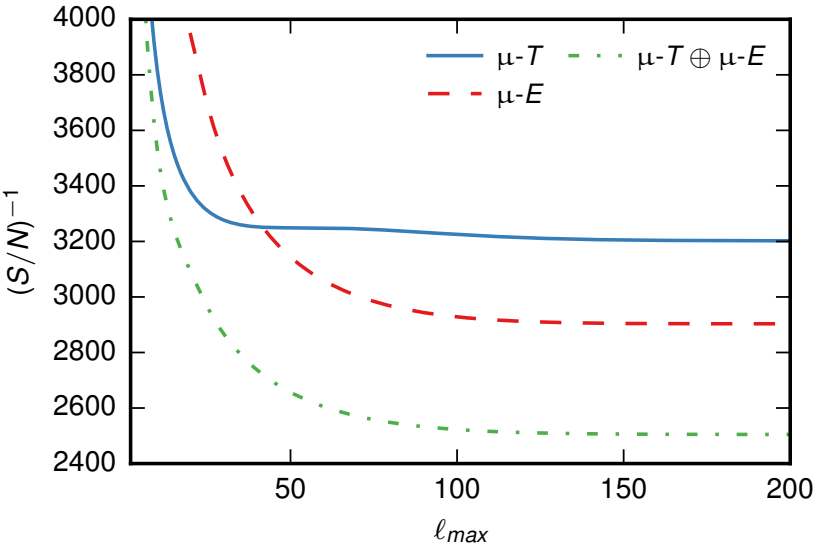

Figure 4.3.: Minimum value of $f^{\mu}_{\rm NL}$ to reject $f\mu_{\rm NL} = 0$ at 1σ, as a function of the maximum multipole. This value is calculated with a 1 parameter Fisher forecast using the PIXIE level of noise. Adding polarization informations tightens the constrain by a factor 1.28. The estimate achieved using temperature alone is in good agreement with [237].

of these foregrounds will have to be modelled with more accuracy in order to give an actual estimate of how much the estimates will degrade in our case.

Under those assumptions

$$(\sigma_\ell^{\mu X})^2 \approx \frac{C_\ell^{XX} C_\ell^{\mu\mu,N}}{2\ell+1} \,. \tag{4.25}$$

Therefore, the signal-to-noise ratio is proportional to the μE contribution — which is underestimated for $\ell > 10$ using the "Sachs-Wolfe"-transfer function — and inversely proportional to the square root of the polarization power spectrum, which peaks on the first 10 multipoles (due to the reionization bump) and decreases afterwards. As a result an explicit numerical evaluation shows that the $f^{\mu}_{\rm NL}$ signal-to-noise ratio from E-μ is actually higher than the one obtained using T-μ, at $\ell_{\rm max} > 50$, see figure 4.3.

We are finally interested in the joint estimate of $f^{\mu}_{\rm NL}$, obtained combining both observations:

$$F = \sum_{\ell}^{\ell_{\rm max}} (2\ell+1) \frac{C_\ell^{TT}(C_\ell^{\mu E})^2 + C_\ell^{EE}(C_\ell^{\mu T})^2 - 2C_\ell^{TE} C_\ell^{\mu T} C_\ell^{\mu E}}{C_\ell^{\mu\mu,N}[C_\ell^{TT} C_\ell^{EE} - (C_\ell^{TE})^2]} \tag{4.26}$$

	Survey	T	E	$T \oplus E$
$1\sigma(f^{\mu}_{\rm NL})$	PIXIE	4200	3800	3300
	PRISM	300	270	230
	CVL	0.67×10^{-3}	0.67×10^{-3}	0.55×10^{-3}

Table 4.1.: 1σ forecasted error bars on $f^{\mu}_{\rm NL}$, calculated using the standard ΛCDM value of $\langle\mu\rangle = 2.3\times10^{-8}$. $T \oplus E$ indicates the joint forecast using both temperature and polarization. We accounted for correlations between T-μ and E-μ using eq. (4.26).

as the covariance matrix is

$$\mathbf{Cov}_\ell = \frac{1}{2\ell+1}\begin{pmatrix} C_\ell^{TT} & C_\ell^{TE} & f^{\mu}_{\rm NL}C_\ell^{\mu T} \\ C_\ell^{TE} & C_\ell^{EE} & f^{\mu}_{\rm NL}C_\ell^{\mu E} \\ f^{\mu}_{\rm NL}C_\ell^{\mu T} & f^{\mu}_{\rm NL}C_\ell^{\mu E} & C_\ell^{\mu\mu,N} \end{pmatrix}. \tag{4.27}$$

As expected for a PIXIE-like survey, the signal-to-noise ratio saturates for $\ell \approx 100$ [221]. We found that adding the polarization cross-correlation to the temperature cross-correlation with the μ-spectral-distortion the constraint on $f_{\rm NL}$ improves by a factor 1.28. In figure 4.3 we show the minimum value of $f^{\mu}_{\rm NL}$ that guarantees a 1σ rejection of $f^{\mu}_{\rm NL} = 0$, as a function of the maximum multipole. Our results are shown in table 4.1. The estimate achieved using temperature alone appears to be slightly different from [237]. The shape of the $C_\ell^{\mu T}$ used in [237], calculated in [221] deviate slightly from ours, and in particular the first zero crossing is located at smaller ℓ with respect to our calculation. Since the signal-to-noise ratio scales logarithmically with the ℓ [221], slightly bigger $C_\ell^{\mu T}$ at small ℓ guarantees more signal to noise with respect to bigger $C_\ell^{\mu T}$ at higher ℓ. If we were to use the same signal as the one provided in [221], we would be completely consistent with [237].

4.1.4. $f^{y}_{\rm NL}$ forecast

We will now come to the main point of this work, namely studying the effects of adding y-distortions in the $f_{\rm NL}$ analysis, including contributions from polarization and exploring methods to clean SZ-contamination via SZ-lensing correlations.

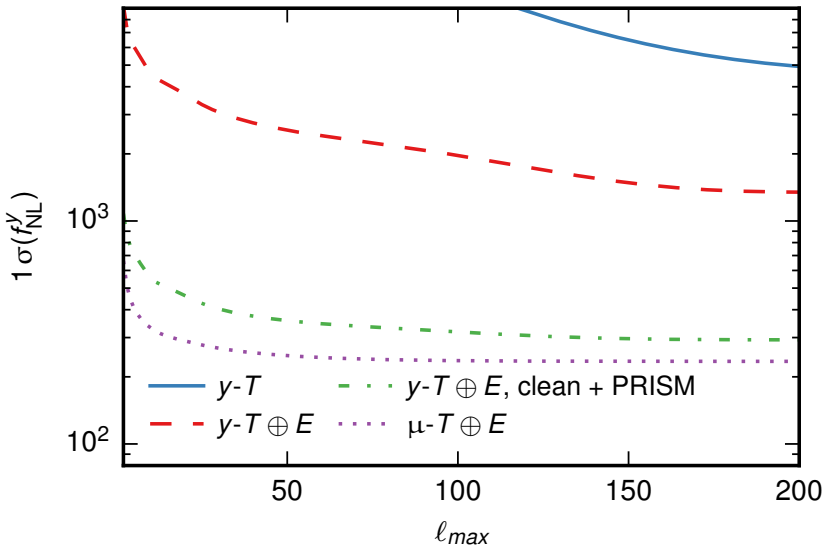

Figure 4.4.: Minimum value of $f_{\rm NL}^{y}$ needed to reject $f_{\rm NL}^{y} = 0$ at 1σ, as a function of the maximum multipole. This value is calculated with a Fisher forecast after marginalizing over all foregrounds and using the PRISM level of noise. We also show the same value for $f_{\rm NL}^{\mu}$ for comparison. We compare the results obtained using no mask and no template subtraction (y-$T \oplus E$) and using the PRISM mask and the template subtraction (y-$T \oplus E$, clean + PRISM) described respectively in table 4.5 and subsection 4.1.4.

T-y forecast and cluster masking.

In our forecasts we have to keep into account theoretical uncertainties of the halo-model, used to predict the correlations. Following [211], we will do this by simply introducing an unknown amplitude parameter α_T, in front of the spectra, and marginalizing over it. This leads to the covariance matrix

$$\mathbf{Cov}_\ell = \frac{1}{2\ell+1}\begin{pmatrix} C_\ell^{TT} & f_{\rm NL}^{y} C_\ell^{yT} + \alpha_T C_\ell^{\rm SZT} \\ f_{\rm NL}^{y} C_\ell^{yT} + \alpha_T C_\ell^{\rm SZT} & C_\ell^{yy,N} + C_\ell^{1h} + C_\ell^{2h} \end{pmatrix}. \tag{4.28}$$

A PIXIE-like experiment is expected to have 5 to 10 better sensitivity to y than to μ. Therefore the noise term is $C_\ell^{yy,N} = 4\pi \times 4 \times 10^{-18} \times e^{\ell^2/84^2}$; the same holds for PRISM for which $C_\ell^{yy,N} = 4\pi \times 4 \times 10^{-20} \times e^{\ell^2/84^2}$ [10, 221]. We forecast $f_{\rm NL}^{y}$ using temperature alone, and marginalizing over the secondary source SZ-T.

	Mask	T	E	$T \oplus E$	$T \oplus E$, clean.
$1\sigma(f_{\rm NL}^{y})$	Unmasked	12700	5500	3300	2900
	eROSITA	8600	4800	2700	2300
	PRISM	5500	4000	2200	2200
	$z > 0.3$	5500	4200	2300	2300

Table 4.2.: 1σ forecasted error bars on $f_{\rm NL}^{y}$ for PIXIE, calculated using the standard ΛCDM value of $\langle y \rangle = 4.2 \times 10^{-9}$. $T \oplus E$ indicates the joint forecast using both temperature and polarization. We accounted for correlations between T-y and E-y using the covariance in eq. (4.31). In all the forecasts we marginalize over the amplitude of every secondary source. $z > 0.3$ performs worse than PRISM mask because the contribution to the total SZ signal coming from small ($M < 10^{13}\ M_{\odot}$) clusters at low ($z < 0.3$) redshift is smaller than that of bigger clusters at higher redshift.

	Mask	T	E	$T \oplus E$	$T \oplus E$, clean.
$1\sigma(f_{\rm NL}^{y})$	Unmasked	4900	3100	1700	1300
	eROSITA	3200	1900	1100	680
	PRISM	1000	630	380	300
	$z > 0.3$	1700	1300	700	620

Table 4.3.: Same as table 4.2 but for PRISM.

In figure 4.4 we show our results as a function of $\ell_{\rm max}$. It is clear not only that the variance is completely dominated by the SZ power spectrum, but also that this effect leads to very poor constraints on the primordial signal.

One way to tighten the constraints is to mask resolved clusters (see e.g [126, 211]), eventually assuming the use of external surveys (e.g. X-ray surveys) to improve performance. We will consider here eROSITA [222] as external survey, and also PRISM itself, and investigate different types of masks, based on more or less futuristic scenarios, in order to understand which level of masking guarantees a signal-to-noise ratio for $f_{\rm NL}^{y}$ similar to the one achieved for $f_{\rm NL}^{\mu}$. Our results are summarized in table 4.2.

We model the effect of masking clusters by changing integration boudaries in the SZ-SZ, SZ-T and SZ-E spectra, in order to exclude regions in the z-M plane where the catalogue of a given experiment is complete [126]. This is a very conservative choice, as in real catalogues a non-negligible part of resolved cluster actually sits in regions where the catalogue is not complete. We have investigated 5 different masks:

	Mask	T	E	$T \oplus E$	$T \oplus E$, clean.
$1\sigma(f_{\rm NL}^{y})$	Unmasked	2300	1400	1000	750
	eROSITA	1700	1100	730	470
	PRISM	400	220	160	130
	$z > 0.3$	1000	710	470	400

Table 4.4.: Same as table 4.2 but for a cosmic-variance limited spectrometer instead of PIXIE, and using $\ell_{\rm max} = 1000$.

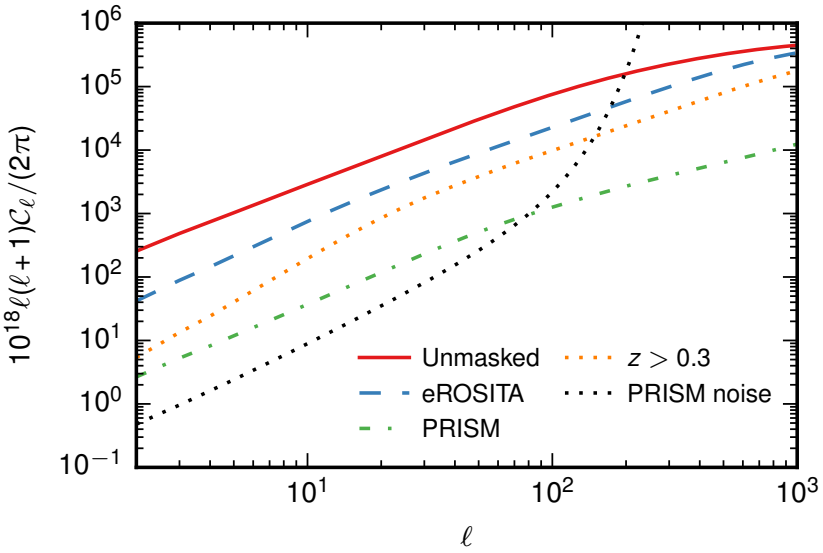

Figure 4.5.: SZ power spectrum, for the different sky-masks defined in table 4.5. For comparison we also plot the PRISM noise level. PIXIE noise level is two orders of magnitude bigger then the PRISM one.

- The vanilla "Unmasked" scenario.
- The one expected from the eROSITA predicted efficiency.
- The one expected from the PRISM predicted efficiency.
- A mask that cuts every cluster under $z < 0.3$ regardless of its size, used to compare our results with [211], "$z > 0.3$". This is also a futuristic scenario.

The adopted integration boundaries for the various cases are shown in table 4.5. In figure 4.5 we compare the total (1-halo + 2-halo) SZ power spectra, obtained using different masks. As shown, using PIXIE with the eROSITA mask, already guarantees a $f_{\rm NL}^{y}$ signal-to-noise ratio comparable with $f_{\rm NL}^{\mu}$.

Unmasked	None
eROSITA	$M < 2 \times 10^{14} M_\odot/h$ for $z < 0.15$
PRISM	$M < 10^{13} M_\odot h^{-1}$
$z > 0.3$	$z > 0.3$

Table 4.5.: Integration boundaries that define the different masks we use.

Masking resolved clusters lowers the noise, but at the same time reduces the level of sky coverage. We get a rough and conservative estimate of the available fraction of the sky after cluster masking ($f_{\rm sky}$) in the following way. We consider the eROSITA and estimate the number of masked clusters (< 1800) based on its expected performance [222]. We then assume that the redshift distribution of clusters is constant in redshift for $z \in [0.02, 0.15]$; this is a conservative choice since the expected redshift distribution increases rapidly with redshift in the considered range. Finally we assume that each cluster has a size of 6 Mpc. This leads to a final estimate

$$f_{\rm sky} \approx 1 - \frac{1}{0.13} \int_{0.02}^{0.15} {\rm d}z \frac{\pi (6\ {\rm Mpc})^2}{4\pi D_A^2(z)} \times 1800 \approx 0.7\ , \tag{4.29}$$

which will be included in our forecasts.

Adding polarization

We consider y-E contributions to the signal, by adapting equation (4.28) into:

$$\mathbf{Cov}_\ell = \frac{1}{2\ell+1} \begin{pmatrix} C_\ell^{EE} & f_{\rm NL}^y C_\ell^{yE} + \alpha_E C_\ell^{{\rm SZ}E} + \beta_E C_\ell^{y_{\rm reio}E} \\ f_{\rm NL}^y C_\ell^{yE} + \alpha_E C_\ell^{{\rm SZ}E} + \beta_E C_\ell^{y_{\rm reio}E} & C_\ell^{yy,N} + C_\ell^{1h} + C_\ell^{2h} \end{pmatrix}. \tag{4.30}$$

The results we get after marginalizing over both α_E and β_E are shown in table 4.2. For a PIXIE-like experiment, just replacing T with E tightens the constraints by more than a factor 2. This comes from two effects. First, the signal-to-noise ratio for y-E is intrinsically higher — just like, and for the same reason as μ-E. Second, marginalizing over secondary signals do not degrades the constraint as much because the primordial and the secondary signal are less correlated as shown in eq. (4.22).

We now want to perform a joint analysis of y-T and y-E signals. In this case the covariance is

$$(2\ell+1)\mathbf{Cov}_\ell = \\ = \begin{pmatrix} C_\ell^{TT} & C_\ell^{TE} & f_{\rm NL}^y C_\ell^{yT} + \alpha_T C_\ell^{{\rm SZ}T} \\ C_\ell^{TE} & C_\ell^{EE} & f_{\rm NL}^y C_\ell^{yE} + \alpha_E C_\ell^{{\rm SZ}E} + \beta_E C_\ell^{y_{\rm reio}E} \\ f_{\rm NL}^y C_\ell^{yT} + \alpha_T C_\ell^{{\rm SZ}T} & f_{\rm NL}^y C_\ell^{yE} + \alpha_E C_\ell^{{\rm SZ}E} + \beta_E C_\ell^{y_{\rm reio}E} & C_\ell^{yy,N} + C_\ell^{1h} + C_\ell^{2h} \end{pmatrix}. \tag{4.31}$$

The $C_\ell^{y_{\rm reio}E}$ contribution is very small and it has a very different slope than the primordial signal, hence marginalizing over β_E changes the final signal-to-noise ratio to a percent level. For this reason in the joint forecast we fixed $\beta_E = 1$. Moreover theoretical uncertainties in the SZ-T and SZ-E correlations, which have been parametrized above in terms of the amplitudes α_T and α_E, are entirely driven by errors in the prediction of the y signal. Therefore, we can also assume $\alpha \equiv \alpha_T = \alpha_E$ and marginalize over α.

Our joint-analysis results are summarized in table 4.2 for PIXIE, in 4.3 for PRISM and in 4.4 for an ideal cosmic-variance limited experiment. There we show how adding polarization tightens the constraints both in the PIXIE and PRISM-like, and in the cosmic-variance limited scenario by a factor between 2.1 and 3.8, depending on the considered survey and mask.

Cross-correlation with external tracers

The dominant term in the variance, in all configurations and for both E and T, is the SZ power spectrum. For this reason the only way to further enhance the signal-to-noise ratio, at this stage, is to remove as much contamination from SZ as possible. Using masks help significantly but, of course, cannot remove the significant contribution from the background of unresolved clusters.

In order to lower the noise contribution coming from this unresolved background, we consider here an approach based on statistical reconstruction of the SZ y-map, via correlations with CMB and galaxy-lensing signals. To do this we adapt the method studied in [243].

In other words, the observed y-distortion is the sum of the primordial component, the SZ component and the noise: $y_{\rm obs}(\hat{\boldsymbol{n}}) = y_p(\hat{\boldsymbol{n}}) + y_{\rm SZ}(\hat{\boldsymbol{n}}) + y_N(\hat{\boldsymbol{n}})$. Given the estimate $\hat{y}_{\rm SZ}$ of $y_{\rm SZ}$, one can use $y_{\rm clean}(\hat{\boldsymbol{n}}) \equiv y_{\rm obs}(\hat{\boldsymbol{n}}) - \hat{y}_{\rm SZ}(\hat{\boldsymbol{n}})$ in place of $y_{\rm obs}(\hat{\boldsymbol{n}})$.

We will start considering the CMB-lensing-potential, ϕ, as our SZ-tracer. Later we will reapply the same procedure using the galaxy-lensing convergence field. The joint probability density function of $y_{\rm SZ}$, ϕ, T, and E is

$$p(\boldsymbol{d}_\ell) = \mathcal{N}(0, \mathbf{A}_\ell), \tag{4.32}$$

where $\mathcal{N}(\boldsymbol{\mu}, \mathbf{Cov})$ is the multivariate Normal distribution with mean $\boldsymbol{\mu}$ and covariance $\mathbf{Cov}$, and we defined

$$\mathbf{A}_\ell = \begin{pmatrix} C_\ell^{\rm SZSZ} & C_\ell^{{\rm SZ}\phi} & C_\ell^{{\rm SZ}T} & C_\ell^{{\rm SZ}E} \\ C_\ell^{{\rm SZ}\phi} & C_\ell^{\phi\phi} & C_\ell^{\phi T} & C_\ell^{\phi E} \\ C_\ell^{{\rm SZ}T} & C_\ell^{\phi T} & C_\ell^{TT} & C_\ell^{TE} \\ C_\ell^{{\rm SZ}E} & C_\ell^{\phi E} & C_\ell^{TE} & C_\ell^{EE} \end{pmatrix} \equiv \begin{pmatrix} C_\ell^{\rm SZSZ} & \mathbf{C}_\ell \\ \mathbf{C}_\ell^T & \mathbf{B}_\ell \end{pmatrix}, \qquad \boldsymbol{d}_\ell \equiv \begin{pmatrix} a_{\ell m}^{\rm SZ} \\ a_{\ell m}^{\phi} \\ a_{\ell m}^{T} \\ a_{\ell m}^{E} \end{pmatrix} \equiv \begin{pmatrix} a_{\ell m}^{\rm SZ} \\ \boldsymbol{t}_{\ell m} \end{pmatrix}. \tag{4.33}$$

The conditional probability distribution of the $a_{\ell m}^{\rm SZ}$ given the measurement of ϕ, T, and E is

$$p(a_{\ell m}^{\rm SZ} | \boldsymbol{t}_{\ell m}) = \mathcal{N}(\mathbf{C}_\ell^T \mathbf{B}_\ell^{-1} \boldsymbol{t}_{\ell m}, C_\ell^{\rm SZSZ} - \mathbf{C}_\ell^T \mathbf{B}_\ell^{-1} \mathbf{C}_\ell) \ . \tag{4.34}$$

The expectation value of $a_{\ell m}^{\rm SZ}$ then is

$$\hat{a}_{\ell m}^{\rm SZ} = \mathbf{C}_\ell^T \mathbf{B}_\ell^{-1} \boldsymbol{t}_{\ell m} \ . \tag{4.35}$$

The probability distribution of $a_{\ell m}^{\rm clean} = a_{\ell m}^{\rm obs} - \hat{a}_{\ell m}^{\rm SZ}$ is

$$p(a_{\ell m}^{\rm clean} | \boldsymbol{t}_{\ell m}) = \mathcal{N}\left(-\mathbf{C}_\ell^T \mathbf{B}_\ell^{-1} \boldsymbol{t}_{\ell m}, Var(a_{\ell m}^{\rm obs}) + Var(\hat{a}_{\ell m}^{\rm SZ}) - 2Cov(a_{\ell m}^{\rm obs}, \hat{a}_{\ell m}^{\rm SZ}) \right). \tag{4.36}$$

The covariance of $a_{\ell m}^{\rm obs}$ and $\hat{a}_{\ell m}^{\rm SZ}$ can be computed using eq. (4.35) to write $a_{\ell m}^{\rm SZ}$ in term of the multipolar coefficients of the tracers. For our fiducial model $f_{\rm NL} = 0$ the only term in $a_{\ell m}^{\rm obs}$ that does contribute to the cross correlation is indeed $a_{\ell m}^{\rm SZ}$.

Note that the non-zero mean appearing in eq. (4.36) is due to the fact that we are considering the probability of $a_{\ell m}^{\rm clean}$, conditional to the specific observed realization of $\boldsymbol{t}_{\ell m}$

in the sky. Of course, if one consider the expectation value over the ensemble of possible realization, one recovers $\langle \boldsymbol{t}_{\ell m} \rangle = 0$ and therefore $\langle a_{\ell m}^{\rm clean} \rangle = 0$ as expected.

Note also that, neglecting temperature and polarization, eq. (4.35) simply becomes $\hat{a}_{\ell m}^{\rm SZ} = (C_\ell^{\phi \rm SZ}/C_\ell^{\phi\phi}) a_{\ell m}^{\phi}$, as expected.

Using $y_{\rm clean}(\hat{\boldsymbol{n}})$ instead of $y_{\rm obs}(\hat{\boldsymbol{n}})$ leaves the numerator of eq. (4.31) unchanged. The variance instead is modified, with the following replacement, which of course lowers the overall SZ-noise contribution:

$$(C_\ell^{1h} + C_\ell^{2h}) \to \langle (a_{\ell m}^{\rm SZ} - \hat{a}_{\ell m})^2 \rangle = (C_\ell^{1h} + C_\ell^{2h}) - \langle \hat{a}_{\ell m}^{\rm SZ} \hat{a}_{\ell m'}^{\rm SZ} \rangle. \tag{4.37}$$

The structure of the 1-halo and 2-halo terms for the CMB lensing potential cross-correlation with the SZ effect is the same as for the SZ power spectrum, reading [244]:

$$\begin{aligned} C_\ell^{{\rm SZ}\phi,1h} &= \int {\rm d}z \frac{{\rm d}^2 V}{{\rm d}x\, {\rm d}\Omega} \int {\rm d}M \frac{{\rm d}n}{{\rm d}M}(z,M) |\tilde{y}_\ell(z,M) \tilde{\phi}_\ell(z,M)| \\ C_\ell^{{\rm SZ}\phi,2h} &= \int {\rm d}z \frac{{\rm d}^2 V}{{\rm d}x\, {\rm d}\Omega} D_+^2(z) P_m(k) \left[\int {\rm d}M \frac{{\rm d}n}{{\rm d}M}(z,M) b(z,M) a(z) \tilde{y}_{3D}(z,M,k) \right] \times \\ &\quad \times \left[\int {\rm d}M \frac{{\rm d}n}{{\rm d}M}(z,M) b(z,M) a(z) \tilde{\phi}_{3D}(z,M,k) \right] \Bigg|_{k=\left(\frac{\ell+1/2}{\chi(z)}\right)}, \end{aligned} \tag{4.38}$$

where $\tilde{\phi}_{3D}(z,M,k)$ is the Fourier transform of the halo contribution to the projected lensing potential,

$$\tilde{\phi}_\ell(z,M) = \frac{2}{\ell(\ell+1)} \frac{4\pi r_{s,\phi}}{\ell_{s,\phi}^2} \int {\rm d}x x^2 j_0\left(\frac{kx}{\ell_s}\right) \frac{4\pi G \chi(z)(\chi_* - \chi(z)) \rho_{\rm NFW}(z,M,k)}{c^2 \chi_* (1+z)}, \tag{4.39}$$

$r_{s,\phi}$ is the typical scale radius for $\tilde{\phi}_{3D}(z,M,k)$ and $\ell_{s,\phi} = a(z)\chi(z)/r_{s,\phi}$ is the associated multipole. One gets the CMB lensing potential power spectrum replacing the remaining $\tilde{y}_\ell(z,M)$ with $\tilde{\phi}_\ell(z,M)$. We checked our spectra against those shown in [244], changing our integration boundaries to match their choices, and we are in very good agreement with them.

As discussed in [244] the correlation of SZ and ϕ is small ($\approx 0.3 - 0.4$) up to $\ell =$ few $\times 10^3$ so we might expect only a small improvement. As a zeroth-order approximation, we can neglect T and E in eq. (4.35) and write $\hat{a}_{\ell m}^{\rm SZ} \approx 0.4 \times a_{\ell m}^{\rm SZ}$. In this limit the relation

in eq. (4.37) becomes

$$(C_\ell^{1h} + C_\ell^{2h}) \to (C_\ell^{1h} + C_\ell^{2h}) - \langle \hat{a}_{\ell m}^{\rm SZ} \hat{a}_{\ell m'}^{\rm SZ} \rangle \approx 0.84 (C_\ell^{1h} + C_\ell^{2h}). \tag{4.40}$$

Therefore using CMB lensing as a tracer should provide a $\approx 10\%$ improvement. Indeed the numerical evaluation of the cross-correlations validates this back-of-the-envelope estimate.

The second tracer we investigate is the galaxy-lensing convergence field. Its cross correlation with the SZ effect can again be computed by replacing, in eq. (4.38), $\tilde{\phi}_\ell(z, M)$ with [245, 246]

$$\tilde{\kappa}_\ell(z, M) = \frac{4\pi r_{s,\kappa}}{\ell_{s,\kappa}^2} \int {\rm d}x x^2 j_0 \left(\frac{kx}{\ell_{s,\kappa}} \right) \frac{4\pi G g(z) \rho_{\rm NFW}(z, M, k)}{c^2 (1+z)}, \tag{4.41}$$

where $r_{s,\kappa}$ is the typical scale radius of the lensing potential of the halo and $\ell_s = a(z)\chi(z)/r_{s,\kappa}$, and we defined

$$g(z) \equiv \int_{\chi(z)}^{\infty} {\rm d}\chi' \frac{\chi(z)[\chi' - \chi(z)]}{\chi'} p_S(\chi'), \tag{4.42}$$

where p_S is the redshift distribution of the sources. Again, one gets the power spectrum replacing the remaining $\tilde{y}_\ell(z, M)$ with $\tilde{\kappa}_\ell(z, M)$.

In this case, due to the higher correlation between the SZ effect and the galaxy lensing, the cleaning procedure performs better than with the CMB lensing. However the signal-to-noise ratio achieved with this procedure alone is still smaller than the S/N achievable via direct cluster masking. The optimal way to proceed is therefore to adopt the two approaches in combination. This can be done by reconstructing the $\hat{y}_{\rm SZ}(\hat{\boldsymbol{n}})$ map using tracers as discussed; then the resolved clusters can be masked in both the $y_{\rm obs}(\hat{\boldsymbol{n}})$ and the $\hat{y}_{\rm SZ}(\hat{\boldsymbol{n}})$ maps. The $y_{\rm clean}(\hat{\boldsymbol{n}})$ masked map is then obtained by difference.

We model this procedure in our forecast by changing the integration boundaries of all the integrals involving at least one power of $\tilde{y}_\ell(z, M)$ as discussed in subsection 4.1.4. The integrals involving only powers of $\tilde{\kappa}_\ell(z, M)$ (e.g. the second square bracket in the 2-halo term, eq. (4.38)) are left unmodified as the mask is applied to the reconstructed $\hat{y}_{\rm SZ}(\hat{\boldsymbol{n}})$ map, and not to the input lensing map. The final results are shown in table 4.2, for PIXIE, in table 4.3 for PRISM and in table 4.4, for an ideal survey.

Considering PIXIE, the forecasted signal-to-noise ratio quickly saturate when using more and more futuristic masks in combination with galaxy lensing, because the SZ power spectrum becomes rapidly sub-dominant with respect to the PIXIE noise. In the cosmic-variance limited case, however, SZ remains by far the dominant source of noise, even after cleaning, and makes y-based constraints much worse than μ-based one. Nonetheless it is important to stress again that y and μ probe very different scales, and thus add complementary information.

The measurement of $f_{\rm NL}^{y}$ that PRISM will achieve, contrary to PIXIE, will not be significantly limited by instrumental noise. In fact the signal-to-noise ratio for PRISM is effectively the same of a cosmic-variance limited experiment. This constraint ($1\sigma(f_{\rm NL}^{y}) = 260$ for PRISM) might not appear significant compared with the current bound set by *Planck* ($f_{\rm NL} = 0.6 \pm 5.0$, 68% C.L.) at first glance. However if one consider that $f_{\rm NL}$ might have a running, its importance change considerably. For example, if we consider a primordial bispectrum of the form [247]

$$B(k_1, k_2, k_3) \propto f_{\rm NL}^{*} \left[P(k_1)P(k2) \left(\frac{k_3}{k^*} \right)^{n_{\rm NG}} + 2 \text{ perm.} \right], \tag{4.43}$$

and use 1σ upper bounds $f_{\rm NL}^{*} = 5$, $n_{\rm NG} = 1$, consistent with current observations [248], we would expect $f_{\rm NL}^{y} \approx 700$ on the y-scales, way above the detectability limit. It is worth noticing that in [237] it has been shown that $n_{\rm NG} \neq 0$ would also enhance the average distortion and thus lead to an additional improvement of the sensitivity, making our point even stronger. Even though the bispectrum in eq. (4.43) is theoretically well-motivated, it has to be considered here just as a toy-model, because we made a choice of values of the parameters that might be outside the range of validity of the model itself. The point here is just to use a phenomenological, toy-model shape, just to show in a simple, quantitative way how y-constraints are useful, even if they turn out 2 orders of magnitude worse than current T, E bispectrum bounds.

Of course one may argue that the same holds, even more so, for $f_{\rm NL}^{\mu}$ on the μ-scales, but to avoid pathologically large non-Gaussianity on the smallest scales, the increasing trend has to stop somewhere. Therefore it is again important to study both the y- and the μ-scales.

4.1.5. Discussion

In this section we investigated in detail the effects of including CMB polarization in NG studies of cross-correlation between CMB primary anisotropies and μ- and y-CMB-distortions. Including the previously unaccounted y-E spectrum, besides adding new signal, has the important advantage of making the primordial NG analysis more robust, since it removes the large bias arising from the ISW-SZ contribution in the y-T spectrum. Potential spurious contamination in the primordial y-E signal can come from reionization, but this turned out to be negligible after a complete numerical analysis at second order in the perturbations. In addition to considering y-E spectra, we also studied in detail how to reduce SZ contamination, thus lowering the overall noise contribution, considering two approaches. The former, already considered in previous works [126, 211], consists in masking low-redshift clusters, detected via X-ray surveys. To this, we add the exploitation of cross-correlation with external tracers, namely CMB and galaxy lensing, as a way to partially reconstruct the y contribution from unresolved clusters. The template so-obtained is then used to clean the y-map from the remaining unresolved contribution.

Using this procedure, we obtain $f_{\rm NL}^{y}$ forecasts for PIXIE, PRISM, and for an ideal cosmic-variance limited experiment. In all cases we find that including y-E leads to improvements in the $f_{\rm NL}^{y}$ constraint by a factor between 2.1 and 3.8, depending on the considered survey and mask. A further error bar improvement of order 25% is expected from external-tracer cross-correlation and template cleaning. Our final forecasts are then $1\sigma(f_{\rm NL}^{y}) = 2300$ for PIXIE, $1\sigma(f_{\rm NL}^{y}) = 300$ for PRISM and $1\sigma(f_{\rm NL}^{y}) = 130$ for the cosmic-variance limited case, thus improving the previous estimates by an overall factor between 2.5 and 4.4.

It is clear that, even in the ideal scenario, $f_{\rm NL}$ constraints based on y are very poor when compared to current *Planck* bispectrum measurements. For the cosmic-variance limited case, the errors achievable using μ, $1\sigma(f_{\rm NL}^{\mu}) = 0.55\times10^{-3}$, are also orders of magnitude smaller than those achievable using y. This is due to residual SZ contamination, still significant even after masking and template reconstruction and cleaning. Nevertheless, two things are worth noticing: first, the constrains on $f_{\rm NL}^{y}$ and $f_{\rm NL}^{\mu}$ achievable with a realistic (not cosmic variance-limited) survey design (e.g. PIXIE, PRISM) are comparable.

Second, and most important, the main goal we consider here is to test NG scale-dependence. In this respect, $f_{\rm NL}^{y}$ measurements are very interesting, even with all the limitations imposed by SZ contamination, because they open a new window on an

otherwise inaccessible range of scales: a simple example to illustrate this point is provided by the bispectrum toy model, characterized by an $f_{\rm NL}$-running parameter, considered at the end of Section 4.1.4.

Conclusions

In this thesis I investigated various methods to determine the physical properties of the primordial perturbation field, that might go beyond the most minimal model of Gaussian adiabatic density perturbations with a power-law primordial power spectrum.

Primordial power spectrum reconstruction. In Section 3.1 we have built on the work of [143, 144] to reconstruct the PPS with a minimally parametric approach, using the cross-validation technique as the smoothness criterion. The analysis is based on a comprehensive set of state-of-the art cosmological data including probes of the Cosmic Microwave Background, and of large scale structure via gravitational lensing and galaxy redshift surveys.

We found that there is no evidence for deviations from a power law PPS, and that errors of the reconstructed PPS are comparable with errors obtained with a power law fit. In fact with current data a scale-invariant power spectrum is highly disfavoured even with this minimally parametric reconstruction. Because of its flexibility, our reconstruction would be able to detect the tell-tale signature of small scale power suppression induced by free streaming of neutrino if they are sufficiently massive.[3] However, our reconstruction detects no such signature, ruling out a model with a power law PPS and sum of neutrino masses of 0.2 eV or larger.

Overall our results, which recover in a model independent way a power law power spectrum with a small but highly significant red tilt, offer a powerful confirmation of the inflationary paradigm, justifying adoption of the inflationary prior in cosmological analyses.

[3] Of course the suppression would happen in the late-time power spectrum, not in the primordial one. However, since we do not include the effect of neutrino masses in the matter transfer function, the reconstruction would recover an "effective" small scale damping.

Compensated isocurvature perturbations. In Section 3.2 I discussed the viability of using cross correlations of y-distortion anisotropies with primary anisotropies to constrain compensated isocurvature perturbations. We provided a new framework to calculate the y-distortions that arise at first order in perturbation theory, and derived its evolution equation. As it turns out, it is directly proportional to baryon isocurvature perturbations. This implies that, since it is not affected by cold dark matter isocurvature perturbation, it can be in principle used to detect CIPs. We produced a forecast for the upper bounds on correlated CIPs for different future observational projects, keeping in consideration the contamination due to SZ effect, but neglecting other foregrounds. Even in this idealized scenario, a signal can be detected only in the presence of CIPs with unnaturally high amplitude. For instance, $f' < 2 \times 10^5$ at 68% C.L. is obtained for LiteBIRD, while $f' < 5 \times 10^4$ for PRISM, and $f' < 2 \times 10^4$ for a cosmic variance limited survey. As we have shown, the fundamental limit is set by the noise contribution due to the SZ powerspectrum.

Primordial non-Gaussianity. In Section 4.1 I developed a set of measures that can be employed to use y-distortions to constrain primordial non-Gaussianity. I investigated in detail the effects of including CMB polarization in NG studies of cross-correlation between CMB primary anisotropies and μ- and y-CMB-distortions, that besides adding new signal, has the important advantage of making the primordial NG analysis more robust, since it removes the large bias arising from the ISW-SZ contribution in the y-T spectrum. In addition to considering y-E spectra, we also studied in detail how to reduce SZ contamination, thus lowering the overall noise contribution, masking low-redshift clusters and exploiting cross-correlation with external tracers, to reconstruct the y contribution from unresolved clusters, and remove it from the analysed maps. Using this procedure, we obtain $f^y_{\rm NL}$ forecasts for PIXIE, PRISM, and for an ideal cosmic-variance limited experiment. Our final forecasts are then $1\sigma(f^y_{\rm NL}) = 2300$ for PIXIE, $1\sigma(f^y_{\rm NL}) = 300$ for PRISM and $1\sigma(f^y_{\rm NL}) = 130$ for the cosmic-variance limited case, thus improving the previous estimates by an overall factor between 2.5 and 4.4.

Appendix A.

Useful mathematical relation involving spherical functions

A.1. Spherical Harmonics

The spherical harmonics are an orthonormal basis of functions defined on the sphere. They are usually defined as

$$Y_{\ell m}(\hat{\boldsymbol{n}}) \equiv Y_{\ell m}(\theta, \phi) \equiv \sqrt{\frac{2\ell+1}{4\pi}\frac{(\ell-m)!}{(\ell+m)!}} P_\ell^m(\cos\theta) e^{im\phi}\,, \tag{A.1}$$

where $P_\ell^m(x)$ is the associate Legendre polynomial, defined through derivatives of the Legendre polynomials as

$$P_\ell^m(x) \equiv (-1)^m (1-x^2)^{m/2} \frac{\mathrm{d}^m}{\mathrm{d}x^m} P_\ell(x)\,. \tag{A.2}$$

As anticipated, the spherical harmonics are orthonormal

$$\int \mathrm{d}^2\,\hat{\boldsymbol{n}} Y_{\ell m}(\hat{\boldsymbol{n}}) Y^*_{\ell' m'}(\hat{\boldsymbol{n}}) = \delta_{\ell\ell'}\,\delta_{mm'}\,, \tag{A.3}$$

and have a definite parity for a given ℓ

$$Y_{\ell m}(-\hat{\boldsymbol{n}}) = (-1)^\ell Y_{\ell m}(\hat{\boldsymbol{n}})\,, \tag{A.4}$$

and under rotations they transform with a spin-weighted spherical harmonics[1]

$$Y_{\ell m}(\hat{\boldsymbol{n}}') = \sum_{m'=-\ell}^{\ell} \left[(-1)^{-m} \sqrt{\frac{4\pi}{2\ell+1}}\, {}_{m'}Y_{\ell -m}(\alpha,\beta) e^{-im'\gamma} \right]^* Y_\ell^{m'}(\hat{\boldsymbol{n}})\,, \tag{A.5}$$

where α, β and γ are the rotation Euler angles.

By explicit calculation of the right hand side we can show that

$$\hat{\boldsymbol{q}}_{\boldsymbol{1}} \cdot \hat{\boldsymbol{q}}_{\boldsymbol{2}} = \frac{4\pi}{3} \sum_{m_2=-1}^{1} Y_1^{m_2 *}(\hat{\boldsymbol{q}}_{\boldsymbol{1}}) Y_1^{m_2}(\hat{\boldsymbol{q}}_{\boldsymbol{2}})\,. \tag{A.6}$$

When dealing with the projection of 3D fields on a sphere, it is often useful to expand plane waves as a sum of spherical harmonics using

$$e^{i\boldsymbol{x}\cdot\boldsymbol{k}} = 4\pi \sum_{\ell m} i^\ell j_\ell(kx) Y_{\ell m}(\boldsymbol{k}) Y^*_{\ell m}(\boldsymbol{x})\,, \tag{A.7}$$

and to express the Dirac delta the Rayleigh expansion, that immediately follows from eq. (A.7)

$$\delta^{(3)}\left(\sum_{i=1}^{n} \boldsymbol{k_i}\right) = (4\pi)^n \int \mathrm{d}x\, x^2 \int \mathrm{d}^2\hat{\boldsymbol{x}} \prod_{i=1}^{n} \left[\sum_{\ell_i m_i} j_{\ell_i}(k_i r)\, Y_{\ell_i m_i}(\hat{\boldsymbol{x}}) Y^*_{\ell_i m_i}(\hat{\boldsymbol{k}}_i) \right]. \tag{A.8}$$

$$\int \mathrm{d}^2\hat{\boldsymbol{x}}\, Y^*_{\ell m}(\hat{\boldsymbol{x}})\, P_{\ell'}(\hat{\boldsymbol{x}}\cdot\hat{\boldsymbol{k}}) = \delta_{\ell\ell'} \frac{4\pi}{2\ell+1} Y_{\ell m}(\hat{\boldsymbol{k}})\,. \tag{A.9}$$

A.2. Wigner 3-j symbols

The Wigner 3-j symbols are defined in terms of Clebsch-Gordan as

$$\begin{pmatrix} \ell_1 & \ell_2 & \ell_3 \\ m_1 & m_2 & m_3 \end{pmatrix} = \frac{(-1)^{\ell_1 - \ell_2 - m_3}}{\sqrt{2\ell_3+1}} \langle \ell_1\, m_1\, \ell_2\, m_2 | \ell_3\, -m_3 \rangle\,. \tag{A.10}$$

[1] We do not define spherical harmonics here, as their analytic expression is not very illuminating. We notice however that a spin 0 spherical harmonic is a normal spherical harmonic.

This relation can be inverted to find

$$\langle \ell_1\, m_1\, \ell_2\, m_2 | \ell_3\, m_3 \rangle = (-1)^{-\ell_1+\ell_2-m_3}\sqrt{2\ell_3+1}\begin{pmatrix} \ell_1 & \ell_2 & \ell_3 \\ m_1 & m_2 & -m_3 \end{pmatrix}. \tag{A.11}$$

Selection rules The 3j-symbols are non-vanishing if and only if

$$|m_i| \leq \ell_i \quad i = 1, 2, 3\,, \tag{A.12}$$

$$m_1 + m_2 + m_3 = 0\,, \tag{A.13}$$

$$|\ell_1 - \ell_2| \leq \ell_3 \leq |\ell_1 + \ell_2|\,. \tag{A.14}$$

Symmetries The 3j-symbols are symmetric under even permutations of the columns

$$\begin{pmatrix} \ell_1 & \ell_2 & \ell_3 \\ m_1 & m_2 & m_3 \end{pmatrix} = \begin{pmatrix} \ell_3 & \ell_1 & \ell_2 \\ m_3 & m_1 & m_2 \end{pmatrix} = \begin{pmatrix} \ell_2 & \ell_3 & \ell_1 \\ m_2 & m_3 & m_1 \end{pmatrix}. \tag{A.15}$$

whereas they gain a ± 1 factor under odd permutations of the column, as follows

$$\begin{pmatrix} \ell_1 & \ell_2 & \ell_3 \\ m_1 & m_2 & m_3 \end{pmatrix} = (-1)^{\ell_1+\ell_2+\ell_3}\begin{pmatrix} \ell_2 & \ell_1 & \ell_3 \\ m_2 & m_1 & m_3 \end{pmatrix}, \tag{A.16}$$

or if the m coefficients signs are reversed

$$\begin{pmatrix} \ell_1 & \ell_2 & \ell_3 \\ -m_1 & -m_2 & -m_3 \end{pmatrix} = (-1)^{\ell_1+\ell_2+\ell_3}\begin{pmatrix} \ell_2 & \ell_1 & \ell_3 \\ m_2 & m_1 & m_3 \end{pmatrix}, \tag{A.17}$$

Orthogonality relations

$$\sum_{M_1\, M_2} \begin{pmatrix} \ell_1 & \ell_2 & \ell \\ M_1 & M_2 & m \end{pmatrix}\begin{pmatrix} \ell_1 & \ell_2 & \ell' \\ M_1 & M_2 & m' \end{pmatrix} = \frac{\delta_m^{m'}\,\delta_\ell^{\ell'}}{2\ell+1}\Big\{ \ell_1 \quad \ell_2 \quad \ell_3 \Big\}, \tag{A.18}$$

where the *triangular delta* $\{\ell_1 \quad \ell_2 \quad \ell_3\} = 1$ if and only if the triangle condition $|\ell_1 - \ell_2| \leq \ell_3 \leq |\ell_1 + \ell_2|$ holds, and is 0 otherwise.

$$\sum_{LM}(2L+1)\begin{pmatrix}\ell_1 & \ell_2 & L\\ m_1 & m_2 & M\end{pmatrix}\begin{pmatrix}\ell_1 & \ell_2 & L\\ m_1 & m_2 & M\end{pmatrix} = \delta^{m_1'}_{m_1}\,\delta^{m_2'}_{m_2} \tag{A.19}$$

Relation with spin weighted spherical harmonics

$$\begin{aligned}\int \mathrm{d}^2\hat{\boldsymbol{x}}\; {}_{s_1}Y_{\ell_1 m_1}(\hat{\boldsymbol{x}})\, {}_{s_2}Y_{\ell_2 m_2}(\hat{\boldsymbol{x}})\, {}_{s_3}Y_{\ell_3 m_3}(\hat{\boldsymbol{x}}) = \\ =(-1)^{m_1+s_1}\sqrt{\frac{(2\ell_1+1)(2\ell_2+1)(2\ell_3+1)}{4\pi}}\begin{pmatrix}\ell_1 & \ell_2 & \ell_3\\ -s_1 & -s_2 & -s_3\end{pmatrix}\begin{pmatrix}\ell_1 & \ell_2 & \ell_3\\ m_1 & m_2 & m_3\end{pmatrix}\end{aligned} \tag{A.20}$$

Useful relations

$$\sum_m (-1)^{\ell-m}\begin{pmatrix}\ell & \ell & L\\ m & -m & 0\end{pmatrix} = \sqrt{2\ell+1}\,\delta^0_L \tag{A.21}$$

A.3. Wigner 6-j symbols

Wigner 6-j symbols are defined in term of sum of products of 3-j symbol

$$\begin{Bmatrix}\ell_1 & \ell_2 & \ell_3\\ \ell_4 & \ell_5 & \ell_6\end{Bmatrix} = \sum_{m_1,\cdots,m_6}(-1)^{\sum_i (j_i - m_i)}\begin{pmatrix}\ell_1 & \ell_2 & \ell_3\\ -m_1 & -m_2 & -m_3\end{pmatrix}\begin{pmatrix}\ell_1 & \ell_5 & \ell_6\\ m_1 & -m_5 & m_6\end{pmatrix}\times \\ \times\begin{pmatrix}\ell_4 & \ell_2 & \ell_6\\ m_4 & m_2 & -m_6\end{pmatrix}\begin{pmatrix}\ell_4 & \ell_5 & \ell_3\\ -m_4 & m_5 & m_3\end{pmatrix} \tag{A.22}$$

A.4. Spherical Bessel functions

It has been shown in [241] that

$$
\begin{aligned}
&I(L_1,L_2,L_3,q_1,q_2,k) \equiv \int x^2\,\mathrm{d}x j_{L_1}(xq_1)j_{L_2}(xq_2)j_L(xk_1) = \\
=&\frac{\pi\beta(\Delta)}{4q_1q_2k} i^{L_1+L_2-L}\sqrt{2L+1}\left(\frac{q_1}{k}\right)^L \begin{pmatrix} L_1 & L_2 & L \\ 0 & 0 & 0 \end{pmatrix}^{-1} \\
&\sum_{\mathcal{L}=0}^{L} \begin{pmatrix} 2L \\ 2\mathcal{L} \end{pmatrix}^{1/2} \left(\frac{q_2}{q_1}\right)^{\mathcal{L}} \sum_l (2l+1) \begin{pmatrix} L_1 & L-\mathcal{L} & l \\ 0 & 0 & 0 \end{pmatrix} \begin{pmatrix} L_2 & \mathcal{L} & l \\ 0 & 0 & 0 \end{pmatrix} \begin{Bmatrix} L_1 & L_2 & L \\ \mathcal{L} & L-\mathcal{L} & l \end{Bmatrix} P_l(\Delta)\ .
\end{aligned}
\tag{A.23}
$$

The triangular condition over the three momenta is enforced by $\beta(x) = \theta_H(1-x)\theta_H(1+x)$, where $\Delta = \frac{q_1^2+q_2^2-k^2}{2q_1q_2}$ and $\theta_H(x)$ is the modified Heaviside function.

In the case $L1 = L2 = L = 0$ the expression simplifies noticibly as we have

$$
\begin{aligned}
&\int \mathrm{d}x\ x^2 j_0(k_1x)j_0(k_2x)j_0(k_3x) = \int \mathrm{d}x \frac{\sin(k_1x)\sin(k_2x)\sin(k_3x)}{k_1k_2k_3x} = \\
&=\frac{1}{4k_1k_2k_3}\int \mathrm{d}x \left\{ \frac{\sin[(k_1+k_2-k_3)x]}{x} + \frac{\sin[(k_2+k_3-k_1)x]}{x} \right. \\
&\qquad\qquad \left. + \frac{\sin[(k_3+k_1-k_2)x]}{x} - \frac{\sin[(k_1+k_2+k_3)x]}{x} \right\} = \\
&=\frac{\pi\left(\sigma(k_1+k_2-k_3)+\sigma(k_2+k_3-k_1)+\sigma(k_3+k_1-k_2)-\sigma(k_1+k_2+k_3)\right)}{8k_1k_2k_3}\ .
\end{aligned}
\tag{A.24}
$$

where $\sigma(x) = x/|x|$ is the sign of x.

Colophon

This thesis was made in LaTeX 2_ε using the "hepthesis" class [249].

Bibliography

[1] Planck collaboration, P.A.R. Ade et al., *Planck 2013 results. I. Overview of products and scientific results*, *Astron. Astrophys.* **571** (2014) A1 [arXiv:1303.5062].

[2] Planck collaboration, P.A.R. Ade et al., *Planck 2015 results. XIII. Cosmological parameters*, *Astron. Astrophys.* **594** (2016) A13 [arXiv:1502.01589].

[3] Planck collaboration, P.A.R. Ade et al., *Planck 2015 results. XVII. Constraints on primordial non-Gaussianity*, arXiv:1502.01592.

[4] V. Miranda and W. Hu, *Inflationary Steps in the Planck Data*, *Phys. Rev.* **D89** (2014) 083529 [arXiv:1312.0946].

[5] P.D. Meerburg and D.N. Spergel, *Searching for oscillations in the primordial power spectrum. II. Constraints from Planck data*, *Phys. Rev.* **D89** (2014) 063537 [arXiv:1308.3705].

[6] X. Chen, M.H. Namjoo and Y. Wang, *Models of the Primordial Standard Clock*, *JCAP* **1502** (2015) 027 [arXiv:1411.2349].

[7] U.H. Danielsson, *A Note on inflation and transPlanckian physics*, *Phys. Rev.* **D66** (2002) 023511 [hep-th/0203198].

[8] C. Gordon and A. Lewis, *Observational constraints on the curvaton model of inflation*, *Phys. Rev.* **D67** (2003) 123513 [astro-ph/0212248].

[9] E. Pajer and M. Zaldarriaga, *A New Window on Primordial non-Gaussianity*, *Phys.Rev.Lett.* **109** (2012) 021302 [arXiv:1201.5375].

[10] R. Emami, E. Dimastrogiovanni, J. Chluba and M. Kamionkowski, *Probing the scale dependence of non-Gaussianity with spectral distortions of the cosmic microwave background*, *Phys. Rev.* **D91** (2015) 123531 [arXiv:1504.00675].

[11] J.P. Ostriker and P.J. Steinhardt, *Cosmic concordance*, astro-ph/9505066.

[12] N.W. Boggess et al., *The COBE mission - Its design and performance two years after launch*, *Astrophys. J.* **397** (1992) 420.

[13] WMAP collaboration, C.L. Bennett et al., *Nine-Year Wilkinson Microwave Anisotropy Probe (WMAP) Observations: Final Maps and Results*, *Astrophys. J. Suppl.* **208** (2013) 20 [arXiv:1212.5225].

[14] Planck collaboration, N. Aghanim et al., *Planck 2018 results. VI. Cosmological parameters*, arXiv:1807.06209.

[15] Supernova Search Team collaboration, A.G. Riess et al., *Observational evidence from supernovae for an accelerating universe and a cosmological constant*, *Astron. J.* **116** (1998) 1009 [astro-ph/9805201].

[16] A.G. Riess et al., *Milky Way Cepheid Standards for Measuring Cosmic Distances and Application to Gaia DR2: Implications for the Hubble Constant*, *Astrophys. J.* **861** (2018) 126 [arXiv:1804.10655].

[17] B.A. Reid, W.J. Percival, D.J. Eisenstein, L. Verde, D.N. Spergel, R.A. Skibba et al., *Cosmological constraints from the clustering of the Sloan Digital Sky Survey DR7 luminous red galaxies*, MNRAS **404** (May, 2010) 60 [arXiv:0907.1659].

[18] D. Parkinson, S. Riemer-Sørensen, C. Blake, G.B. Poole, T.M. Davis, S. Brough et al., *The WiggleZ Dark Energy Survey: Final data release and cosmological results*, Phys. Rev. D **86** (Nov., 2012) 103518 [arXiv:1210.2130].

[19] D.W. Hogg, D.J. Eisenstein, M.R. Blanton, N.A. Bahcall, J. Brinkmann, J.E. Gunn et al., *Cosmic homogeneity demonstrated with luminous red galaxies*, *Astrophys. J.* **624** (2005) 54 [astro-ph/0411197].

[20] P. Sarkar, J. Yadav, B. Pandey and S. Bharadwaj, *The scale of homogeneity of the galaxy distribution in SDSS DR6*, *Mon. Not. Roy. Astron. Soc.* **399** (2009) L128 [arXiv:0906.3431].

[21] M. Scrimgeour et al., *The WiggleZ Dark Energy Survey: the transition to large-scale cosmic homogeneity*, *Mon. Not. Roy. Astron. Soc.* **425** (2012) 116 [arXiv:1205.6812].

[22] S. Weinberg, *Gravitation and Cosmology*, John Wiley and Sons, New York (1972), http://www-spires.fnal.gov/spires/find/books/www?cl=QC6.W431.

[23] S. Dodelson, *Modern cosmology*, Elsevier (2003).

[24] S. Weinberg, *Cosmology*, Oxford University Press (2008).

[25] S. Carroll, *Spacetime and Geometry: An Introduction to General Relativity*, Pearson (2003).

[26] D. Baumann, *Cosmology*, `http://www.damtp.cam.ac.uk/user/db275/Cosmology/Lectures.pdf`.

[27] E. Kolb, *The early universe*, CRC Press (2018).

[28] J. Chluba, *Science with Spectral Distortions of the Cosmic Microwave Background*, `http://www.jb.man.ac.uk/%7Ejchluba/Science/CUSO_Lecture_Notes_JC.pdf`.

[29] L. Hart and J. Chluba, *New constraints on time-dependent variations of fundamental constants using Planck data*, *Mon. Not. Roy. Astron. Soc.* **474** (2018) 1850 [`arXiv:1705.03925`].

[30] J. Chluba and R. Sunyaev, *The evolution of CMB spectral distortions in the early Universe*, *Mon.Not.Roy.Astron.Soc.* **419** (2012) 1294 [`arXiv:1109.6552`].

[31] J. Chluba, R. Khatri and R.A. Sunyaev, *CMB at 2x2 order: The dissipation of primordial acoustic waves and the observable part of the associated energy release*, *Mon.Not.Roy.Astron.Soc.* **425** (2012) 1129 [`arXiv:1202.0057`].

[32] A. Kompaneets, *The establishment of thermal equilibrium between quanta and electrons*, *Soviet Physics JETP* **4** (1957) 730.

[33] Ya.B. Zeldovich and R.A. Sunyaev, *The Interaction of Matter and Radiation in a Hot-Model Universe*, *Astrophys. Space Sci.* **4** (1969) 301.

[34] R.A. Sunyaev and Ya.B. Zeldovich, *The Interaction of matter and radiation in the hot model of the universe*, *Astrophys. Space Sci.* **7** (1970) 20.

[35] A.H. Guth, *The Inflationary Universe: A Possible Solution to the Horizon and Flatness Problems*, *Phys. Rev.* **D23** (1981) 347.

[36] A.H. Guth and S.Y. Pi, *Fluctuations in the New Inflationary Universe*, *Phys. Rev. Lett.* **49** (1982) 1110.

[37] A.D. Linde, *Scalar Field Fluctuations in Expanding Universe and the New*

Inflationary Universe Scenario, *Phys. Lett.* **116B** (1982) 335.

[38] J. Martin, C. Ringeval and V. Vennin, *Encyclopædia Inflationaris*, *Phys. Dark Univ.* **5-6** (2014) 75 [arXiv:1303.3787].

[39] D. Polarski and A.A. Starobinsky, *Isocurvature perturbations in multiple inflationary models*, *Phys. Rev.* **D50** (1994) 6123 [astro-ph/9404061].

[40] V.F. Mukhanov and P.J. Steinhardt, *Density perturbations in multifield inflationary models*, *Phys. Lett.* **B422** (1998) 52 [astro-ph/9710038].

[41] N. Bartolo, S. Matarrese and A. Riotto, *Adiabatic and isocurvature perturbations from inflation: Power spectra and consistency relations*, *Phys. Rev.* **D64** (2001) 123504 [astro-ph/0107502].

[42] D.H. Lyth and D. Wands, *Generating the curvature perturbation without an inflaton*, *Phys. Lett.* **B524** (2002) 5 [hep-ph/0110002].

[43] D. Wands, N. Bartolo, S. Matarrese and A. Riotto, *An Observational test of two-field inflation*, *Phys. Rev.* **D66** (2002) 043520 [astro-ph/0205253].

[44] R. Easther, J. Frazer, H.V. Peiris and L.C. Price, *Simple predictions from multifield inflationary models*, *Phys. Rev. Lett.* **112** (2014) 161302 [arXiv:1312.4035].

[45] A. Golovnev, V. Mukhanov and V. Vanchurin, *Vector Inflation*, *JCAP* **0806** (2008) 009 [arXiv:0802.2068].

[46] S. Yokoyama and J. Soda, *Primordial statistical anisotropy generated at the end of inflation*, *JCAP* **0808** (2008) 005 [arXiv:0805.4265].

[47] M. Karciauskas, K. Dimopoulos and D.H. Lyth, *Anisotropic non-Gaussianity from vector field perturbations*, *Phys. Rev.* **D80** (2009) 023509 [arXiv:0812.0264].

[48] N. Bartolo, E. Dimastrogiovanni, S. Matarrese and A. Riotto, *Anisotropic bispectrum of curvature perturbations from primordial non-Abelian vector fields*, *JCAP* **0910** (2009) 015 [arXiv:0906.4944].

[49] E. Dimastrogiovanni, N. Bartolo, S. Matarrese and A. Riotto, *Non-Gaussianity and Statistical Anisotropy from Vector Field Populated Inflationary Models*, *Adv. Astron.* **2010** (2010) 752670 [arXiv:1001.4049].

[50] N. Bartolo, S. Matarrese, M. Peloso and A. Ricciardone, *Anisotropic power*

spectrum and bispectrum in the $f(\phi)F^2$ mechanism, *Phys.Rev.* **D87** (2013) 023504 [arXiv:1210.3257].

[51] M.P. Hertzberg, *On Inflation with Non-minimal Coupling*, *JHEP* **11** (2010) 023 [arXiv:1002.2995].

[52] D. La and P.J. Steinhardt, *Extended Inflationary Cosmology*, *Phys. Rev. Lett.* **62** (1989) 376.

[53] A.A. Starobinsky, *Spectrum of adiabatic perturbations in the universe when there are singularities in the inflation potential*, *JETP Lett.* **55** (1992) 489.

[54] J.E. Lidsey, A.R. Liddle, E.W. Kolb, E.J. Copeland, T. Barreiro and M. Abney, *Reconstructing the inflation potential : An overview*, *Rev. Mod. Phys.* **69** (1997) 373 [astro-ph/9508078].

[55] A.R. Liddle, P. Parsons and J.D. Barrow, *Formalizing the slow roll approximation in inflation*, *Phys. Rev.* **D50** (1994) 7222 [astro-ph/9408015].

[56] D.H. Lyth and A. Riotto, *Particle physics models of inflation and the cosmological density perturbation*, *Phys. Rept.* **314** (1999) 1 [hep-ph/9807278].

[57] J. Lesgourgues, D. Polarski and A.A. Starobinsky, *CDM models with a BSI step - like primordial spectrum and a cosmological constant*, *Mon. Not. Roy. Astron. Soc.* **297** (1998) 769 [astro-ph/9711139].

[58] L.M. Wang and M. Kamionkowski, *The Cosmic microwave background bispectrum and inflation*, *Phys. Rev.* **D61** (2000) 063504 [astro-ph/9907431].

[59] J.A. Adams, B. Cresswell and R. Easther, *Inflationary perturbations from a potential with a step*, *Phys. Rev.* **D64** (2001) 123514 [astro-ph/0102236].

[60] J.O. Gong, *Breaking scale invariance from a singular inflaton potential*, *JCAP* **0507** (2005) 015 [astro-ph/0504383].

[61] D. Cannone, N. Bartolo and S. Matarrese, *Perturbative Unitarity of Inflationary Models with Features*, *Phys. Rev.* **D89** (2014) 127301 [arXiv:1402.2258].

[62] C. Pahud, M. Kamionkowski and A.R. Liddle, *Oscillations in the inflaton potential?*, *Phys. Rev.* **D79** (2009) 083503 [arXiv:0807.0322].

[63] R. Flauger, L. McAllister, E. Pajer, A. Westphal and G. Xu, *Oscillations in the CMB from Axion Monodromy Inflation*, *JCAP* **1006** (2010) 009

[arXiv:0907.2916].

[64] R. Flauger and E. Pajer, *Resonant Non-Gaussianity*, *JCAP* **1101** (2011) 017 [arXiv:1002.0833].

[65] M. Alishahiha, E. Silverstein and D. Tong, *DBI in the sky*, *Phys. Rev.* **D70** (2004) 123505 [hep-th/0404084].

[66] J. Ganc, *Calculating the local-type fNL for slow-roll inflation with a non-vacuum initial state*, *Phys. Rev.* **D84** (2011) 063514 [arXiv:1104.0244].

[67] J.M. Bardeen, *Gauge Invariant Cosmological Perturbations*, *Phys. Rev.* **D22** (1980) 1882.

[68] H. Kodama and M. Sasaki, *Cosmological Perturbation Theory*, *Prog. Theor. Phys. Suppl.* **78** (1984) 1.

[69] C.P. Ma and E. Bertschinger, *Cosmological perturbation theory in the synchronous and conformal Newtonian gauges*, *Astrophys. J.* **455** (1995) 7 [astro-ph/9506072].

[70] V.F. Mukhanov, H.A. Feldman and R.H. Brandenberger, *Theory of cosmological perturbations. Part 1. Classical perturbations. Part 2. Quantum theory of perturbations. Part 3. Extensions*, *Phys. Rept.* **215** (1992) 203.

[71] K.A. Malik and D. Wands, *Cosmological perturbations*, *Phys. Rept.* **475** (2009) 1 [arXiv:0809.4944].

[72] K.A. Malik, D. Wands and C. Ungarelli, *Large scale curvature and entropy perturbations for multiple interacting fluids*, *Phys. Rev.* **D67** (2003) 063516 [astro-ph/0211602].

[73] Planck collaboration, Y. Akrami et al., *Planck 2018 results. X. Constraints on inflation*, arXiv:1807.06211.

[74] N. Bartolo, E. Komatsu, S. Matarrese and A. Riotto, *Non-Gaussianity from inflation: Theory and observations*, *Phys. Rept.* **402** (2004) 103 [astro-ph/0406398].

[75] E. Komatsu et al., *Non-Gaussianity as a Probe of the Physics of the Primordial Universe and the Astrophysics of the Low Redshift Universe*, arXiv:0902.4759.

[76] X. Chen, *Primordial Non-Gaussianities from Inflation Models*, *Adv. Astron.* **2010** (2010) 638979 [arXiv:1002.1416].

[77] A.P.S. Yadav and B.D. Wandelt, *Primordial Non-Gaussianity in the Cosmic Microwave Background*, *Adv. Astron.* **2010** (2010) 565248 [arXiv:1006.0275].

[78] M. Liguori, E. Sefusatti, J.R. Fergusson and E.P.S. Shellard, *Primordial non-Gaussianity and Bispectrum Measurements in the Cosmic Microwave Background and Large-Scale Structure*, *Adv. Astron.* **2010** (2010) 980523 [arXiv:1001.4707].

[79] V. Acquaviva, N. Bartolo, S. Matarrese and A. Riotto, *Second order cosmological perturbations from inflation*, *Nucl. Phys.* **B667** (2003) 119 [astro-ph/0209156].

[80] J.M. Maldacena, *Non-Gaussian features of primordial fluctuations in single field inflationary models*, *JHEP* **05** (2003) 013 [astro-ph/0210603].

[81] P. Creminelli, *On non-Gaussianities in single-field inflation*, *JCAP* **0310** (2003) 003 [astro-ph/0306122].

[82] A.D. Linde and V.F. Mukhanov, *Nongaussian isocurvature perturbations from inflation*, *Phys. Rev.* **D56** (1997) R535 [astro-ph/9610219].

[83] N. Bartolo, S. Matarrese and A. Riotto, *On nonGaussianity in the curvaton scenario*, *Phys. Rev.* **D69** (2004) 043503 [hep-ph/0309033].

[84] M. Zaldarriaga, *Non-Gaussianities in models with a varying inflaton decay rate*, *Phys. Rev.* **D69** (2004) 043508 [astro-ph/0306006].

[85] G. Dvali, A. Gruzinov and M. Zaldarriaga, *Cosmological perturbations from inhomogeneous reheating, freezeout, and mass domination*, *Phys. Rev.* **D69** (2004) 083505 [astro-ph/0305548].

[86] D. Seery and J.E. Lidsey, *Primordial non-Gaussianities from multiple-field inflation*, *JCAP* **0509** (2005) 011 [astro-ph/0506056].

[87] G.I. Rigopoulos, E.P.S. Shellard and B.J.W. van Tent, *Large non-Gaussianity in multiple-field inflation*, *Phys. Rev.* **D73** (2006) 083522 [astro-ph/0506704].

[88] M. Sasaki, J. Valiviita and D. Wands, *Non-Gaussianity of the primordial perturbation in the curvaton model*, *Phys. Rev.* **D74** (2006) 103003 [astro-ph/0607627].

[89] C.T. Byrnes, K.Y. Choi and L.M.H. Hall, *Conditions for large non-Gaussianity in two-field slow-roll inflation*, *JCAP* **0810** (2008) 008 [arXiv:0807.1101].

[90] C.T. Byrnes and G. Tasinato, *Non-Gaussianity beyond slow roll in multi-field inflation*, *JCAP* **0908** (2009) 016 [arXiv:0906.0767].

[91] D. Babich, P. Creminelli and M. Zaldarriaga, *The Shape of non-Gaussianities*, *JCAP* **0408** (2004) 009 [astro-ph/0405356].

[92] X. Chen, M.x. Huang, S. Kachru and G. Shiu, *Observational signatures and non-Gaussianities of general single field inflation*, *JCAP* **0701** (2007) 002 [hep-th/0605045].

[93] R. Holman and A.J. Tolley, *Enhanced Non-Gaussianity from Excited Initial States*, *JCAP* **0805** (2008) 001 [arXiv:0710.1302].

[94] D.S. Salopek and J.R. Bond, *Nonlinear evolution of long wavelength metric fluctuations in inflationary models*, *Phys. Rev.* **D42** (1990) 3936.

[95] A. Gangui, F. Lucchin, S. Matarrese and S. Mollerach, *The Three point correlation function of the cosmic microwave background in inflationary models*, *Astrophys. J.* **430** (1994) 447 [astro-ph/9312033].

[96] L. Verde, L.M. Wang, A. Heavens and M. Kamionkowski, *Large scale structure, the cosmic microwave background, and primordial non-gaussianity*, *Mon. Not. Roy. Astron. Soc.* **313** (2000) L141 [astro-ph/9906301].

[97] E. Komatsu and D.N. Spergel, *Acoustic signatures in the primary microwave background bispectrum*, *Phys. Rev.* **D63** (2001) 063002 [astro-ph/0005036].

[98] P. Creminelli and M. Zaldarriaga, *Single field consistency relation for the 3-point function*, *JCAP* **0410** (2004) 006 [astro-ph/0407059].

[99] E. Pajer, F. Schmidt and M. Zaldarriaga, *The Observed Squeezed Limit of Cosmological Three-Point Functions*, *Phys. Rev.* **D88** (2013) 083502 [arXiv:1305.0824].

[100] G. Cabass, E. Pajer and F. Schmidt, *How Gaussian can our Universe be?*, *JCAP* **1701** (2017) 003 [arXiv:1612.00033].

[101] N. Bartolo, S. Matarrese and A. Riotto, *CMB Anisotropies at Second Order I*, *JCAP* **0606** (2006) 024 [astro-ph/0604416].

[102] N. Bartolo, S. Matarrese and A. Riotto, *CMB Anisotropies at Second-Order. 2. Analytical Approach*, *JCAP* **0701** (2007) 019 [astro-ph/0610110].

[103] C. Pitrou, *Gauge invariant Boltzmann equation and the fluid limit*, *Class. Quant. Grav.* **24** (2007) 6127 [arXiv:0706.4383].

[104] C. Pitrou, *The radiative transfer for polarized radiation at second order in cosmological perturbations*, *Gen. Rel. Grav.* **41** (2009) 2587 [arXiv:0809.3245].

[105] M. Beneke and C. Fidler, *Boltzmann hierarchy for the cosmic microwave background at second order including photon polarization*, *Phys. Rev.* **D82** (2010) 063509 [arXiv:1003.1834].

[106] A. Naruko, C. Pitrou, K. Koyama and M. Sasaki, *Second-order Boltzmann equation: gauge dependence and gauge invariance*, *Class. Quant. Grav.* **30** (2013) 165008 [arXiv:1304.6929].

[107] G.W. Pettinari, *The intrinsic bispectrum of the Cosmic Microwave Background*, Ph.D. thesis, Portsmouth U., ICG, 2013-09. arXiv:1405.2280. 10.1007/978-3-319-21882-3.

[108] U. Seljak and M. Zaldarriaga, *A Line of sight integration approach to cosmic microwave background anisotropies*, *Astrophys. J.* **469** (1996) 437 [astro-ph/9603033].

[109] J. Lesgourgues, *The Cosmic Linear Anisotropy Solving System (CLASS) I: Overview*, arXiv:1104.2932.

[110] W. Hu and M.J. White, *CMB anisotropies: Total angular momentum method*, *Phys. Rev.* **D56** (1997) 596 [astro-ph/9702170].

[111] J. Lesgourgues and S. Pastor, *Massive neutrinos and cosmology*, *Phys. Rept.* **429** (2006) 307 [astro-ph/0603494].

[112] W.H. Press and P. Schechter, *Formation of galaxies and clusters of galaxies by selfsimilar gravitational condensation*, *Astrophys. J.* **187** (1974) 425.

[113] J.A. Peacock and A.F. Heavens, *Alternatives to the Press-Schechter cosmological mass function*, *Mon. Not. Roy. Astron. Soc.* **243** (1990) 133.

[114] J.R. Bond, S. Cole, G. Efstathiou and N. Kaiser, *Excursion set mass functions for hierarchical Gaussian fluctuations*, *Astrophys. J.* **379** (1991) 440.

[115] P.P. Avelino and P.T.P. Viana, *The cloud-in-cloud problem for nonGaussian density fields*, *Mon. Not. Roy. Astron. Soc.* **314** (2000) 354 [astro-ph/9907209].

[116] R.K. Sheth, H.J. Mo and G. Tormen, *Ellipsoidal collapse and an improved model for the number and spatial distribution of dark matter haloes*, *Mon. Not. Roy. Astron. Soc.* **323** (2001) 1 [astro-ph/9907024].

[117] R.K. Sheth and G. Tormen, *An Excursion Set Model of Hierarchical Clustering : Ellipsoidal Collapse and the Moving Barrier*, *Mon. Not. Roy. Astron. Soc.* **329** (2002) 61 [astro-ph/0105113].

[118] M. Maggiore and A. Riotto, *The Halo Mass Function from Excursion Set Theory. I. Gaussian fluctuations with non-Markovian dependence on the smoothing scale*, *Astrophys. J.* **711** (2010) 907 [arXiv:0903.1249].

[119] J.L. Tinker, A.V. Kravtsov, A. Klypin, K. Abazajian, M.S. Warren, G. Yepes et al., *Toward a halo mass function for precision cosmology: The Limits of universality*, *Astrophys. J.* **688** (2008) 709 [arXiv:0803.2706].

[120] E. Komatsu and U. Seljak, *The Sunyaev-Zel'dovich angular power spectrum as a probe of cosmological parameters*, *Mon. Not. Roy. Astron. Soc.* **336** (2002) 1256 [astro-ph/0205468].

[121] Planck collaboration, N. Aghanim et al., *Planck 2015 results. XXII. A map of the thermal Sunyaev-Zeldovich effect*, *Astron. Astrophys.* **594** (2016) A22 [arXiv:1502.01596].

[122] N. Battaglia, J.R. Bond, C. Pfrommer and J.L. Sievers, *On the Cluster Physics of Sunyaev-Zel'dovich Surveys II: Deconstructing the Thermal SZ Power Spectrum*, *Astrophys. J.* **758** (2012) 75 [arXiv:1109.3711].

[123] P. Bode, J.P. Ostriker, R. Cen and H. Trac, *Calibration of Nonthermal Pressure in Global Dark Matter Simulations of Clusters of Galaxies*, arXiv:1204.1762.

[124] M. Arnaud, G.W. Pratt, R. Piffaretti, H. Boehringer, J.H. Croston and E. Pointecouteau, *The universal galaxy cluster pressure profile from a representative sample of nearby systems (REXCESS) and the Y_{SZ}-M_{500} relation*, *Astron. Astrophys.* **517** (2010) A92 [arXiv:0910.1234].

[125] N. Taburet, C. Hernández-Monteagudo, N. Aghanim, M. Douspis and R.A. Sunyaev, *The ISW-tSZ cross-correlation: integrated Sachs-Wolfe extraction out of pure cosmic microwave background data*, MNRAS **418** (Dec., 2011) 2207 [arXiv:1012.5036].

[126] J.C. Hill and E. Pajer, *Cosmology from the thermal Sunyaev-Zel'dovich power spectrum: Primordial non-Gaussianity and massive neutrinos*, *Phys. Rev.* **D88** (2013) 063526 [arXiv:1303.4726].

[127] J.D. Romano and N.J. Cornish, *Detection methods for stochastic gravitational-wave backgrounds: a unified treatment*, *Living Rev. Rel.* **20** (2017) 2 [arXiv:1608.06889].

[128] R. Trotta, *Bayesian Methods in Cosmology*, arXiv:1701.01467.

[129] A. Heavens, *Statistical techniques in cosmology*, arXiv:0906.0664.

[130] J. Hamann, S. Hannestad, G.G. Raffelt and Y.Y.Y. Wong, *Observational bounds on the cosmic radiation density*, *JCAP* **0708** (2007) 021 [arXiv:0705.0440].

[131] L. Verde, *A practical guide to Basic Statistical Techniques for Data Analysis in Cosmology*, *ArXiv e-prints* (Dec., 2007) [arXiv:0712.3028].

[132] N. Christensen and R. Meyer, *Using Markov chain Monte Carlo methods for estimating parameters with gravitational radiation data*, *Phys. Rev.* **D64** (2001) 022001 [gr-qc/0102018].

[133] C. Robert and G. Casella, *Monte Carlo Statistical Methods*, Springer (2005).

[134] C.W. Gardiner, *Handbook of Stochastic Methods: For Physics, Chemistry and Natural Sciences*, Springer (1985).

[135] A. Gelman and D.B. Rubin, *Inference from iterative simulation using multiple sequences*, *Statistical Science* **7** (1992).

[136] L. Verde, *A practical guide to Basic Statistical Techniques for Data Analysis in Cosmology*, arXiv:0712.3028.

[137] M. Zaldarriaga and U. Seljak, *An all sky analysis of polarization in the microwave background*, *Phys. Rev.* **D55** (1997) 1830 [astro-ph/9609170].

[138] D. Babich and M. Zaldarriaga, *Primordial bispectrum information from CMB polarization*, *Phys. Rev.* **D70** (2004) 083005 [astro-ph/0408455].

[139] D. Babich, *Optimal estimation of non-Gaussianity*, *Phys. Rev.* **D72** (2005) 043003 [astro-ph/0503375].

[140] J.R. Fergusson, M. Liguori and E.P.S. Shellard, *General CMB and Primordial*

Bispectrum Estimation I: Mode Expansion, Map-Making and Measures of $f_N L$, *Phys. Rev.* **D82** (2010) 023502 [arXiv:0912.5516].

[141] A.P.S. Yadav, E. Komatsu and B.D. Wandelt, *Fast Estimator of Primordial Non-Gaussianity from Temperature and Polarization Anisotropies in the Cosmic Microwave Background*, *Astrophys. J.* **664** (2007) 680 [astro-ph/0701921].

[142] E. Komatsu, D.N. Spergel and B.D. Wandelt, *Measuring primordial non-Gaussianity in the cosmic microwave background*, *Astrophys. J.* **634** (2005) 14 [astro-ph/0305189].

[143] C. Sealfon, L. Verde and R. Jimenez, *Smoothing spline primordial power spectrum reconstruction*, *Phys. Rev.* **D72** (2005) 103520 [astro-ph/0506707].

[144] L. Verde and H.V. Peiris, *On Minimally-Parametric Primordial Power Spectrum Reconstruction and the Evidence for a Red Tilt*, *JCAP* **0807** (2008) 009 [arXiv:0802.1219].

[145] H.V. Peiris and L. Verde, *The shape of the primordial power spectrum: A last stand before Planck data*, Phys. Rev. D **81** (Jan., 2010) 021302 [arXiv:0912.0268].

[146] Planck collaboration, P.A.R. Ade et al., *Planck 2015 results. XX. Constraints on inflation*, *Astron. Astrophys.* **594** (2016) A20 [arXiv:1502.02114].

[147] J.A. Vázquez, M. Bridges, M.P. Hobson and A.N. Lasenby, *Model selection applied to reconstruction of the Primordial Power Spectrum*, JCAP **6** (June, 2012) 006 [arXiv:1203.1252].

[148] C. Gauthier and M. Bucher, *Reconstructing the primordial power spectrum from the CMB*, JCAP **10** (Oct., 2012) 050 [arXiv:1209.2147].

[149] G. Aslanyan, L.C. Price, K.N. Abazajian and R. Easther, *The Knotted Sky I: Planck constraints on the primordial power spectrum*, *JCAP* **1408** (2014) 052 [arXiv:1403.5849].

[150] D.K. Hazra, A. Shafieloo and G.F. Smoot, *Reconstruction of broad features in the primordial spectrum and inflaton potential from Planck*, *JCAP* **1312** (2013) 035 [arXiv:1310.3038].

[151] E. Di Valentino, S. Gariazzo, M. Gerbino, E. Giusarma and O. Mena, *Dark Radiation and Inflationary Freedom after Planck 2015*, *Phys. Rev.* **D93** (2016) 083523 [arXiv:1601.07557].

[152] L. Verde, P. Protopapas and R. Jimenez, *Planck and the local Universe: Quantifying the tension*, *Phys. Dark Univ.* **2** (2013) 166 [arXiv:1306.6766].

[153] R.A. Battye and A. Moss, *Evidence for Massive Neutrinos from Cosmic Microwave Background and Lensing Observations*, *Phys. Rev. Lett.* **112** (2014) 051303 [arXiv:1308.5870].

[154] M. Wyman, D.H. Rudd, R.A. Vanderveld and W. Hu, *Neutrinos Help Reconcile Planck Measurements with the Local Universe*, *Phys. Rev. Lett.* **112** (2014) 051302 [arXiv:1307.7715].

[155] J. Hamann and J. Hasenkamp, *A new life for sterile neutrinos: resolving inconsistencies using hot dark matter*, *JCAP* **1310** (2013) 044 [arXiv:1308.3255].

[156] BOSS collaboration, F. Beutler et al., *The clustering of galaxies in the SDSS-III Baryon Oscillation Spectroscopic Survey: signs of neutrino mass in current cosmological data sets*, *Mon. Not. Roy. Astron. Soc.* **444** (2014) 3501 [arXiv:1403.4599].

[157] E. Giusarma, E. Di Valentino, M. Lattanzi, A. Melchiorri and O. Mena, *Relic Neutrinos, thermal axions and cosmology in early 2014*, *Phys. Rev.* **D90** (2014) 043507 [arXiv:1403.4852].

[158] Planck collaboration, P.A.R. Ade et al., *Planck 2013 results. XVI. Cosmological parameters*, *Astron. Astrophys.* **571** (2014) A16 [arXiv:1303.5076].

[159] S.M. Feeney, H.V. Peiris and L. Verde, *Is there evidence for additional neutrino species from cosmology?*, *JCAP* **1304** (2013) 036 [arXiv:1302.0014].

[160] J.W. Hu, R.G. Cai, Z.K. Guo and B. Hu, *Cosmological parameter estimation from CMB and X-ray cluster after Planck*, *JCAP* **1405** (2014) 020 [arXiv:1401.0717].

[161] L. Verde, S.M. Feeney, D.J. Mortlock and H.V. Peiris, *(Lack of) Cosmological evidence for dark radiation after Planck*, *JCAP* **1309** (2013) 013 [arXiv:1307.2904].

[162] G. Efstathiou, *H0 Revisited*, *Mon. Not. Roy. Astron. Soc.* **440** (2014) 1138 [arXiv:1311.3461].

[163] B. Leistedt, H.V. Peiris and L. Verde, *No new cosmological concordance with massive sterile neutrinos*, *Phys. Rev. Lett.* **113** (2014) 041301 [arXiv:1404.5950].

[164] A.J. Cuesta, V. Niro and L. Verde, *Neutrino mass limits: robust information from the power spectrum of galaxy surveys*, *Phys. Dark Univ.* **13** (2016) 77 [arXiv:1511.05983].

[165] N. Palanque-Delabrouille et al., *Neutrino masses and cosmology with Lyman-alpha forest power spectrum*, *JCAP* **1511** (2015) 011 [arXiv:1506.05976].

[166] P. Green and B. Silverman, *Nonparametric regression and generalized linear models: a roughness penalty approach*, Chapman & Hall (1994).

[167] C. De Boor, *A practical guide to splines*, vol. 27, Springer-Verlag New York (1978).

[168] D. Blas, J. Lesgourgues and T. Tram, *The Cosmic Linear Anisotropy Solving System (CLASS). Part II: Approximation schemes*, JCAP **7** (July, 2011) 034 [arXiv:1104.2933].

[169] B. Audren, J. Lesgourgues, K. Benabed and S. Prunet, *Conservative constraints on early cosmology with MONTE PYTHON*, JCAP **2** (Feb., 2013) 001 [arXiv:1210.7183].

[170] Planck collaboration, P.A.R. Ade et al., *Planck 2013 results. XV. CMB power spectra and likelihood*, *Astron. Astrophys.* **571** (2014) A15 [arXiv:1303.5075].

[171] Planck collaboration, N. Aghanim et al., *Planck 2015 results. XI. CMB power spectra, likelihoods, and robustness of parameters*, *Astron. Astrophys.* **594** (2016) A11 [arXiv:1507.02704].

[172] Planck collaboration, P.A.R. Ade et al., *Planck 2013 results. XVII. Gravitational lensing by large-scale structure*, *Astron. Astrophys.* **571** (2014) A17 [arXiv:1303.5077].

[173] C. Heymans, L. Van Waerbeke, L. Miller, T. Erben, H. Hildebrandt, H. Hoekstra et al., *CFHTLenS: the Canada-France-Hawaii Telescope Lensing Survey*, MNRAS **427** (Nov., 2012) 146 [arXiv:1210.0032].

[174] T. Erben, H. Hildebrandt, L. Miller, L. van Waerbeke, C. Heymans, H. Hoekstra et al., *CFHTLenS: the Canada-France-Hawaii Telescope Lensing Survey - imaging data and catalogue products*, MNRAS **433** (Aug., 2013) 2545 [arXiv:1210.8156].

[175] L. Miller, C. Heymans, T.D. Kitching, L. van Waerbeke, T. Erben, H. Hildebrandt et al., *Bayesian galaxy shape measurement for weak lensing surveys - III. Application to the Canada-France-Hawaii Telescope Lensing Survey*, MNRAS **429**

(Mar., 2013) 2858 [arXiv:1210.8201].

[176] H. Hildebrandt, T. Erben, K. Kuijken, L. van Waerbeke, C. Heymans, J. Coupon et al., *CFHTLenS: improving the quality of photometric redshifts with precision photometry*, MNRAS **421** (Apr., 2012) 2355 [arXiv:1111.4434].

[177] C. Heymans, B. Rowe, H. Hoekstra, L. Miller, T. Erben, T. Kitching et al., *The impact of high spatial frequency atmospheric distortions on weak-lensing measurements*, MNRAS **421** (Mar., 2012) 381 [arXiv:1110.4913].

[178] J. Benjamin, L. Van Waerbeke, C. Heymans, M. Kilbinger, T. Erben, H. Hildebrandt et al., *CFHTLenS tomographic weak lensing: quantifying accurate redshift distributions*, MNRAS **431** (May, 2013) 1547 [arXiv:1212.3327].

[179] Planck collaboration, P.A.R. Ade et al., *Planck 2013 results. XX. Cosmology from Sunyaev–Zeldovich cluster counts*, *Astron. Astrophys.* **571** (2014) A20 [arXiv:1303.5080].

[180] N. MacCrann, J. Zuntz, S. Bridle, B. Jain and M.R. Becker, *Cosmic Discordance: Are Planck CMB and CFHTLenS weak lensing measurements out of tune?*, *Mon. Not. Roy. Astron. Soc.* **451** (2015) 2877 [arXiv:1408.4742].

[181] S. Joudaki et al., *CFHTLenS revisited: assessing concordance with Planck including astrophysical systematics*, *Mon. Not. Roy. Astron. Soc.* **465** (2017) 2033 [arXiv:1601.05786].

[182] T.D. Kitching, L. Verde, A.F. Heavens and R. Jimenez, *Discrepancies between CFHTLenS cosmic shear and Planck: new physics or systematic effects?*, *Mon. Not. Roy. Astron. Soc.* **459** (2016) 971 [arXiv:1602.02960].

[183] A. Choi, C. Heymans, C. Blake, H. Hildebrandt, C.A.J. Duncan, T. Erben et al., *CFHTLenS and RCSLenS: Testing Photometric Redshift Distributions Using Angular Cross-Correlations with Spectroscopic Galaxy Surveys*, *Mon. Not. Roy. Astron. Soc.* **463** (2016) 3737 [arXiv:1512.03626].

[184] D.J. Schwarz, C.J. Copi, D. Huterer and G.D. Starkman, *CMB Anomalies after Planck*, *Class. Quant. Grav.* **33** (2016) 184001 [arXiv:1510.07929].

[185] C.J. Copi, D. Huterer, D.J. Schwarz and G.D. Starkman, *Lack of large-angle TT correlations persists in WMAP and Planck*, *Mon. Not. Roy. Astron. Soc.* **451** (2015) 2978 [arXiv:1310.3831].

[186] C. He, D. Grin and W. Hu, *Compensated isocurvature perturbations in the curvaton model*, *Phys. Rev.* **D92** (2015) 063018 [arXiv:1505.00639].

[187] A. De Simone and T. Kobayashi, *Cosmological Aspects of Spontaneous Baryogenesis*, *JCAP* **1608** (2016) 052 [arXiv:1605.00670].

[188] D. Grin, O. Dore and M. Kamionkowski, *Compensated Isocurvature Perturbations and the Cosmic Microwave Background*, *Phys. Rev.* **D84** (2011) 123003 [arXiv:1107.5047].

[189] J.B. Munoz, D. Grin, L. Dai, M. Kamionkowski and E.D. Kovetz, *Search for Compensated Isocurvature Perturbations with Planck Power Spectra*, *Phys. Rev.* **D93** (2016) 043008 [arXiv:1511.04441].

[190] C. Heinrich, *Lensing bias to CMB polarization measurements of compensated isocurvature perturbations*, *Phys. Rev.* **D97** (2018) 023513 [arXiv:1708.01276].

[191] J. Valiviita, *Power Spectra Based Planck Constraints on Compensated Isocurvature, and Forecasts for LiteBIRD and CORE Space Missions*, *JCAP* **1704** (2017) 014 [arXiv:1701.07039].

[192] D. Grin, D. Hanson, G.P. Holder, O. Doré and M. Kamionkowski, *Baryons do trace dark matter 380,000 years after the big bang: Search for compensated isocurvature perturbations with WMAP 9-year data*, *Phys. Rev.* **D89** (2014) 023006 [arXiv:1306.4319].

[193] CMB-S4 collaboration, K.N. Abazajian et al., *CMB-S4 Science Book, First Edition*, arXiv:1610.02743.

[194] M.T. Soumagnac, R. Barkana, C.G. Sabiu, A. Loeb, A.J. Ross, F.B. Abdalla et al., *Large-Scale Distribution of Total Mass versus Luminous Matter from Baryon Acoustic Oscillations: First Search in the Sloan Digital Sky Survey III Baryon Oscillation Spectroscopic Survey Data Release 10*, *Phys. Rev. Lett.* **116** (2016) 201302 [arXiv:1602.01839].

[195] M.T. Soumagnac, C.G. Sabiu, R. Barkana and J. Yoo, *Large scale distribution of mass versus light from Baryon Acoustic Oscillations: Measurement in the final SDSS-III BOSS Data Release 12*, arXiv:1802.10368.

[196] C. Gordon and J.R. Pritchard, *Forecasted 21 cm constraints on compensated isocurvature perturbations*, *Phys. Rev.* **D80** (2009) 063535 [arXiv:0907.5400].

[197] A. Stebbins, *CMB Spectral Distortions from the Scattering of Temperature Anisotropies*, *Submitted to: Phys. Rev. D* (2007) [astro-ph/0703541].

[198] C. Pitrou and A. Stebbins, *Parameterization of temperature and spectral distortions in future CMB experiments*, *Gen. Rel. Grav.* **46** (2014) 1806 [arXiv:1402.0968].

[199] A. Ota, *CMB spectral distortions as solutions to the Boltzmann equations*, *JCAP* **1701** (2017) 037 [arXiv:1611.08058].

[200] J. Chluba and D. Grin, *CMB spectral distortions from small-scale isocurvature fluctuations*, *Mon. Not. Roy. Astron. Soc.* **434** (2013) 1619 [arXiv:1304.4596].

[201] D. Blas, J. Lesgourgues and T. Tram, *The Cosmic Linear Anisotropy Solving System (CLASS) II: Approximation schemes*, *JCAP* **1107** (2011) 034 [arXiv:1104.2933].

[202] A. Kompaneets, *The Establishment of Thermal Equilibrium between Quanta and Electrons*, *Sov. Phys.* **JETP 4, 730** (1957) 730.

[203] L. Senatore, S. Tassev and M. Zaldarriaga, *Cosmological Perturbations at Second Order and Recombination Perturbed*, *JCAP* **0908** (2009) 031 [arXiv:0812.3652].

[204] S. Naoz and R. Barkana, *Growth of linear perturbations before the era of the first galaxies*, *Mon. Not. Roy. Astron. Soc.* **362** (2005) 1047 [astro-ph/0503196].

[205] B. Novosyadlyj, *Perturbations of ionization fractions at the cosmological recombination epoch*, *Mon. Not. Roy. Astron. Soc.* **370** (2006) 1771 [astro-ph/0603674].

[206] A. Lewis and A. Challinor, *The 21cm angular-power spectrum from the dark ages*, *Phys. Rev.* **D76** (2007) 083005 [astro-ph/0702600].

[207] A. Lewis, *Linear effects of perturbed recombination*, *Phys. Rev.* **D76** (2007) 063001 [arXiv:0707.2727].

[208] A. Kogut, D. Fixsen, D. Chuss, J. Dotson, E. Dwek et al., *The Primordial Inflation Explorer (PIXIE): A Nulling Polarimeter for Cosmic Microwave Background Observations*, *JCAP* **1107** (2011) 025 [arXiv:1105.2044].

[209] PRISM collaboration, P. André et al., *PRISM (Polarized Radiation Imaging and Spectroscopy Mission): An Extended White Paper*, *JCAP* **1402** (2014) 006

[arXiv:1310.1554].

[210] T. Matsumura et al., *Mission design of LiteBIRD*, arXiv:1311.2847.

[211] C. Creque-Sarbinowski, S. Bird and M. Kamionkowski, *Cross-correlation between thermal Sunyaev-Zeldovich effect and the integrated Sachs-Wolfe effect*, *Phys. Rev.* **D94** (2016) 063519 [arXiv:1606.00839].

[212] A. Ravenni, M. Liguori, N. Bartolo and M. Shiraishi, *Primordial non-Gaussianity with μ-type and y-type spectral distortions: exploiting Cosmic Microwave Background polarization and dealing with secondary sources*, *JCAP* **1709** (2017) 042 [arXiv:1707.04759].

[213] M. Remazeilles and J. Chluba, *Extracting foreground-obscured μ-distortion anisotropies to constrain primordial non-Gaussianity*, arXiv:1802.10101.

[214] B. Bolliet, B. Comis, E. Komatsu and J.F. Macias-Perez, *Dark Energy from the Thermal Sunyaev Zeldovich Power Spectrum*, arXiv:1712.00788.

[215] L. Salvati, M. Douspis and N. Aghanim, *Constraints from thermal Sunyaev-Zeldovich cluster counts and power spectrum combined with CMB*, arXiv:1708.00697.

[216] G. Hurier and F. Lacasa, *Combined analysis of galaxy cluster number count, thermal Sunyaev-Zel'dovich power spectrum, and bispectrum*, *Astron. Astrophys.* **604** (2017) A71 [arXiv:1701.09067].

[217] A. Cooray, *Integrated sachs-wolfe effect: Large scale structure correlation*, *Phys. Rev. D* **65** (Apr, 2002) 103510, http://link.aps.org/doi/10.1103/PhysRevD.65.103510.

[218] J.L. Tinker, B.E. Robertson, A.V. Kravtsov, A. Klypin, M.S. Warren, G. Yepes et al., *The Large-scale Bias of Dark Matter Halos: Numerical Calibration and Model Tests*, ApJ **724** (Dec., 2010) 878 [arXiv:1001.3162].

[219] WMAP collaboration, E. Komatsu et al., *First year Wilkinson Microwave Anisotropy Probe (WMAP) observations: tests of gaussianity*, *Astrophys. J. Suppl.* **148** (2003) 119 [astro-ph/0302223].

[220] M. Liguori, S. Matarrese and L. Moscardini, *High-resolution simulations of cosmic microwave background non-gaussian maps in spherical coordinates*, *Astrophys. J.* **597** (2003) 57 [astro-ph/0306248].

[221] J. Ganc and E. Komatsu, *Scale-dependent bias of galaxies and mu-type distortion of the cosmic microwave background spectrum from single-field inflation with a modified initial state*, *Phys.Rev.* **D86** (2012) 023518 [arXiv:1204.4241].

[222] eROSITA collaboration, A. Merloni et al., *eROSITA Science Book: Mapping the Structure of the Energetic Universe*, arXiv:1209.3114.

[223] CORE collaboration, F. Finelli et al., *Exploring Cosmic Origins with CORE: Inflation*, arXiv:1612.08270.

[224] N. Dalal, O. Dore, D. Huterer and A. Shirokov, *The imprints of primordial non-gaussianities on large-scale structure: scale dependent bias and abundance of virialized objects*, *Phys. Rev.* **D77** (2008) 123514 [arXiv:0710.4560].

[225] S. Matarrese and L. Verde, *The effect of primordial non-Gaussianity on halo bias*, *Astrophys. J.* **677** (2008) L77 [arXiv:0801.4826].

[226] M. Biagetti, H. Perrier, A. Riotto and V. Desjacques, *Testing the running of non-Gaussianity through the CMB μ-distortion and the halo bias*, *Phys.Rev.* **D87** (2013) 063521 [arXiv:1301.2771].

[227] K. Miyamoto, T. Sekiguchi, H. Tashiro and S. Yokoyama, *CMB distortion anisotropies due to the decay of primordial magnetic fields*, *Phys.Rev.* **D89** (2014) 063508 [arXiv:1310.3886].

[228] K.E. Kunze and E. Komatsu, *Constraining primordial magnetic fields with distortions of the black-body spectrum of the cosmic microwave background: pre- and post-decoupling contributions*, *JCAP* **1401** (2014) 009 [arXiv:1309.7994].

[229] J. Ganc and M.S. Sloth, *Probing correlations of early magnetic fields using mu-distortion*, *JCAP* **1408** (2014) 018 [arXiv:1404.5957].

[230] A. Ota, T. Sekiguchi, Y. Tada and S. Yokoyama, *Anisotropic CMB distortions from non-Gaussian isocurvature perturbations*, *JCAP* **1503** (2015) 013 [arXiv:1412.4517].

[231] M. Shiraishi, M. Liguori, N. Bartolo and S. Matarrese, *Measuring primordial anisotropic correlators with CMB spectral distortions*, *Phys. Rev.* **D92** (2015) 083502 [arXiv:1506.06670].

[232] N. Bartolo, M. Liguori and M. Shiraishi, *Primordial trispectra and CMB spectral distortions*, *JCAP* **1603** (2016) 029 [arXiv:1511.01474].

[233] A. Ota, *Cosmological constraints from μE cross-correlations*, *Phys. Rev.* **D94** (2016) 103520 [arXiv:1607.00212].

[234] G.W. Pettinari, C. Fidler, R. Crittenden, K. Koyama and D. Wands, *The intrinsic bispectrum of the cosmic microwave background*, *J. Cosmology Astropart. Phys.* **4** (Apr., 2013) 3 [arXiv:1302.0832].

[235] G.W. Pettinari, C. Fidler, R. Crittenden, K. Koyama, A. Lewis and D. Wands, *Impact of polarization on the intrinsic cosmic microwave background bispectrum*, *Phys. Rev. D* **90** (Nov, 2014) 103010 [arXiv:1406.2981], http://link.aps.org/doi/10.1103/PhysRevD.90.103010.

[236] G.W. Pettinari, *The Intrinsic Bispectrum of the Cosmic Microwave Background*, Springer Theses, Springer International Publishing (2015), 10.1088/1475-7516/2013/04/003, http://www.springer.com/gp/book/9783319218816.

[237] J. Chluba, E. Dimastrogiovanni, M.A. Amin and M. Kamionkowski, *Evolution of CMB spectral distortion anisotropies and tests of primordial non-Gaussianity*, arXiv:1610.08711.

[238] J. Chluba, *Which spectral distortions does ΛCDM actually predict?*, *Mon. Not. Roy. Astron. Soc.* **460** (2016) 227 [arXiv:1603.02496].

[239] S. Renaux-Petel, C. Fidler, C. Pitrou and G.W. Pettinari, *Spectral distortions in the cosmic microwave background polarization*, *JCAP* **1403** (2014) 033 [arXiv:1312.4448].

[240] W.T. Hu, *Wandering in the Background: A CMB Explorer*, Ph.D. thesis, UC, Berkeley, 1995. astro-ph/9508126.

[241] R. Mehrem, J.T. Londergan and M.H. Macfarlane, *Analytic expressions for integrals of products of spherical Bessel functions*, *Journal of Physics A: Mathematical and General* **24** (1991) 1435, http://stacks.iop.org/0305-4470/24/i=7/a=018.

[242] M.H. Abitbol, J. Chluba, J.C. Hill and B.R. Johnson, *Prospects for Measuring Cosmic Microwave Background Spectral Distortions in the Presence of Foregrounds*, arXiv:1705.01534.

[243] A. Manzotti and S. Dodelson, *Mapping the Integrated Sachs-Wolfe Effect*, *Phys.*

Rev. **D90** (2014) 123009 [arXiv:1407.5623].

[244] J.C. Hill and D.N. Spergel, *Detection of thermal SZ-CMB lensing cross-correlation in Planck nominal mission data*, *JCAP* **1402** (2014) 030 [arXiv:1312.4525].

[245] L. Van Waerbeke, G. Hinshaw and N. Murray, *Detection of warm and diffuse baryons in large scale structure from the cross-correlation of gravitational lensing and the thermal Sunyaev-Zeldovich effect*, *Phys. Rev.* **D89** (2014) 023508 [arXiv:1310.5721].

[246] Y.Z. Ma, L. Van Waerbeke, G. Hinshaw, A. Hojjati, D. Scott and J. Zuntz, *Probing the diffuse baryon distribution with the lensing-tSZ cross-correlation*, *JCAP* **1509** (2015) 046 [arXiv:1404.4808].

[247] C.T. Byrnes, M. Gerstenlauer, S. Nurmi, G. Tasinato and D. Wands, *Scale-dependent non-Gaussianity probes inflationary physics*, *JCAP* **1010** (2010) 004 [arXiv:1007.4277].

[248] A. Becker and D. Huterer, *First constraints on the running of non-Gaussianity*, *Phys. Rev. Lett.* **109** (2012) 121302 [arXiv:1207.5788].

[249] A. Buckley, *The hepthesis LaTeX class*, .

List of figures

List of tables